



HAL
open science

Development of mechanical characterization tests at very high temperature with contactless instrumentation : Application to the identification by inverse analysis of the behavior of In718 nickel-based superalloy under conditions of additive manufacturing by LPBF process

Feng Gao

► **To cite this version:**

Feng Gao. Development of mechanical characterization tests at very high temperature with contactless instrumentation : Application to the identification by inverse analysis of the behavior of In718 nickel-based superalloy under conditions of additive manufacturing by LPBF process. Mechanics of materials [physics.class-ph]. Université Paris sciences et lettres, 2021. English. NNT : 2021UPSLM045 . tel-03772722

HAL Id: tel-03772722

<https://pastel.hal.science/tel-03772722>

Submitted on 8 Sep 2022

HAL is a multi-disciplinary open access archive for the deposit and dissemination of scientific research documents, whether they are published or not. The documents may come from teaching and research institutions in France or abroad, or from public or private research centers.

L'archive ouverte pluridisciplinaire **HAL**, est destinée au dépôt et à la diffusion de documents scientifiques de niveau recherche, publiés ou non, émanant des établissements d'enseignement et de recherche français ou étrangers, des laboratoires publics ou privés.

THÈSE DE DOCTORAT
DE L'UNIVERSITÉ PSL

Préparée à MINES ParisTech

Development of mechanical characterization tests at very high temperature with contactless instrumentation. Application to the identification by inverse analysis of the behavior of In718 nickel-based superalloy under conditions of additive manufacturing by LPBF process

Développement d'essais de caractérisation mécanique à très haute température avec instrumentation sans contact. Application à l'identification par analyse inverse du comportement du superalliage base nickel In718 en condition de fabrication additive par le procédé L-PBF

Soutenue par

Feng GAO

Le 27 juillet 2021

Ecole doctorale n° 364

**SCIENCES
FONDAMENTALES ET
APPLIQUÉES**

Spécialité

**MÉCANIQUE NUMÉRIQUE ET
MATÉRIAUX**

Jury:

Jean-Michel BERGHEAU Prof., École nationale d'ingénieurs de Saint-Étienne	Président
Daniel NELIAS Prof., INSA Lyon	Rapporteur
Philippe Dal SANTO Prof., Arts et Métiers ParisTech	Rapporteur
Yuanyuan LU Associate professor, Beihang University	Examineur
Yancheng ZHANG Chargé de recherche, Mines ParisTech	Examineur
Michel BELLET Prof., Mines ParisTech	Directeur de thèse

Acknowledgments

Above all, I would like to give my sincere thanks to Prof. Michel BELLET, associate Prof. Yancheng ZHANG, and Dr. Bruno MACQUAIRE for their guidance in my Ph. D project. Whenever there is crossroads they can provide me with signpost, whenever there is fog they will equip me with torch light, so that I can go through the mysteries. Special thanks to Michel for offering training of mechanics and the way to research, to Yancheng for training of coding, and to Bruno for engineering guidance.

Afterwards, let me sing a song of grateful words to the individuals in Cemef to (of academic help) Mr. Sélim KRARIA, Mr. Christophe PRADILLE, Mr. Emile ROUX, Mr. Yannick TILLIER, Mr. Qiang CHEN, (of technical help) Mr. Arnaud PIGNOLET, Mr. Gilbert FIORUCCI, Mr. Francis FOURNIER, Mr. Erick BROTONS, Mr. Cyrille COLLIN, Ms. Suzanne JACOMET, Mr. Emile HAZEMANN, Mr. Karim INAL, Mr. Guillaume CORVEC for their kind and patient assistance during the process of this project.

Also, my heart beats with appreciation for the aids from Mr. Ning DANG who introduced this project to me, from (Cemef staff) Ms. Marie-Françoise GUENEGAN, Mr. Patric COELS, Ms. Florence MORCAMP, Ms. Elena-Roxana POPESCU, Ms. Christelle COMBEAUD who assist my administration issues in France, from Mr. Shaojie ZHANG, Mr. Qichao MA, Mr. Rou DU, Mr. Di LI who cheered me up in my initial hard and dark days in France.

And I am obliged to appreciate the supports from my parents, and I am grateful to Ms. Yifan MA and (Mr.) Malo for the companion in France. I thank Mr. Haiping ZHANG and Mr. Yanbo SUN for their trust on me. I owe my thanks to the staff in Chinese Embassy in France for the “sanitation package”, and to Ms. Jing SHI for her overseas mailing of masks at the beginning of the epidemic of Covid-19.

As a strong fundamental, it is never too much to use grateful words to CSC and Armies for their financial support, for either individual or the project. It is an impossible mission without your funding.

At last, I would thank all the people coming and going during these years for the direct and non-direct help and assistance. You may be not here in the manuscript, because you are born in my mind.

Contents

Context and Objective.....	1
1.1 Problematics in LPBF Processing.....	1
1.2 Features of the Objective Rheological Law.....	3
1.2.1 Wide Temperature Range.....	3
1.2.2 Low Strain Range during the Solidification Period in AM Process.....	4
1.2.3 Varying Strain Rates.....	4
1.2.4 Applicable to Cyclic Stress Condition.....	4
1.2.5 Elastic-viscoplastic.....	4
1.2.6 Transverse Isotropy.....	5
1.2.7 As-Built Condition.....	5
1.3 Structure of the Manuscript.....	5
1.4 Appeals.....	6
Experimental Part.....	12
2.1 Description of Home-developed Machine.....	12
2.2 Specimen Design.....	14
2.2.1 Reminder on Resistive Heating: Governing Equations.....	14
2.2.2 Sample Shape and Geometry Optimization.....	15
2.3 Temperature Signal, Control and Calibration.....	18
2.3.1 Temperature Signals/Measurements.....	18
2.3.1.1 Thermocouple.....	18
2.3.1.2 Bichromatic Pyrometer.....	19
2.3.1.3 Bichromatic Infrared Camera.....	22

2.3.2 Temperature Control.....	22
2.3.2.1 PID and Parameter Selection.....	22
2.3.2.2 Selection of Signal for Temperature Control.....	24
2.3.3 Calibration of Temperature Field from IR Camera.....	24
2.4 Displacement Measurement.....	27
2.4.1 Introduction to DIC measurement.....	27
2.4.2 Camera positioning.....	29
2.4.3 High Temperature DIC.....	30
2.4.4 Atmosphere during Displacement Measurement.....	31
2.4.5 DIC Measuring Condition Summary.....	32
2.5 Testing Preparation.....	33
2.5.1 Geometry Refinement.....	33
2.5.2 Surface Pre-treatment.....	34
2.5.3 Geometry Measurement.....	35
2.5.4 Preparation of Speckle.....	35
2.5.5 Thermo-couple Welding and Testing.....	36
2.6 Illustration of an Experimental Test.....	36
2.7 Chapter Summary.....	39
Numerical Implementation.....	42
3.1 Brief Introduction of the FEM Frame.....	43
3.2 Governing Equations.....	44
3.3 Thermo-Elastic-viscoplastic (TEVP) Constitutive Model.....	45
3.3.1 General Formulation of an Anisotropic Elastic-viscoplastic Behavior Law.....	45
3.3.2 Temperature Effect on Viscoplastic Strain Rate Hardening.....	51

3.3.3	Temperature Effect on Initial Yield Stress and Isotropic Strain Hardening.....	51
3.3.4	Effect of Static Recovery.....	53
3.4	Incremental Resolution in the Context of a Velocity-Pressure Formulation.....	55
3.4.1	Decomposition in Deviatoric and Spherical Parts.....	55
3.4.1.1	Deviatoric part.....	55
3.4.1.2	Spherical part.....	55
3.4.2	Time Discretization.....	56
3.5	Steps of Building a Direct Simulation.....	58
3.5.1	Select a ZOI.....	59
3.5.2	Create a Mesh.....	60
3.5.2.1	Create a Mesh Configuration.....	60
3.5.2.2	Optimize the Mesh Size.....	62
3.5.3	Temporally Simulation Sequence.....	63
3.5.3.1	Incremental Time Step.....	63
3.5.3.2	Updating $T(z)$ and Corresponding Parameters.....	63
3.5.3.3	Mechanical Resolution and Boundary Conditions.....	63
3.5.4	Outputs from Calculation.....	64
3.6	Imposing Experimental Data to Simulation.....	64
3.6.1	Reference Frame Transformation.....	64
3.6.1.1	Set up RF^{sim} from RF^{DIC}	64
3.6.1.2	Projection of Temperature Field from RF^{IR} to RF^{sim}	67
3.6.2	Boundary Conditions.....	70
3.6.2.1	Boundary Condition for Imposing Loading Information.....	70

3.6.2.2 Boundary Conditions to Avoid Rigid Movement.....	71
3.6.3 Pretreatment and Imposing of Temperature Field.....	71
3.6.3.1 Pretreatment of T Field before RF Transformation.....	71
3.6.3.2 Temperature Field Storage and Imposing.....	72
3.7 Self-Consistence of the Local Simulation Strategy.....	73
3.8 Chapter Summary.....	74
Optimization for Identification of Constitutive Parameters.....	78
4.1 Optimization Strategy.....	78
4.2 Introduction of MOOPI.....	79
4.3 Building a Cost Function.....	80
4.3.1 Interpolate the Simulation Data.....	80
4.3.2 Temporal Weights.....	80
4.3.3 Candidates for Cost Function.....	81
4.4 Database and Settings of Optimization.....	82
4.4.1 Database of Optimization.....	82
4.4.2 Settings of Optimization.....	84
4.5 Optimization Results.....	85
4.5.1 Choice of the Final Cost Function.....	85
4.5.2 Optimization Result with NMAE.....	87
4.5.3 Optimized Parameters and Correlation.....	89
4.5.3.1 Q_1 and Q_2	89
4.5.3.2 Correlation of $\sigma_{Y,ref}$, $Q_{r,ref}$ and b	90
4.5.3.3 Correlation of k_{ref} and m	91

4.5.4 Final Results.....	92
4.6 Testing of Characterized Rheological Law.....	94
4.6.1 Verifying Test Design.....	94
4.6.2 Experimental and Simulation Results.....	95
4.7 Chapter Summary.....	97
Probe into Anisotropy.....	100
5.1 Orientation of the Material.....	102
5.2 Two Strategies to Calculate Hill48 Parameters.....	103
5.2.1 Direct Strategy.....	103
5.2.1.1 r Method.....	103
5.2.1.2 σ Method.....	107
5.2.2 Inverse Strategy.....	108
5.3 On Direct Strategy.....	108
5.3.1 Determination of Hill's Parameters at 1100°C by r Method.....	108
5.3.2 Characterization of Rheological Law on Preset Hill's Parameters.....	110
5.4 On Inverse Strategy.....	111
5.4.1 Alternated Optimization Method.....	111
5.4.2 Cost Function by Both Force and Deformation.....	112
5.4.3 On Inverse Strategy at All Temperature Levels and All Orientations.....	113
5.4.4 Optimization Results.....	115
5.4.5 Influence of Cost Function Components.....	118
5.4.6 Final Optimized Parameters.....	119
5.5 Exploration of the Source of the Anisotropy Evolution.....	125

5.5.1 Residual Stress.....	125
5.5.1.1 Residual Stress Removal during Heating with Free Expansion.....	126
5.5.1.2 Tensile Tests on Samples with/without Solution Treatment.....	126
5.5.2 Back Stress.....	129
5.5.3 Microstructure Evolution.....	132
5.6 Chapter Summary.....	133
Conclusions and Prospects.....	137
6.1 Conclusions.....	137
6.2 Prospects.....	138
Appendices.....	141
A. 1 How to well weld a thermocouple.....	141
A. 2 How to Apply the Speckle onto the Sample Surface.....	143
A. 2.1 Pre-treatment by Sand-blasting.....	143
A. 2.2 Brush spattering.....	143
A. 3 Method to Calculate the Dot Areas in a Speckle.....	143
A. 4 Influence of Wavelength on a Shape Image for the Post-calibration.....	144
A. 4.1 Focal Length as a Function of Refractive Index.....	144
A. 4.2 Refractive Index as Function of Wavelength.....	145
A. 4.3 Focusing Influenced by Wavelength.....	146
A. 4.4 Small Aperture Influences.....	146
A. 5 Typical Temperature Variation during Test.....	147
A. 6 Why We Can Deem That through the Thickness the Temperature Is Uniform.....	148
A. 7 Data Smoothing Method for Displacement.....	151
A. 8 Improvement Work since the Beginning of the Project.....	154

A. 8.1 Automatic Changing of Temperature Control Signal.....	154
A. 8.2 Water Cooling System.....	156
A. 8.3 Blue Lighting System.....	157
A. 9 Infrared Camera Coordinates, from Pixels to Millimeters.....	158
A. 10 Optimization within Orientation Based on von Mises.....	160
A. 11 Calculating Lankford Coefficient.....	162
A. 12 Calculation of Young's Modulus for Transverse Isotropy.....	169
A. 12.1 FR transformation for Strain and Stress Tensors.....	169
A. 12.2 Application of Transverse Isotropy of Young's Module.....	172
A. 12.3 Find Apparent Young's Modulus in a Given Direction.....	174
A. 13 Why Only Exponential Part of Rheological Law Is Enough.....	176
A. 14 Demonstration of $F + 2H = N$	177
A. 15 Scheil Summation to Predict Nucleation of γ' Phase.....	179
A. 16 Error Analysis.....	181
A. 16.1 Source of Errors.....	182
A. 16.1.1 Error Introduced by Geometry Measurement.....	182
A. 16.1.2 Error Introduced by Temperature Measurement.....	182
A. 16.1.3 Error Introduced by Displacement Measurement.....	183
A. 16.1.4 Error Introduced by Force Measurement.....	184
A. 16.2 Influence on Calculation Results.....	184

Nomenclature

Acronyms and Abbreviations (in alphabet)

AM	Additive Manufacturing
BP	Bichromatic Pyrometer
CCD	Charge-Coupled Device
Cemef	Centre de mise en forme des matériaux
CMOS	Complementary Metal–Oxide–Semiconductor
Dedimet	Deformation Dilatation des Métaux
DIC	Digital Image Correlation
DOE	Design of Experiments
EI	Expected Improvement
EGO	Efficient Global Optimization
FEM	Finite Element Method
IR	Infrared
LPBF	Laser Powder Bed Fusion
NMAE	Normalized Mean Absolute Error
MOOPI	MOdular software for Optimization and Parameters Identification
MAPE	Mean Absolute Percentage Error
NMALE	Normalized Mean Absolute Logarithmic Error
PBF	Power Bed Fusion
PID	Proportional–Integral–Derivative
RF	Reference Frame

RT	Room Temperature
TC	Thermocouple
TEC	Thermal expansion coefficient
TEVP	Thermo-Elasto-viscoplastic
ZNSSD	Zero-mean normalized sum of squared differences
ZOI	Zone of Interest

Scalars (*in light italic*)

Symbol	Meaning	unit
$B_{\lambda}^0(T)$	Black body spectral radiance at wavelength λ at temperature T	$\text{W}\cdot\text{m}^{-3}\cdot\text{sr}^{-1}$
$B_{\lambda}(T)$	Grey body spectral radiance at wavelength λ at temperature T	$\text{W}\cdot\text{m}^{-3}\cdot\text{sr}^{-1}$
C	Material parameter related to kinematic hardening	Pa
C_p	Specific heat capacity at constant pressure	$\text{J}\cdot\text{K}^{-1}\cdot\text{kg}^{-1}$
E	Young's Modulus	Pa
H	Strain hardening coefficient	Pa
H_{ref}	Pre-exponential factor of Arrhenius relation for H	Pa
K	Material parameter associated with static recovery softening	—
M	Taylor factor	—
Q	Internal energy	$\text{J}\cdot\text{m}^{-3}$
Q_r	Constant associated with dynamic recovery hardening	Pa
$Q_{r,ref}$	Pre-exponential factor of Arrhenius relation for Q_r	Pa
Q_{vp}	Activation energy of phenomena governing viscoplastic flow	$\text{J}\cdot\text{mol}^{-1}$

Q_g	Activation energy of dislocation gliding phenomenon	$\text{J}\cdot\text{mol}^{-1}$
Q_c	Activation energy of dislocation climbing phenomenon	$\text{J}\cdot\text{mol}^{-1}$
Q_1, Q_2, \bar{Q}	“Averaged” activation energies	$\text{J}\cdot\text{mol}^{-1}$
R	Isotropic hardening function	Pa
R_g	Gas constant	$\text{J}\cdot\text{mol}^{-1}\cdot\text{K}^{-1}$
T	Temperature	K, °C
T_{IR}	Temperature measured by IR camera	K, °C
T_{TC}	Temperature measured by thermocouple	K, °C
T_s	Sample temperature at starting moment of tensile test	K, °C
T_{ext}	Environment temperature	K, °C
$T_{set}(t)$	Set (objective) temperature at time t	K, °C
$T_{exp}(t)$	Measured experimental temperature at time t	K, °C
T_0	Room temperature	K, °C
\hat{T}	Estimated temperature	K, °C
U	electric potential	V
V	volume	m^3
b	Constant associated with dynamic recovery	—
c	Light speed	$\text{m}\cdot\text{s}^{-1}$
b_d	Module of the Burgers vector	m
$e(t)$	temperature bias, $e(t) = T_{set}(t) - T_{exp}(t)$	°C
e_0	Sample thickness measured at room temperature	m
e_s	Sample thickness at starting moment of tensile test	m

h	Free energy contributed by plastic deformation	$\text{J}\cdot\text{m}^{-1}$
h_p	Planck's constant	$\text{J}\cdot\text{s}$
h_c	Convective heat transfer coefficient	$\text{W}\cdot\text{m}^{-2}\cdot\text{K}^{-1}$
$i(t)$	Current to be imposed in the sample at instant t	A
k_p, k_i, k_d	PID constants	—
k_1	Constant associated with dislocation gliding	—
k_2	Variable associated with dislocation climbing	—
k_c	Thermal conductivity	$\text{W}\cdot\text{m}^{-1}\cdot\text{K}^{-1}$
m	Strain rate sensitivity	—
n	Strain hardening exponent	—
p	Hydrostatic stress, pressure	Pa
\dot{p}	Pressure rate	$\text{Pa}\cdot\text{s}^{-1}$
r^{exp}	Experimental Lankford coefficient	—
\bar{r}^{exp}	Averaged experimental Lankford coefficient	—
$r^{theo, vp}$	Theoretical visco-plastic Lankford coefficient	—
\bar{r}^{sim}	Averaged simulation Lankford coefficient	—
s	Specific entropy	$\text{J}\cdot\text{K}^{-1}\cdot\text{kg}^{-1}$
w_s	Sample width at starting moment of tensile test	m
w_0	Sample width measured at room temperature	m
Ω	Dissipation potential	$\text{J}\cdot\text{m}^{-3}\cdot\text{s}^{-1}$
Ω^{ext}	Extended dissipation potential	$\text{J}\cdot\text{m}^{-3}\cdot\text{s}^{-1}$
α	Material constant	—

α_T	Thermal expansion coefficient	K^{-1}
k_d, β, o	Material parameters associated with static recovery	—
γ	Material constant related to kinematic hardening	—
ϵ_λ	Specific Emissivity for wavelength of λ	—
ϵ_r	Relative emissivity	—
$\dot{\bar{\epsilon}}$	Equivalent strain rate in von Mises case	s^{-1}
λ	Wavelength	m
λ_L	Lamé's first parameter	Pa
μ	Elastic shear modulus, Lamé's second parameter	Pa
ν	Poisson's Ratio	—
κ_B	Boltzmann's constant	$J \cdot K^{-1}$
κ	Internal variable for plastic deformation	—
$\dot{\kappa}$	Rate of κ	s^{-1}
ρ	Density (mass per unit volume)	$kg \cdot m^{-3}$
ρ_d	Dislocation density	m^{-2}
σ_e	electrical conductivity	$S \cdot m^{-1}$
$\bar{\sigma}$	Equivalent stress	<i>MPa</i>
σ_s	Yield stress	Pa
σ_{SB}	Stefan-Boltzmann constant	$W \cdot m^{-2} \cdot K$
σ_Y	Initial yield stress	Pa
$\sigma_{Y,ref}$	Pre-exponential factor of Arrhenius relation for σ_Y	Pa
φ	Heat flux	$W \cdot m^{-2}$

χ_b	Bulk modulus	Pa
ψ	Free energy per unit of mass	J·kg ⁻¹
ψ^{el}	Elastic free energy	J·kg ⁻¹

Tensors and matrices of $n \times n$ format (in bold normal)

Symbol	Meaning	unit
C^{el}	Matrix of elastic compliance	Pa ⁻¹
C_χ	Matrix for constructing back stress tensor	Pa
D^{el}	Inversion of matrix C^{el}	Pa
I	Identity matrix	—
M_μ	Neutralized D^{el}	Pa
M	Matrix of $\partial \tilde{s} / \partial \tilde{\sigma}$	—
P	Matrix for constructing equivalent stress	—
Q	Matrix for calculating equivalent strain rate in von Mises case	—
s	Deviatoric stress tensor	Pa
α	Tensor of internal variables for kinematic hardening	Pa
α̇	Rate of α	Pa·s ⁻¹
ε̇	Strain rate tensor	s ⁻¹
ε̇^{el}	Elastic strain rate tensor	s ⁻¹
ε̇^{vp}	Viscoplastic strain rate tensor	s ⁻¹
ε̇th	Thermal strain rate tensor	s ⁻¹
σ	Stress tensor	Pa

\mathbf{X}	Back stress tensor for kinematic hardening	Pa
$\dot{\mathbf{X}}$	Rate of \mathbf{X}	Pa·s ⁻¹
ξ	Tensor calculated by $\mathbf{s} - \mathbf{X}$	Pa

Vectors in $n \times 1$ format (*in bold italic*)

Symbol	Meaning	unit
$\check{\mathbf{e}}$	Deviatoric part of strain rate tensor in Voigt's notation	s ⁻¹
$\check{\mathbf{e}}^{el}$	Deviatoric part of elastic strain rate tensor in Voigt's notation	s ⁻¹
$\check{\mathbf{e}}^{vp}$	Deviatoric part of viscoplastic strain rate tensor in Voigt's notation	s ⁻¹
\mathbf{f}_{imp}	Imposed force on unit surface	Pa
\mathbf{g}	Gravity vector	m·s ⁻²
\mathbf{j}	Electrical current density	A·m ⁻²
\mathbf{n}	Outward unit normal vector	—
\mathbf{p}	A vector containing all parameters to be optimized	—
\mathbf{q}	Heat flux density	W·m ⁻²
\mathbf{v}	Velocity	m·s ⁻²
$\check{\mathbf{s}}$	Deviatoric stress tensor in Voigt's notation	Pa
$\dot{\xi}$	Strain rate tensor in Voigt's notation	s ⁻¹
$\dot{\xi}^{vp}$	Viscoplastic strain rate tensor in Voigt's notation	s ⁻¹
\mathbf{E}	Electric field	V·m ⁻¹
\mathbf{I}_V	vector form of the identity matrix	—
$\tilde{\xi}$	Tensor $\xi = \mathbf{s} - \mathbf{X}$ in Voigt's notation	Pa

Mathematical functions

Symbol	Meaning
$\arg_{\min} x$	Argument to minimize the expression of x
\mathbf{x}^T	Transposition of matrix \mathbf{x}
\mathbf{x}^{-1}	Inversion of matrix \mathbf{x}
$\langle x \rangle$	Macaulay brackets, $\langle x \rangle = \begin{cases} x, & \text{if } x \geq 0 \\ 0, & \text{if } x < 0 \end{cases}$
\cdot	Scalar product of vectors
$\ \mathbf{x}\ $	Norm of the vector \mathbf{x}
$ x $	Absolute value of a scalar x
$\tilde{\mathbf{x}}$	Voigt's notation of tensor \mathbf{x} (vector)
∇x	Gradient of x
$\text{tr} \mathbf{x}$	Trace of matrix \mathbf{x}

Chapter 1 Context and Objective

1.1 Problematics in LPBF Processing

Additive manufacturing (AM), which is also known as 3D printing, becomes very important in industry, and is applied in various fields, because of significant advantages, such as material savings, customization and fast production for complex parts without additional cost [1]. There are essentially two classes of AM manufacturing methods, which are direct metal deposition (powder or wire) and powder bed fusion (PBF). Laser powder bed fusion (LPBF, or Selective laser melting SLM, or laser beam melting LBM) is one of the mostly used PBF methods. As illustrated in Fig. 1- 1, in SLM process, one or several lasers are used to melt and solidify the surface of a powder bed to form solid tracks according to selective laser trajectories. Then the base plate goes downwards and a new fresh powder layer is spread by a roller. The laser scans again to form a new solid layer added to the part under construction. This process is repeated to complete the final part. The direction Z along which the base plate moves will be called the building direction while (X, Y) defines the transverse plane.

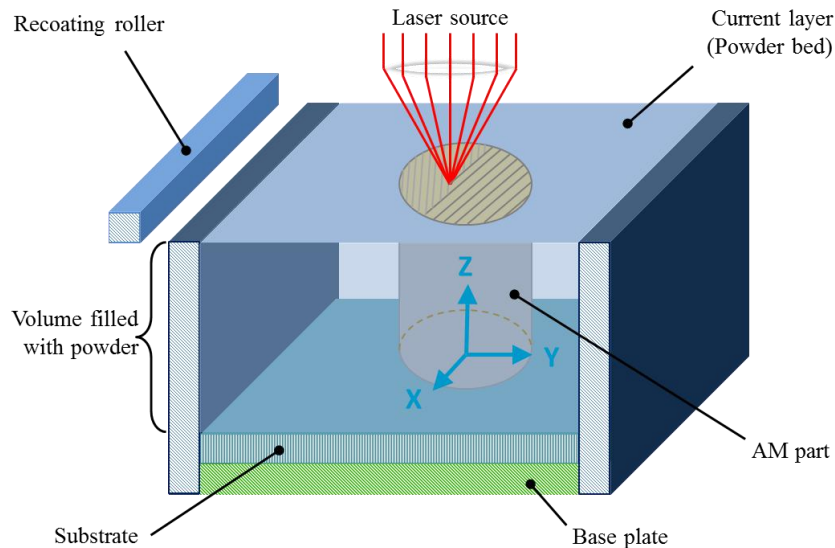


Fig. 1- 1 Schematic representation of LPBF process [2]

AM processes consist of rapid and successive fusion and solidification, developing thermal gradients in the vicinity of the fusion zone and at the scale of the part being built. The important thermal gradients generate thermal stresses possibly inducing hot cracks, which are consistently found to propagate in an intergranular mode from microscopic point of view [3], as shown in Fig. 2(a). From a macroscopic point of view, residual stress is also associated with distortions: deflections of the thin sections of constructed parts, or of support structures, may be significant and

have an impact on dimensional accuracy. When residual stress exceeds the tensile strength of the printing material or substrate, defects, such as cracking in the part (shown in Fig. 2(b)), could occur [4]. In addition, delamination may also occur, leading to cracks between layers (Fig. 2(c)) [5]. Delamination may happen as a result of the insufficient melting (lack of fusion) between successive layers, or between successive tracks in a layer. Some cracks may be repaired through post-processing, but delamination does not have access to this reparability.

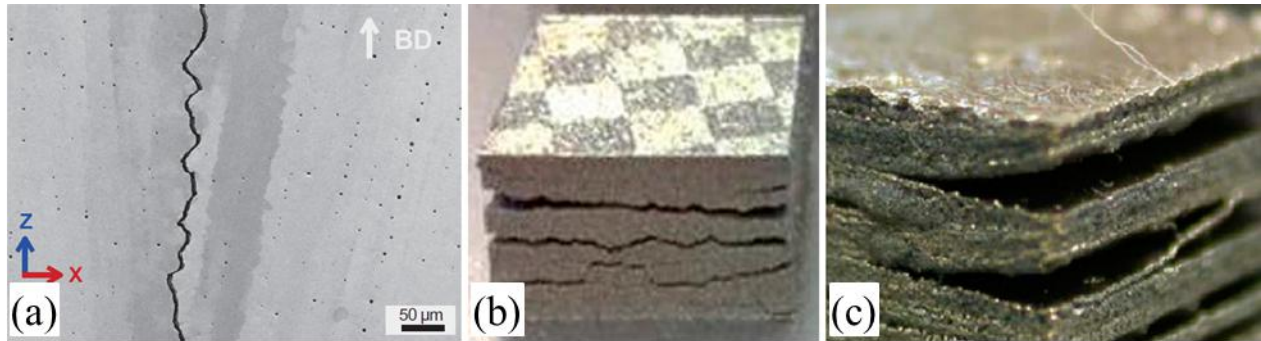


Fig. 1-2 (a) Hot crack in Ni-based AM material along the build direction [3] (b) Cracks in as-built M2 HSS material by AM [4] (c) Delamination in electron beam additive manufacturing of a stainless steel [5]

Considering AM processing, a huge group of parameters is needed to be optimized to avoid those defects, which is composed of but not limited to laser power, layer thickness, scanning speed, pre-heating... For small pieces of work piece, engineers can take the trial-and-error method in workshop to find the optimized processing parameters. However, on big pieces of part, the laboratory work will be time-and-finance costly. One alternative way is to take simulations of the processing.

So far there are many studies on the simulation of the AM process, with the aim to predict the thermo-mechanical response from simulation [6,7]. Generally speaking there are two kinds of simulations. The first one focuses on the “mesoscopic” scale, which considers only one or several track(s) of the scanning [8,9,10,11,12,13], and this mesoscopic approach focuses on the mechanisms of heat transfer, energy consumption, local defects such as pores, intergranular hot cracking etc. Another one is the “macroscopic” approach, which aims at predicting the defects such as residual stress, distortion [14,15,16,17,18]. Some work in Cemef is shown in Fig. 1-3, where:

- Chen et al. [11] developed a simulation for LPBF process for alumina. In their work, a level-set based thermo-hydrodynamic model has been developed in the "mesoscopic" scale, using a continuum approach for the powder bed. The melt pool profile, track shape and temperature mapping as well as local stress can be predicted, the result of which enlightens the possibility of the application for the metal alloys. See Fig. 1-3 (a).

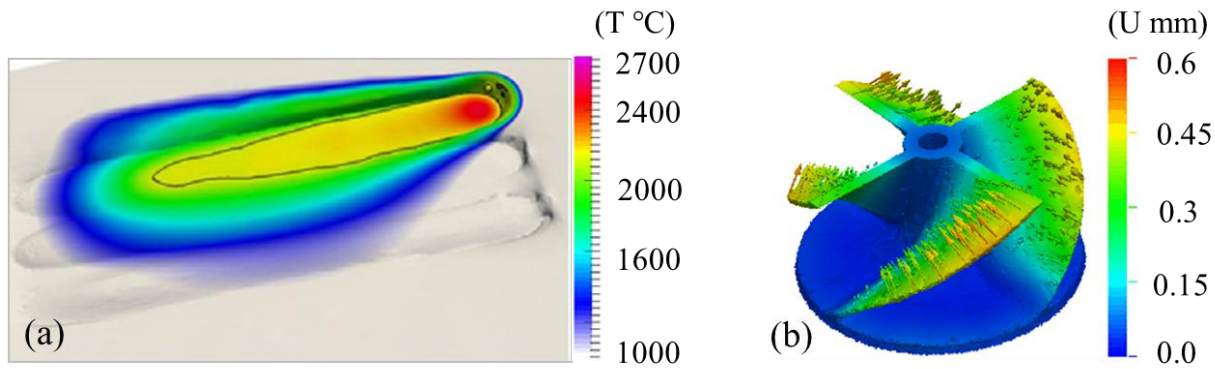


Fig. 1-3 (a): Temperature field at 9 ms of the third pass for an alternate scanning for mesoscopic model [11], and (b): temperature field of the as-simulated turbine part in the macroscopic scale [16]

- Zhang et al. [16] have developed a part scale simulation. In their work, they also use the level set function to track the interface between the constructed part and the non-exposed powder, and the interface between the powder bed and gas zone. Dynamic adaptive local re-meshing is employed. The approach is able to simulate parts with complex geometry. See Fig. 1-3 (b).

In fact, in order to construct the numerical simulation of the processing, three essential bricks are fundamental, which are:

- The development of new and sophisticated numerical simulation packages for multi-pass material and energy deposition [19]
- The development of criteria being able to predict the occurrence of defects, given local thermomechanical and microstructural features provided by the afore-mentioned numerical simulation [20], and
- The characterization of metal mechanical behavior on a large temperature range, especially at very high temperature, up to fusion. Such constitutive equations are critical inputs to the thermo-mechanical solvers of numerical simulation codes [21]

In all the three bricks, the mechanical constitutive model is a must. Considering the AM process, the selected constitutive model should possess the following features.

1.2 Features of the Objective Rheological Law

1.2.1 Wide Temperature Range

As previously stated in last section, the powder is melted during the AM process, then the melt pool is cooled down to certain temperature. During that heat routine, the material undergoes a severe heating up and cooling down, in quite a wide temperature range [22,23]. In this range, the material will present different states. When the temperature is higher than the liquidus the material is in total

liquid status, with partial vaporization; when temperature is within the liquidus and the solidus the material is in the mushy state; when the temperature is lower than the solidus, the material is in the solid state. It is easy to see that for the microscopic approach and hot cracking, focus is on very high temperature, while for predicting the defects associated with thermal cycling and for formation of residual stress, focus is on a law covering a wide temperature range.

1.2.2 Low Strain Range during the Solidification Period in AM Process

In AM process, thermal, elastic and (visco)plastic deformation will happen. One can see that the thermal strain is quite limited [24,25]. The elastic and viscoplastic strains are also found not big from researches by Panwisawas C. and Yamada J. [26,27] when they considered solidification in laser welding, which is close to the solidification in AM process. Even though it is difficult to measure the plastic strain during solidification, it is possible to estimate the strain threshold for cracking during the solidification by controlled tensile weldability test [28] or Trans-Varestraint testing [29]. By whatever method, the strain can be deemed lower than 5%.

1.2.3 Varying Strain Rates

The strain rate during the AM process is also difficult to measure, but one can check the thermal strain rate by cooling (or heating rate) to estimate the strain rate. In the liquid, mushy and solid states the cooling rate is different given the same scanning strategy [30,31], while cooling rate at solid state is the lowest among the three states. The typical cooling rate after solidification in AM process is found lower than around $1 \times 10^3 \text{ }^\circ\text{C} \cdot \text{s}^{-1}$ [30,32]. Considering the thermal expansion coefficient of IN718 of value at $\sim 15 \times 10^{-6} \text{ }^\circ\text{C}^{-1}$ [93~97], the maximum thermal strain rate can be found around 0.015 s^{-1} . Thus, during the AM process the maximum strain rate can be estimated lower than this value under condition of no external constraint on velocity. As cooling down continues, the strain rate will also decrease. In one word, the strain rate is low and varying in the solid state.

1.2.4 Applicable to Cyclic Stress Condition

In AM process the material undergoes repeated heating and cooling [30]. The local material undergoes compressive stress when the melt pool is around it while heating up, and it suffers tensile stress when the energy source moves away following cooling down [33]. This effect can introduce residual stress [34], and the cyclic tensile-compressive load will also introduce back stress, which is linked with kinematic hardening.

1.2.5 Elastic-viscoplastic

Viscoplastic behavior is adopted for most of ductile metals when deformation happens from moderate to high temperature [35]. For IN718, strain rate dependence is also found, whatever wrought condition or as-built condition from AM [36,37,38]. In AM process, the material is heated

and cooled down repeatedly, in which the strain rate varies. However, elastic-plastic models are widely adopted in the literature so far, probably for simplicity reason [11~18].

1.2.6 Transverse Isotropy

In AM process within each layer, certain scanning strategy is used [39]. Generally speaking, a rotation angle is selected between two layers to avoid anisotropy in three directions. However, there is crystal preferred orientation. For FCC structured alloy IN718 the orientation is $\langle 001 \rangle$ along building direction to form the columnar microstructure [23,40, 41]. The rotation between layers and the crystal preferred orientation brings the access to transverse isotropy, whose symmetric axis along the building direction. The Young's modulus along the building direction is then found close to the Young's modulus of a single crystal along the $\langle 001 \rangle$ direction for IN718. whose value Young's modulus along the building direction is the smallest [42,43,44]. But for the initial yield strength, some researchers found the value in the transverse direction is higher [43,44,45], while some found the one along building direction is higher [42] after post heat treatments.

1.2.7 As-Built Condition

In order to predict potential defects during the AM process, the constitutive law is supposed to work at the material state of being-manufactured. However, there is no access to such a state to test. Thus, the as-built condition will be used because it is closest to the being-manufactured state with accessibility.

In order to identify a rheological law with those 7 features, experimental tests, simulation tools and optimization trials are necessary. All the three parts constitute the basic frame of this work. In this work, LPBF samples with various building directions (provided by Safran) are tested on a home-developed machine. The elasticity model is isotropy based with adapted factor corresponding to the building directions. The viscoplastic model is anisotropic with an associated law based on the Hill48 criterion. The studied temperature range is from 800°C to 1100°C.

1.3 Structure of the Manuscript

In the present chapter, the problematic in AM process and the expected features of the rheological law.

In Chapter 2, the experimental device is introduced, together with the routine for the tests.

In Chapter 3, the numerical implementation is detailed, including the way to link experimental data to boundary conditions in numerical work.

In Chapter 4, the optimization with von Mises hypothesis on the as-built samples is presented, accompanied with expressions of cost function.

In Chapter 5, anisotropy of the as-built samples is studied on the hypothesis of Hill48, with more complicated cost function.

In Chapter 6, an overall conclusion of this work is collected, and expects are also given, and finally

In Appendices, lots of tips are given. Some of them are equally important as in the main text, but for the sake of a concise manuscript structure they are organized in the last part.

1.4 Appeals

Safran is developing parts and components fabricated by AM process. In 2017 this company published its power unit: a turbine nozzle of nickel-based material [46]. During the AM process, distortion is simulated [47], and a reasonable constitutive model is preferable from side of enterprise.

China Scholarship Council (CSC) is an organization offering funds for Chinese to study abroad and foreigners to study in China. It was searching a research position in the domain of characterization of rheological law by inverse method. The two appeals produced this project.

Chapter Reference

- 1 Campbell, T., Williams, C., Ivanova, O. and Garrett, B., 2011. Could 3D printing change the world. *Technologies, Potential, and Implications of Additive Manufacturing*, Atlantic Council, Washington, DC, 3.
- 2 Grasso, M. and Colosimo, B.M., 2017. Process defects and in situ monitoring methods in metal powder bed fusion: a review. *Measurement Science and Technology*, 28(4), p.044005.
- 3 Chauvet, E., Kontis, P., Jägle, E.A., Gault, B., Raabe, D., Tassin, C., Blandin, J.J., Dendievel, R., Vayre, B., Abed, S. and Martin, G., 2018. Hot cracking mechanism affecting a non-weldable Ni-based superalloy produced by selective electron Beam Melting. *Acta Materialia*, 142, pp.82-94.
- 4 Kempen, K., Thijs, L., Vrancken, B., Bols, S., Van Humbeeck, J. and Kruth, J.P., 2013, August. Producing crack-free, high density M2 Hss parts by selective laser melting: pre-heating the baseplate. In Proc. 24th Int. Solid Free. *Fabr. Symp* (pp. 131-139).
- 5 Zäh, M.F. and Lutzmann, S., 2010. Modelling and simulation of electron beam melting. *Production Engineering*, 4(1), pp.15-23.
- 6 Bikas, H., Stavropoulos, P. and Chryssolouris, G., 2016. Additive manufacturing methods and modelling approaches: a critical review. *The International Journal of Advanced Manufacturing Technology*, 83(1-4), pp.389-405.
- 7 Schoinochoritis, B., Chantzis, D. and Salonitis, K., 2017. Simulation of metallic powder bed additive manufacturing processes with the finite element method: A critical review. Proceedings of the Institution of Mechanical Engineers, Part B: *Journal of Engineering Manufacture*, 231(1), pp.96-117.
- 8 Khairallah, S.A., Anderson, A.T., Rubenchik, A. and King, W.E., 2016. Laser powder-bed fusion additive manufacturing: Physics of complex melt flow and formation mechanisms of pores, spatter, and denudation zones. *Acta Materialia*, 108, pp.36-45.
- 9 Yan, W., Ge, W., Qian, Y., Lin, S., Zhou, B., Liu, W.K., Lin, F. and Wagner, G.J., 2017. Multi-physics modeling of single/multiple-track defect mechanisms in electron beam selective melting. *Acta Materialia*, 134, pp.324-333.

-
- 10 Tang, C., Tan, J.L. and Wong, C.H., 2018. A numerical investigation on the physical mechanisms of single track defects in selective laser melting. *International Journal of Heat and Mass Transfer*, 126, pp.957-968.
- 11 Chen, Q., Guillemot, G., Gandin, C.A. and Bellet, M., 2017. Three-dimensional finite element thermomechanical modeling of additive manufacturing by selective laser melting for ceramic materials. *Additive Manufacturing*, 16, pp.124-137.
- 12 Heigel, J.C., Michaleris, P. and Reutzel, E.W., 2015. Thermo-mechanical model development and validation of directed energy deposition additive manufacturing of Ti-6Al-4V. *Additive manufacturing*, 5, pp.9-19.
- 13 Mukherjee, T., Zhang, W. and DebRoy, T., 2017. An improved prediction of residual stresses and distortion in additive manufacturing. *Computational Materials Science*, 126, pp.360-372.
- 14 Denlinger, E.R., Irwin, J. and Michaleris, P., 2014. Thermomechanical modeling of additive manufacturing large parts. *Journal of Manufacturing Science and Engineering*, 136(6).
- 15 Neugebauer, F., Keller, N., Ploshikhin, V., Feuerhahn, F. and Köhler, H., 2014, April. Multi scale FEM simulation for distortion calculation in additive manufacturing of hardening stainless steel. In *Proceedings of the international workshop on thermal forming and welding distortion* (Vol. 54).
- 16 Zhang, Y., Chen, Q., Guillemot, G., Gandin, C.A. and Bellet, M., 2018. Numerical modelling of fluid and solid thermomechanics in additive manufacturing by powder-bed fusion: Continuum and level set formulation applied to track-and part-scale simulations. *Comptes Rendus Mécanique*, 346(11), pp.1055-1071.
- 17 Cheng, B. and Chou, K., 2015. Geometric consideration of support structures in part overhang fabrications by electron beam additive manufacturing. *Computer-Aided Design*, 69, pp.102-111.
- 18 Cheng, B., Shrestha, S. and Chou, K., 2016. Stress and deformation evaluations of scanning strategy effect in selective laser melting. *Additive Manufacturing*, 12, pp.240-251.
- 19 Desmaison, O., Bellet, M. and Guillemot, G., 2014. A level set approach for the simulation of the multipass hybrid laser/GMA welding process. *Computational materials science*, 91, pp.240-250.

-
- 20 Koshikawa, T., Bellet, M., Gandin, C.A., Yamamura, H. and Bobadilla, M., 2016. Study of hot tearing during steel solidification through ingot punching test and its numerical simulation. *Metallurgical and Materials Transactions A*, 47(8), pp.4053-4067.
- 21 Pradille, C., Bellet, M. and Chastel, Y., 2010. A complete method for rheological characterization of steel at high temperature. *In EPJ Web of Conferences* (Vol. 6, p. 17001). EDP Sciences.
- 22 Bai, X., Colegrove, P., Ding, J., Zhou, X., Diao, C., Bridgeman, P., roman Hönnige, J., Zhang, H. and Williams, S., 2018. Numerical analysis of heat transfer and fluid flow in multilayer deposition of PAW-based wire and arc additive manufacturing. *International Journal of Heat and Mass Transfer*, 124, pp.504-516.
- 23 Wei, H.L., Mazumder, J. and DebRoy, T., 2015. Evolution of solidification texture during additive manufacturing. *Scientific reports*, 5(1), pp.1-7.
- 24 Mukherjee, T., Manvatkar, V., De, A. and DebRoy, T., 2017. Mitigation of thermal distortion during additive manufacturing. *Scripta materialia*, 127, pp.79-83.
- 25 Mukherjee, T., Zuback, J.S., De, A. and DebRoy, T., 2016. Printability of alloys for additive manufacturing. *Scientific reports*, 6(1), pp.1-8.
- 26 Panwisawas, C., Gebelin, J.C., Warnken, N., Broomfield, R.W. and Reed, R.C., 2011. Numerical modelling of stress and strain evolution during solidification of a single crystal superalloy. *In Advanced Materials Research* (Vol. 278, pp. 204-209). Trans Tech Publications Ltd.
- 27 Yamada, J., Okano, S., Hiroaki, M., Mochizuki, M. and Nishimoto, K., 2009, July. Numerical Study On Strain Behavior During Solidification Evaluation of Solidification Cracking Susceptibility In Low-carbon Austenitic Stainless Steel Laser Weld. *In The Nineteenth International Offshore and Polar Engineering Conference*. OnePetro.
- 28 Coniglio, N. and Cross, C.E., 2009. Mechanisms for solidification crack initiation and growth in aluminum welding. *Metallurgical and Materials Transactions A*, 40(11), pp.2718-2728.
- 29 Arata, Y., Matsuda, F., Nakagawa, H., Katayama, S. and Ogata, S., 1977. Solidification crack susceptibility in weld metals of fully austenitic stainless steels (Report III): effect of strain rate on cracking threshold in weld metal during solidification. *Transactions of JWRI*, 6(2), pp.197-206.

-
- 30 Xiao, H., Li, S., Han, X., Mazumder, J. and Song, L., 2017. Laves phase control of Inconel 718 alloy using quasi-continuous-wave laser additive manufacturing. *Materials & Design*, 122, pp.330-339.
- 31 Li, S., Xiao, H., Liu, K., Xiao, W., Li, Y., Han, X., Mazumder, J. and Song, L., 2017. Melt-pool motion, temperature variation and dendritic morphology of Inconel 718 during pulsed-and continuous-wave laser additive manufacturing: A comparative study. *Materials & design*, 119, pp.351-360.
- 32 Bennett, J.L., Kafka, O.L., Liao, H., Wolff, S.J., Yu, C., Cheng, P., Hyatt, G., Ehmann, K. and Cao, J., 2018. Cooling rate effect on tensile strength of laser deposited Inconel 718. *Procedia Manufacturing*, 26, pp.912-919.
- 33 Patterson, A.E., Messimer, S.L. and Farrington, P.A., 2017. Overhanging features and the SLM/DMLS residual stresses problem: Review and future research need. *Technologies*, 5(2), p.15.
- 34 Fergani, O., Berto, F., Welo, T. and Liang, S.Y., 2017. Analytical modelling of residual stress in additive manufacturing. *Fatigue & Fracture of Engineering Materials & Structures*, 40(6), pp.971-978.
- 35 Lemaitre, J., Chaboche, J.L., Benallal, A. and Desmorat, R., 2020. *Mécanique des matériaux solides-3e éd.* Dunod. Page 262
- 36 Zhou, L.X. and Baker, T.N., 1994. Effects of strain rate and temperature on deformation behaviour of IN 718 during high temperature deformation. *Materials Science and Engineering: A*, 177(1-2), pp.1-9.
- 37 Lin, Y.C., Li, K.K., Li, H.B., Chen, J., Chen, X.M. and Wen, D.X., 2015. New constitutive model for high-temperature deformation behavior of inconel 718 superalloy. *Materials & Design*, 74, pp.108-118.
- 38 Pröbstle, M., Neumeier, S., Hopfenmüller, J., Freund, L.P., Niendorf, T., Schwarze, D. and Göken, M., 2016. Superior creep strength of a nickel-based superalloy produced by selective laser melting. *Materials Science and Engineering: A*, 674, pp.299-307.
- 39 Jia, H., Sun, H., Wang, H., Wu, Y. and Wang, H., 2021. Scanning strategy in selective laser melting (SLM): a review. *The International Journal of Advanced Manufacturing Technology*, pp.1-23.

40 Wan, H.Y., Zhou, Z.J., Li, C.P., Chen, G.F. and Zhang, G.P., 2018. Effect of scanning strategy on grain structure and crystallographic texture of Inconel 718 processed by selective laser melting. *Journal of materials science & technology*, 34(10), pp.1799-1804.

41 Kunze, K., Etter, T., Grässlin, J. and Shklover, V., 2015. Texture, anisotropy in microstructure and mechanical properties of IN738LC alloy processed by selective laser melting (SLM). *Materials Science and Engineering: A*, 620, pp.213-222.

42 Deng, D., Moverare, J., Peng, R.L. and Söderberg, H., 2017. Microstructure and anisotropic mechanical properties of EBM manufactured Inconel 718 and effects of post heat treatments. *Materials Science and Engineering: A*, 693, pp.151-163.

43 Chlebus, E., Gruber, K., Kuźnicka, B., Kurzac, J. and Kurzynowski, T., 2015. Effect of heat treatment on the microstructure and mechanical properties of Inconel 718 processed by selective laser melting. *Materials Science and Engineering: A*, 639, pp.647-655.

44 Kumara, C., Deng, D., Moverare, J. and Nylén, P., 2018. Modelling of anisotropic elastic properties in alloy 718 built by electron beam melting. *Materials Science and Technology*, 34(5), pp.529-537.

45 Ni, M., Chen, C., Wang, X., Wang, P., Li, R., Zhang, X. and Zhou, K., 2017. Anisotropic tensile behavior of in situ precipitation strengthened Inconel 718 fabricated by additive manufacturing. *Materials Science and Engineering: A*, 701, pp.344-351.

46 Safran obtains the first certification for a 3D-printed gas turbine engine major part | Safran Power Units, <https://www.safran-power-units.com/media/safran-obtains-first-certification-3d-printed-gas-turbine-engine-major-part-20170619>, visited June 08th, 2021

47 Clara Moriconi, Simufact Additive: Collaborative Simultaneous Engineering Tool for Additive Manufacturing, Volume IX - Summer 2019, 27-29, mscsoftware.com

Chapter 2 Experimental Part

Résumé

Une machine développée à la maison pour tester le comportement thermomécanique est brièvement présentée. Les manières de concevoir la géométrie de l'éprouvette, de contrôler la température et la vitesse de l'objectif sont indiquées. Une caméra infrarouge est utilisée pour mesurer le champ de température, et la technique DIC est adoptée pour enregistrer le champ de déplacement à température élevée (avec une méthode sans contact dans la littérature). Une procédure expérimentale typique est donnée, suivie de la démonstration d'un test expérimental.

Chapter Introduction

The objective of this project is to optimize the parameters of rheological models of metal at high temperature during deformation, thus it can be easily inferred that temperature, displacement field and load are essential data to be precisely measured. In addition, there are some difficulties to overcome during the tests, such as how to maintain the temperature at a required value at a selected position, how to calibrate the measured temperature field, and how to measure the displacement field in intense thermal radiation conditions.

In order to overcome those difficulties a lot of preparation was done, partly by the technical support team of the lab. They are to determine the sample shape via simulation, to control temperature via Proportional–Integral–Derivative (PID) algorithm with certain feedback signal (thermocouple or bichromatic pyrometer), to measure displacement field in wide temperature range with different lighting methods... All these items will be mainly discussed in the present chapter, while some details will be embedded in appendices. At the end of the chapter, a typical testing processing will be given.

2.1 Description of Home-developed Machine

All tests were carried out with a machine developed in the laboratory and named Dedimet (abbreviation for "**d**éformation et **d**ilatation des **m**étaux", in French). Dedimet, see Fig. 2- 1, is based on an Adamel electromechanical 30kN tensile test machine housing, with addition of a chamber with selectable atmosphere (air, nitrogen, argon), the pressure of which can be reduced to a few mbar at the lowest by using a dry scroll vacuum pump (Leybold SCROLLVAC SC5D). The mechanical solicitation of the material sample results from the vertical motion of the lower beam of the machine with a controlled velocity (minimum $0.011\text{ mm}\cdot\text{s}^{-1}$).

Inside the chamber is the force sensor (HBM – 1-U10M/25kN) which is connected to the fixed upper beam of the machine. Other measuring instruments are located outside the chamber and proceed through two lateral windows allowing an optical access to the mounted sample. On one side are installed a bichromatic infra-red (IR) pyrometer (Marathon series MR1S™, Thermalert®, USA) providing temperature spot measurement with a diameter approaching the width of the specimen, and a bichromatic IR camera (Q-Pyrocam, IMS-Chips, Germany) providing a field measurement covering the whole working zone. These two measures are operated through a sapphire window which is transparent to IR radiation. On the other side are installed two high-speed cameras (Point Grey Research Inc, Canada) providing – through a standard glass window – field images of the working zone to serve as raw data for displacement field measurement by DIC analysis (VIC-3D system, by Correlated Solutions Inc, USA).

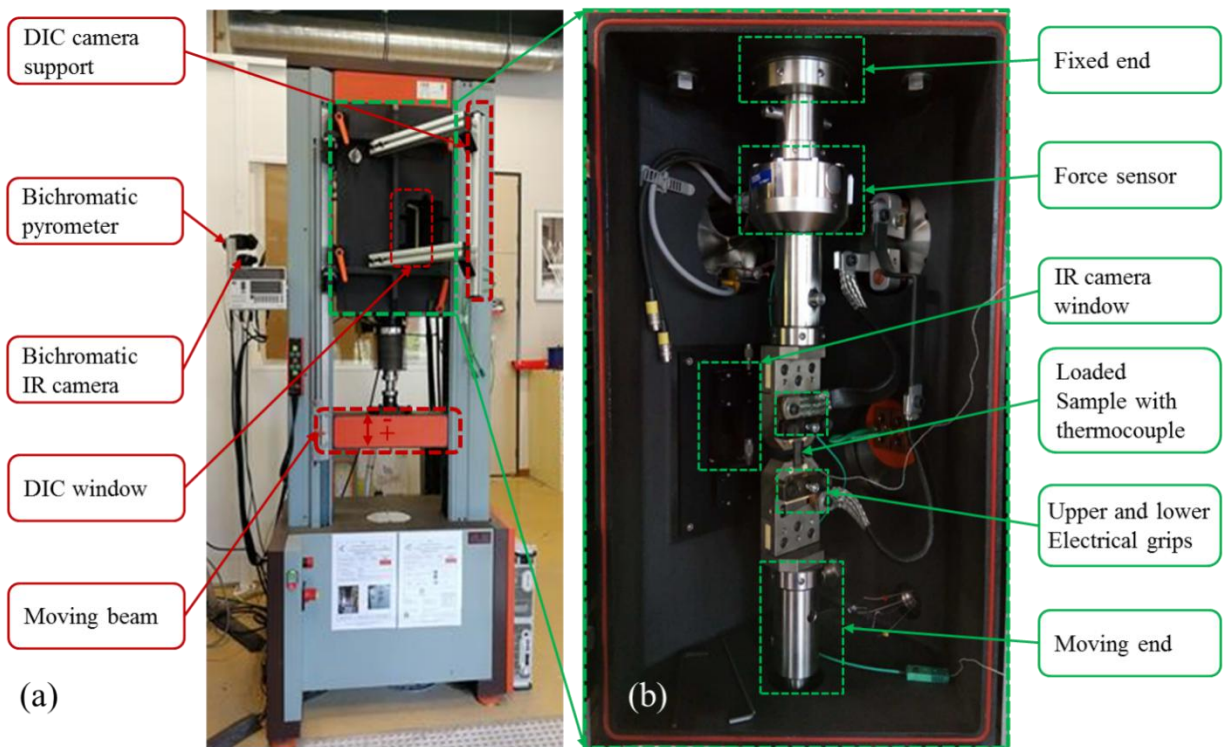


Fig. 2-1 Dedimet profile: a) Outside of Dedimet and, b) Inside of chamber on Dedimet

Table 1 presents the basic parameters of the Dedimet machine.

Table 1 Hardware capacities of Dedimet machine

Items	Ranges	Remarks
Vacuum	1 – 10mbar	1 at RT, 10 at 1200°C
Heating source	400A, 3.8kW	Direct current
Bichromatic IR camera	600 to 1900°C	640×480 pixels

Bichromatic Pyrometer	620 to 1400°C	
Servo motor	$\geq 0.011 \text{ mm} \cdot \text{s}^{-1}$	Transformed beam velocity
Force sensor	up to 25kN	
Note: RT short for room temperature		

2.2 Specimen Design

The sample geometry was designed by simulation via an electrical-thermal solver in commercial FEM software FORGE[®] which was originally developed in Cemef. The governing equations for resistive heating are introduced first, followed by the design objective and optimization result.

2.2.1 Reminder on Resistive Heating: Governing Equations

The electrical current density vector \mathbf{j} can be written as:

$$\mathbf{j} = \sigma_e \mathbf{E} = -\sigma_e \nabla U \quad (2-1)$$

where σ_e is the electrical conductivity with unit $\text{S} \cdot \text{m}^{-1}$, \mathbf{E} is the electric field with unit $\text{V} \cdot \text{m}^{-1}$, and U is the electric potential with unit V. The interaction between circulating electrons and atoms results in heat dissipation. The dissipated power per volume p_e is:

$$p_e = \mathbf{j} \cdot \mathbf{E} = \sigma_e \mathbf{E} \cdot \mathbf{E} = \sigma_e \|\mathbf{E}\|^2 = \sigma_e \|\nabla U\|^2 \quad (2-2)$$

The Fourier's law for heat conduction is expressed as:

$$\mathbf{q} = -k_c \nabla T \quad (2-3)$$

where \mathbf{q} is the local heat flux density with unit of $\text{W} \cdot \text{m}^{-2}$, k_c is the thermal conductivity of the material with unit of $\text{W} \cdot \text{m}^{-1} \cdot \text{K}^{-1}$. The change of internal energy per unit volume, dQ is proportional to the change of the temperature:

$$dQ = \rho C_p dT \quad (2-4)$$

where C_p is the heat capacity at constant pressure with unit of $\text{J} \cdot \text{K}^{-1} \cdot \text{kg}^{-1}$. Using the principle of conservation of electrical charge to the eq. 2-1, and conservation law of energy in which Joule effect behaves as the internal heat source:

$$\begin{cases} \nabla \cdot (\sigma_e \nabla U) & = & 0 \\ \rho C_p \frac{dT}{dt} - \nabla \cdot (k_c \nabla T) & = & \sigma_e \|\nabla U\|^2 \end{cases} \quad (2-5)$$

Eq. 2-5 indicates that volumetric heat source ($\sigma_e \|\nabla U\|^2$) affects the local temperature, through the heat capacity C_p and heat diffusion.

The two conservation equations above are submitted to boundary conditions.

The electrical boundary conditions include all exchanges between air and surface of the sample where the electric flux is zero, in this case $\sigma_e \nabla U = \mathbf{0}$. For the exchange between the samples and the tools, a Neumann condition is imposed on the surface which is in contact with the cathode. In addition, a Dirichlet condition is imposed on the other side, on the surface in contact with the anode. These conditions can be expressed as follows:

$$\begin{cases} \sigma_e \nabla U \cdot \mathbf{n} = -\mathbf{J} \cdot \mathbf{n} = J_{imp} & \text{on cathode} \\ U = 0 & \text{on anode} \end{cases} \quad (2-6)$$

where \mathbf{n} is the outward unit normal vector. The first limit condition corresponds to the application of an electric current density J_{imp} . The value of J_{imp} can be automatically regulated by a control loop in PID.

The heat flux φ ($\text{W}\cdot\text{m}^{-2}$) emitted from any point of the surface is expressed by:

$$\varphi = -k_c \nabla T \cdot \mathbf{n} \quad (2-7)$$

where \mathbf{n} is the outward unit normal vector. It can be decomposed in two parts: convection and gray body radiation:

$$\varphi = -k_c \nabla T \cdot \mathbf{n} = h_c (T - T_{ext}) + \varepsilon_r \sigma_{SB} (T^4 - T_{ext}^4) \quad (2-8)$$

where h_c is the convective heat transfer coefficient with unit of $\text{W}\cdot\text{m}^{-2}\cdot\text{K}^{-1}$, ε_r is the relative emissivity, σ_{SB} is the Stefan-Boltzmann constant (equal to $5.67 \times 10^{-8} \text{W}\cdot\text{m}^{-2}\cdot\text{K}^{-4}$), T_{ext} is the environment temperature with unit of K .

2.2.2 Sample Shape and Geometry Optimization

Generally speaking, there are two widely used shapes for tensile tests, which are the round bar specimen (the preferred default shape) and the flat parallelepipedal specimen (also called “dog-bone” shape). Theoretically, either shape can be selected. However, considering the to-be-measured

information, we would rather choose the flat form, because in this case an IR camera can be easily adjusted so that its axis is normally facing the sample surface, which makes the temperature field measurement more reliable. Besides, the thickness of the flat sample is small, which makes a hypothesis of uniform temperature along the thickness reasonable. And the displacement field of a flat sample is prone to be measured.

Once the basic shape of the sample is decided, it is necessary to optimize its geometry. The geometry of the sample concerns with the machine space limitations, fixtures and electric contact, and especially the temperature field. Due to resistive heating, the temperature field shows a maximum in the central part of the specimen. A compromise should be found then between two objectives that seem paradoxical:

- Firstly, the temperature in the regions close to the end of the specimen and the grip system should be moderate, in order to minimize the heat transmitted to the machine by diffusion through the mechanical chain, and especially minimize the temperature of the grips during tests and protect the force sensor from high temperature.
- Secondly, it would be desirable to have a central zone with a rather uniform temperature, close to the maximum. In other words, a central plateau-like profile would be better than a marked peak. As this hottest part of the specimen will act as a weak mechanical link, this central plateau-like profile would avoid an excessive strain concentration that would lead to a severe and early necking during loading.

Consequently, a good design should consist of a flat specimen that would be more massive when approaching the two ends. By increasing the transverse section, the electric resistance is decreased, so the temperature decreases associated with the Joule effect. That should help meet the temperature requirement. Also, without special consideration for fabrication by additive manufacturing, we should keep in mind the issue of the global machining of the specimen, which should remain easy. In total, a design like the one illustrated in Fig. 2-2 (a) should be appropriate.

The sample is 140mm long in total and is divided into three parts: the heads, the shoulders and the working zone. The working zone has a length of 60mm and a width of 8mm, the shoulders have a length of 20mm and a width of 12mm, and the heads are 20mm long and 20mm wide. The width is designed like this so that the sample can be exactly put in the fixture with little clearance as shown in Fig. 2-2 (b), and the reinforced width of 12mm also reduces the electrical resistance within this shoulder domain. As regards the design optimization with respect to the temperature profile, that was studied by Y. ZHANG [48] prior to the beginning of the present work, using numerical simulation, as reported hereafter.

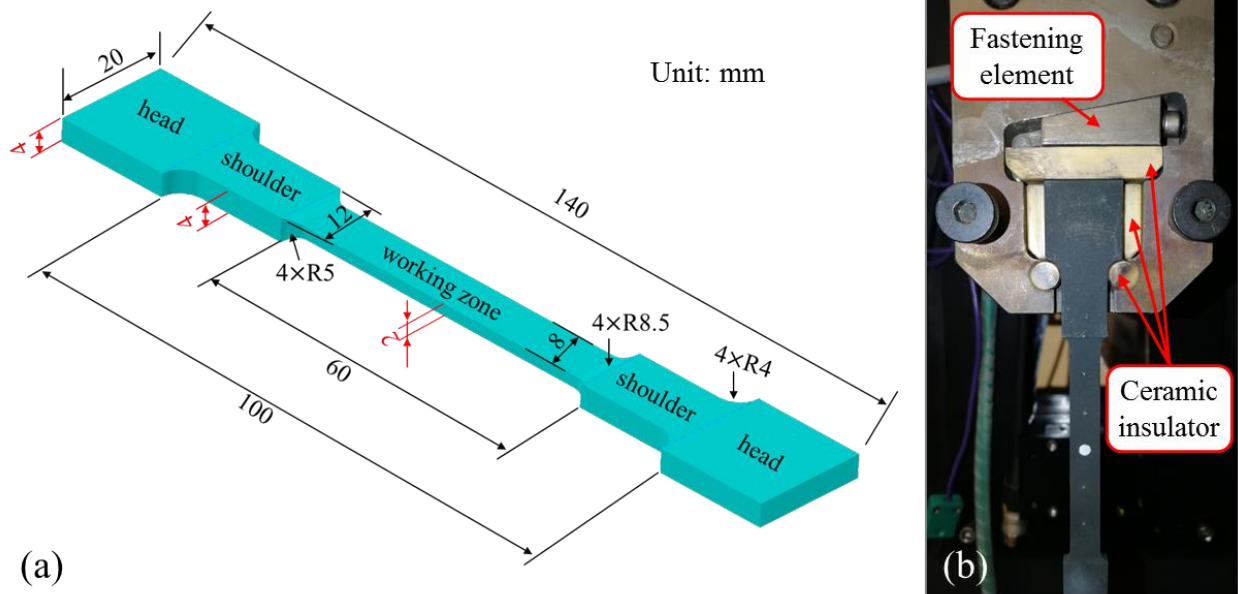


Fig. 2-2 (a): Geometry of the sample with name of 4-4-2, (b): Isolation and fixture mechanism

In order to meet the requirements, three sample designs were selected, with almost the same geometry: the dimensions indicated in black in Fig. 2-2 (a) remain, but the red ones, i.e., the thickness of the different regions, are different. From ends to middle, there are three sets of thickness, i.e., 4-4-2, 4-2-2 and 2-2-2. Then FORGE[®] equipped with thermal-electrical solver was used to solve concurrently the electrical and the thermal problem, in order to simulate the evolution of the temperature map in the specimen during heating and stay at high temperature. The following conditions were considered:

- Material: In718
- Sample shapes: 4-4-2, 4-2-2 and 2-2-2
- Heating route: 25 to 1200°C linearly within 50s; maintain at 1200°C for 40s
- Temperature control point: center point of the samples
- Initial temperature: tools (grip system): 25°C, specimen 25°C
- Ambient temperature 25°C
- Convective-radiative heat transfer between the specimen surface and ambient environment
- Sliding contact between the specimen and the tools

Fig. 2-3 shows the results at the end of heating (a: at 50s) and at the end of simulation (b: 90s). The 4-4-2 geometry meets the objective, with an end temperature relatively low, and a central part with a kind of plateau. As expected, the 2-2-2 type suffers from high temperatures at the ends, due to a two weak thickness in these regions. The 4-2-2 type appears as a good candidate, with a longer central plateau than the 4-4-2. However, it was finally chosen to favor the geometry minimizing temperature at ends. So, finally the 4-4-2 type was retained as the sample geometry. There is a little difference between the geometry in Fig. 2-2 (a) and the one in the reference [48] at the chamfer position, which was optimized during this work.

It should be mentioned that there is a slight asymmetry at the two heads, which is induced by the different potential gradients of the two heads, ∇U . The value of ∇U is zero in the anode head as indicated by the boundary condition (Eq. 2-6).

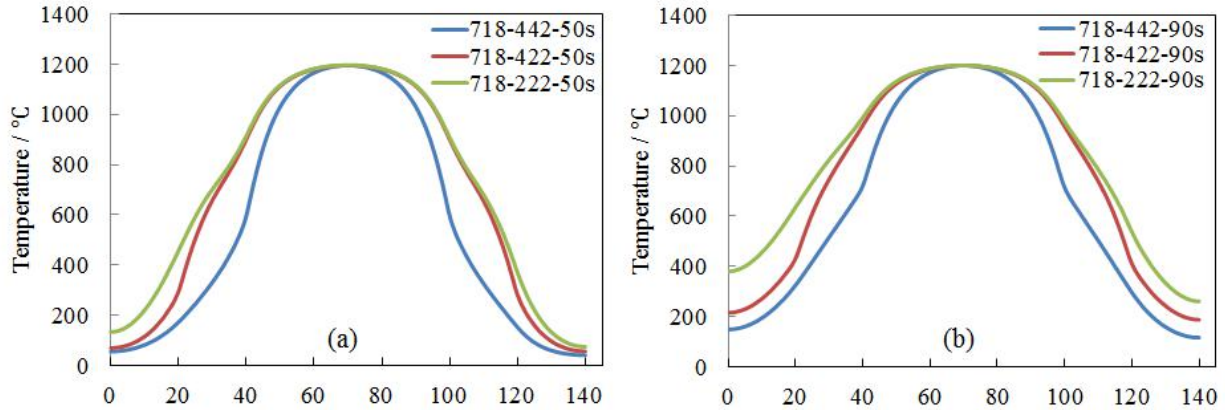


Fig. 2-3 Axial temperature profile in samples of different thickness, (a) at 50s, and (b) at 90s

2.3 Temperature Signal, Control and Calibration

Three types of temperature signal can be accessed on Dedimet machine, which are provided by either a welded thermocouple for a point, the bichromatic pyrometer for a narrow field, or the bichromatic infrared camera for a full field. One of the three signals can be used for the temperature control by PID algorithm, and PID parameters should be carefully selected for a robust control.

2.3.1 Temperature Signals/Measurements

Depending on the technique, temperature signal from a certain technique is the electrical potential or a photocurrent, and it should be transformed to temperature value in unit of Kelvin or Celsius for measurement. The different techniques are presented and commented in the following three sections.

2.3.1.1 Thermocouple

Two types of thermocouples can be used in the machine, which are *K* type or *R/S* type.

- *K* type. Positive wire: chromel (Ni90wt%-Cr10%), negative wire: alumel (Ni95wt%, Mn2%, Al2%, Si1%). The measuring range is -270 to 1260°C with precision of $\pm 2.2^\circ\text{C}$ or $\pm 0.75\%$ (whichever is greater) [49]. Maximum continuous temperature measurement should not exceed 1100°C.
- *R* and *S* types are made of Pt-Rh13wt%/Pt, and Pt-Rh10wt%/Pt, respectively. The measuring range is -50 to 1480°C with precision of $\pm 1.5^\circ\text{C}$ or $\pm 0.25\%$ (whichever is greater).

Their resistance to oxidation is better than for K type. Their cost is significantly higher (~2500 times of K type).

The thermocouples should be welded onto the sample surface to precisely measure the temperature of the sample. From test to test, the welded part of the thermocouple should be removed to make sure the measurement is reliable. Thus, the thermocouples presently used in our work are K type, essentially for economic reasons, as they are much cheaper.

K type thermocouples are welded onto test samples by electric discharge method before mounted on the machine. This operation is quite delicate, because of the very thin diameter of the wires (about 0.3mm). Thermocouple works on the thermoelectric effect, and it can be immediately imagined that when the thermocouple is welded on the sample which is heated by Joule effect, the electrical potential on the sample caused by the imposed current could have an influence on the measurement of the thermocouple. Thus, thermocouple response by imposing an instant current into the sample must be checked before the test. Appendix A. 1 presents how a thermocouple should be welded.

2.3.1.2 Bichromatic Pyrometer

A bichromatic pyrometer (BP) uses two wave lengths of infrared light (this is why it is called “bichromatic”) to offer a non-contact measurement of temperature. Let us have a short review of how a BP works. First, according to Planck’s law, the spectral radiance of the black body, for a wavelength λ and at temperature T , is defined by:

$$B_{\lambda}^0(T) = \frac{2h_p c^2}{\lambda^5} \frac{1}{e^{\frac{h_p c}{\kappa_B \lambda T}} - 1} \quad (2-9)$$

This quantity is the flux of emitted power per unit surface ($W \cdot m^{-2}$), per wavelength interval (m^{-1}), and per unit of solid angle (sr^{-1}): its unit is $W \cdot m^{-3} \cdot sr^{-1}$. h_p is the Planck’s constant, c is the light speed, and κ_B is the Boltzmann’s constant. From the literature, h_p is $6.626 \times 10^{-34} kg \cdot m^2 \cdot s^{-1}$ or $J \cdot s$, κ_B is $1.381 \times 10^{-23} kg \cdot m^2 \cdot s^{-2} \cdot K^{-1}$ or $J \cdot K^{-1}$.

When $h_p c \gg \kappa_B \lambda T$, $\frac{1}{e^{\frac{h_p c}{\kappa_B \lambda T}} - 1} \rightarrow e^{-\frac{h_p c}{\kappa_B \lambda T}}$. This approximation holds as soon as $\lambda \ll \frac{h_p c}{\kappa_B T}$. Eq. 2-9

then becomes:

$$B_{\lambda}^0(T) = \frac{2h_p c^2}{\lambda^5} e^{-\frac{h_p c}{\kappa_B \lambda T}} \quad (2-10)$$

This approximation is called Wien approximation. Typical wavelength of infrared camera is in range of about $0.75 \mu m$ and $14 \mu m$, and for bichromatic objective short wave length in range of 0.75 and $1.1 \mu m$ is widely used[50,51,52]. For the temperature range of 600 and $1400^{\circ}C$ and wavelength

range of 0.75 and 1.1 μm , the minimum value of $e^{\frac{hpc}{\kappa_B\lambda T}}$ is bigger than 2490, which is much bigger than 1.

If now we consider a real body (non-black), characterized by its spectral emissivity $\epsilon_\lambda = \epsilon(\lambda)$, the expression of its spectral radiance is now:

$$B_\lambda(T) = \epsilon_\lambda \frac{2hpc^2}{\lambda^5} e^{-\frac{hpc}{\kappa_B\lambda T}} \quad (2-11)$$

For a given installation of the BP with respect to the specimen, the energy received by the phototube, which is changed to the electrical energy, is proportional to this spectral radiance. Thus, given two selected wave lengths λ_1 and λ_2 at any temperature T :

$$B_{\lambda_1}(T) = \epsilon_{\lambda_1} \frac{2hpc^2}{\lambda_1^5} e^{-\frac{hpc}{\kappa_B\lambda_1 T}} \quad (2-12)$$

$$B_{\lambda_2}(T) = \epsilon_{\lambda_2} \frac{2hpc^2}{\lambda_2^5} e^{-\frac{hpc}{\kappa_B\lambda_2 T}} \quad (2-13)$$

Taking the ratio of the left and right members of the two expressions, separately, we get:

$$\frac{B_{\lambda_1}(T)}{B_{\lambda_2}(T)} = \frac{\epsilon_{\lambda_1}}{\epsilon_{\lambda_2}} \left(\frac{\lambda_2}{\lambda_1}\right)^5 e^{-\frac{hpc}{\kappa_B T} \left(\frac{1}{\lambda_1} - \frac{1}{\lambda_2}\right)} \quad (2-14)$$

Taking the logarithm form, we will finally get:

$$T = \frac{hpc(\lambda_1 - \lambda_2)}{\kappa_B \lambda_1 \lambda_2} \frac{1}{\ln \left[\frac{B_{\lambda_1}(T) \epsilon_{\lambda_2} \left(\frac{\lambda_1}{\lambda_2}\right)^5}{B_{\lambda_2}(T) \epsilon_{\lambda_1}} \right]} \quad (2-15)$$

It is then possible to deduce the temperature directly from the ratio of the radiances (and therefore from the ratio of energetic quantities directly proportional to them), provided that the emissivity ratio $\frac{\epsilon_{\lambda_2}}{\epsilon_{\lambda_1}}$ is known. Using different but close wavelengths, it is generally admitted [53] that this ratio can be taken as the unity (hypothesis of same spectral emissivity for the two wavelengths used). As a matter of fact, the approximation of the emissivity ratio to unity may also motivate or justify possible calibration or correction procedures. Anyway, this explains why temperature measurement by BP is not emissivity-dependent (Notice: the expression of Eq. 2-15 is based on only unit surface and unit solid angle for a simplified explanation. In reality radiances of two wavelength bands are used rather than just two exact wavelengths, see [52]). This is a clear advantage of this technique, as quite often the emissivity is not precisely known. Note that this is the

case for our application, especially because samples undergo some surface oxidation during testing at high temperature, which may change their emissivity during testing.

Dedimet is equipped with a BP (Thermalert[®] Marathon series MR1S[™]) working from 630 to 1400°C with two near infrared wavelengths taken in the intervals 0.75 – 1.1µm and 0.95 – 1.1µm [50]. The BP is mounted outside the chamber, facing one of the wide faces of the sample through a sapphire glass window, whose transmission is over 80% for wavelengths between 0.3 and 5µm.

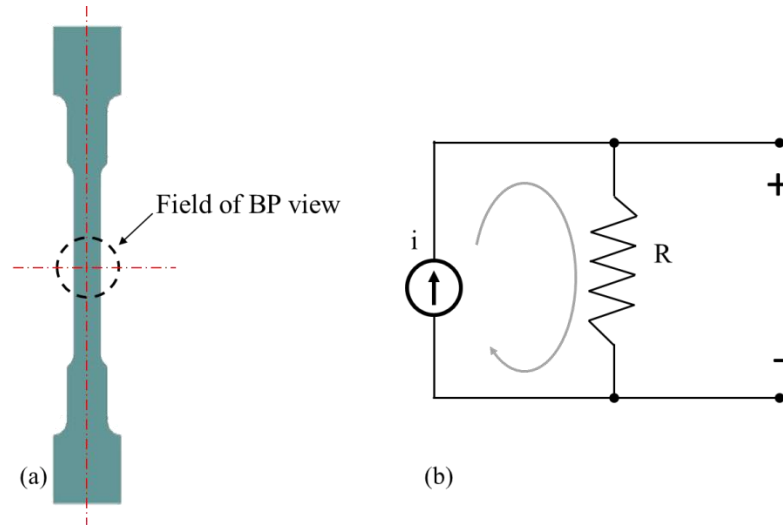


Fig. 2-4 (a) Field of view of the BP compared with sample configuration, and (b) Electrical circuit for transforming electrical current signal to voltage signal of B.P.

Based on the overall spatial setup of the Dedimet machine, the “best” or the “minimum” field of BP view is still larger than the width of the sample, as shown by the circle in Fig. 2-4 (a). A pyrometer with single color cannot measure the temperature in this case because it needs to detect the average radiation value within the whole field of view. However, with the merits of measurement of bichromatic pyrometer, we can still measure the temperature of the sample even if the measurement area is not filled by the target objective [52,50].

The output of a pointwise BP is a current which is linearly dependent on the temperature of the sample. Given unchanged emissivity ratio of the two wavelength bands, the output current is linear to the temperature. There is an electrical resistance connected in series in the circuit, as shown in Fig. 2-4 (b), where the phototube can be deemed as the electrical current source, and the electrical potential will be also linearly linked to the temperature, so that it can be used as control signal. Certain coefficients should be identified then, to convert the potential to temperature, and their values can be different, according to the target material, surface aspect, view angle... The calibration procedure can be found in Appendix A. 8.1

2.3.1.3 Bichromatic Infrared Camera

The IMS-HDRC[®]-Q-PyroCam bichromatic IR camera was used, and this camera can officially measure temperature from 600 to 1900°C (in fact from about 750°C the measurement becomes precise based on the default factory system calibration based on our test), and it can also use visible light as signal for positioning. The visible light signal is used to link pixels with millimeters, see Appendix A. 9. This camera has a vision field of 640×480 pixels resolution. Each pixel can be deemed as a tiny BP. Accordingly, no emissivity knowledge is required.

The temperature values from the camera are arranged in a numerical array shaped as [..., (pixel_ID, T_value), ...] which can be accessed by an interface of dynamic-link library. However, this development potential remains untouched during this research work.

Provided some calibration is done adequately (see just hereafter in Section 2.3.3) the infrared camera gives access to the surface temperature field. In the present context of thin samples, it can be shown (see details in Appendix A. 6) that the temperature difference between the central core and the surface is quite limited. It can be estimated to of 3 to 4°C at 1000°C. Hence, as the field of view of our IR field measurement covers the whole surface of the working zone, it offers a good knowledge of the overall temperature distribution in the volume of the sample possibly affected by deformation.

2.3.2 Temperature Control

2.3.2.1 PID and Parameter Selection

The sample is heated up by Joule effect, thus it is very convenient to control the temperature by adjusting the imposed electrical current. The PID algorithm preset in Labview is expressed by [54]:

$$i(t) = k_p e(t) + k_i \int_0^t e(\tau) d\tau + k_d \frac{de(t)}{dt} \quad (2-16)$$

where $i(t)$ is the current to be imposed in the sample at instant t , namely the control output, $e(t) = T_{set}(t) - T_{exp}(t)$ is the temperature bias between the set (objective) temperature $T_{set}(t)$ and the measured temperature $T_{exp}(t)$, and k_p , k_i and k_d are the associated constants for proportional, integral and derivative terms, respectively, to be adjusted in the PID algorithm. The derivative response is sensitive to the noise of the signal. One considers this derivative part when the system undergoes rapid control loop. If the control loop rate is too small (at which case the noise becomes relevant), the derivative response could lead the control system to an unstable state [55]. In our case, even though during heating-up period the temperature rate is big, the temperature remains almost constant at the control point all through the loading-relaxation period of the test. In other words, the temperature at the control point has an increasing speed of zero, thus, there is no need to consider the derivative part of the PID algorithm because what we do care is the load-relaxation period.

Before studying a new alloy, or rather a new alloy family, or/and a new sample geometry, an appropriate set of PID parameters should be found so that the temperature can be precisely and robustly controlled. A good set of PID parameters should have the following characteristics: when the control input signal $T_{exp}(t)$ by feedback sensor deviates from the set value $T_{set}(t)$, the control output signal $i(t)$ should be adjusted so that the deviation can be reduced quickly, but without generating an opposite deviation (overshoot or undershoot).

In this project there are at least two successive loading-relaxation sequences in each experiment (refer to section 2.6). It can be inferred that when the loading is taken, the sample becomes thinner in its central part, making in this region the electrical resistance per length larger. The Joule heat source will tend to increase if the electrical intensity is maintained, resulting in a temperature increase in the central position. Therefore, we need to find a set of PID parameters to ensure that the temperature is always close to the set value whatever the deformation of the sample.

Fig. 2-5 shows the temperature response during loading and relaxation. It shows that the parameters are appropriate.

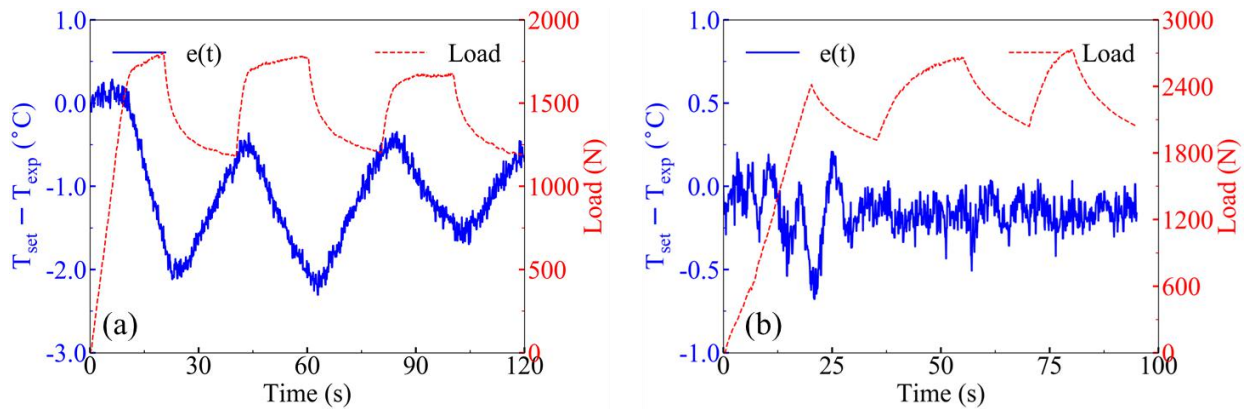


Fig. 2-5 PID temperature control during three successive loading and relaxation sequences. Two sets of PID parameters are tested: (a) $k_p = 0.45$, $k_i = 6.7$, and (b) $k_p = 1$, $k_i = 100$. Red curves present the force evolution, blue curves show the temperature difference with respect to the set value (here 900°C).

For (a) $k_p = 0.45$, and $k_i = 6.7$, it can be observed that during loading the temperature tends to increase, and during relaxation the temperature tends to decrease. Such trends are expected from the explanations given above regarding the variation of the local resistance in the central region. The control algorithm only limits the deviation, but it does not really succeed to maintain it around zero. It is to be noted however that the amplitude of the two phenomena is similar, with an error reaching here $\sim 1.8^\circ\text{C}$.

For (b) $k_p = 1$, and $k_i = 100$, the temperature is adjusted in a more dynamic way thanks to higher k_p and k_i parameter values. During loading-relaxation step the temperature bias is restrained smaller than 0.6°C . This set of parameters appears to be better than the previous one.

2.3.2.2 Selection of Signal for Temperature Control

From the above introduction of the various techniques, the following conclusion can be drawn regarding temperature control; that is the choice of the signal to be provided to the control procedure responsible for respecting a certain thermal history $T(t)$:

- From room temperature to about 1150°C, K type thermocouple is used.
- When testing temperature is higher than 1150°C, or when K type thermocouple cannot be used (when temperature is higher than 940°C for Ti alloy, for example [56]) BP should be used.

Whatever the contact way (TC) or non-contact way (BP) is chosen, only one signal channel will be used for temperature control. At each moment, the temperature of the sample at a selected position will be controlled either by thermocouple signal or by BP signal. In our case, the central position, which shows the highest temperature, is selected as the control position. In case of thermocouple control, it will be welded, on the small lateral surface at mid-height of the work zone. In case of BP control, the BP target zone will be initially centered on the wide face of the sample at mid-height. Note that the BP remains fixed, but during a test the target zone will slightly deviate from the current mid-height location. This is not a problem, considering the small displacements and the reasonable uniformity of the temperature profile close to the center.

2.3.3 Calibration of Temperature Field from IR Camera

The as-received temperature field should be calibrated. The assumption is adopted that the temperature measured by K type thermocouple is the reference one. The main idea of the calibration is that temperature values at selected positions extracted from the infrared camera record should become close to the values at the equivalent positions measured by thermocouples. The calibration method is based on a least square smoothing and is detailed below.

Five testing positions were selected along the wide face of the working zone of the specimen, with a 10mm interval along length direction between them, as shown in Fig. 2-6 (a). Thermocouples, labeled K1 (top) to K5 (bottom), were welded at these positions. K3 at the central position was selected as the PID control signal for heating the specimen by Joule effect. Heating was processed by successive increasing temperatures: each time a new aimed temperature was reached, a control plateau was respected to wait for the establishment of a steady state regime in the sample, as illustrated in Fig. 2-6 (c). The measured temperature provided by each of the five thermocouples was then recorded at mid time of the plateau. Concurrently, the temperature field was also recorded by the bichromatic IR camera on the opposite wide side of the sample. As shown in Fig. 2-6 (b), five square zones of 9×9 pixels (~1.7mm²) were selected in the temperature field. They are labeled R1 to R5 and have their centers in the same positions as the thermocouples. For comparison purpose, the output IR value was the average value in each square. The comparison was done on a temperature range from 800°C to 1200°C, with 25°C increments, because the IR camera is suited for

temperature higher than 750°C (see Section 2.3.1.3), and the maximum measuring temperature of K type thermocouples is about 1200°C, for a short duration.

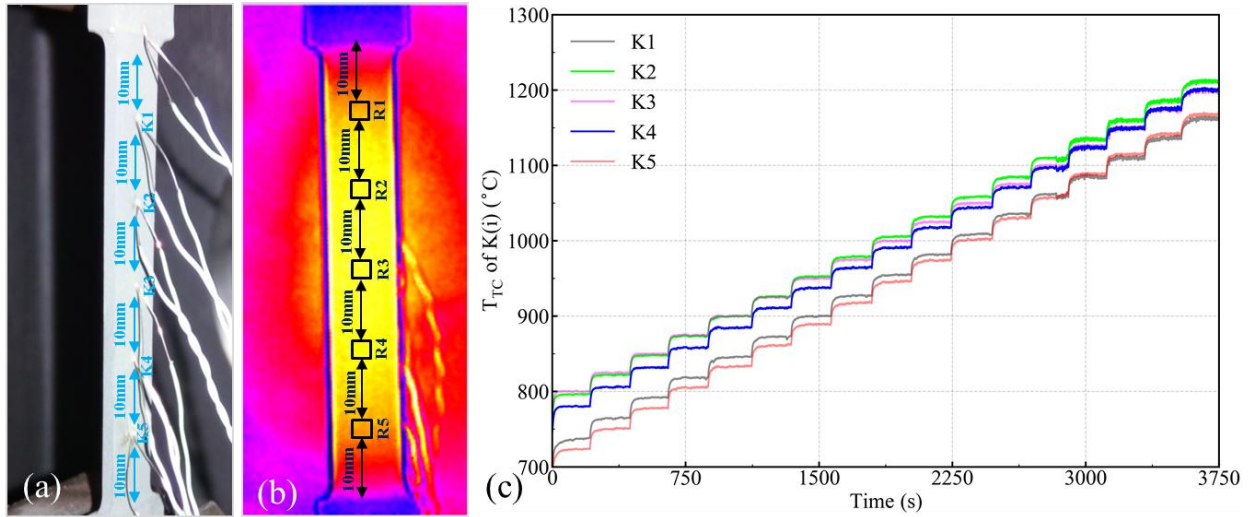


Fig. 2-6 Setup for temperature comparison: a) Positions where thermocouples were welded, b) Square zones where averaged data were extracted from IR bichromatic field measurement, and c) Temperature evolution at thermocouples.

It can be seen in Fig. 2-6 (c) that – as often in Dedimet tests – the parabolic-like temperature profile somewhat deviates toward the top half of the specimen, showing a maximum temperature above the mid-height of the working zone: temperatures at K2 and K3 are almost identical, higher than K4, with K1 higher than K5. It is worth noticing that this calibration is taken under air pressure of 1 bar, which introduces convection making the highest temperature position not at the central position of K3, but upper than it. This is also the reason for which K2 and K3 values are so close, and K1 is higher than K5.

Fig. 2-7 shows the plot of T_{IR} (IR measure) vs T_{TC} (TC measure) for the five positions, and on the entire temperature range. The following observations can be achieved:

- T_{IR} is systematically higher than T_{TC} . The line labeled R(i) is the line with slope equal to one, indicating an ideal correspondence between IR and TC measures. For each temperature level the value measured by thermocouple is lower than that by IR camera.
- The overall trend of the plot between T_{TC} and T_{IR} is a straight-line shape, which indicates a linear relation.

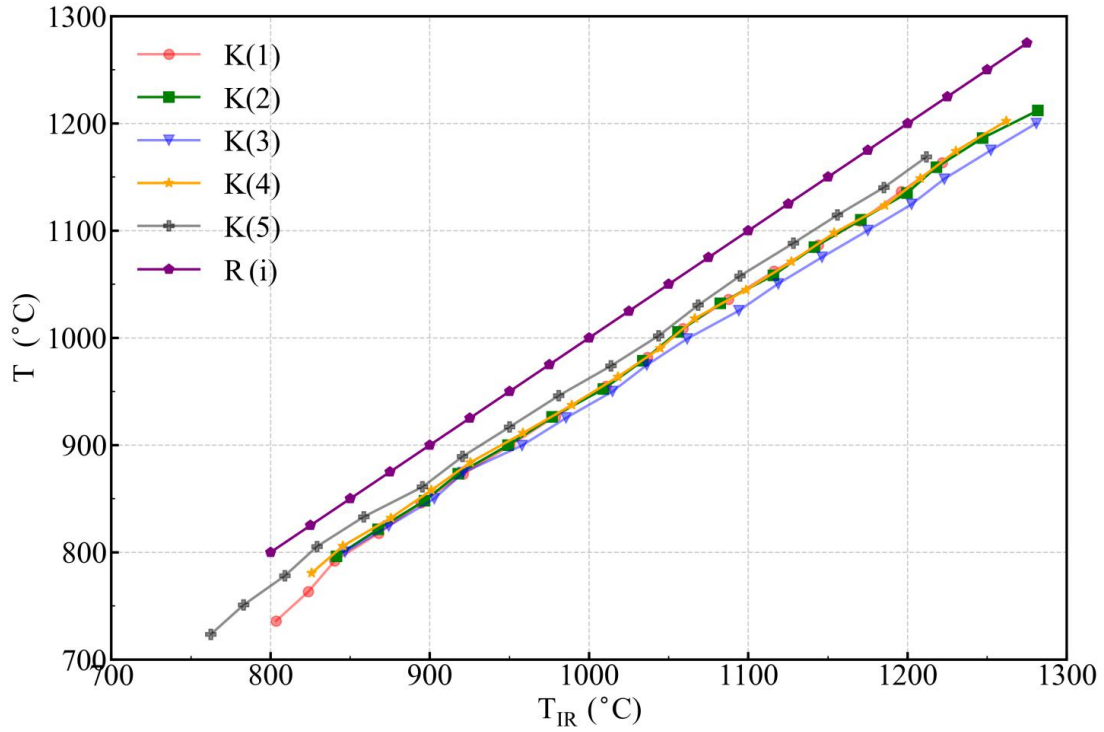


Fig. 2-7 Comparison between IR measurement and thermocouple measurement for each of the five testing locations.

With a linear relation assumption, given T_{IR} , the thermocouple measure T_{TC} can be approached by the following linear expression:

$$\hat{T} = k \cdot T_{IR} + b \quad (2-17)$$

Parameters k and b can be identified by minimizing the following argument, with a least squares approach:

$$\arg_{min} \Psi = \sum_{j=1}^5 \sum_{i=1}^n \left(\frac{\hat{T}^{i,j} - T_{TC}^{i,j}}{T_{TC}^{i,j}} \right)^2 \quad (2-18)$$

where j stands for the sampling position, and i indicates the measured temperature level.

This optimization problem can be easily solved and returns the following values:

$$k = 0.939$$

$$b = 1.8^\circ\text{C}$$

Considering the measuring precision of thermocouple, it can be even simplified as

$$k = 0.939$$

$$b = 0$$

With this simplification for each real test, it is possible to calibrate the temperature with temperature at only one position, and the k parameters in all tests are close to 0.93.

2.4 Displacement Measurement

There are basically two kinds of methods to measure the displacement field, which are interferometric and non-interferometric techniques [57]. Digital image correlation (DIC) belongs to the non-interferometric category. In this section the DIC background is firstly introduced, and then the way to measure the displacement field by DIC in this project is presented.

2.4.1 Introduction to DIC measurement

A brief introduction of DIC-2D is given here [58]. Let's remind first that the basic idea of the DIC method is to track the displacement of local material patches at the surface of the specimen. Such speckle is attached on material surface by gridded-paper adhesion or paint spray or other methods. When light (usually exterior light) illuminates this speckle, contrast is returned in reflection light, which is mostly expressed by grey level. In other words, any point in the speckle has coordinates in the DIC reference frame and a gray value at its position. This provides to record a series of gray value field that evolves with time. The DIC algorithm is working on these grey fields.

Fig. 2-8 gives a schematic diagram explaining how DIC works. Initially a reference point P_c^t is selected in a tiny zone of Ω^t , and any other point in this Ω^t is assigned as P_i^t . For convenience, the Ω^t called subset is selected as a $(2M + 1) \cdot (2M + 1)$ square, where M is an integer, and P_c^t is assigned at the center position of this subset. After deformation, the reference point goes to P_c^{t+1} , and P_i^t goes to P_i^{t+1} , i.e.:

$$\mathbf{p}_c^{t+1} = \mathbf{p}_c^t + \mathbf{u}_c \quad (2-19)$$

$$\mathbf{p}_i^{t+1} = \mathbf{p}_i^t + \mathbf{u}_i$$

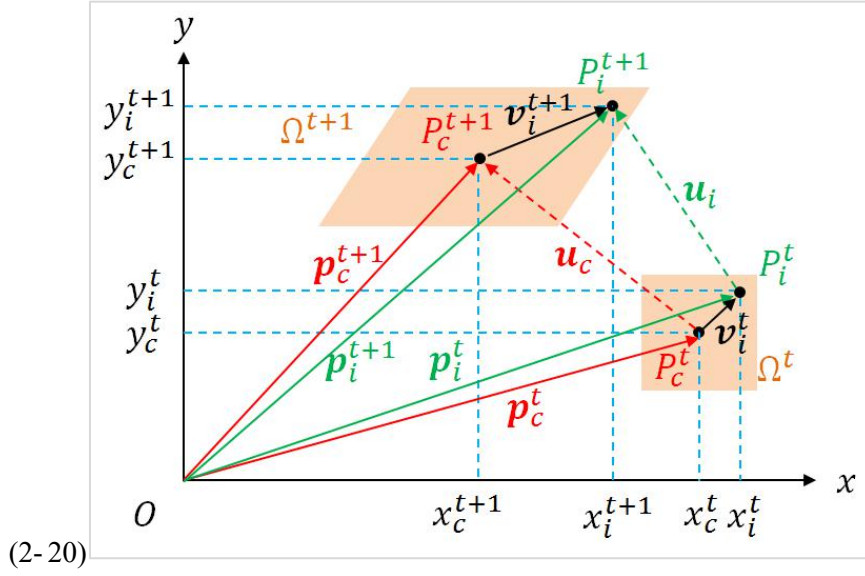


Fig. 2-8 Schematic diagram of DIC theory

where $\mathbf{u}_c = (u_{c_x}, u_{c_y})$. Take the first order derivative of Eq. 2-19 (could be second order or even higher based on requirement):

$$d\mathbf{p}_c^{t+1} = (\mathbf{I} + \nabla \mathbf{u}_c) d\mathbf{p}_c^t \quad (2-21)$$

The $d\mathbf{p}_c^{t+1}$ and $d\mathbf{p}_c^t$ correspond to the vectors from P_c^{t+1} to P_i^{t+1} (\mathbf{v}_i^{t+1}) and P_c^t to P_i^t (\mathbf{v}_i^t), respectively, i.e.:

$$\begin{pmatrix} x_i^{t+1} - x_c^{t+1} \\ y_i^{t+1} - y_c^{t+1} \end{pmatrix} = \begin{pmatrix} 1 + \frac{\partial u_{c_x}}{\partial x_c} & \frac{\partial u_{c_x}}{\partial y_c} \\ \frac{\partial u_{c_y}}{\partial x_c} & 1 + \frac{\partial u_{c_y}}{\partial y_c} \end{pmatrix} \begin{pmatrix} x_i^t - x_c^t \\ y_i^t - y_c^t \end{pmatrix} \quad (2-22)$$

Re-organize this equation to get:

$$\begin{cases} x_i^{t+1} = x_i^t + u_{c_x} + \frac{\partial u_{c_x}}{\partial x_c} (x_i^t - x_c^t) + \frac{\partial u_{c_x}}{\partial y_c} (y_i^t - y_c^t) \\ y_i^{t+1} = y_i^t + u_{c_y} + \frac{\partial u_{c_y}}{\partial x_c} (x_i^t - x_c^t) + \frac{\partial u_{c_y}}{\partial y_c} (y_i^t - y_c^t) \end{cases} \quad (2-23)$$

So the guessed coordinates (x_i^{t+1}, y_i^{t+1}) of any point P_i at time step $t + 1$ can be expressed by 4 known coordinates $(x_i^t, y_i^t, x_c^t, y_c^t)$ at time step t , together with 6 unknowns $\mathbf{p} = (u_{c_x}, u_{c_y}, \frac{\partial u_{c_x}}{\partial x_c}, \frac{\partial u_{c_x}}{\partial y_c}, \frac{\partial u_{c_y}}{\partial x_c}, \frac{\partial u_{c_y}}{\partial y_c})^T$.

With Eq. 2-23 a deformed zone Ω^{t+1} can be guessed. Any point P_i^t in Ω^t has a grey value $f(x_i^t, y_i^t)$, i.e. the grey value distribution on Ω^t : given the coordinates (x_i^t, y_i^t) the grey value $f(x_i^t, y_i^t)$ is known from DIC camera records. Correspondingly the point $P_i^{t+1}(x_i^{t+1}, y_i^{t+1})$ in the guessed Ω^{t+1} has a grey value $g(x_i^{t+1}, y_i^{t+1})$ from DIC records, i.e. the grey value distribution on the guessed Ω^{t+1} . Based on the primary hypothesis of DIC:

- Throughout the entire measurement the relative grey value of each point on the surface of the sample varies little in order to trace it.
- The point dispersion in the speckle is random so that each reference zone is unique.

A correlation function can be defined. It has a lot of possible expressions, and one of them (for example) is the zero-mean normalized sum of squared differences (ZNSSD), as follows:

$$C(\mathbf{p}) = \sum_{x_i^t=-M}^{x_i^t=+M} \sum_{y_i^t=-M}^{y_i^t=+M} \left(\frac{f(x_i^t, y_i^t) - f_m}{\sqrt{\sum_{x_i^t=-M}^{x_i^t=+M} \sum_{y_i^t=-M}^{y_i^t=+M} (f(x_i^t, y_i^t) - f_m)^2}} - \frac{g(x_i^{t+1}, y_i^{t+1}) - g_m}{\sqrt{\sum_{x_i^t=-M}^{x_i^t=+M} \sum_{y_i^t=-M}^{y_i^t=+M} (g(x_i^t, y_i^t) - g_m)^2}} \right)^2 \quad (2-24)$$

where $f_m = \frac{1}{(2M+1)^2} \sum_{x_i^t=-M}^{x_i^t=+M} \sum_{y_i^t=-M}^{y_i^t=+M} f(x_i^t, y_i^t)$ is the average grey value in the Ω^t ; $g_m = \frac{1}{(2M+1)^2} \sum_{x_i^t=-M}^{x_i^t=+M} \sum_{y_i^t=-M}^{y_i^t=+M} g(x_i^t, y_i^t)$ is the average grey value in the Ω^{t+1} . By minimization of $C(\mathbf{p})$ we can finally find \mathbf{p} , in which we can obtain the displacement and deformation information. That is the mathematical background of DIC. With the help of DIC we can measure the displacement field. It is at once inferred that the local velocity field can be calculated as long as the displacement field is obtained. It must be mentioned that there are also others ways to calculate the displacement field and deformation field, which is quite beyond the objective of introduction here. Generally speaking, when a 2D displacement is measured, in order to decrease the measuring error, it is necessary to make sure that the sensor (CMOS or CCD matrix) plane is parallel to the plane of the sample surface, which is quite difficult to meet [59]. In our project two cameras are used, which allows measuring the displacement in 3D. Thus, it is possible to measure the 2D displacement even in presence of a certain non-parallelism between planes.

2.4.2 Camera positioning

The positioning/support of the two DIC cameras is integrated to the Dedimet machine, as shown in Fig. 2-1 (a). They are attached to the door in such a way that when the chamber is closed, the two cameras are adequately positioned with respect to the door window and the sample. As shown in Fig.

2-9, the central normal line of the sample (red center line) and the two DIC camera axes (blue center lines) are in the same plane, and the longitudinal direction of the sample is in that plane too. By this setup, the reference frame transformation can be simplified, which will be further explained in 3.6.1 of Chapter 3. The sampling frequency of the DIC cameras can vary (from 100 to 0.01Hz), among which 10 Hz is used.

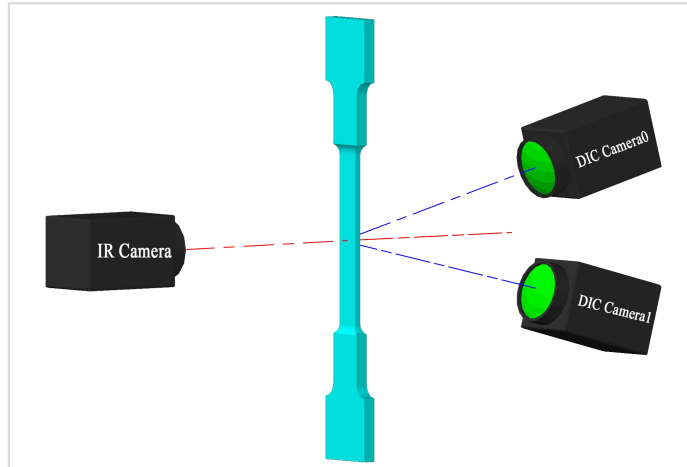


Fig. 2-9 Spatial positioning of IR and DIC cameras

2.4.3 High Temperature DIC

It is expected to measure the displacement field of the sample in a large temperature range, from room temperature to $\sim 1200^{\circ}\text{C}$. This is important regarding the choice of the speckle material and of the deposition technique. At temperature lower than 600°C , commercial high temperature spray paints can be used to prepare the speckle, while for higher temperatures, the paint will deteriorate soon. Thus, the use of a solution of special ceramic powder should be preferred to prepare the speckle. “Pyro-Paint 634-AL Alumina Based Refractory Coating” is adopted as the ceramic paint, which is applied on the sand-blasted sample surface to finally get the white dots of the speckle. Details to prepare the speckle are given in Appendix A. 2.

Aside of the paint, the lighting system requires attention too. The speckle used for DIC is in form of paint dots on grey sample surface, thus it is necessary to select the right light source so that the contrast between dots and sample surface be strong enough. According to Planck’s law, from room temperature to about 700°C , the heat radiation emitted by the sample surface is mainly situated in the infra-red spectrum. It is not in the visible light domain, thus DIC cameras can see the speckle clearly with additional white light source, i.e., bright dots and dark sample surface. Conversely, when the temperature is higher than 700°C the sample starts to emit in the visible light spectrum (in addition to the IR). Consequently, the contrast between the paint dots and sample surface becomes weak. A popular solution in this case consists in using an additional blue lighting, provided by LED matrix, and band-pass filters of the same wavelength. The sample surface reflects the blue light, and at the same time emits the thermal radiation (partly in the visible spectrum, and

mainly in the infra-red spectrum). The band-pass filters positioned in front of the cameras permit the blue light only to go through, blocking the thermal radiation. This preserves a good speckle contrast in the images recorded by the cameras.

The blue lighting with band-pass strategy sounds a good solution if the light emitted from the sample does not have a main spectrum length around the value of the band-pass filter [57,60,61,62]. However, the fact is that this strategy no longer works well based on the apparatus in our project when the temperature is higher than 900°C. Then an alternative strategy to measure the displacement field is selected, which is based on the light emitted from the sample itself (self-emitting strategy).

When the sample of IN718 is heated to a temperature range of 750 ~ 1200°C, the emitted thermal radiation includes visible light, which is strong enough to be used as the lighting source. In this case, the speckle composed of ceramic paint behaves like a thermal barrier, which blocks – or at least significantly reduces – visible emission at paint dots. Thus, places not painted emit more visible light and appear clearer than painted dots. There are three key points to correctly use this self-emitting method:

- The size of the deposited dots must be carefully controlled. Ceramic dots should not be too small, otherwise the speckle loses contrast at high temperature. At the same time, they should not be too big: a too sparse speckle cannot provide “just right” information [63]. This is the first compromise. However, at a higher temperature level, our experimental feed-back is that bigger dots are to be preferred. The typical dot diameters produced during the present study vary between 70 and 600µm. Refer to Appendix A. 3 for more detail.
- The light emitted by the sample itself is not as strong as that from an external (blue) light source. Given fixed short exposure time, large diaphragm aperture is necessary to reach a correct exposure. However, as the sample deforms during the test, its surface slightly departs from the focal point. Therefore, a good balance must be found: the aperture must not be too large, in order to get enough depth of field. This is the second compromise.
- Calibration of the DIC system is done after testing (contrary to the conventional sequence: calibration before test). This is because the camera, although well focused on target (the wide face of the specimen) at room temperature, will lose focus at high temperature. Therefore, for a precise record of speckle motion, the focus must be done at testing temperature: after a test is finished, calibration is done on the condition that the cameras should maintain their lens positions. Only the aperture is decreased, and exposure time is increased. One can see that the DIC system has a little change between calibration and testing, but only the aperture and exposure time, not the most important lens position. This is the third compromise. More explanation for this post-calibration is given in Appendix A. 4.

2.4.4 Atmosphere during Displacement Measurement

In the literature it is known that when there is gas convection, the measurement is influenced, or even impossible due to thermal plumes along the specimen surface [64,65]. In this project, the

sample being heated up to 1100°C, there is no doubt that this issue must be solved. Imposing a strong wind blasting or a vacuum are two possible solutions. The vacuum was preferred, as surface temperature is more stable, by fully avoiding gas flow. This is why it is chosen to operate testing under vacuum condition (~10mbar) in a chamber. Although this vacuum is not high enough to avoid oxidation ($\sim 1 \times 10^{-3}$ mbar needed [66,67]) and convection, it can strongly reduce the adverse effects.

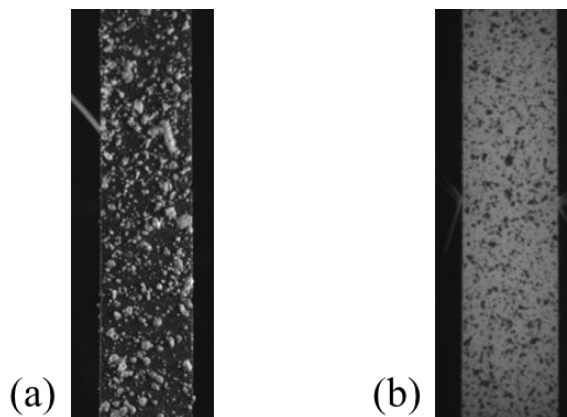
2.4.5 DIC Measuring Condition Summary

Summary of the displacement field measurement is given in Table 2.

Table 2 Displacement measurement summary covering RT to 1200°C

<i>T</i> range	RT to 600°C	600 to 900°C	800 to 1200°C
Lighting method	Blue LED (430nm) + Band pass filter (430nm)	Blue LED (430nm) + Band pass filter (430nm)	Self-emitting
Atmosphere	Vacuum (~10mbar)	Vacuum (~10mbar)	Vacuum (~10mbar)
Speckle and application	“Jelt” high temperature paint, white dots + black background, spraying	“Pyro-Paint 634-AL” ceramic paint, white dots, brush spattering	“Pyro-Paint 634-AL” ceramic paint, white dots, brush spattering
Field effect	Bright speckle in dark background	Bright speckle in dark background	Dark speckle in bright background

It can be seen that there is conjunction or overlap of the temperature ranges, which makes it possible to measure the displacement field for all the temperature range. The typical field effect aforementioned is shown in Fig. 2- 10.



- **Fig. 2- 10 DIC image field effect for test (a): from room temperature to 900°C with blue light and band-pass filter, and (b): self-emitting method from 800 to 1200°C**

2.5 Testing Preparation

Some sample preparations must be done to ensure precise measurements. The main steps are in the following sequence: geometry refinement, surface refinement, geometry measurement, speckle preparation, and finally thermocouple welding and testing. They are introduced in the following paragraphs.

2.5.1 Geometry Refinement



Fig. 2-11 Typical sample, as received from Safran. The specimen is in its rough state, after LPBF processing, and separation by Electrical discharge machining (EDM) from the build plateau.

As shown in Fig. 2-11, samples in their rough state post LPBF manufacturing have a geometry which is not suited for mounting on Dedimet. This is due to the specificity of LPBF processing. For certain orientations of the sample geometry with respect to the build direction, the LPBF manufacturing requires some additional portions to the initial design or some additional thin supporting structures. This can be seen in the right part of Fig. 2-11, where such an appendice was cut, affecting the geometry of the end of the specimen. Depending on the selected orientation, these extra appendices may affect the ends of the specimen but also the working zone. All these extra of the as-EDM separated sample were removed via an electrical rotary cutter with water as the cutting fluid.

Besides, the Dedimet mechanical tests being uni-axial tests – at least at the scale of the specimen, and regarding the applied boundary conditions – it is thus expected that the centers of the four fillets be at the vertices of a rectangle, and the fillets have the same radius, see Fig. 2-12 (a). This is quite important because those four fillet regions are the places for load transmission, from the ceramic pins of the machine to the sample: a geometrical defect would create a deviation with respect to a supposed uniaxial testing. As shown in Fig. 2-12 (b), as-built AM samples suffer from dimensional inaccuracies, particularly in these regions. Additional machining was then done at Cemef to meet the pre-described requirement.

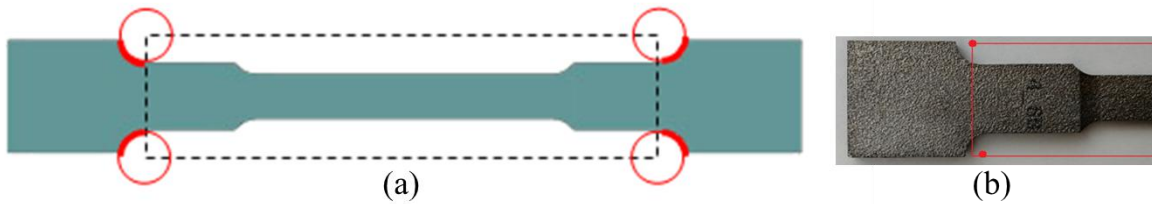


Fig. 2- 12 Nominal position of the four fillets with a unique radius, and b) a detailed view showing the inaccurate shape in the as-built state.

2.5.2 Surface Pre-treatment

The second step comes once the sample geometry is well adjusted. Step 2 consists in modifying the surface status by sand blasting. Fig. 2- 13 shows the different surface states of the sample with and without sand blasting. This step is necessary for different reasons.

- A first objective is to smooth the surface, in order to uniformize emissivity, and so to increase the robustness of following IR temperature measurement. Indeed, local surface irregularities may cause stronger emissivity at abrupt positions, and the precision of the temperature measurement would be reduced [68,69].
- The second motivation relates to the speckle quality. Sand blasting activates the sample surface, in order that the paint to be applied on the sample has a strong adherence. Besides, when the sample is in the as-received state, since the surface roughness is big, there is strong wetting which makes the speckle preparation difficult. And when the roughness is aligned with a direction, a series of light bands can be observed when the sample is heated and emits light, as seen in Fig. 2- 14.
- Finally, a strong roughness induces precision error when we measure the geometry.

One could wonder about the influence of potential residual stress introduced by sandblasting. It should be noted here that the fabrication process such as LPBF may also generate residual stress, which is introduced firstly by laser processing, and then by machining and support removal. It can be thought, however, that all residual stress could be ignored. This is because of Joule heating and maintaining at high temperature before testing which should promote stress release by annealing effect. More details are given in Section 5.5.1.



Fig. 2-13 Surface state of sample. (a): as received, and (b): after sandblasting

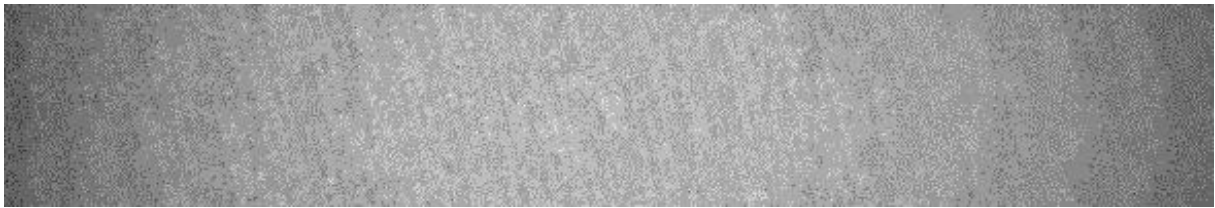


Fig. 2-14 Light bands (wrinkles) when the as-received sample is heated with Joule effect (Image treated so that the light bands can be seen more obviously)

2.5.3 Geometry Measurement

The geometry of each sample is measured after sand blasting, because the sand blasting reduces the size of the sample. Three positions within the zone of interest (namely the central portion) are measured for the width and thickness and then an average value is considered. Besides, even though the surface roughness has been reduced after sand blasting, it still makes sense to take surface roughness into consideration, but only at the error analysis step. Details about the geometrical contribution to error analysis can be found in Appendix A. 16.1.1.

2.5.4 Preparation of Speckle

After the sample is sand blasted, the speckle preparation should be done. The application of the paint should be done in a short delay in order to obtain good adherence between the paint and the sample since the sand-blast procedure is in fact a step of activation, as is used in most surface treatment procedure. Then a solution of Pyro-Paint 634-AL-P Powder and Pyro-Paint 634-AL-L Liquid is applied on the sample surface to obtain randomly dispersed points which cover the whole 60mm working zone. Fig. 2-15 shows one of the samples with prepared speckle.



Fig. 2- 15 Sample with speckle prepared by brush spattering

2.5.5 Thermo-couple Welding and Testing

Three thermocouples are generally welded in the working zone. Two of them are welded at the central position, one at each side of the lateral surfaces, and the last is welded at about 15 mm off the center in upper or lower direction at the lateral surface. Within the two central-welded thermocouples, the first one is used for monitoring the temperature and its signal is used in the PID algorithm to control the temperature, the other one is for insurance in case the first one falls during the test. As for the last one, it is used for recording temperature change at a position which is not the control point. The first two thermocouples at the central position are mandatory, and the last one is optional for a controlled test.

2.6 Illustration of an Experimental Test

After preparation, samples are mounted on Dedimet machine. A test is carried out in the following steps:

- (1) Load the sample, connect the thermocouples to control channels of Dedimet, close the door of the chamber and start the pump.
- (2) Set the testing routine (temperature, loading velocity and duration, etc.) and control parameters (PID parameters, control signal, etc.).
- (3) Start the test (i.e., heating up with free thermal expansion) when the vacuum is lower than 1mbar.
- (4) When temperature is stable, focus DIC cameras, IR camera and BP. Typically the duration between the end of heating up and the start of the first loading is 180s. The heating up itself takes also 180s.
- (5) Start DIC recording at about 10s before the start of the first loading (1st velocity imposition).
- (6) Start IR recording the moment step (5) is taken (synchronizing is later done manually).

- (7) Wait till the end of the test, when Joule effect and loading/relaxation will be stopped automatically.
- (8) Remove the sample when it is cooled down (~20min after the test).
- (9) Calibrate DIC system with a calibration grid provided by the VIC-3D solution company.
- (10) Take an image of the DIC calibration grid via IR camera with visible light.

Note that the two last steps are particularly important. Step 9 ensures that the calibration of the DIC system is performed based on the as-focused camera setup (also read Step 4 above, also refer to Section 2.4.3 of this chapter). Step 10 provides the necessary information to transform the length unit from pixel to millimeter, see Appendix A. 9.

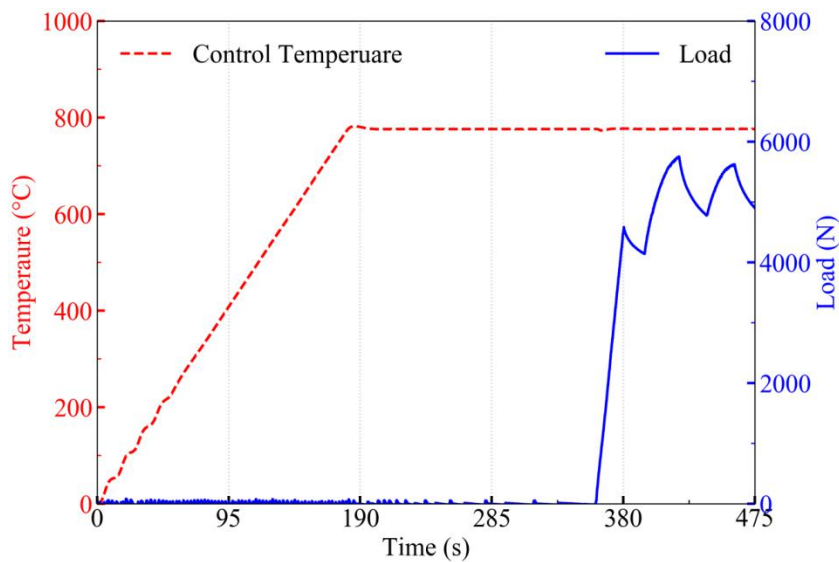


Fig. 2-16 Temperature and force records during a test operated at 800°C. Blue dashed curve: temperature, red solid curve: force.

Fig. 2-16 presents a typical test record, in terms of temperature (red dashed line) and force (blue solid line). In the first 180 seconds the sample is heated to the desired temperature (in this case 800°C), then it is maintained at this temperature for 180s so that the temperature profile is stable. During this first 360s, dilatation effects are compensated by an automatic control (PID type) of the beam movement in order that the force applied to the specimen be zero. In other words, during the heating the sample can expand freely. This results in slight force oscillations that can be seen during this period. Then three cycles of loading-relaxation are imposed to the sample with different beam velocities and durations, while the temperature at the control point is maintained at 800°C unchanged (PID controlled).

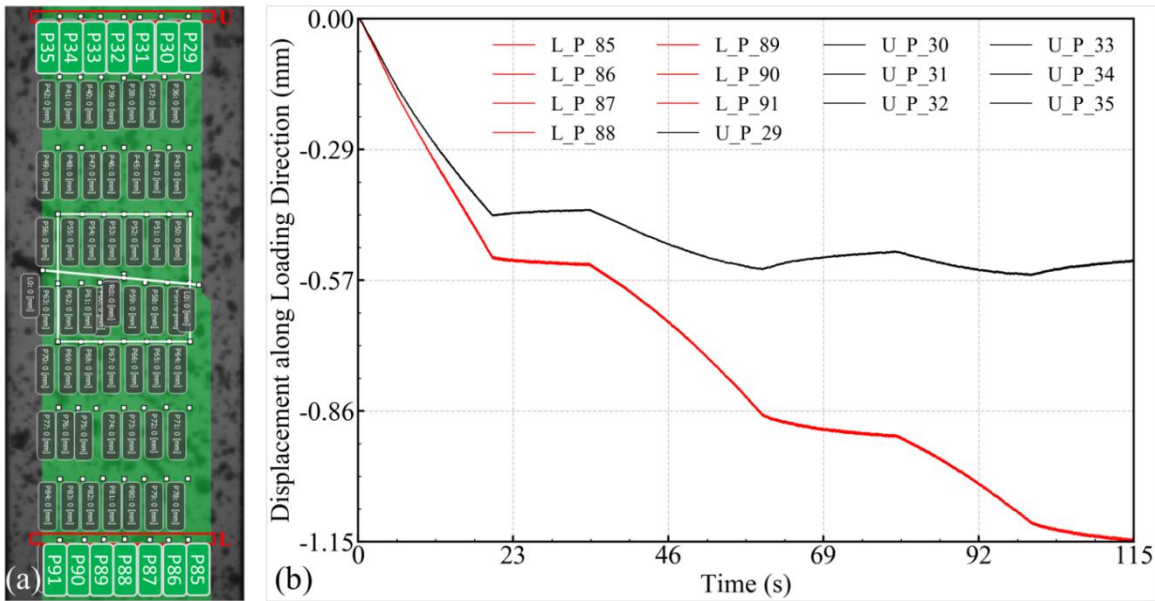


Fig. 2-17 Illustration of DIC measurement at the beginning of the first load step. (a) Initial surface as visualized by VIC-3D with a series of user-defined virtual Lagrangian sensors for the capture of displacement vs time for specific material points; (b) the horizontal ranks of sensors (U and L) have superimposed displacement component along loading direction.

During a test the two DIC cameras capture a series of images, which are later analyzed by VIC-3D software, so that a displacement field is returned, with the components of the displacement being expressed in the length and width directions of the sample. They can be then visualized. As shown in Fig. 2-17 (a) numerical Lagrangian sensors can be defined to output the displacement information for selected material points, having selected positions in the initial state at reference instant (360s in w.r.t. Fig. 2-16). In this figure a sensor matrix (7×9) is selected. The 7 sensors of the lower line (group labelled L) and the 7 sensors of the upper line (labelled U) are strictly selected so that they are in line in each of the two groups. The central sensors in these two groups are also aligned along the axial (vertical) symmetry line in the middle of the wide face of the specimen. After analysis by VIC-3D, the displacement components along the sample direction of the sensors of group L and U are extracted in Fig. 2-17 (b). It is worth noticing that the displacement components along the loading direction of the sensors in the upper group (U: P29-P35) are almost the same, and similarly in the lower group (L: P85-P91). That proves that the deformation of the sample concentrates in its central zone, which constitutes a weak zone due to its maximum temperature. However, it can be seen that, even though the upper group of sensors is located on the side of the fixed end of the specimen, the recorded displacement there is not null. This is due to the fact that the upper part of the specimen (above the U sensor group) deforms a little anyway. This may be also due to a certain insufficient rigidity of the machine, or at least of the mechanical assembly linking the sample to the machine. The information recorded at these two groups of sensors will be used later to define the boundary conditions applied to the so-called “zone of interest” (ZOI) in the numerical simulation of the tests (see section 3.6.2.1 in Chapter 3). Indeed, defining a ZOI in between the two groups of sensors, it can be seen from Fig. 2-17 (b) that the total elongation in z direction of the ZOI is the

difference between the two sets of 7 curves. It is interesting to note that this total elongation is continuously growing, even during the relaxation steps.

2.7 Chapter Summary

In this chapter the global setup of the machine Dedimet has been first introduced. Sample type selection, control conditions and response measurement have been briefly described too. Based on that, the definition of the geometry of the specimen, and its preparation prior testing (surface state, speckle deposition, thermocouple welding) have been presented. Finally, some elements regarding DIC and IR measurement and calibration have been reported and discussed. An illustrative example of the different records performed upon testing at high temperature has been shown.

In the next chapter, we will explain how this experimental information will be used when proceeding to identification of constitutive parameters. There is no doubt that a good mastering of testing control and instrumentation accuracy is a key point for success.

Chapter Reference

- 48 Pignolet, A., Combeaud, C., Fournier, F., Fiorucci, G., Pradille, C., Zhang, Y., Pinto-Mora, A., Gao, F. and Bellet, M., 2018. Experimental Approach for Metals Mechanical Behavior Characterization at High Temperature: Development of a Complex Tensile Test Machine. *In Multidisciplinary Digital Publishing Institute Proceedings* (Vol. 2, No. 8, p. 355).
- 49 ASTM E230 / E230M - 17. Standard specification and temperature-electromotive force (emf) tables for standardized thermocouples.
- 50 Marathon MR 2-color infrared thermometer, Operating instructions, Raytek, Rev.E3 Feb 2017, 56913
- 51 FLIR, A., 2010. The ultimate infrared handbook for R&D professionals. *Boston: FLIR Systems*. Document ID: T559243(en-SV)_A
- 52 BOOK, A, Principle, advantages, limitations and applications of two-colour pyrometer in thermal processes, technical reports by KELLER HCW GmbH, Germany, TR_006_201507_en
- 53 Lienhard IV, John H. and Lienhard V, John H. *A heat transfer textbook. fourth*. Cambridge : Phlogiston Press, 2017. p. 531.
- 54 Aström, Karl Johan and Murray, Richard M. *Feedback Systems: An Introduction for Scientists and Engineers*. New Jersey 08540 : Princeton university press, 2010. pp. 293-302.
- 55 PID Theory Explained - National Instruments, <https://www.ni.com/fr-fr/innovations/white-papers/06/pid-theory-explained.html>, visited May 10th, 2020
- 56 Ni-Ti phase diagram, *Journal of Phase Equilibria* Vol. 12 No. 5 1991
- 57 Pan, B., Wu, D., Wang, Z. and Xia, Y., 2010. High-temperature digital image correlation method for full-field deformation measurement at 1200 C. *Measurement science and technology*, 22(1), p.015701.
- 58 <http://www.ncorr.com/index.php>, Ncorr - Open source 2D digital image correlation MATLAB software, visited Jan.07,2021

-
- 59 Sutton, M.A., Yan, J.H., Tiwari, V., Schreier, H.W. and Orteu, J.J., 2008. The effect of out-of-plane motion on 2D and 3D digital image correlation measurements. *Optics and Lasers in Engineering*, 46(10), pp.746-757.
- 60 Wang, W., Xu, C., Jin, H., Meng, S., Zhang, Y. and Xie, W., 2017. Measurement of high temperature full-field strain up to 2000°C using digital image correlation. *Measurement science and technology*, 28(3), p.035007.
- 61 Valeri, G., Koohbor, B., Kidane, A. and Sutton, M.A., 2017. Determining the tensile response of materials at high temperature using DIC and the virtual fields method. *Optics and Lasers in Engineering*, 91, pp.53-61.
- 62 Blaber, J., Adair, B.S. and Antoniou, A., 2015. A methodology for high resolution digital image correlation in high temperature experiments. *Review of Scientific Instruments*, 86(3), p.035111.
- 63 <https://digitalimagecorrelation.org/>, visited Feb. 01, 2021
- 64 Jones, E.M.C. and Reu, P.L., 2018. Distortion of digital image correlation (DIC) displacements and strains from heat waves. *Experimental Mechanics*, 58(7), pp.1133-1156.
- 65 Qiyuan, D.U.A.N., Wenran, G.O.N.G., Baoqiao, G.U.O., Lifu, W.U., Xingzhe, Y.U. and Huimin, X.I.E., 2019. Techniques of speckle fabrication and image processing for high temperature digital image correlation. *Journal of Tsinghua University (Science and Technology)*, 59(6), pp.425-431.
- 66 Vacuum Heat Treatment of Fasteners, <https://vacaero.com/information-resources/vac-aero-training/6909-vacuum-heat-treatment-fasteners.html>, visited March. 10, 2021
- 67 SECO/Warwick, 2011 *Heat Treating Data Book*, Tenth Edition E-Book, p59
- 68 Keller, B.P., Nelson, S.E., Walton, K.L., Ghosh, T.K., Tompson, R.V. and Loyalka, S.K., 2015. Total hemispherical emissivity of Inconel 718. *Nuclear Engineering and Design*, 287, pp.11-18.
- 69 Greene, G.A., Finfrock, C.C. and Irvine Jr, T.F., 2000. Total hemispherical emissivity of oxidized Inconel 718 in the temperature range 300–1000°C. *Experimental Thermal and Fluid Science*, 22(3-4), pp.145-153.

Chapter 3 Numerical Implementation

Résumé

Dans un premier temps, un modèle de comportement élastique-viscoplastique (EVP) de type loi associé est détaillé. Dans ce modèle, l'élasticité isotrope et la viscoplasticité anisotrope (basée sur Hill48) sont combinées, intégrées à l'écroutissage isotrope et à l'écroutissage cinématique. La dépendance à la température est considérée dans les paramètres du model constitutif.

Ensuite, le package numérique par la méthode des éléments finies est construit pour simuler la partie la plus chaude au milieu de l'échantillon sous chauffage par effet joule.. Pendant la simulation, le champ de température expérimental est imposé dans le maillage, et la vitesse extraite du champ de déplacement expérimental est imposée comme condition aux limites dans la simulation.

Enfin, la transformation des informations expérimentales vers le maillage est détaillée, suivie de la preuve de l'efficacité par la simulation numérique.

Chapter Introduction

In the previous chapter the experimental method related to the characterization of mechanical behavior at high temperature has been explained. The data acquisition of the three physical quantities (load, displacement field and temperature field) has been described. These data will be later used for identifying the behavior-law-related parameters by use of an inverse finite element method. Before presenting the identification process, the present chapter deals with the so-called direct simulations of the tests. Generally speaking, two direct simulation strategies can be envisaged:

The first strategy consists in simulating the global electrical-thermal-mechanical problem, as stated in the prior works of C. Pradille [70] or C. Zhang [71] in Cemef. The simulation is conducted on the overall sample. In that case three kinds of solvers are needed, i.e., the electrical solver, the thermal solver and the mechanical solver, possibly coupled to solve this complex problem. It can be seen in the references that a lot of boundary conditions are required regarding the various solvers, especially the knowledge of heat and electrical contact resistances. Besides, plenty of physical parameters such as electrical conductivity, thermal conductivity and specific heat capacity are also unavoidably required for the simulation, including their temperature dependence. Besides, more solvers mean more time consuming because they are not running in parallel but in sequence sometimes. However, there are also some strong points in such a global strategy. For example, it can provide a good probe into the complex problem.

The second strategy, on the contrary, is called the local strategy. As the name suggests, this strategy simulates only a portion of the tested sample, not all of it. Thus, there will be more convenience compared with the global strategy. For example, if the IR camera can only measure partially the sample, for a global strategy this non-full-field measurement is a problem but for a local strategy it can work. Moreover, the local strategy simulates only a part of the sample, which indicates that CPU time will be less too. The drawback of the local strategy is that sometimes it is difficult to extract the boundary conditions from experiment to simulation.

Given the strong and weak points of the two possible candidates, the local strategy is selected. The drive of such a choice lies in:

- Indifference with respect to a poor knowledge of certain physical parameters of the material (as aforementioned that are difficult to measure), and
- Reduction of computation time in view of further identification algorithm.

With the selected local simulation strategy as introduced above, the FEM frame for direct simulations in the inverse method will be introduced in this chapter. Especially, a candidate anisotropic Thermo-elasto-viscoplastic constitutive model for the characterization will be presented. The interaction between experimental method and direct simulation concerning reference frame transformation will be also presented.

3.1 Brief Introduction of the FEM Frame

The CimLib library is a C++ numerical parallel computation platform developed in-house in Cemef. This library allows developing a wide variety of applications in numerical modeling of material processing and its environment. CimLib offers different three-dimensional finite element solvers for aerodynamics, liquid flow, turbulence, solid mechanics, heat, and mass transport... Mechanical solvers are based on a mixed velocity-pressure formulation, with linear tetrahedral finite elements. In all cases, there are 4 unknowns per node: 3 velocity components, and the pressure.

For solid mechanics, the tetrahedral element is enriched with a “bubble” function to avoid locking (additional internal degrees of freedom that can be eliminated locally, prior to global resolution for nodal velocity and pressure). The P1+/P1 mini-element initially proposed by Arnold *et al* [72] and Fortin [73] is taken in Cimlib.

For fluid flow it is stabilized by SUPG-PSPG formulation. For the computation of momentum conservation equation, a Variational MultiScale (VMS) method is chosen. This method was initially proposed by Tezduyar *et al.* [74,75]. The SUPG-PSPG solver in CimLib consists of a stabilized P1 formulation and results from developments conducted by Gouttebroze [76,77] and Hachem *et al.* [78,79].

CimLib also contains procedures for error estimation, and automatic adaptive remeshing, which are especially designed for such tetrahedral elements [80]. The idea is to deduce a metric tensor at each node according to the edge length distribution tensor.

3.2 Governing Equations

The modeling of solid mechanics consists in coupling the conservation equations of momentum and mass [81,82]. Starting from the strain rate relation:

$$\nabla \cdot \mathbf{v} = \text{tr} \dot{\boldsymbol{\varepsilon}} = \text{tr} \dot{\boldsymbol{\varepsilon}}^{el} + \text{tr} \dot{\boldsymbol{\varepsilon}}^{th} + \text{tr} \dot{\boldsymbol{\varepsilon}}^{vp} \quad (3-1)$$

where \mathbf{v} is the velocity field, $\dot{\boldsymbol{\varepsilon}}$ is the strain rate tensor, $\dot{\boldsymbol{\varepsilon}}^{el}$ is the elastic strain rate tensor, $\dot{\boldsymbol{\varepsilon}}^{th}$ is the thermal strain rate tensor (noticing that the trace of the viscoplastic strain rate tensor is always zero, i.e. $\text{tr} \dot{\boldsymbol{\varepsilon}}^{vp} \equiv 0$).

Isotropic Hook's law is given as:

$$\begin{bmatrix} \varepsilon_{11} \\ \varepsilon_{22} \\ \varepsilon_{33} \\ 2\varepsilon_{23} \\ 2\varepsilon_{31} \\ 2\varepsilon_{12} \end{bmatrix} = \frac{1}{E} \begin{bmatrix} 1 & -\nu & -\nu & 0 & 0 & 0 \\ -\nu & 1 & -\nu & 0 & 0 & 0 \\ -\nu & -\nu & 1 & 0 & 0 & 0 \\ 0 & 0 & 0 & 2(1+\nu) & 0 & 0 \\ 0 & 0 & 0 & 0 & 2(1+\nu) & 0 \\ 0 & 0 & 0 & 0 & 0 & 2(1+\nu) \end{bmatrix} \begin{bmatrix} \sigma_{11} \\ \sigma_{22} \\ \sigma_{33} \\ \sigma_{23} \\ \sigma_{31} \\ \sigma_{12} \end{bmatrix} \quad (3-2)$$

where E is the Young's modulus, ν is the Poisson's ratio. One can easily find the following relation:

$$\text{tr} \dot{\boldsymbol{\varepsilon}}^{el} = \frac{1-2\nu}{E} \text{tr} \dot{\boldsymbol{\sigma}} \quad (3-3)$$

where $\boldsymbol{\varepsilon}^{el}$ is the elastic strain tensor, $\boldsymbol{\sigma}$ is the stress tensor. Calculate the time derivative to get:

$$\text{tr} \dot{\boldsymbol{\varepsilon}}^{el} = \frac{1-2\nu}{E} \text{tr} \dot{\boldsymbol{\sigma}} = -\frac{\dot{p}}{\chi_b} + \frac{1}{\chi_b^2} \frac{d\chi_b}{dt} \dot{p} \quad (3-4)$$

where p is the pressure equal to $(-\frac{1}{3})\text{tr} \boldsymbol{\sigma}$, t is the time and $\chi_b = \frac{E}{3(1-2\nu)}$ is the bulk elastic modulus. The thermal strain rate is given by:

$$\dot{\boldsymbol{\varepsilon}}^{th} = \alpha_T \dot{T} \mathbf{I} \quad (3-5)$$

where \mathbf{I} is the unit tensor, α_T is the linear thermal expansion coefficient, and \dot{T} is the temperature rate. Immediately the isotropic thermal strain rate tensor has the following relation:

$$tr \dot{\boldsymbol{\epsilon}}^{th} = 3\alpha_T \dot{T} \quad (3-6)$$

Injecting Eqs. 3-4 and 3-6 into Eq. 3-1, and considering the force equilibrium (in the present case of small working piece, the inertia effect and mass force are ignored), one can get the following governing equations:

$$\begin{cases} \nabla \cdot \boldsymbol{\sigma} & = \mathbf{0} \quad \dots \quad (a) \\ \nabla \cdot \mathbf{v} + \frac{\dot{p}}{\chi_b} - \frac{1}{\chi_b^2} \frac{d\chi_b}{dt} \frac{\dot{p}}{\chi_b} - 3\alpha_T \dot{T} & = 0 \quad \dots \quad (b) \end{cases} \quad (3-7)$$

The stress tensor, $\boldsymbol{\sigma}$, can be decomposed into two parts. The first one is deviatoric stress tensor (\mathbf{s}) and the second one is related to the pressure field by:

$$\boldsymbol{\sigma} = \mathbf{s} - p\mathbf{I} \quad (3-8)$$

The boundary conditions are:

$$\begin{cases} \mathbf{v} & = \mathbf{v}_{imp} \text{ on } \Gamma_v \\ \boldsymbol{\sigma} \cdot \mathbf{n}_\Omega & = \mathbf{f}_{imp} \text{ on } \Gamma \end{cases} \quad (3-9)$$

Eq. 3-7 (1), which is mainly governed by the constitutive law describing the relation between stress and strain, will be introduced in section 3.3 in this chapter.

3.3 Thermo-Elastic-viscoplastic (TEVP) Constitutive Model

3.3.1 General Formulation of an Anisotropic Elastic-viscoplastic Behavior Law

The objective of this subsection is to determine the nature of a candidate Thermo-Elasto-viscoplastic (TEVP) constitutive model for Dedimet identification purpose. More precisely, the objective is to describe the expression of the viscoplastic strain rate, $\dot{\boldsymbol{\epsilon}}^{vp}$, and especially the temperature dependence. Moreover, the anisotropy, isotropic hardening and kinematic hardening aspects are also treated here.

The general formulation is derived from the one developed by Chaboche [83], in the framework of generalized standard materials under small deformation.

First, an additive partition of the total strain rate into elastic, plastic and thermal parts is assumed, i.e.

$$\dot{\boldsymbol{\varepsilon}} = \dot{\boldsymbol{\varepsilon}}^{el} + \dot{\boldsymbol{\varepsilon}}^{vp} + \dot{\boldsymbol{\varepsilon}}^{th} \quad (3-10)$$

where $\dot{\boldsymbol{\varepsilon}}$ is the overall strain rate calculated by: $\dot{\boldsymbol{\varepsilon}} = \frac{1}{2}(\nabla \mathbf{v} + (\nabla \mathbf{v})^T)$.

The free energy per unit of mass, ψ , is defined as [84]:

$$\rho\psi = \underbrace{\rho\psi^{el}}_{elastic} + \underbrace{\frac{1}{3}C\boldsymbol{\alpha}:\boldsymbol{\alpha} + h(\kappa)}_{plastic} \quad (3-11)$$

with ψ^{el} the elastic free energy, κ the internal variable for plastic deformation, $\boldsymbol{\alpha}$ the tensor of internal variables for kinematic hardening, and C a material parameter.

By definition of the associated variables, it can be deduced that:

$$\left\{ \begin{array}{l} \boldsymbol{\sigma} = \rho \frac{\partial \psi}{\partial \boldsymbol{\varepsilon}^{el}} = \rho \frac{\partial \psi^{el}}{\partial \boldsymbol{\varepsilon}^{el}} \quad \dots \quad (a) \\ s = -\frac{\partial \psi}{\partial T} \quad \dots \quad (b) \end{array} \right. \quad (3-12)$$

where s is the specific entropy. The thermodynamic forces (stresses, actually) corresponding to $\boldsymbol{\alpha}$ and κ are, respectively the back stress tensor \mathbf{X} and the increase in the size of the elastic domain in isotropic hardening:

$$\left\{ \begin{array}{l} \mathbf{X} = \rho \frac{\partial \psi}{\partial \boldsymbol{\alpha}} = \frac{2}{3}C\boldsymbol{\alpha} \quad \dots \quad (a) \\ R = \rho \frac{\partial \psi}{\partial \kappa} = \frac{\partial h(\kappa)}{\partial \kappa} \quad \dots \quad (b) \end{array} \right. \quad (3-13)$$

In order to define additional laws for the dissipative phenomena, the following power-law type dissipation potential is considered:

$$\Omega = \frac{k}{n+1} \left(\frac{\bar{\sigma}(\boldsymbol{\sigma}-\mathbf{X}) - (\sigma_Y + R)}{k} \right)^{n+1} \quad (3-14)$$

The material parameters k and $m = 1/n$ are the viscoplastic consistency and the strain-rate sensitivity index, respectively. $\bar{\sigma}$ is a function defining the equivalent stress. Assuming an anisotropic material obeying the criterion of Hill48 [85], the expression of $\bar{\sigma}(\boldsymbol{\sigma})$ can be defined as the following:

$$\bar{\sigma} = \sqrt{F(\sigma_{YY} - \sigma_{ZZ})^2 + G(\sigma_{ZZ} - \sigma_{XX})^2 + H(\sigma_{XX} - \sigma_{YY})^2 + 2L\sigma_{YZ}^2 + 2M\sigma_{ZX}^2 + 2N\sigma_{XY}^2} \quad (3-15)$$

where the capital letters X , Y and Z are adopted for the subscript of the stress tensor to define stress component in orthotropic directions of the material frame, i.e., the anisotropy reference frame. The additional laws can then be expressed as:

$$\begin{cases} \dot{\boldsymbol{\varepsilon}}^{vp} = \frac{\partial \Omega}{\partial \boldsymbol{\sigma}} \cdots & (a) \\ \dot{\kappa} = -\frac{\partial \Omega}{\partial R} \cdots & (b) \end{cases} \quad (3-16)$$

After calculation, we get:

$$\dot{\kappa} = \left(\frac{\langle \bar{\sigma}(\boldsymbol{\sigma} - \mathbf{X}) - (\sigma_Y + R) \rangle}{k} \right)^{\frac{1}{m}} \quad (3-17)$$

where the Macaulay brackets " $\langle \cdot \rangle$ " is used with the meaning of:

$$\langle x \rangle = \begin{cases} 0 & \text{if } x < 0 \\ x & \text{if } x \geq 0 \end{cases} \quad (3-18)$$

so that the $\dot{\kappa}$ continues only in the non-elastic domain. Note that we have also, from Eq. 3-14:

$$\frac{\partial \Omega}{\partial \bar{\sigma}} = \left(\frac{\langle \bar{\sigma}(\boldsymbol{\sigma} - \mathbf{X}) - (\sigma_Y + R) \rangle}{k} \right)^n = \left(\frac{\langle \bar{\sigma}(\boldsymbol{\sigma} - \mathbf{X}) - (\sigma_Y + R) \rangle}{k} \right)^{\frac{1}{m}} = \dot{\kappa} \quad (3-19)$$

The expressions of the evolution laws defining $\dot{\mathbf{X}}$ and $\dot{\boldsymbol{\alpha}}$ can be defined by the derivation of the extended dissipation potential:

$$\Omega^{ext} = \frac{k}{n+1} \left(\frac{\bar{\sigma}(\boldsymbol{\sigma} - \mathbf{X}) - (\sigma_Y + R) + \frac{3\gamma}{4C} \mathbf{X} : \mathbf{X} - \frac{\gamma}{3} C \boldsymbol{\alpha} : \boldsymbol{\alpha}}{k} \right)^{n+1} \quad (3-20)$$

Note that because of Eq. 3-13 a, the sum of the two additional terms $(\frac{3\gamma}{4C} \mathbf{X} : \mathbf{X} - \frac{\gamma}{3} C \boldsymbol{\alpha} : \boldsymbol{\alpha})$ in Ω^{ext} is always null, so that $\Omega^{ext} = \Omega$. It can be shown that the evolution law for $\boldsymbol{\alpha}$ is:

$$\dot{\boldsymbol{\alpha}} = -\frac{\partial \Omega^{ext}}{\partial \boldsymbol{\alpha}} = \boldsymbol{\varepsilon}^{vp} - \frac{3\gamma}{2C} \dot{\kappa} \mathbf{X} \quad (3-21)$$

where γ is an additional material parameter. From that, and considering that $\mathbf{X} = \frac{2}{3} C \boldsymbol{\alpha}$, we obtain:

$$\dot{\mathbf{X}} = \frac{2C}{3} \boldsymbol{\varepsilon}^{vp} - \gamma \kappa \mathbf{X} \quad (3-22)$$

Unless specific notice, tensors will be hereafter noted using Voigt's notation:

$$\tilde{\mathbf{s}} = \begin{bmatrix} s_1 \\ s_2 \\ s_3 \\ s_4 \\ s_5 \\ s_6 \end{bmatrix} \equiv \begin{bmatrix} S_{XX} \\ S_{YY} \\ S_{ZZ} \\ S_{YZ} \\ S_{ZX} \\ S_{XY} \end{bmatrix} \quad (3-23)$$

and

$$\dot{\boldsymbol{\varepsilon}} = \begin{bmatrix} \dot{\varepsilon}_1 \\ \dot{\varepsilon}_2 \\ \dot{\varepsilon}_3 \\ \dot{\varepsilon}_4 \\ \dot{\varepsilon}_5 \\ \dot{\varepsilon}_6 \end{bmatrix} \equiv \begin{bmatrix} \dot{\varepsilon}_{XX} \\ \dot{\varepsilon}_{YY} \\ \dot{\varepsilon}_{ZZ} \\ 2\dot{\varepsilon}_{YZ} \\ 2\dot{\varepsilon}_{ZX} \\ 2\dot{\varepsilon}_{XY} \end{bmatrix} \quad (3-24)$$

In case of the anisotropic quadratic criterion of Hill48, it can be shown that:

$$\bar{\sigma} = f_{Hill}(\boldsymbol{\sigma}) = \sqrt{\tilde{\boldsymbol{\sigma}}^T \mathbf{P} \tilde{\boldsymbol{\sigma}}} \quad (3-25)$$

where \mathbf{P} is a 6×6 symmetric matrix:

$$\mathbf{P} = \begin{bmatrix} G+H & -H & -G & 0 & 0 & 0 \\ -H & F+H & -F & 0 & 0 & 0 \\ -G & -F & F+G & 0 & 0 & 0 \\ 0 & 0 & 0 & 2L & 0 & 0 \\ 0 & 0 & 0 & 0 & 2M & 0 \\ 0 & 0 & 0 & 0 & 0 & 2N \end{bmatrix} \quad (3-26)$$

Note that the isotropic von Mises criterion is retrieved by choosing: $F = G = H = 1/2$ and $L = M = N = 3/2$.

In presence of kinematic hardening, we have

$$\bar{\sigma} = f_{Hill}(\boldsymbol{\sigma} - \mathbf{X}) = \sqrt{\tilde{\boldsymbol{\xi}}^T \mathbf{P} \tilde{\boldsymbol{\xi}}} \quad (3-27)$$

where $\tilde{\xi}$ is Voigt's notation of tensor $\xi = \mathbf{s} - \mathbf{X}$, which is the difference between the deviatoric stress tensor \mathbf{s} and the back stress tensor \mathbf{X} (which is a deviator according to Eq. 3-22.).

Using the expression of the potential of Eq. 3-14, the viscoplastic flow rule can be written as follows:

$$\dot{\boldsymbol{\varepsilon}}^{vp} = \frac{\partial \Omega}{\partial \boldsymbol{\sigma}} = \frac{\partial \Omega}{\partial \bar{\sigma}} \frac{\partial \bar{\sigma}}{\partial \boldsymbol{\sigma}} = \frac{\partial \Omega}{\partial \bar{\sigma}} \frac{\partial \bar{\sigma}}{\partial \xi} \frac{\partial \xi}{\partial \boldsymbol{\sigma}} \quad (3-28)$$

From Eq. 3-14, we have:

$$\frac{\partial \Omega}{\partial \bar{\sigma}} = \left(\frac{(\bar{\sigma}(\boldsymbol{\sigma} - \mathbf{X}) - (\sigma_Y + R))}{k} \right)^{\frac{1}{m}} \quad (3-29)$$

and, from Eq. 3-27

$$\frac{\partial \bar{\sigma}}{\partial \tilde{\xi}} = \frac{1}{\bar{\sigma}} \mathbf{P} \tilde{\xi} \quad (3-30)$$

Let's denote \mathbf{M} the matrix linking the deviator to the stress tensor in Voigt notation:

$$\tilde{\mathbf{s}} = \mathbf{M} \tilde{\boldsymbol{\sigma}} \rightarrow \mathbf{M} = \frac{\partial \tilde{\mathbf{s}}}{\partial \tilde{\boldsymbol{\sigma}}} \quad (3-31)$$

$$\mathbf{M} = \frac{1}{3} \begin{bmatrix} 2 & -1 & -1 & 0 & 0 & 0 \\ -1 & 2 & -1 & 0 & 0 & 0 \\ -1 & -1 & 2 & 0 & 0 & 0 \\ 0 & 0 & 0 & 3 & 0 & 0 \\ 0 & 0 & 0 & 0 & 3 & 0 \\ 0 & 0 & 0 & 0 & 0 & 3 \end{bmatrix} \quad (3-32)$$

The viscoplastic flow rule, Eq. 3-28, writes, for any component $i = 1, 2, \dots, 6$ in Voigt notation:

$$\dot{\boldsymbol{\varepsilon}}^{vp}_i = \frac{\partial \Omega}{\partial \bar{\sigma}} \frac{\partial \bar{\sigma}}{\partial \xi_j} \frac{\partial \xi_j}{\partial \sigma_i} = \frac{\partial \Omega}{\partial \bar{\sigma}} \frac{1}{\bar{\sigma}} P_{jk} \xi_k M_{ji} = \frac{1}{\bar{\sigma}} \frac{\partial \Omega}{\partial \bar{\sigma}} (M^T)_{ij} P_{jk} \xi_k \quad (3-33)$$

The matrix \mathbf{M} being symmetric, this leads to:

$$\dot{\boldsymbol{\varepsilon}}^{vp} = \frac{1}{\bar{\sigma}} \left(\frac{(\bar{\sigma}(\boldsymbol{\sigma} - \mathbf{X}) - (\sigma_Y + R))}{k} \right)^{\frac{1}{m}} \mathbf{M} \mathbf{P} \tilde{\xi} \quad (3-34)$$

It can be noticed that $\mathbf{MP} = \mathbf{P}$, so that:

$$\dot{\boldsymbol{\epsilon}}^{vp} = \frac{1}{\bar{\sigma}} \left(\frac{(\bar{\sigma}(\boldsymbol{\sigma} - \mathbf{X}) - (\sigma_Y + R))}{k} \right)^{\frac{1}{m}} \mathbf{P} \tilde{\boldsymbol{\xi}} = \frac{\dot{\kappa}}{\bar{\sigma}} \mathbf{P} \tilde{\boldsymbol{\xi}} \quad (3-35)$$

with $\bar{\sigma} = f_{Hill}(\boldsymbol{\sigma} - \mathbf{X}) = \sqrt{\tilde{\boldsymbol{\xi}}^T \mathbf{P} \tilde{\boldsymbol{\xi}}}$.

From that expression of the viscoplastic flow rule, the generalized strain rate in the von Mises sense, $\dot{\bar{\epsilon}} = \sqrt{(2/3) \dot{\boldsymbol{\epsilon}}^{vp} : \dot{\boldsymbol{\epsilon}}^{vp}}$, can be calculated. In Voigt notation,

$$\dot{\bar{\epsilon}} = \sqrt{\dot{\boldsymbol{\epsilon}}^{vp T} \mathbf{Q} \dot{\boldsymbol{\epsilon}}^{vp}} \quad (3-36)$$

with \mathbf{Q} being defined as:

$$\mathbf{Q} = \frac{1}{3} \begin{bmatrix} 2 & 0 & 0 & 0 & 0 & 0 \\ 0 & 2 & 0 & 0 & 0 & 0 \\ 0 & 0 & 2 & 0 & 0 & 0 \\ 0 & 0 & 0 & 1 & 0 & 0 \\ 0 & 0 & 0 & 0 & 1 & 0 \\ 0 & 0 & 0 & 0 & 0 & 1 \end{bmatrix} \quad (3-37)$$

We get, by injecting Eq. 3-35 into Eq. 3-36:

$$\dot{\bar{\epsilon}}^2 = \frac{\dot{\kappa}^2}{\bar{\sigma}^2} (\mathbf{P} \tilde{\boldsymbol{\xi}})^T \mathbf{Q} \mathbf{P} \tilde{\boldsymbol{\xi}} = \frac{\dot{\kappa}^2}{\bar{\sigma}^2} \tilde{\boldsymbol{\xi}}^T \mathbf{P}^T \mathbf{Q} \mathbf{P} \tilde{\boldsymbol{\xi}} \quad (3-38)$$

As $\mathbf{P}^T \mathbf{Q} \mathbf{P} \neq \mathbf{P}$, we notice that in general, in presence of an anisotropic plastic criterion, $\dot{\bar{\epsilon}} \neq \dot{\kappa}$. Conversely, for an isotropic von Mises criterion, it can be checked that $\tilde{\boldsymbol{\xi}}^T \mathbf{P}^T \mathbf{Q} \mathbf{P} \tilde{\boldsymbol{\xi}} = \bar{\sigma}^2$, so that we can write $\dot{\kappa} = \dot{\bar{\epsilon}}$.

Finally, we have – in condition of elastic-viscoplastic flow – the following scalar relation linking $\bar{\sigma}$, κ , and $\dot{\kappa}$ can be gotten from Eqs. 3-17 and 3-27:

$$\bar{\sigma} = f_{Hill}(\boldsymbol{\sigma} - \mathbf{X}) = \sigma_Y + R(\kappa) + k \dot{\kappa}^m \quad (3-39)$$

3.3.2 Temperature Effect on Viscoplastic Strain Rate Hardening

The temperature dependency is generally introduced, first, by an Arrhenius law affecting the viscoplastic consistency. Thus, Eq. 3-17 can be extended to:

$$\dot{\kappa} = \left(\frac{\langle \bar{\sigma}(\boldsymbol{\sigma} - \mathbf{X}) - (\sigma_Y + R) \rangle}{k} \right)^{\frac{1}{m}} \exp \left(-\frac{Q_{vp}}{R_g T} \right) \quad (3-40)$$

where Q_{vp} denotes the activation energy of phenomena governing viscoplastic flow, and R_g is the gas constant. Hence we have:

$$\langle f \rangle = \langle \bar{\sigma}(\boldsymbol{\sigma} - \mathbf{X}) - (\sigma_Y + R) \rangle = k \dot{\kappa}^m \exp \left(\frac{m Q_{vp}}{R_g T} \right) \quad (3-41)$$

where f denotes the plastic yield function. Introducing a reference temperature T_{ref} to Eq. 3-41 we can get:

$$\langle f \rangle = \langle \bar{\sigma}(\boldsymbol{\sigma} - \mathbf{X}) - (\sigma_Y + R) \rangle = k_{ref} \dot{\kappa}^m \exp \left(\frac{m Q_{vp}}{R_g T} - \frac{m Q_{vp}}{R_g T_{ref}} \right) \quad (3-42)$$

where k_{ref} is the consistency at the reference temperature T_{ref} .

3.3.3 Temperature Effect on Initial Yield Stress and Isotropic Strain Hardening

Temperature also affects the initial yield stress, and stress hardening. Before discussing this in detail, it is necessary to present the possible expression of the strain hardening function R . For that, we can start from the classical equation of the KME model suggested by Kocks, Mecking and Estrin [86,87]. Denoting ρ_d the dislocation density, its evolution is modelled by the following differential equation:

$$\frac{d\rho_d}{dt} = \kappa M (k_1 \sqrt{\rho_d} - k_2 \rho_d) \quad (3-43)$$

where M is the Taylor factor, k_1 is a constant associated with strain hardening by dislocation glide, and k_2 a variable characterizing the softening effect associated with dynamic recovery by dislocation climb. The following alternative form is often used, although it can be derived from the equation above only if $\dot{\kappa}$ is a constant, or if k_2 is assumed independent of $\dot{\kappa}$:

$$\frac{d\rho_d}{d\kappa} = M (k_1 \sqrt{\rho_d} - k_2 \rho_d) = h \sqrt{\rho_d} - r \rho_d \quad (3-44)$$

In order to establish a candidate expression of the strain hardening function $R(\kappa)$, the Taylor expression of the yield stress of a polycrystal is considered [88]:

$$\sigma_s = M\alpha\mu b_d\sqrt{\rho_d} \quad (3-45)$$

where σ_s denotes the stress threshold ($\sigma_s = \sigma_Y + R(\kappa)$), α a material constant, μ the elastic shear modulus, and b_d the module of the Burgers vector. It is then possible to justify – through some calculations (partially done in Blaizot *et al* [89]) – the following form of the strain hardening function, composed of two terms, a first one expressing strain-hardening, and a second one expressing the moderating effect of dynamic recovery.

$$R(\kappa) = H\kappa^n + Q_r(1 - \exp(-b\kappa)) \quad (3-46)$$

where H is the strength coefficient, n is the strain hardening exponent, Q_r is the saturation value of dynamic recovery. Introducing the temperature dependence from moderate to high temperature, one could suggest introducing additional Arrhenius-type terms:

$$\begin{cases} \sigma_Y = \sigma_{Y,ref} \exp\left(\frac{Q_g}{R_g T} - \frac{Q_g}{R_g T_{ref}}\right) \dots (a) \\ H = H_{ref} \exp\left(\frac{Q_g}{R_g T} - \frac{Q_g}{R_g T_{ref}}\right) \dots (b) \\ Q_r = Q_{r,ref} \exp\left(\frac{Q_c}{R_g T} - \frac{Q_c}{R_g T_{ref}}\right) \dots (c) \end{cases} \quad (3-47)$$

where Q_g and Q_c are activation energies characteristic of dislocation glide and climb phenomena (index g and c , respectively), σ_{Y0} , H_0 and Q_{r0} are the reference value of σ_Y , H , and Q_r at the reference temperature T_0 , respectively. Altogether, the expression of the generalized stress, as a function of plastic strain, strain rate and temperature, becomes:

$$\begin{aligned} \bar{\sigma} = & \underbrace{\sigma_{Y,ref} \exp\left(\frac{Q_g}{R_g T} - \frac{Q_g}{R_g T_{ref}}\right)}_{\sigma_Y(T)} + \underbrace{H_{ref} \exp\left(\frac{Q_g}{R_g T} - \frac{Q_g}{R_g T_{ref}}\right) \kappa^n + Q_{r,ref} \exp\left(\frac{Q_c}{R_g T} - \frac{Q_c}{R_g T_{ref}}\right) (1 - \exp(-b\kappa))}_{R(\kappa,T)} \\ & \underbrace{+ k_{ref} \exp\left(\frac{mQ_{vp}}{R_g T} - \frac{mQ_{vp}}{R_g T_{ref}}\right) \dot{\kappa}^m}_{overstress(\kappa,T)} \end{aligned} \quad (3-48)$$

A simpler model consists in considering only two, or even one, “averaged” activation energy(ies), using then one of the two following expressions:

$$\bar{\sigma} = \left(\sigma_{Y,ref} + H_{ref} \kappa^n + Q_{r,ref} (1 - \exp(-b\bar{\kappa})) \right) \exp\left(\frac{Q_1}{R_g T} - \frac{Q_1}{R_g T_{ref}}\right) + k_{ref} \exp\left(\frac{Q_2}{R_g T} - \frac{Q_2}{R_g T_{ref}}\right) \dot{\kappa}^m \quad (3-49)$$

$$\bar{\sigma} = \left(\sigma_{Y,ref} + H_{ref} \kappa^n + Q_{r,ref} (1 - \exp(-b\kappa)) \right) + k_{ref} \dot{\kappa}^m \exp\left(\frac{\bar{Q}}{R_g T} - \frac{\bar{Q}}{R_g T_{ref}}\right) \quad (3-50)$$

Finally, the model is governed by the following equations, in Voigt notation:

$$\begin{cases} \dot{\boldsymbol{\xi}} &= \boldsymbol{\xi}^{el} + \boldsymbol{\xi}^{vp} + \boldsymbol{\xi}^{th} & \dots & (a) \\ \boldsymbol{\xi}^{el} &= \mathbf{C}^{el}(T) \tilde{\boldsymbol{\sigma}} & \dots & (b) \\ \dot{\boldsymbol{\xi}}^{vp} &= \frac{1}{\bar{\sigma}} \left(\frac{\bar{\boldsymbol{\sigma}}(\boldsymbol{\sigma} - \mathbf{X}) - (\sigma_Y(T) + R(\kappa, T))}{k(T)} \right)^{\frac{1}{m}} \mathbf{P} \tilde{\boldsymbol{\xi}} & \dots & (c) \\ \dot{\boldsymbol{\xi}}^{th} &= \alpha_T \dot{T} \mathbf{I}_V & \dots & (d) \end{cases} \quad (3-51)$$

with $\mathbf{C}^{el}(T)$ in Eq. 3-51(b) the matrix of elastic compliance depending on temperature, and \mathbf{I}_V in Eq. 3-51 (d) the vector form of the unity tensor:

$$\mathbf{C}^{el} = \frac{1}{E} \begin{bmatrix} 1 & -\nu & -\nu & 0 & 0 & 0 \\ -\nu & 1 & -\nu & 0 & 0 & 0 \\ -\nu & -\nu & 1 & 0 & 0 & 0 \\ 0 & 0 & 0 & 2(1+\nu) & 0 & 0 \\ 0 & 0 & 0 & 0 & 2(1+\nu) & 0 \\ 0 & 0 & 0 & 0 & 0 & 2(1+\nu) \end{bmatrix}, \quad \mathbf{I}_V = \begin{bmatrix} 1 \\ 1 \\ 1 \\ 0 \\ 0 \\ 0 \end{bmatrix} \quad (3-52)$$

The relation of Eq. 3-51 (d) can be obtained from Eqs.3-5 and 3-6.

3.3.4 Effect of Static Recovery

Static recovery may affect the dislocation density at high temperature, in addition to the viscoplastic deformation. A decrease of this density may occur when dislocations annihilate each other by different phenomena, among which dislocations climb. This decrease affects in turn the plastic yield stress, according to Eq. 3-45.

In the literature [90,91,92], different models have been proposed for static recovery. Most of them use the following general equation:

$$\frac{d\rho_d}{dt} = -k_d(\rho_d - \beta)^o \quad (3-53)$$

where β and o are constant coefficients characteristic of the considered material, while coefficient k_d depends on temperature. A combination of a threshold temperature and an Arrhenius activation law can be proposed:

$$k_d = \begin{cases} k_{d|T_{minSR}} \exp\left(\frac{Q_c}{R_g T_{minSR}} - \frac{Q_c}{RT}\right) & \text{if } T \geq T_{minSR} \\ 0 & \text{if } T < T_{minSR} \end{cases} \quad (3-54)$$

where T_{minSR} is the minimum temperature to active the static recovery. Eqs. 3-53 and 3-54 are intended for stress threshold. For the simplification of numerical implementation, the assumption that static recovery affects σ_Y (rather than $\sigma_s = \sigma_Y + R$) is taken. Referring to Eq 3-45, we write $\sigma_Y = A\sqrt{\rho_d}$, which allows expressing a time differential equation for σ_Y :

$$\frac{d\sigma_Y}{dt} = A \frac{d}{dt}(\sqrt{\rho_d}) \quad (3-55)$$

Using Eq. 3-53, we get:

$$\frac{d\sigma_Y}{dt} = -\frac{k_d A^2}{2\sigma_Y} \left(\frac{\sigma_Y^2}{A^2} - \beta\right)^o \quad (3-56)$$

Taking for instance the simplest model $\frac{d\rho_d}{dt} = -K\rho_d$ that is 3-53 with $k_d = K$, $\beta = 0$, and $o = 1$, we obtain:

$$\frac{d\sigma_Y}{dt} = -\frac{K}{2} \sigma_Y(T) \quad (3-57)$$

which is an exponential decay of σ_Y with time, depending on temperature.

Hence, the proposed solution strategy for TEVP is the following:

- Updating of σ_Y with temperature.
- Updating of σ_Y with time (static recovery, Eq. 3-56 based on Eqs. 3-54 and 3-55).
- Resolution of Eqs. 3-51 for κ .

3.4 Incremental Resolution in the Context of a Velocity-Pressure Formulation

3.4.1 Decomposition in Deviatoric and Spherical Parts

3.4.1.1 Deviatoric part

The deviatoric part can be expressed as follows:

$$\begin{cases} \dot{\boldsymbol{\epsilon}} &= \dot{\boldsymbol{\epsilon}}^{el} + \dot{\boldsymbol{\epsilon}}^{vp} & \dots & (a) \\ \dot{\boldsymbol{\epsilon}}^{el} &= \mathbf{C}^{el} \dot{\boldsymbol{\xi}} & \dots & (b) \\ \dot{\boldsymbol{\epsilon}}^{vp} &= \frac{1}{\bar{\sigma}} \left(\frac{\bar{\sigma} - (\sigma_Y + R(\kappa))}{k} \right)^{\frac{1}{m}} \mathbf{P} \tilde{\boldsymbol{\xi}} & \dots & (c) \end{cases} \quad (3-58)$$

where $\dot{\boldsymbol{\epsilon}} = \mathbf{M} \dot{\boldsymbol{\xi}}$ is the deviatoric part of the strain rate tensor in Voigt notation. Note that in the second equation, $\dot{\boldsymbol{\epsilon}}^{el} = \mathbf{M} \dot{\boldsymbol{\xi}}^{el} = \mathbf{M} \mathbf{C}^{el} \dot{\boldsymbol{\sigma}} = \mathbf{C}^{el} \mathbf{M} \dot{\boldsymbol{\sigma}} = \mathbf{C}^{el} \dot{\boldsymbol{\xi}}$. It can be checked that for any ij tensor component we have $\dot{\epsilon}_{ij}^{el} = (1/2\mu) \dot{\sigma}_{ij}$, with μ Lamé's second parameter (also known as elastic shear modulus $\mu = E/(2(1+\nu))$). In the third equation we have $\dot{\boldsymbol{\epsilon}}^{vp} = \dot{\boldsymbol{\xi}}^{vp}$, which can also be expressed as:

$$\dot{\boldsymbol{\epsilon}}^{vp} = \frac{\kappa}{\bar{\sigma}} \mathbf{P} \tilde{\boldsymbol{\xi}} \quad (3-59)$$

3.4.1.2 Spherical part

The spherical part can be expressed using the elastic compression module $\chi = E/(3(1-2\nu))$, and the hydrostatic pressure $p = -(\text{tr} \boldsymbol{\sigma})/3$. Using Voigt notation, the trace operator is defined by:

$$\text{tr} \boldsymbol{\epsilon} = \mathbf{I}_V \cdot \dot{\boldsymbol{\epsilon}} = \mathbf{I}_V^T \dot{\boldsymbol{\epsilon}} \quad (3-60)$$

Hence, we have:

$$\begin{cases} \mathbf{I}_V^T \dot{\boldsymbol{\epsilon}} &= \mathbf{I}_V^T \dot{\boldsymbol{\epsilon}}^{el} + \mathbf{I}_V^T \dot{\boldsymbol{\epsilon}}^{th} & \dots & (a) \\ \mathbf{I}_V^T \dot{\boldsymbol{\epsilon}}^{el} &= \frac{1-2\nu}{E} \mathbf{I}_V^T \dot{\boldsymbol{\sigma}} = -\frac{1}{\chi} \dot{p} & \dots & (b) \\ \mathbf{I}_V^T \dot{\boldsymbol{\epsilon}}^{th} &= 3\alpha_T \dot{T} & \dots & (c) \end{cases} \quad (3-61)$$

3.4.2 Time Discretization

Regarding time discretization, it is assumed that the variation of the elastic parameters over the time increment can be neglected. The coefficients E and ν can be either calculated as $E^{t+\Delta t} = E(T^{t+\Delta t})$ or as $E^t = E(T^t)$. Having solved the heat transfer problem before the mechanical problem on the time increment, values of E and ν are taken at time $t + \Delta t$. A similar approximation is done for matrix \mathbf{P} containing the anisotropy coefficients.

For the spherical part, the following scheme is used on the time increment:

$$\nabla \cdot \mathbf{v} = \mathbf{I}_V^T \dot{\boldsymbol{\xi}} = -\frac{1}{\chi} \frac{p^{t+\Delta t} - p^t}{\Delta t} + 3\alpha_T \frac{T^{t+\Delta t} - T^t}{\Delta t} \quad (3-62)$$

In the velocity-pressure formulation, the expression involved in the weak form is thus:

$$\nabla \cdot \mathbf{v} + \frac{1}{\chi} \frac{p^{t+\Delta t} - p^t}{\Delta t} - 3\alpha_T \frac{T^{t+\Delta t} - T^t}{\Delta t} = 0 \quad (3-63)$$

For the deviatoric part, we have, still in Voigt notation:

$$\dot{\boldsymbol{s}} = (\mathbf{C}^{el})^{-1} \left(\dot{\boldsymbol{\epsilon}} - \frac{\kappa}{\sigma} \mathbf{P} \tilde{\boldsymbol{\xi}} \right) \quad (3-64)$$

The equation is then time discretized by:

$$\frac{1}{\Delta t} (\boldsymbol{s}^{t+\Delta t} - \boldsymbol{s}^t) = (\mathbf{C}^{el})^{-1} \left(\dot{\boldsymbol{\epsilon}} - \frac{\kappa}{\sigma^{t+\Delta t}} \mathbf{P} \tilde{\boldsymbol{\xi}}^{t+\Delta t} \right) \quad (3-65)$$

The inverse of the elastic compliance tensor is defined by:

$$\mathbf{D}^{el} = (\mathbf{C}^{el})^{-1} = \begin{bmatrix} 2\mu + \lambda_L & \lambda_L & \lambda_L & 0 & 0 & 0 \\ \lambda_L & 2\mu + \lambda_L & \lambda_L & 0 & 0 & 0 \\ \lambda_L & \lambda_L & 2\mu + \lambda_L & 0 & 0 & 0 \\ 0 & 0 & 0 & \mu & 0 & 0 \\ 0 & 0 & 0 & 0 & \mu & 0 \\ 0 & 0 & 0 & 0 & 0 & \mu \end{bmatrix} \quad (3-66)$$

with λ_L the Lamé's first parameter: $\lambda_L = E\nu/((1+\nu)(1-2\nu))$. Note that when this elasticity tensor \mathbf{D}^{el} is applied to a deviatoric tensor, the λ_L components are neutralized. In other words, we have $\mathbf{D}^{el} \dot{\boldsymbol{\epsilon}} = \mathbf{M}_\mu \dot{\boldsymbol{\epsilon}}$ with:

$$\mathbf{M}_\mu = \begin{bmatrix} 2\mu & 0 & 0 & 0 & 0 & 0 \\ 0 & 2\mu & 0 & 0 & 0 & 0 \\ 0 & 0 & 2\mu & 0 & 0 & 0 \\ 0 & 0 & 0 & \mu & 0 & 0 \\ 0 & 0 & 0 & 0 & \mu & 0 \\ 0 & 0 & 0 & 0 & 0 & \mu \end{bmatrix} \quad (3-67)$$

This allows writing:

$$\frac{1}{\Delta t} (\tilde{\mathfrak{s}}^{t+\Delta t} - \tilde{\mathfrak{s}}^t) = \mathbf{M}_\mu \left(\dot{\tilde{\mathfrak{e}}} - \frac{\dot{\kappa}}{\bar{\sigma}^{t+\Delta t}} \mathbf{P} \tilde{\xi}^{t+\Delta t} \right) \quad (3-68)$$

or:

$$\tilde{\mathfrak{s}}^{t+\Delta t} = \Delta t \mathbf{M}_\mu \left(\dot{\tilde{\mathfrak{e}}} - \frac{\dot{\kappa}}{\bar{\sigma}^{t+\Delta t}} \mathbf{P} \tilde{\xi}^{t+\Delta t} \right) + \tilde{\mathfrak{s}}^t \quad (3-69)$$

in which $\tilde{\mathfrak{s}}^t + \Delta t \mathbf{M}_\mu \dot{\tilde{\mathfrak{e}}}$ can be deemed as an elastic predictor ($\tilde{\mathfrak{s}}^{elP,t+\Delta t}$) of the deviatoric stress tensor at time $t + \Delta t$:

$$\tilde{\mathfrak{s}}^{t+\Delta t} = \underbrace{\tilde{\mathfrak{s}}^t + \Delta t \mathbf{M}_\mu \dot{\tilde{\mathfrak{e}}}}_{\tilde{\mathfrak{s}}^{elP,t+\Delta t}} - \frac{\Delta t \dot{\kappa}}{\bar{\sigma}^{t+\Delta t}} \mathbf{M}_\mu \mathbf{P} \tilde{\xi}^{t+\Delta t} \quad (3-70)$$

Regarding now the time discretization of the back stress evolution law, Eq. 3-22, we define the following matrix \mathbf{C}_χ :

$$\mathbf{C}_\chi = \frac{1}{3} \begin{bmatrix} 2C & 0 & 0 & 0 & 0 & 0 \\ 0 & 2C & 0 & 0 & 0 & 0 \\ 0 & 0 & 2C & 0 & 0 & 0 \\ 0 & 0 & 0 & C & 0 & 0 \\ 0 & 0 & 0 & 0 & C & 0 \\ 0 & 0 & 0 & 0 & 0 & C \end{bmatrix} \quad (3-71)$$

Eq. 3-22 in Voigt notation is time-discretized as:

$$\frac{1}{\Delta t} (\tilde{\mathbf{X}}^{t+\Delta t} - \tilde{\mathbf{X}}^t) = \mathbf{C}_\chi \dot{\tilde{\mathbf{e}}}^{vp} - \gamma \dot{\kappa} \tilde{\mathbf{X}}^{t+\Delta t} \quad (3-72)$$

so that,

$$\tilde{\mathbf{X}}^{t+\Delta t} = \frac{1}{1+\Delta t\gamma\dot{\kappa}} \left(\tilde{\mathbf{X}}^t + \Delta t \mathbf{C}_\chi \dot{\boldsymbol{\epsilon}}^{vp} \right) \quad (3-73)$$

Injecting Eq. 3-59 into 3-73, we get:

$$\tilde{\mathbf{X}}^{t+\Delta t} = \frac{1}{1+\Delta t\gamma\dot{\kappa}} \left(\tilde{\mathbf{X}}^t + \Delta t \mathbf{C}_\chi \frac{\dot{\kappa}}{\bar{\sigma}} \mathbf{P} \tilde{\boldsymbol{\xi}}^{t+\Delta t} \right) \quad (3-74)$$

Injecting Eq. 3-70 and Eq. 3-74 into the right hand side of $\tilde{\boldsymbol{\xi}}^{t+\Delta t} = \tilde{\mathbf{s}}^{t+\Delta t} - \tilde{\mathbf{X}}^{t+\Delta t}$, we get:

$$\tilde{\boldsymbol{\xi}}^{t+\Delta t} = \mathbf{Z}^{-1} \left(\underbrace{\tilde{\mathbf{s}}^t + \Delta t \mathbf{M}_\mu \dot{\boldsymbol{\epsilon}}}_{\tilde{\mathbf{s}}^{elP,t+\Delta t}} - \frac{\tilde{\mathbf{X}}^t}{1+\Delta t\gamma\dot{\kappa}} \right) \quad (3-75)$$

where

$$\mathbf{Z} = \mathbf{I} + \frac{\Delta t \dot{\kappa}}{\bar{\sigma}^{t+\Delta t}} \left(\mathbf{M}_\mu + \frac{\mathbf{C}_\chi}{1+\Delta t\gamma\dot{\kappa}} \right) \mathbf{P} \quad (3-76)$$

The final scalar equation to be solved is expressed as:

$$Y(\dot{\kappa}^{t+\Delta t}) \equiv \underbrace{\bar{\sigma}(\tilde{\boldsymbol{\xi}}^{t+\Delta t})}_{part\ 1} - \underbrace{\bar{\sigma}(\sigma_{Y^{t+\Delta t}}, R(\dot{\kappa}^{t+\Delta t}), \dot{\kappa}^{t+\Delta t})}_{part\ 2} = 0 \quad (3-77)$$

The first part is the definition of equivalent stress of Eq. 3-27 with $\tilde{\boldsymbol{\xi}}^{t+\Delta t}$ expressed by Eq 3-75, and the second part is expressed by the rheological law such as Eq. 3-49. Solving this $Y(\dot{\kappa}^{t+\Delta t}) = 0$ equation to get the value of scalar $\dot{\kappa}$ realized by Newton method is not detailed here. Once the value of $\dot{\kappa}$ is obtained, $\tilde{\boldsymbol{\xi}}^{t+\Delta t}$, $\tilde{\mathbf{X}}^{t+\Delta t}$, $\tilde{\mathbf{s}}^{t+\Delta t}$ and $\dot{\boldsymbol{\epsilon}}^{vp,t+\Delta t}$ by Eqs. 3-75, 3-74, 3-69 and 3-59, respectively.

3.5 Steps of Building a Direct Simulation

The way to build a local simulation corresponding to an experimental Dedimet test is shown in Fig. 3-1. The field of view relation in Fig. 3-1 (a) is always kept for each Dedimet test, i.e., the DIC field of view is contained in the wider field of view of the IR camera. After the Dedimet test has been performed, a zone of interest (ZOI) is selected at the central part of the tested sample, and that is based on the DIC result. Then a mesh is created based on the size of this ZOI, as shown in Fig. 3-1 (b). The mechanical boundary conditions to be applied to the ZOI are extracted from the experimental displacement field (by DIC) and imposed to the corresponding boundaries. The measured temperature field is directly imposed to the mesh in simulation.

The steps mentioned above are detailed in the following.

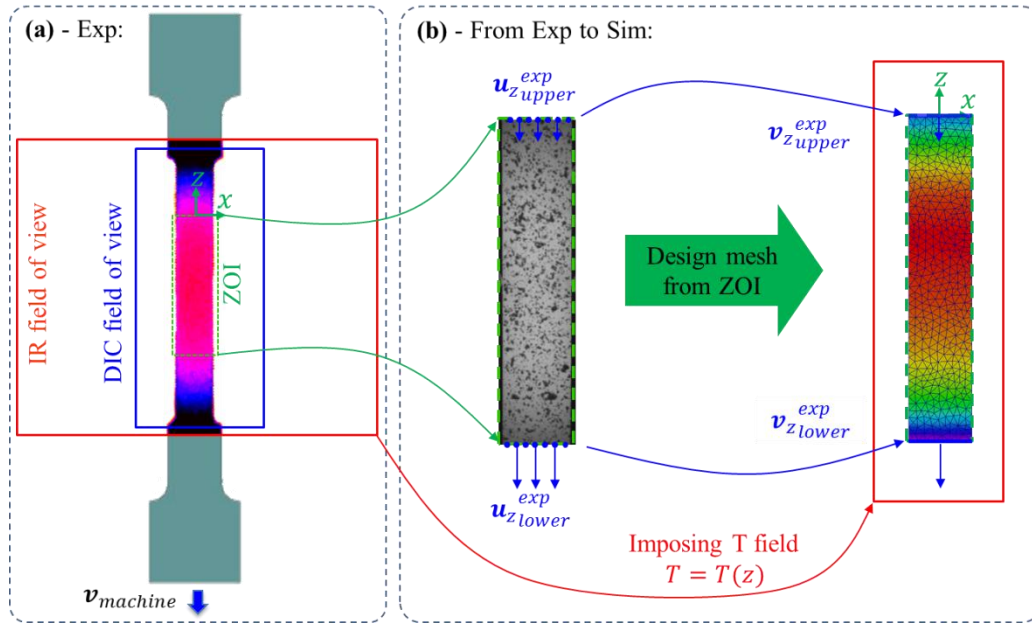


Fig. 3-1 flow chart of local strategy to build numerical simulation from an experiment (the ZOI with speckle is a little wider than the mesh because of the DIC camera projection)

3.5.1 Select a ZOI

Selection of a ZOI is based on both temperature field and displacement field, and it is shown in Fig. 3-2. In Fig. 3-2 (a) the temperature profile (averaged value within the two vertical lines) along the tensile direction is shown (for more detail of the temperature profile, see Section 3.6.3.1). One can see that only at the central portion the valid temperature profile is measured due to the measuring range of IR camera, and this portion is defined by the upper and lower T limits and considered as the usable field. Then, based on the self-emitting method for the displacement field, only the speckle at the central portion of the sample can be recorded, thus a limit for displacement field is constrained by the upper and lower DIC limits, as shown in Fig. 3-2 (b). Obviously, the intersection of the two limits is considered as the ZOI domain, only in which a ZOI can be selected.

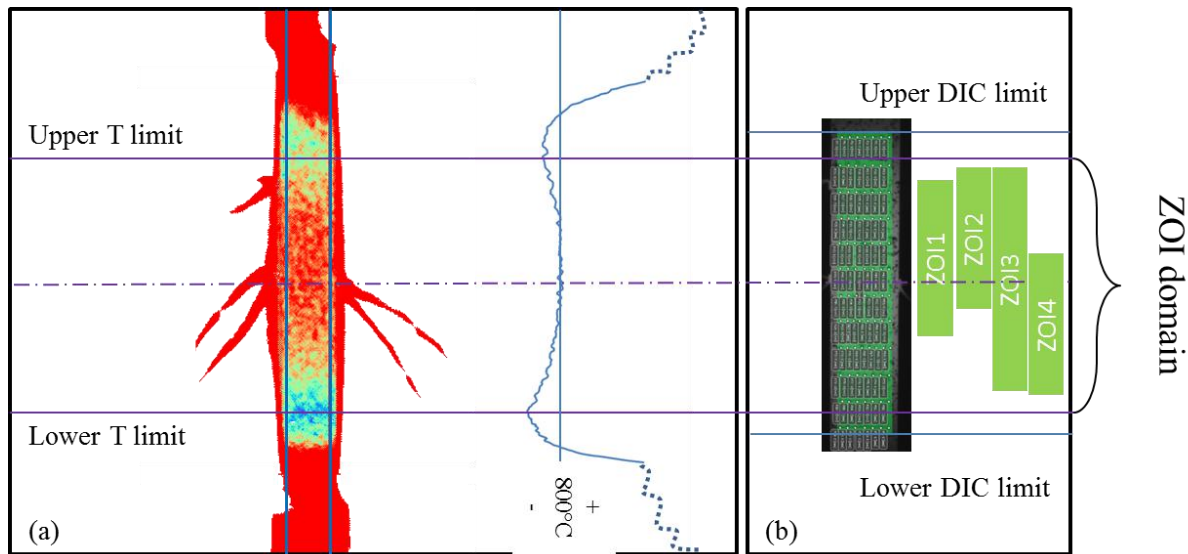


Fig. 3-2 Way to select a ZOI of the case of 800°C level (a): T field by IR camera and extracted T profile along vertical (testing) direction, (b): the ZOI domain defined by the intersection of T limit and DIC limit

There are various choices to select a ZOI, as shown in Fig. 3-2 (b), but only one way is “the best”, which is corresponding to the “ZOI3” case. In this case, the length of ZOI covers a great part of the ZOI domain, and that will make the ends of the ZOI have relative lower temperature than the center of ZOI. As the ZOI will deform during the tensile test, the lower boundary of ZOI goes downwards too. Thus, the lower boundary of ZOI should have an offset from lower boundary of ZOI domain. Generally, this offset is close to the total elongation of the whole sample.

One thing interesting is that in this 800°C case the usable T field is smaller than that of displacement field, but this is not always true at other temperature levels. As a consequence of increasing range of usable T field as well as the evaluating range of usable DIC field when T increases, the length of ZOI domain also increases, which makes it possible to define a ZOI of longer length. This phenomenon is shown later in Fig. 4-2 in next chapter.

3.5.2 Create a Mesh

A mesh is then created based on the selected ZOI. It contains two steps, which are calculating the mesh configuration, and optimizing the mesh.

3.5.2.1 Create a Mesh Configuration

The mesh is set up based on the middle part (or working zone) of the tested samples and the mesh geometry size is different for each of the experimental test. The mesh geometry is selected in the following way:

Firstly, measure the geometry (the thickness e_0 and width w_0 , respectively) of the samples before experimental test at room temperature (T_0). For different samples the geometries are different because of the manufacturing bias.

Secondly, select the ZOI in the DIC result which is taken at high temperature, and measure the length along the tensile direction at the reference moment, i.e. the moment when the first loading velocity starts to be imposed on Dedimet machine. Thus, the start length (l_s) imbeds the thermal dilation at tested temperature.

Thirdly, calculate the thickness and width at tested temperature at the start moment, via:

$$\begin{cases} w_s = w_0 + w_0 \cdot (T_s - T_0) \cdot \alpha_T \\ e_s = e_0 + e_0 \cdot (T_s - T_0) \cdot \alpha_T \end{cases} \quad (3-78)$$

where α_T is the thermal expansion coefficient (TEC). Noticing that along the length direction of the mesh there is a temperature profile of parabola shape, and the maximum to the minimum value could be $\sim 60\text{K}$ when the controlled temperature at the central position is 1273K , for example. During the creation of the mesh this temperature difference is not considered, and only the nominal central temperature is used for calculating the thermal expansion for all the positions of the selected zone. The ‘reasonable’ TEC used in this project is the averaged value from different sources as shown in Fig. 3-3 [93~97].

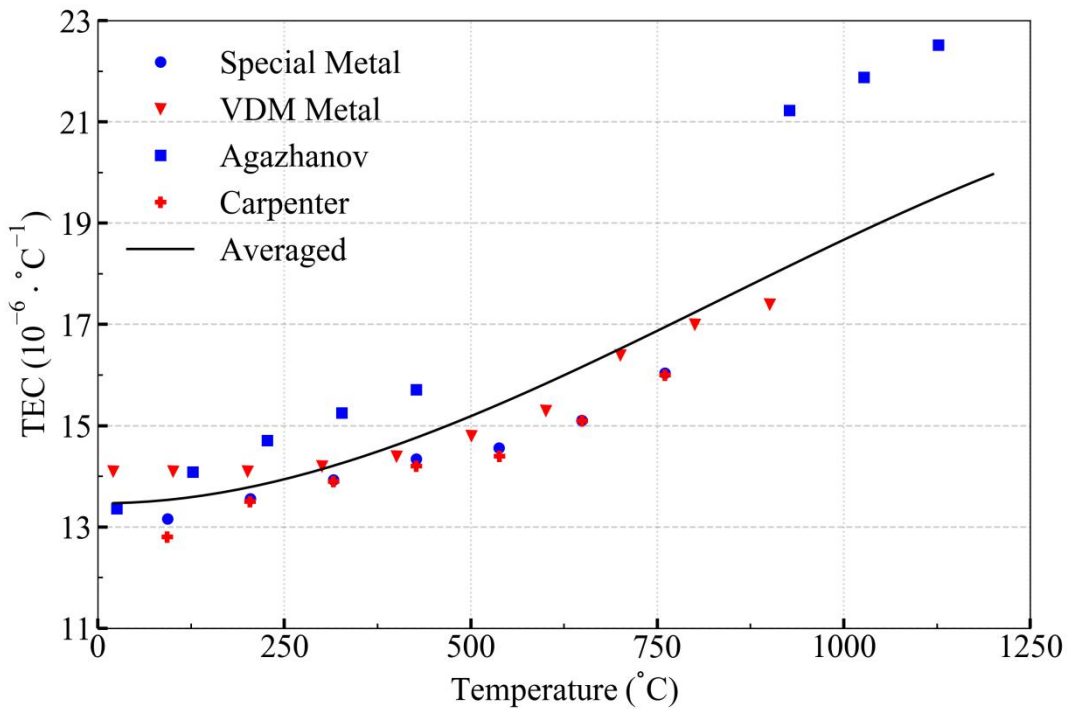


Fig. 3-3 Thermal expansion coefficient (TEC, α_T) from different sources, where Special Metal [94], VDM Metal [93], Agazhanov [96] and Carpenter [95].

Finally, based on the l_s , e_s and w_s , a cuboid is created which follows the coordinate system as shown in Fig. 3-4 (a). The upper middle position is the mesh origin, the width direction is x , and the thickness direction is y . All the y coordinates are equal or greater than 0, and all the z coordinates are equal or smaller than 0.

3.5.2.2 Optimize the Mesh Size

The ZOI parallelepipedic domain of dimensions l_s , w_s , and e_s is meshed with finite elements in order to solve the mechanical problem for times greater than t_s . A non-structured mesh made of linear tetrahedral elements is automatically generated by means of procedures included in the home developed library CimLib [98]. In section 3.5.2.1 only the overall geometry of the mesh is considered. In view of further optimization, it is important to define the mesh in order to get a good compromise between accuracy and computational cost. The question then is how to minimize the number of nodes while preserving a good accuracy. From sensitivity tests, it was concluded that a good solution consists in having three layers of elements in the 2 mm thickness of the specimen (that is a mesh size of about 0.7 mm in each direction), as shown in Fig. 3-4 when information of deformation and load is considered. For domains with typical dimensions $2 \times 8 \times 33$ mm, the number of nodes is about 4200 (ZOI mesh in Fig. 3-4 (a) 3 iso). When comes to calculation time consumption, 5 cores of CPU were used for the 4 types of mesh, and the parallel calculation time is (3 iso) 1217s, (2 iso) 376s, (1 iso) 56s, and (1 ani) 31s. From Fig. 3-4 (b) it can be inferred to use 1 ani type mesh to conduct the simulation when only force is considered.

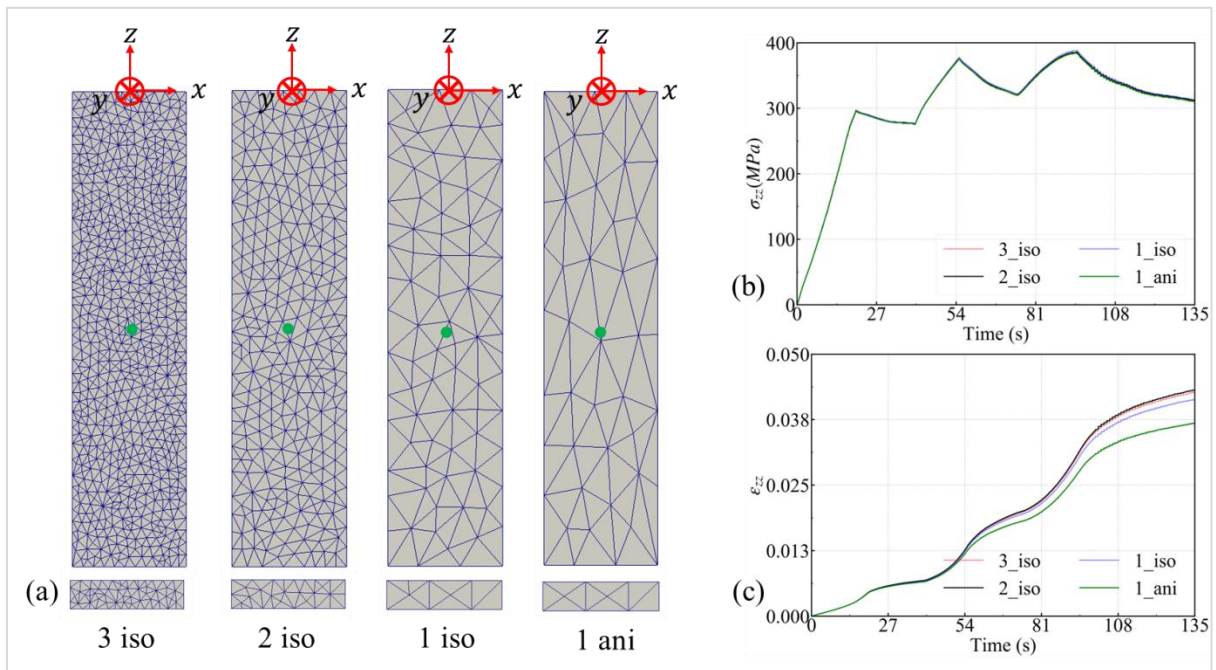


Fig. 3-4 Optimization of mesh size. (a) along thickness direction 3, 2, 1 layers of isotropic elements, 1 layer of anisotropic elements, with a Lagrange sensor of green rounds attached at $z = -15$ mm, (b): σ_{zz} from sensor for all 4 types of mesh, and (c): ϵ_{zz} from sensor for all 4 types of mesh

3.5.3 Temporally Simulation Sequence

After initiation, the temporally simulation sequence (an incremental type algorithm) starts.

3.5.3.1 Incremental Time Step

The simulation instants for calculating the time step for the incremental type algorithm are extracted from the DIC results. The moment at which the first imposing of velocity in the experimental test is set as 0 in the time series of simulation.

As is stated before, the DIC records have a frequency of about 10Hz, which gives the temporal increment of about 100ms. Because of the writing delay of the results of DIC software or some other reasons, the real sampling time interval is not strictly 100ms, and it is in fact some values such as 98ms, 101.5ms... The sampling interval is anyway quite close to each other and it is also short enough for the incremental solver in this project. Thus, the DIC record instants are directly used in the simulation, and no interpolation is used.

3.5.3.2 Updating $T(z)$ and Corresponding Parameters

The $T(z)$ profile is firstly updated by imposing data from experiment. And then material parameters (material density, thermal conductivity, and thermal expansion coefficient) are automatically calculated as functions of the local nodal temperature. This updating can be chosen off when needed, for example, during the optimization the T updating is selected off, first because the temperature variations are fairly low during a test, and second because of the risk of generating instabilities in the simulation, due to possible inaccuracies in IR field imaging. A typical temperature variation is given in Appendix A. 5.

3.5.3.3 Mechanical Resolution and Boundary Conditions

Eq. 3-51 coupled with material constitutive law is solved by finite element method, particularly with a P1+/P1 formulation [99], in which the instability with simple P1 formulation for both velocity and pressure can be overcome with additional degree of freedom introduced by bubble function in velocity field. This is implemented in Cimlib. As the stress-strain relation is nonlinear, the search for the equilibrium state of the whole system uses the Newton-Raphson iteration. The stress-strain relation is determined by one of the constitutive laws detailed in the previous section when calculating the contribution of each element into the residual vector and the stiffness matrix at each iteration. As mentioned at the end of Section 3.4, in the case of TEVP constitutive law, this needs a local resolution of a nonlinear scalar equation with Newton-Raphson iteration to find the unknown $\dot{\kappa}$.

The Dirichlet boundary condition is applied in the mechanical solver based on the experimental data, i.e. $\mathbf{v} = \mathbf{v}_{exp}$ on Γ_{ZOI} , where Γ_{ZOI} are the upper and lower faces of the ZOI selected in each

test. More details of boundary conditions are given in section 3.6.2. For surfaces other than Γ_{ZOI} , free.

3.5.4 Outputs from Calculation

Two kinds of information are output.

The first type covers the fields of the interesting quantities for checking, such as the equivalent stress, the equivalent strain, the stress tensor, the displacement, the velocity, the strain tensor, Lankford coefficient...

The second type is the sensors of Lagrange type attached at different positions of the mesh (which are corresponding to those sensors in DIC results). Those sensors record the strain components of ε_{xx} and ε_{zz} during the simulation as a function of time.

The global force along the loading direction (F_z) as a function of time is also calculated by expression $F_z = \sum_i^N S_i \cdot \sigma_{i,zz}$, where S_i is the area of the i^{th} elemental section which is cut by a plane perpendicular to z direction, $\sigma_{i,zz}$ is the zz stress component of the i^{th} element, and N is the total elements that are cut by the plane. The value of F_z is also embedded in the Lagrange sensors of the second type of output. It is the information from sensors that are used for optimization in the next chapter.

3.6 Imposing Experimental Data to Simulation

In this section the detailed method to transfer the experimental data to simulation is introduced, including the reference frame (RF) transformation, and preparation of data for simulation.

3.6.1 Reference Frame Transformation

The IR camera and the DIC cameras have different RFs. And for the simulation it has another reference frame. Thus, it is quite necessary to link the three reference frames, in other words, to transform the experimental data from experimental reference frames to simulation reference frame. When the reference frame transformation is done, the temperature projection and the velocity boundary condition can be easily achieved. It is necessary to mention that the IR camera and the DIC cameras are fixed in space in one test, but from test to test they could be adjusted or moved. Thus, the transformation between reference frames should be defined for each test.

3.6.1.1 Set up RF^{sim} from RF^{DIC}

The relation between field of view of DIC cameras and ZOI is again referred in

Fig. 3-1 (a), after calibration, the DIC reference frame (RF^{DIC}) is created automatically by the software VIC-3D. RF^{DIC} has its length unit is millimeter. The coordinate data of displacement field expressed in RF^{DIC} can be reached at any sampling instant from DIC results, which contains time, displacement field and Hencky strain tensor.

Fig. 3-5 presents how a simulation reference frame (RF^{sim}) is created by the results in RF^{DIC} . Fig. 3-5 (a) shows the field of view relation of DIC and the ZOI. It can be seen in Fig. 3-5 (b) that only a portion of the DIC result is used, i.e., the ZOI. The upper middle of ZOI is selected as the origin for RF^{sim} . For each test, the ZOI is unique, so the origin of RF^{sim} for each experiment is individually selected, which is set at the reference instant (the instant to impose the first loading) of DIC results. The simulation reference frame is then selected uniquely as that of the experimental one as shown in Fig. 3-5 (c). Thus, it can be said that the experiment and the simulation have unique reference frame (i.e. $RF^{exp} \equiv RF^{sim}$). In the following only RF^{sim} will be used.

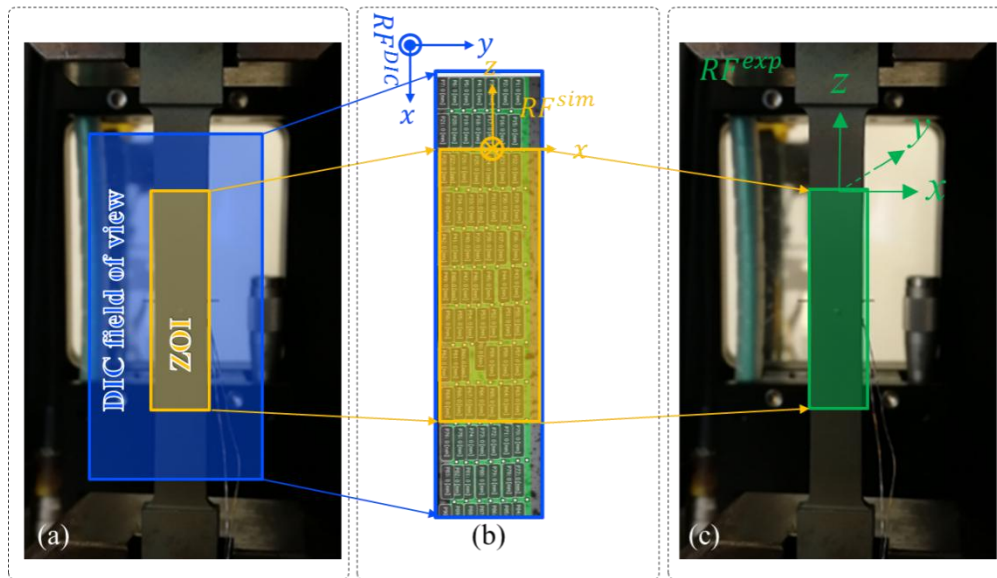


Fig. 3-5 (a): Selected ZOI contained in field of view of DIC, (b) Origin of RF^{sim} set at upper middle of ZOI, and (c) RF^{exp} as a copy of RF^{sim}

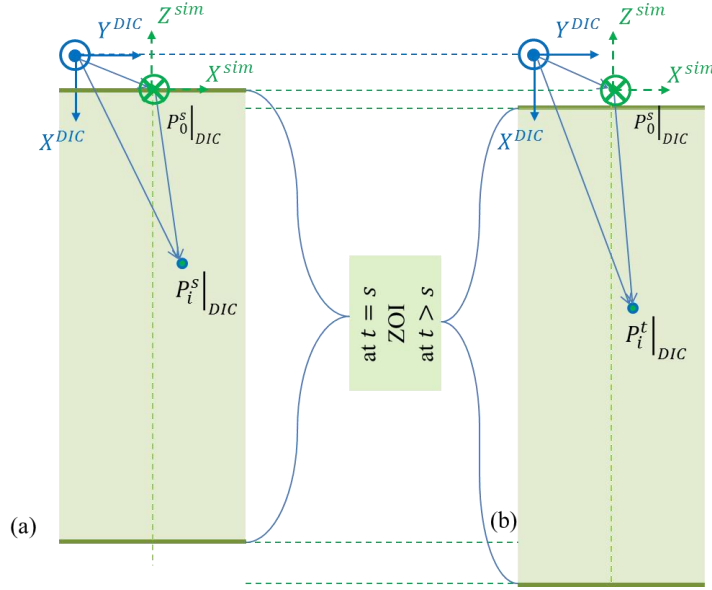


Fig. 3-6 RF^{sim} extracted from RF^{DIC} at sampling instant: (a) $t = s$, and (b) $t > s$

The DIC result at the reference instant ($t = s$ in experimental time series, which is also $t = 0$ in simulation time series) is shown in Fig. 3-6 (a). The RF with blue solid lines is the RF^{DIC} . The origin of RF^{DIC} is somewhere and it does not really concern. Among all the sampling instants the one at which the first loading starts to be imposed to machine is selected as the reference instant (at which both the deformation and displacement are set as zero), and all the following mathematical treatment is done with respect to this reference instant.

In the DIC result window a ZOI (shown in green mask in Fig. 3-6 (a)) is selected (by defining a point matrix) on the sample at the reference instant. Then in the DIC result window, a point $P_0^s|DIC$ whose coordinate vector is $\mathbf{x}_0^s|DIC$ is selected as the origin for the RF^{sim} , and this point is set as the $P_0^s|sim$ (The superscript indicates the time, and subscript indicates the point ID). In our case we allocate the $P_0^s|sim$ at the middle of the upper boundary of the ZOI, so that the RF^{sim} set up in Fig. 3-6 (a) could be the same as shown in Fig. 3-5.

Now coordinates of any material point i at any sampling instant t in RF^{DIC} ($\mathbf{x}_i^t|DIC$) can be written in RF^{sim} ($\mathbf{x}_i^t|sim$) as:

$$\mathbf{x}_i^t|sim = \mathbf{T}_1(\mathbf{x}_i^t|DIC - \mathbf{x}_0^s|DIC) \quad (3-79)$$

where

$$\mathbf{T}_1 = \begin{bmatrix} 0 & 1 & 0 \\ 0 & 0 & -1 \\ -1 & 0 & 0 \end{bmatrix} \quad (3-80)$$

The spatial relation at $t > s$ is shown in Fig. 3-6 (b). Since $\mathbf{x}_i^t|_{DIC}$ can be any point, the projection from DIC to simulation is done based on equation Eq. 3-79. Now the displacement transformation from experimental to simulation is done.

3.6.1.2 Projection of Temperature Field from RF^{IR} to RF^{sim}

The raw temperature data obtained from IR camera are stored in the form that at any sampling instant t (unit: s), the temperature of any material point P_i is a function of its coordinates (length unit: mm) in the IR camera reference frame (RF^{IR}), i.e.

$$T(P_i^t) = T(\mathbf{x}_i^t|_{IR}) \quad (3-81)$$

where P_i^t means the material point i at sampling instant t , and $\mathbf{x}_i^t|_{IR}$ stands for the coordinates of the point P_i at this instant t in RF^{IR}

The projection is based on the fact that for any material point i at sampling instant t (noted as P_i^t), its temperature value should be the same in different RFs, i.e.:

$$T(P_i^t) = T(\mathbf{x}_i^t|_{sim}) = T(\mathbf{x}_i^t|_{IR}) \quad (3-82)$$

The main idea for the temperature transformation is to find the corresponding coordinates in different RFs for the same material point. For the temperature field transformation, two hypotheses are hold:

- Deformation of the sample at the two faces is the same when small deformation happens.
- Transverse temperature gradient along thickness direction (y direction in RF^{sim} can be ignored.

In fact before conducting the following part of transformation, the length unit in RF^{sim} has been converted from pixels to millimeter (refer to Appendix A. 9), and an image rotation is also taken so that the image of IR camera looks as if it were taken from the unique side of DIC cameras, as shown in Fig. 3-7.

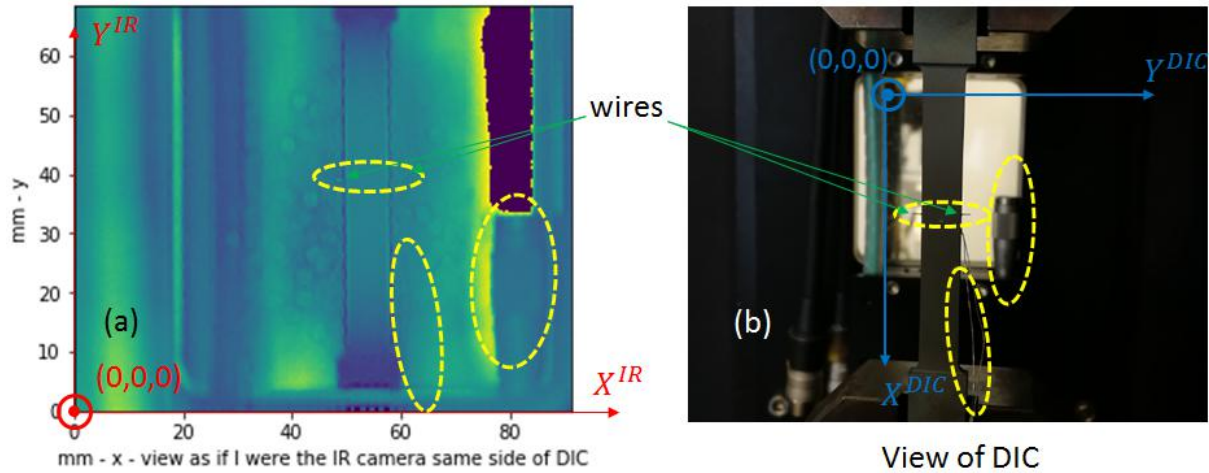


Fig. 3-7 (a) view of temperature field after rotation, (b) image taken from the side of DIC camera

In Fig. 3-7 the yellow ovals are used to indicate the orientation of the images. Two wires can be seen, and they are used for locating the reference point position, which will be used later.

Now RF^{IR} is put into Fig. 3-6 (b) to get Fig. 3-8. Though the RF^{IR} is in fact a 2D reference frame, still a 3D case is considered, whose third component will be finally attributed as zero. The three RFs, their spatial relation at sampling instant $t > s$ is shown in Fig. 3-8:

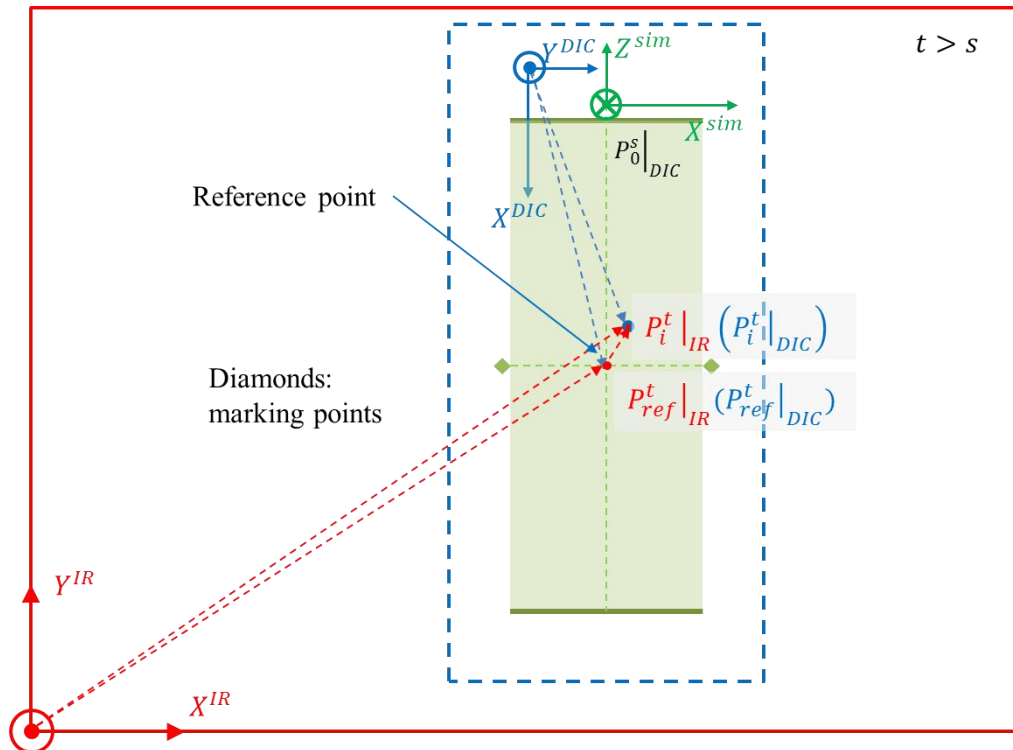


Fig. 3-8 spatial relation between RF^{DIC} , RF^{sim} and RF^{IR} at any sampling instant $t > s$

A fast fact will easily be found that for any point i at sampling instant t , i.e. P_i^t

$$\left\| \overrightarrow{P_{ref}^t|_{IR} P_i^t|_{IR}} \right\| = \left\| \overrightarrow{P_{ref}^t|_{DIC} P_i^t|_{DIC}} \right\| \quad (3-83)$$

where $P_{ref}^t|_{IR}$ is the reference point which is found by selecting the central position of the section line between the two welding points of the wires, i.e. the marking points. That induces:

$$\left(\mathbf{x}_i^t|_{IR} - \mathbf{x}_{ref}^t|_{IR} \right) = \mathbf{T}_2 \left(\mathbf{x}_i^t|_{DIC} - \mathbf{x}_{ref}^t|_{DIC} \right) \quad (3-84)$$

where

$$\mathbf{T}_2 = \begin{bmatrix} 0 & 1 & 0 \\ -1 & 0 & 0 \\ 0 & 0 & 1 \end{bmatrix} \quad (3-85)$$

Since the $P_{ref}^t|_{IR}$ is hard to be tracked in real time, a good solution is to link this moving point with DIC information based on the first hypothesis, i.e.

$$\left\| \overrightarrow{P_{ref}^s|_{IR} P_{ref}^t|_{IR}} \right\| = \left\| \overrightarrow{P_{ref}^s|_{DIC} P_{ref}^t|_{DIC}} \right\| \quad (3-86)$$

If we take the coordinates into consideration, we will have:

$$\mathbf{x}_{ref}^t|_{IR} - \mathbf{x}_{ref}^s|_{IR} = \mathbf{T}_2 \left(\mathbf{x}_{ref}^t|_{DIC} - \mathbf{x}_{ref}^s|_{DIC} \right) \quad (3-87)$$

i.e.

$$\mathbf{x}_{ref}^t|_{IR} = \mathbf{T}_2 \left(\mathbf{x}_{ref}^t|_{DIC} - \mathbf{x}_{ref}^s|_{DIC} \right) + \mathbf{x}_{ref}^s|_{IR} \quad (3-88)$$

Injecting Eq. 3-88 into Eq. 3-84, we get:

$$\mathbf{x}_i^t|_{IR} = \mathbf{T}_2 \left(\mathbf{x}_i^t|_{DIC} - \mathbf{x}_{ref}^s|_{DIC} \right) + \mathbf{x}_{ref}^s|_{IR} \quad (3-89)$$

i.e.

$$\mathbf{x}_i^t|_{DIC} = \mathbf{T}_2^{-1} \left(\mathbf{x}_i^t|_{IR} - \mathbf{x}_{ref}^s|_{IR} \right) + \mathbf{x}_{ref}^s|_{DIC} \quad (3-90)$$

Inject Eq. 3-90 into Eq. 3-79, we get:

$$\mathbf{x}_i^t|_{sim} = \mathbf{T}_3 \left(\mathbf{x}_i^t|_{IR} - \mathbf{x}_{ref}^s|_{IR} \right) + \mathbf{T}_1 \left(\mathbf{x}_{ref}^s|_{DIC} - \mathbf{x}_0^s|_{DIC} \right) \quad (3-91)$$

where

$$\mathbf{T}_3 = \mathbf{T}_1 \mathbf{T}_2^{-1} = \begin{bmatrix} 1 & 0 & 0 \\ 0 & 0 & -1 \\ 0 & 1 & 0 \end{bmatrix} \quad (3-92)$$

Therefore, for any point $P_i^t|_{IR}$, we can extract its coordinate in RF^{IR} , then we can find its corresponding coordinates in RF^{sim} by Eq. 3-91. Based on the above-mentioned relation of Eq. 3-82: the temperature value of $P_i^t|_{sim}$ is the same as that of $P_i^t|_{IR}$, or we say we project the points and their temperature values from RF^{IR} to RF^{sim} .

Now the two projections are done.

The cameras mentioned in the following 2 sections are adjusted by level tool so that their axis are simply in $\sim 90^\circ$ rotation. However, it is impossible to set them in perfect alignment. The error caused by the deviation of alignment is given in Appendix [A. 16.1.3](#).

3.6.2 Boundary Conditions

There are two kinds of boundary conditions. The first type is to impose the velocity extracted from the experiment, and in fact only one component of the velocity vector is used. The other kind of boundary condition is used to avoid the rigid movement caused by oscillation in the simulation.

3.6.2.1 Boundary Condition for Imposing Loading Information

It is necessary to refer Fig. 2-17 here. One can see that based on the method of selecting a ZOI in section 3.5.1, quite a good uniformity of the z component of velocity through a transverse section (that is more precisely, the uniformity through a rank of DIC sensors) is observed. This would introduce quite naturally the idea of averaging those (very slightly) different velocities in order to form a unique boundary condition that is applied to all nodes located in the upper face (or in the lower face) of the ZOI boundary, i.e. the faces ABFE and DCGH in Fig. 3-9. The boundary condition that we use is the velocity component along the loading direction, i.e. the v_z^t at sampling instant t . This velocity component is obtained by the following expression:

$$v_z^t = \frac{u_z^t - u_z^{t-\Delta t}}{\Delta t} \quad (3-93)$$

Although the boundary condition of velocity component can be simply extracted via Eq. 3-93, it is not a good choice to use the u_z^t from the DIC data directly, because the random error of DIC recording will generate strong oscillation of velocity values. Thus, the displacement data (u_z^t) must

be fitted before using. The way to fit the displacement data consists of a so-called “master-slave” fitting, and is detailed in Appendix A. 7.

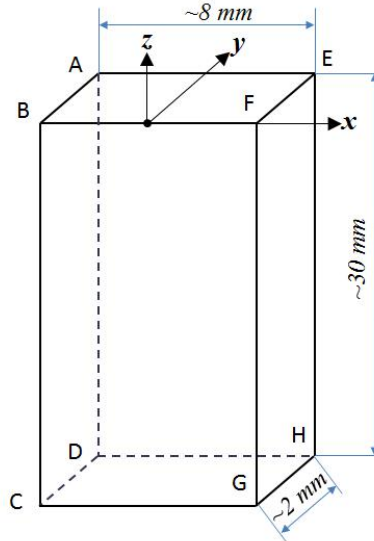


Fig. 3-9 ZOI and its coordinate system in simulation, where x width, y thickness, and z length or tensile direction

3.6.2.2 Boundary Conditions to Avoid Rigid Movement

Again as shown in Fig. 3-9, for nodes on edges AB and CD , velocity component along x direction is imposed as 0. For nodes on edges AE and DH , velocity component along y direction is imposed as 0. Thus, the rigid movement is avoided by imposing artificial constraints that do not modify the physical problem.

3.6.3 Pretreatment and Imposing of Temperature Field

Before reference frame transformation, an additional pretreatment of temperature field is carried out to smooth the data measured from IR camera. The treated data of temperature is then stored in a text format file, and used for imposing the T field in simulation.

3.6.3.1 Pretreatment of T Field before RF Transformation

Fig. 3-10(a) is taken from one experiment at nominal 1000°C for the explanation. Firstly, select the upper and lower horizontal lines to define the useful length of T field along y direction, as mentioned in section 3.53.5.1. Secondly, select the left and right vertical lines to remove the pixels at the ends whose data is abnormal because of edge effect. Thirdly, the raw averaged values (\bar{T}_{raw}), the standard deviation (ΔT) along x direction within the vertical lines are calculated for each increment of y . Fourthly, a polynomial fitting of 6 order is used to smooth \bar{T}_{raw} , and the fitted values are marked as \bar{T}_{fitted} . Finally, for each increment of y , the values of \bar{T}_{raw} , \bar{T}_{fitted} , $\bar{T}_{raw} - \Delta T$, $\bar{T}_{raw} + \Delta T$ are plotted in Fig. 3-10(b).

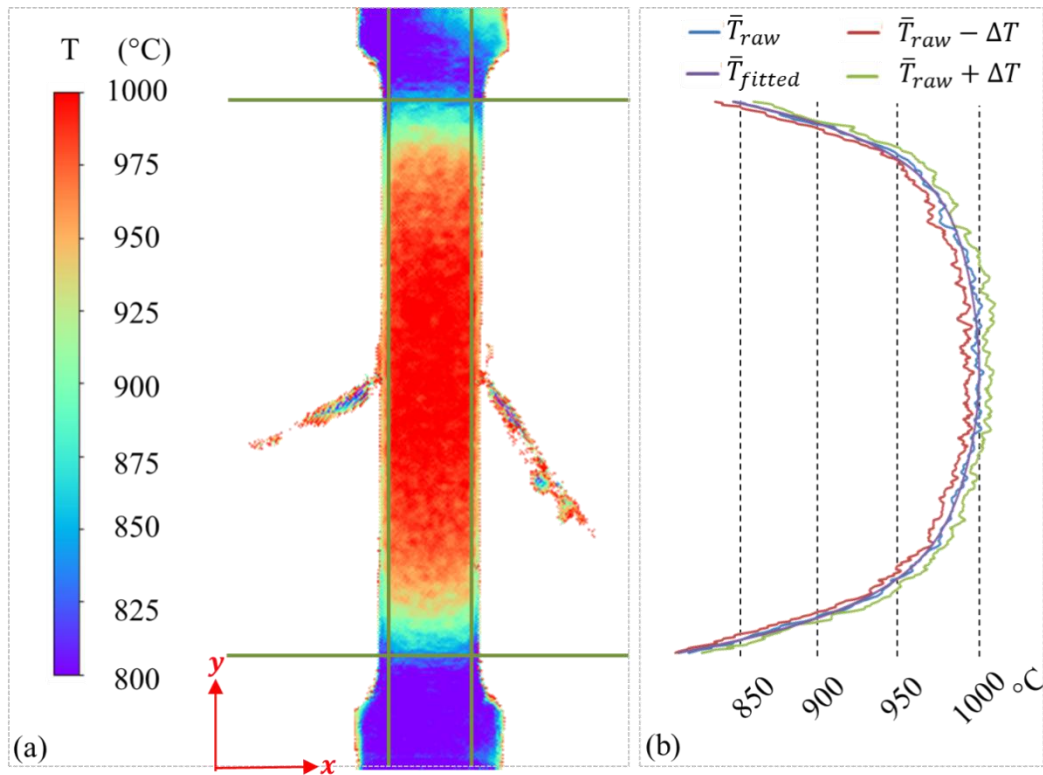


Fig. 3-10 (a) Typical temperature profile obtained by Q-pyro cam at nominal temperature 1000°C after calibration, with vertical and horizontal boundaries for data treatment, and (b) averaged temperature (with) standard deviation within vertical boundaries for all y values within horizontal boundaries

From calculation it is found that all along the x direction, the $\max(\Delta T)$ is smaller than 16°C. When looking at the variation of \bar{T} , one can see that it goes across more than 150°C, which is much bigger than the ΔT . Besides, from Appendix A. 6 one can see that the temperature variation through the thickness of the sample is also quite small compared with the variation along the loading direction. Based on those, it is reasonable to consider a \bar{T}_{fitted} profile which depends only on the vertical direction, which simplifies the simulation too.

In fact, for all tests, a fitting order of 4 ~ 6 is used for calculating the \bar{T}_{fitted} .

3.6.3.2 Temperature Field Storage and Imposing

Because the sampling frequency of the temperature field by IR camera (\sim every 3s) is much longer than the incremental time step (\sim 0.1s) identical with that of DIC, when storing the T data, a linear interpolation is used based on DIC time series: in each time step the information is arranged in the format of $(\boldsymbol{x}, T(\boldsymbol{x}))$ in a text file, where \boldsymbol{x} is the coordinate vector in the simulation reference frame. Then during T imposing, for each of the mesh nodes, if it's close enough (close enough means the distance of the mesh node and material point is smaller than a pre-set value) to one or more material points in the text file at a given sampling instant, the average temperature of the corresponding material point(s) is considered as the temperature value of the mesh node. We can

select 1 to 3 component dependence of vector \mathbf{x} to impose the T field, and for present work only the z direction, i.e. the loading direction is considered to simplify the work. Now the temperature imposing is done.

3.7 Self-Consistence of the Local Simulation Strategy

The local strategy should be ZOI independent. In other words, when different ZOIs are selected, the calculated values should be the same or quite close to each other, and that is called “self-consistence”.

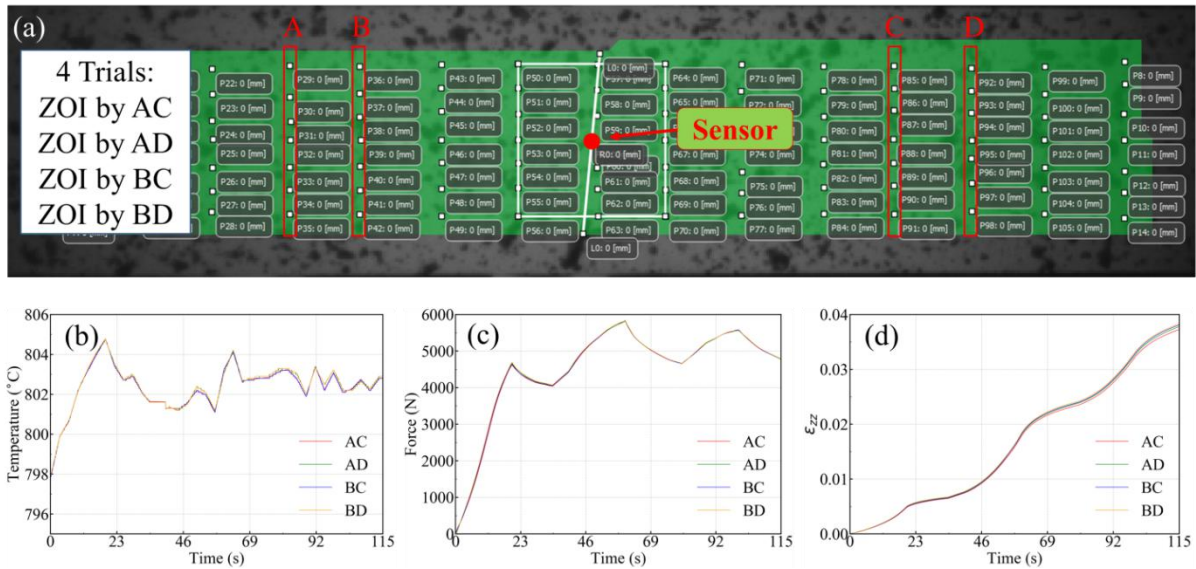


Fig. 3-11 Proof of self-consistence on the 800°C test. (a) positions of different selected pairs of sensor lines serving for the definition of boundaries; (b) calculated temperature evolution at the central sensor (red dot in figure (a)), (c) calculated force evolution, and (d) calculated ϵ_{zz} component at the central sensor.

As illustrated in Fig. 3-11, there are multiple choices for the definition of the ZOI: for instance, it can be defined in between the sensor lines A and D, or in between B and C. As a consequence, it is necessary to check that the optimization is not "ZOI-dependent". To proceed to this verification, four different ZOI of different lengths are considered: between A and C (AC), A and D (AD), B and C (BC), B and D (BD). All simulation parameters are the same, except mesh geometries, mechanical boundary conditions (*i.e.*, imposed velocities), and initial temperature distribution (but note that these distributions are deduced from a unique profile $T(z)$ provided by IR imaging). In Fig. 3-11 c, it is observed that the calculated load response does not depend on the ZOI definition. This result is definitely expected. More interestingly, it is observed that at a central fixed sensor (the red dot in Fig. 3-11 a), both the calculated temperature evolution and the calculated deformation evolution are quasi-identical, whatever the ZOI. This demonstrates that the proposed local simulation method is self-consistent (in other words ZOI-independent). This ensures that the parameter identification will not depend on the choice of the ZOI, provided that its limit be reasonably far enough from the very central region of the specimen.

3.8 Chapter Summary

In this chapter the FEM frame of Cimlib is concisely introduced. The Thermo-elasto-viscoplastic constitutive law is given, which is then used in the direct simulation. The way to organize the direct simulation is introduced, together with the self-consistence proving the validity of the local strategy. The boundary conditions constraining direct simulation are then given during the reference frame transformation.

With all the above preparation of direct simulation, it is ready to do the optimization in the next chapter, where the simulation result is used as input for the optimization.

Chapter Reference

- 70 Pradille, Christophe. Vers une meilleure compréhension et caractérisation du comportement des aciers à très haute température. s.l. : *Doctoral dissertation*, École Nationale Supérieure des Mines de Paris, 2011. pp. 135-146.
- 71 Zhang, C., Bellet, M., Bobadilla, M., Shen, H. and Liu, B., 2011. Inverse finite element modelling and identification of constitutive parameters of UHS steel based on Gleeble tensile tests at high temperature. *Inverse problems in Science and Engineering*, 19(4), pp.485-508.
- 72 Arnold, D.N., Brezzi, F. and Fortin, M., 1984. A stable finite element for the Stokes equations. *Calcolo*, 21(4), pp.337-344.
- 73 Fortin, M. and Fortin, A., 1985. Experiments with several elements for viscous incompressible flows. *International Journal for numerical methods in Fluids*, 5(10), pp.911-928.
- 74 Tezduyar, T.E., 1991. Stabilized finite element formulations for incompressible flow computations. *Advances in applied mechanics*, 28, pp.1-44.
- 75 Hughes, T.J., 1995. Multiscale phenomena: Green's functions, the Dirichlet-to-Neumann formulation, subgrid scale models, bubbles and the origins of stabilized methods. *Computer methods in applied mechanics and engineering*, 127(1-4), pp.387-401.
- 76 Gouttebroze, S., Fachinotti, V.D., Bellet, M. and Combeau, H., 2005. 3D-FEM modeling of macrosegregation in solidification of binary alloys. *International Journal of Forming Processes*, 8, pp.203-203.
- 77 Gouttebroze, S., Bellet, M. and Combeau, H., 2007. 3D macrosegregation simulation with anisotropic remeshing. *Comptes Rendus Mécanique*, 335(5-6), pp.269-279.
- 78 Hachem, E., 2009. Stabilized finite element method for heat transfer and turbulent flows inside industrial furnaces (*Doctoral dissertation*, Ecole Nationale Supérieure des Mines de Paris).
- 79 Hachem, E., Rivaux, B., Kloczko, T., Digonnet, H. and Coupez, T., 2010. Stabilized finite element method for incompressible flows with high Reynolds number. *Journal of computational physics*, 229(23), pp.8643-8665.
- 80 Coupez, T., 2011. Metric construction by length distribution tensor and edge based error for anisotropic adaptive meshing. *Journal of computational physics*, 230(7), pp.2391-2405.

-
- 81 Chen, Q., Bellet, M., Gandin, C.A. and Guillemot, G., 2016, May. Finite Element Modeling of Additive Manufacturing by Selective Laser Melting. In *4th International Symposium on Cutting Edge of Computer Simulation of Solidification, Casting and Refining, CSSCR 2016*.
- 82 Zhang, S., 2020. Numerical simulation of mechanical interactions between liquid and solid phase in solidification processes (*Doctoral dissertation*, Paris Sciences et Lettres).
- 83 Chaboche, J.L., 2008. A review of some plasticity and viscoplasticity constitutive theories. *International journal of plasticity*, 24(10), pp.1642-1693.
- 84 Lemaitre, J., Chaboche, J.L., Benallal, A. and Desmorat, R., 2020. *Mécanique des matériaux solides-3e éd.* Dunod. Page 197
- 85 Hill, R., 1948. A theory of the yielding and plastic flow of anisotropic metals. *Proceedings of the Royal Society of London. Series A. Mathematical and Physical Sciences*, 193(1033), pp.281-297.
- 86 Estrin, Y. and Mecking, H., 1984. A unified phenomenological description of work hardening and creep based on one-parameter models. *Acta metallurgica*, 32(1), pp.57-70.
- 87 Estrin, Y., 1996. Dislocation-density-related constitutive modeling. *Unified constitutive laws of plastic deformation*, 1, pp.69-106.
- 88 Davoudi, K.M. and Vlassak, J.J., 2014. Dislocation evolution during plastic deformation: equations vs. discrete dislocation simulations. *arXiv preprint arXiv:1408.6609*
- 89 Blaizot, J., Chaise, T., Nélias, D., Perez, M., Cazottes, S. and Chaudet, P., 2016. Constitutive model for nickel alloy 690 (Inconel 690) at various strain rates and temperatures. *International Journal of Plasticity*, 80, pp.139-153.
- 90 Beltran, O., Huang, K. and Logé, R.E., 2015. A mean field model of dynamic and post-dynamic recrystallization predicting kinetics, grain size and flow stress. *Computational Materials Science*, 102, pp.293-303.
- 91 Schall, P., Feuerbacher, M., Bartsch, M., Messerschmidt, U. and Urban, K., 2000. Dislocation arrangement and density in deformed Al-Pd-Mn single-quasicrystals. *Materials Science and Engineering: A*, 294, pp.765-768.

92 Farla, R.J.M., Kokkonen, H., Gerald, J.F., Barnhoorn, A., Faul, U.H. and Jackson, I., 2011. Dislocation recovery in fine-grained polycrystalline olivine. *Physics and Chemistry of Minerals*, 38(5), pp.363-377.

93 VDM metal Material Data Sheet No. 4127 June 2016

94 Publication Number SMC-045, Copyright@ Special Metals Corporation,2007(Sept 07)

95 Carpenter Technology, Technical data sheet for 718 alloy,
<https://www.spacematdb.com/spacemat/manudatasheets/inconel%20718.pdf>, visited: Mar.19th, 2021

96 Agazhanov, A.S., Samoshkin, D.A. and Kozlovskii, Y.M., 2019, November. Thermophysical properties of Inconel 718 alloy. In *Journal of Physics: Conference Series* (Vol. 1382, No. 1, p. 012175). IOP Publishing.

97 James, J.D., Spittle, J.A., Brown, S.G.R. and Evans, R.W., 2001. A review of measurement techniques for the thermal expansion coefficient of metals and alloys at elevated temperatures. *Measurement Science and Technology*, 12(3), p.R1.

98 Zhang, Y., Guillemot, G., Bernacki, M. and Bellet, M., 2018. Macroscopic thermal finite element modeling of additive metal manufacturing by selective laser melting process. *Computer Methods in Applied Mechanics and Engineering*, 331, pp.514-535.

99 Jaouen, O., 1998. Modélisation tridimensionnelle par éléments finis pour l'analyse thermo-mécanique du refroidissement des pièces coulées (*Doctoral dissertation*, École Nationale Supérieure des Mines de Paris).Chapter 2.

Chapter 4 Optimization for Identification of Constitutive Parameters

Résumé

Dans les deux derniers chapitres, les enregistrements de force sont obtenus à la fois des tests expérimentaux et des simulations correspondantes, et ils sont utilisés pour construire une fonction de coût qui est détaillée dans ce chapitre. Différents candidats de fonction de coût sont vérifiés avant de démarrer l'optimisation en minimisant la fonction de coût. L'optimisation est réalisée sur la base de l'algorithme EGO intégré à MOOPI, une plateforme d'optimisation développée à domicile. Les paramètres optimisés sont ensuite adoptés dans la simulation pour produire des informations de force qui sont comparées à celles expérimentales correspondantes. On constate que la force expérimentale et la force simulée correspondent bien. Enfin, un test avec des températures variables sous chargement et relaxation est effectué pour vérifier si les paramètres optimisés peuvent bien fonctionner dans des cas compliqués.

Chapter Introduction

After the introduction of experimental and simulation in the previous chapters, optimization will be given in this chapter in the view of determining the constitutive parameters of a selected behavior law. Firstly the optimization strategy is introduced, followed by introduction of optimization platform MOOPI together with way to build a cost function and the candidates for the cost function. Then optimization result will be presented and analysis of the convergence and parameter coupling effect will be probed. Finally, a verification test is given based on the optimized parameters.

Vertical build sample, i.e. the sample built along the loading direction (i.e. the O1 in Chapter 5) is used in this chapter. The parameters of Hill48 are so selected that the yield criterion is the same as von Mises. No kinematic hardening is considered in this chapter. The meshes of 1 ani were used for the optimization, and meshes of 2 iso were used to calculate the data used in discussion with optimized parameters (refer to Fig. 3-4) in this chapter.

4.1 Optimization Strategy

A global introduction of the optimization strategy can be seen in Fig. 4-1. The experimental plan consists of mechanical tests performed at different nominal temperature levels: 800, 900, 1000 and 1100 °C. Nominal beam velocity v.s. time is the second characteristic of such tests. During each test, the time recorded information consists of the force, the surface displacement field, the surface temperature distribution. As explained above, from this information, and for each test, a ZOI and its

finite element mesh are defined. A steady initial temperature distribution and time-varying mechanical boundary conditions are determined. The elastic-viscoplastic behavior model defined in Eq. 3-49 is considered, and vector \mathbf{p} containing the initial values of the set of parameters is to be identified. This allows simulating, as explained in Section 3.4, each of the tests. Then a cost function f_c (also called objective function or loss function) can be defined and calculated, expressing the difference between measured and calculated quantities. A minimization procedure is then started: the \mathbf{p} values are iteratively modified in order to converge towards a minimal value for f_c . While the cost function value does not meet a predefined stop criterion (a certain small value) the iterative optimization process generates new parameter vector values, and automatically triggers a new series of simulations of the different tests.

Optimization flow of all steps presented in Fig. 4-1 is called inverse method (for more information of inverse method, refer to book by Buljak [100]).

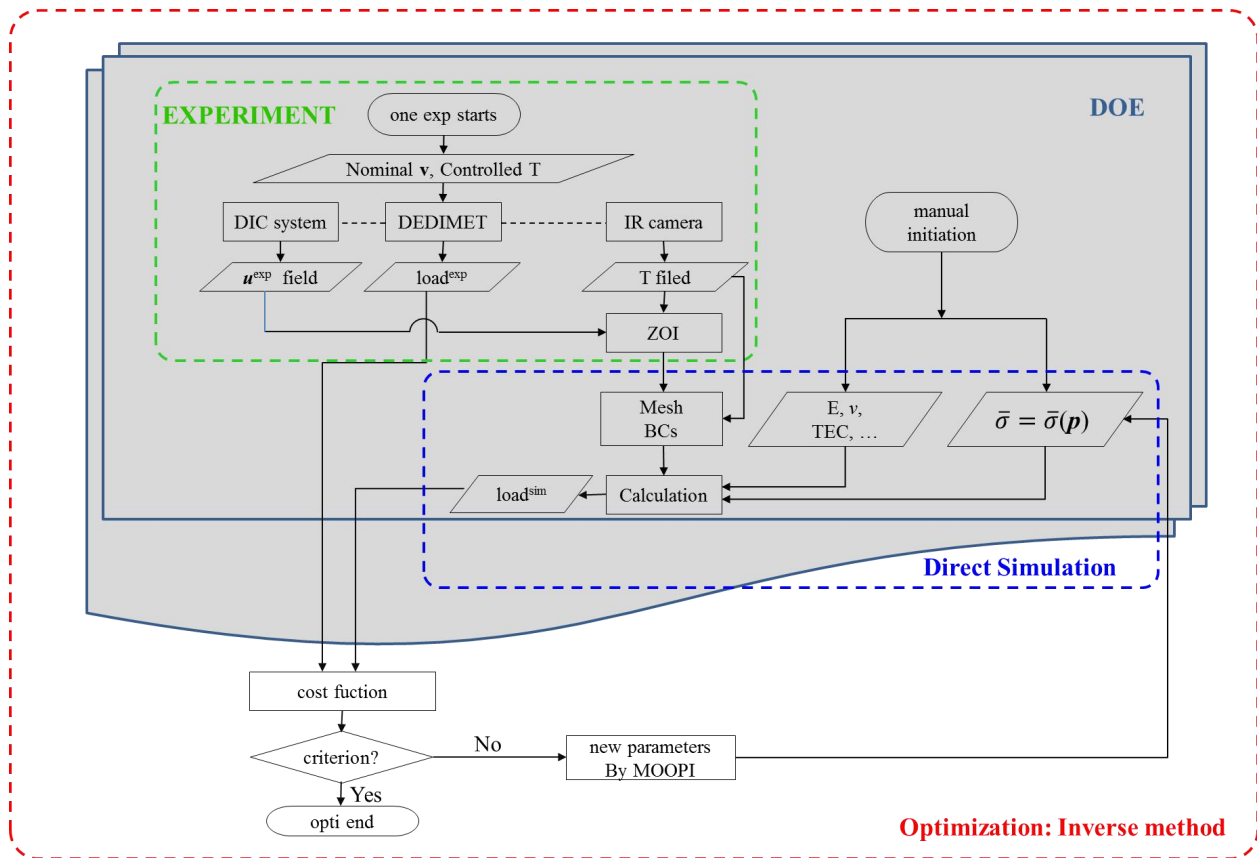


Fig. 4-1 Global view of optimization strategy for automatic identification of constitutive parameters

4.2 Introduction of MOOPI

The inverse method is carried out on a home-developed optimization platform MOOPI (MODular software for Optimization and Parameters Identification) [101]. MOOPI was designed to resolve non-linear optimization problems, the algorithms for which can be grouped into derivative-

based and derivative-free ones [102]. The Broyden–Fletcher–Goldfarb–Shanno (BFGS) [103] and the efficient global optimization (EGO) [104] integrated in MOOPI are the widely used two. The BFGS method demands the calculation of the Hessian matrix, and for a FEM based non-linear minimization problem this is really costly. Besides, the BFGS method is prone to find a local minimum, not necessarily a global minimum. On the contrary, EGO avoids those drawbacks, at least theoretically. The EGO method is suitable for black-box minimization problem. It takes a surrogate model (in MOOPI, kriging is selected) to generate the f_c response surface on the identification domain of \mathbf{p} . The response surface is updated with new estimates of \mathbf{p} . As the number of \mathbf{p} estimations increases, the minimum position of the response surface will be revealed. Although the calculation of expected improvement (EI) in EGO is also a heavy processing [105], comparing with the time-costing by FEM processing, calculation of EI in EGO becomes rather acceptable. Thus, the EGO method is selected as the optimization method in the present study.

4.3 Building a Cost Function

4.3.1 Interpolate the Simulation Data

The time series in the laboratory tests could be different from those in the simulation. A reasonable way to overcome this is to consider the time series in laboratory experiment as the master one, and project this laboratory time series to the simulation results to get the corresponding data. In this work linear relation is used for the projection.

4.3.2 Temporal Weights

In the laboratory time series, the interval between any two points could be different. The point adjacent to big intervals has a bigger temporal weight compared with the point adjacent to small intervals. Thus, temporal weights can be defined as follows. For any sampling instants t_{j-1} , t_j , and t_{j+1} ($j = 0, 1, 2, \dots, n - 1$), the time duration assigned to t_j is calculated as:

$$\Delta t_j = \begin{cases} \frac{1}{2}(t_1 - t_0) & , \text{if } j = 0 \\ \frac{1}{2}(t_j - t_{j-1}) + \frac{1}{2}(t_{j+1} - t_j) = \frac{1}{2}(t_{j+1} - t_{j-1}) & , \text{if } 1 \leq j \leq n - 2 \\ \frac{1}{2}(t_{n-1} - t_{n-2}) & , \text{if } j = n - 1 \end{cases} \quad (4-1)$$

Then the weight of each sampling instant j is defined as:

$$\theta_j = \frac{\Delta t_j}{\sum \Delta t_j} \quad (4-2)$$

And in the i^{th} laboratory test, this equation is re-assigned as:

$$\theta_{i,j} = \frac{\Delta t_{i,j}}{\sum_{j=0}^{M_i-1} \Delta t_{i,j}} \quad (4-3)$$

where M_i is the total sampling instants in the i^{th} laboratory test, and $\sum_j \theta_{i,j} = 1$ is met.

4.3.3 Candidates for Cost Function

The most used cost functions are mean absolute error (MAE), mean squared error (MSE), root mean square error (RMSE), mean absolute percentage error (MAPE) and root mean squared logarithmic error (RMSLE) [106,107]. It should be beard in mind that no cost function is perfect for all the problems, and one should chose the “right one” based on the problem that he studies. In the following, the normalized mean absolute error (NMAE), MAPE, and the normalized mean absolute logarithmic error (NMALE) are tested for this project, whose expressions are given in Eq. 4-4. Only force information is used in building the cost function.

$$f_c(\mathbf{p}) = \begin{cases} \sum_{i=0}^{N-1} \omega_i \frac{\sum_{j=0}^{M_i-1} |F_{i,j}^{exp} - F_{i,j}^{sim}| \theta_{i,j}}{\sum_{j=0}^{M_i-1} |F_{i,j}^{exp}| \theta_{i,j}} & \text{NMAE} \\ \sum_{i=0}^{N-1} \omega_i \sum_{j=0}^{M_i-1} \left| \frac{F_{i,j}^{exp} - F_{i,j}^{sim}}{F_{i,j}^{exp}} \right| \theta_{i,j} & \text{MAPE} \\ \sum_{i=0}^{N-1} \omega_i \frac{\sum_{j=0}^{M_i-1} |\lg(F_{i,j}^{exp} + 1) - \lg(F_{i,j}^{sim} + 1)| \theta_{i,j}}{\sum_{j=0}^{M_i-1} |\lg(F_{i,j}^{exp} + 1)| \theta_{i,j}} & \text{NMALE} \end{cases} \quad (4-4)$$

where i is the test index (N tests in total). In test i , there are M_i sampling instants for force measurement, whose temporal weight are denoted as $\theta_{i,j}$ with j varying from 0 to $M_i - 1$. Accordingly, $F_{i,j}^{exp}$ and $F_{i,j}^{sim}$ are the measured and calculated force values (in fact the absolute value of the force component along the loading direction) at time $t_{i,j}$, respectively. And coefficients ω_i allow a possible weighting procedure between the different tests (in this project $\omega_i = 1$ is always met).

The “mean” of each formulation is expressed by temporal weight $\theta_{i,j}$, and “normalization” is expressed by the Σ part at denominator in NMAE and NMALE. In fact, in MAPE there is also normalization, which is contained in the percentage error itself. The normalization is whatever important, because in tests at various temperature levels the magnitudes of load are quite different. Besides, no “Squared” cost function such as RMSE is adopted, because in EGO method no differentiation of cost function is calculated and thus, there is no need to consider the differentiability of the cost function.

In the following optimization results for each of the three cost functions will be presented.

4.4 Database and Settings of Optimization

4.4.1 Database of Optimization

The temperature field initially projected onto the mesh of the ZOI is shown in Fig. 4-2, for the four tests. As previously shown in Fig. 3-6, all nodes of the mesh are assigned with a negative z coordinate value during the reference frame transformation, the top of each ZOI being at $z = 0$. The effective length of each ZOI is indicated just below them in the figure. At 800°C the selected ZOI length is much shorter than the others because at this tested temperature level the lower values of the temperature profile reach the lower bound of the use domain of the IR camera (Refer to Section 3.5.1).

In the present study, elastic parameters are not identified. The Poisson coefficient is assumed as constant, equal to 0.3. The variation of the Young modulus with temperature is taken from literature [108] and the data are multiplied by 0.82 as a compensation of reduction caused by orientation of columnar microstructure of additive manufactured material [44], where the value 0.82 was determined by optimization during the starting several seconds of all the tests. Detailed calculation of Young's module along given direction is given in Appendix A. 12.

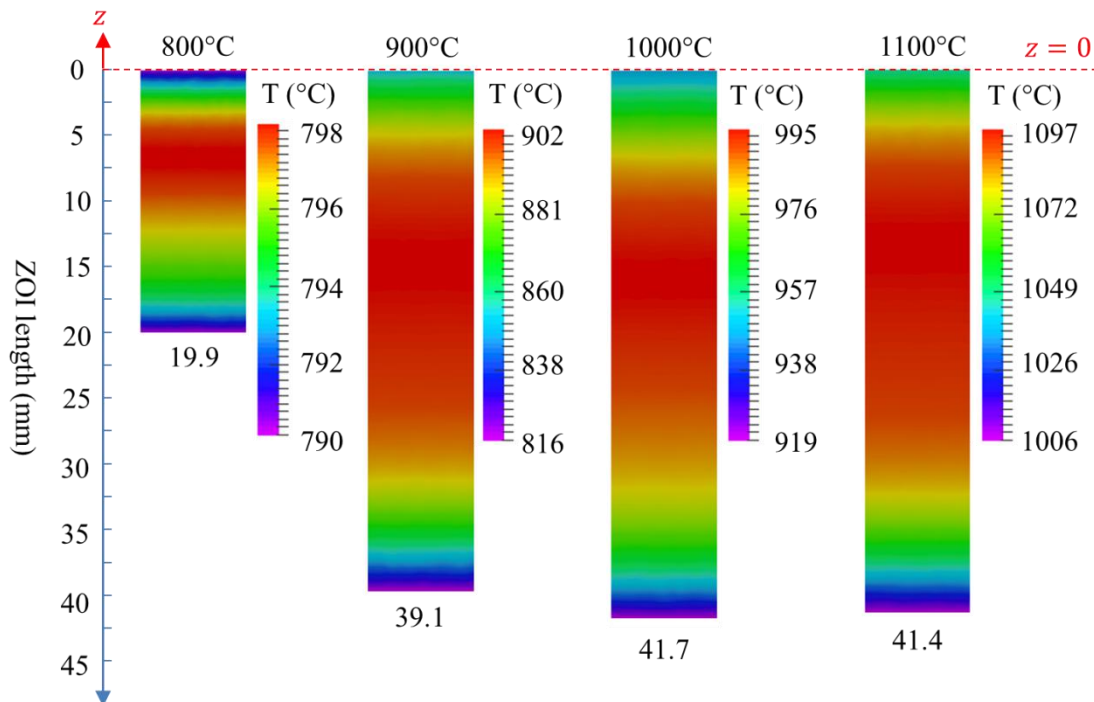


Fig. 4-2 Measured temperature as a function of z at the beginning of the first loading step, for the 4 tests.

Fig. 4-3 introduces the four different tests performed at different nominal temperatures. All tests consist of a sequence of three load and relaxation steps, except the test at 900°C, which has only two steps, as shown by the dashed lines in Fig. 4-3. Altogether, this allows identifying the constitutive equation on a series of 11 load and relaxation combinations at different temperatures. Load steps are performed at imposed constant beam velocity, indicated by the red dashed lines on the figure. Beam velocity varies from 0.01 to 0.05 mm·s⁻¹. Assuming that the deformation affects principally the central hottest region with a quasi-uniform temperature, and estimating its length to be 20 mm, this yields a nominal strain rate varying from 0.5 to 2.5 × 10⁻³ s⁻¹. Relaxation steps, during which the beam velocity is maintained null (zero displacement), have different durations, from 15 to 60s. The blue solid curves in Fig. 4-3 show the measured evolution of the force. It can be seen that the response of the material clearly expresses elasto-viscoplasticity, at all temperature levels. The decrease of the force (so the stress) after load, when deformation stops, is progressive, expressing viscous effects. Also, despite the rather short relaxation steps, stress relaxation appears as only partial, revealing a non-zero stress threshold.

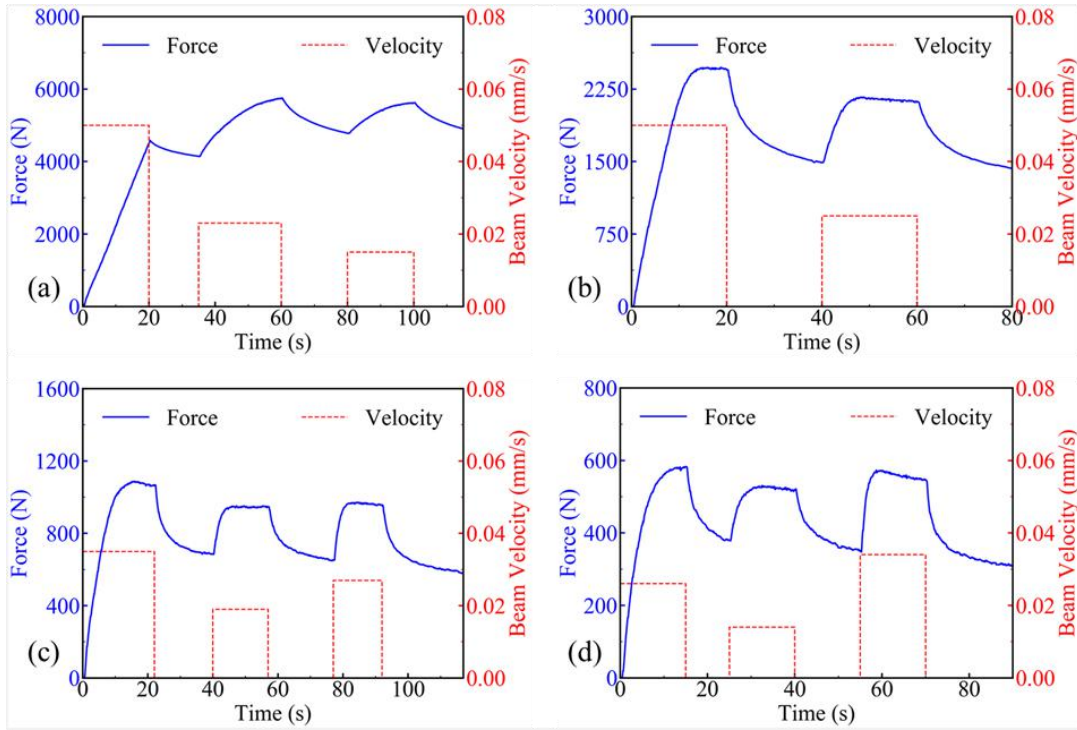


Fig. 4-3 Summary of the experimental plan consisting of load and relaxation steps at different temperatures (a): 800°C, (b): 900°C, (c): 1000°C and (d) 1100°C. The four charts show the imposed beam velocity vs time (in red dashed segments), and the measured load response vs time (blue solid curves).

Thanks to the temperature profile as shown in Fig. 4-2 and the velocity imposed on the ends of the sample as shown in Fig. 4-3, the lengths of selected ZOIs evolve with time too, which is given in Fig. 4-4. The lengths of ZOI at time t (l_{ZOI}^t) is calculated by:

$$l_{ZOI}^t = |\bar{z}_{lower}^t - \bar{z}_{upper}^t| \quad (4-5)$$

where \bar{z} is the averaged displacement component along loading direction of the grouped points that define the upper and lower boundaries of ZOI, as shown in Fig. 2-17 (a) and Fig. 3-1(b). It can be seen that the length of ZOI continues to increase, whenever at loading or relaxation period. In Section 3.6.2.1 the experimental velocities at upper and lower boundaries of ZOI are imposed into the corresponding meshes, which in turn become the evolution of length of ZOI. In other words, one can consider the evolution of length of ZOI as the boundary conditions. (This is also one tip for operating the master-slave fitting in Appendix A. 7, and see also Section 3.6.2.1)

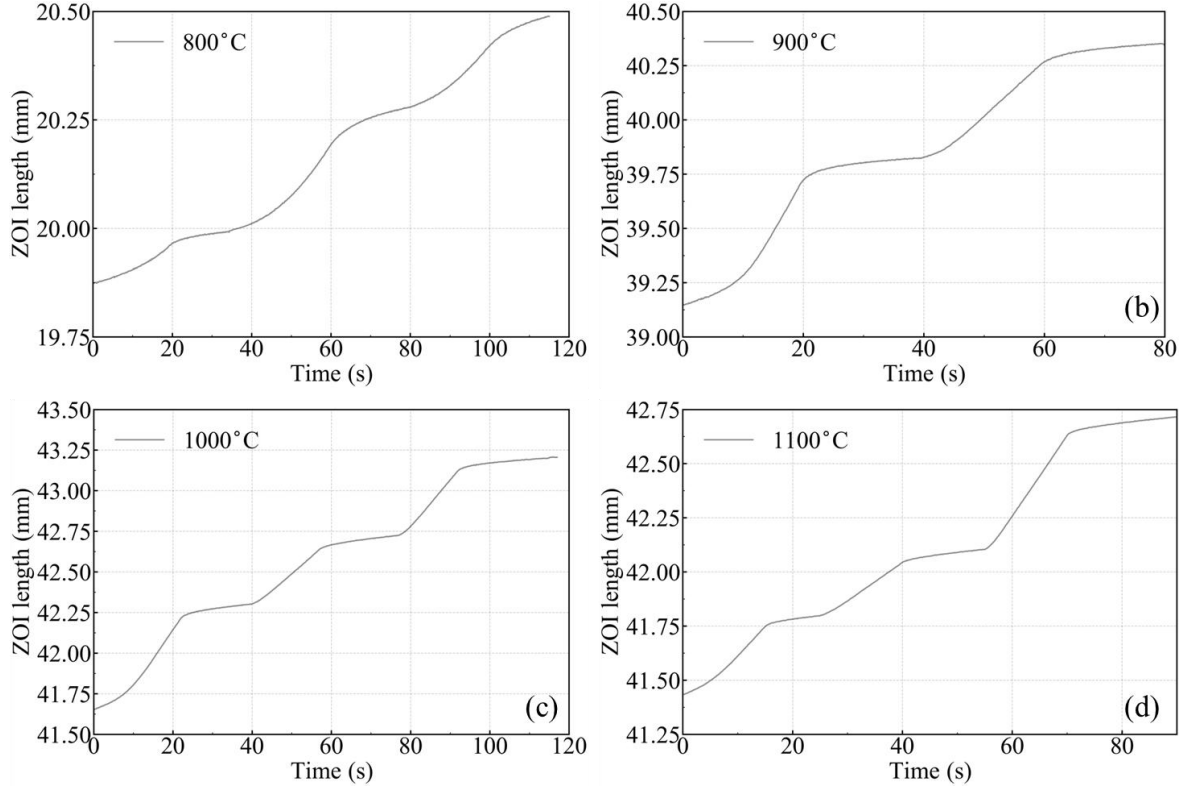


Fig. 4-4 Evolution of experimental ZOI lengths with time in the test of (a): 800°C, (b): 900°C, (c): 1000°C and (d): 1100°C

4.4.2 Settings of Optimization

The rheological law for characterization is reduced from Eq. 3-49 (see Appendix A. 13), and it is

$$\bar{\sigma} = \underbrace{\left(\sigma_{Y,ref} + Q_{r,ref} (1 - \exp(-b\bar{\epsilon})) \right)}_{\sigma_s} \exp\left(\frac{Q_1}{R_g T} - \frac{Q_1}{R_g T_{ref}} \right) + \underbrace{k_{ref} \exp\left(\frac{Q_2}{R_g T} - \frac{Q_2}{R_g T_{ref}} \right)}_{\sigma_{overstress}} \dot{\bar{\epsilon}}^m \quad (4-6)$$

The search intervals for all the parameters are given in Table 3, with T_{ref} assigned with 1073K. Those boundary settings are used in all the optimizations of the three cost functions. The other settings are (for reason of choosing such initial parameters, refer to reference [101]):

Kriging exploitation type: expected improvement (EI)

Kriging calibration type: Likelihood

Kriging parameters: Theta

Initial database: 128 (= 2^7)

Maximum database: 500

Table 3 Boundary values of the parameters for the optimizations and optimized values on various cost functions

Parameter (Unit)	Boundaries		Optimized Values		
	Minimum	Maximum	MAPE	NMAE	NMALE
$\sigma_{Y,ref}$ (MPa)	60	160	92	94	148
$Q_{r,ref}$ (MPa)	63	103	102	102	66
b	171	571	570	322	241
Q_1 kJ·mol ⁻¹	140	180	150	163	153
k_{ref} (MPa)	677	1595	1365	1112	1430
m	0.15	0.35	0.277	0.252	0.303
Q_2 kJ·mol ⁻¹	56	96	83	77	71
$min(f_c)$	—	—	0.284	0.0404	0.00785

4.5 Optimization Results

4.5.1 Choice of the Final Cost Function

After 500 hundred calculations, the optimized parameters were found by MOOPI, and the values are given in Table 3. The final cost function values given in Table 3 by different expressions are **not** comparable. Then, based on the optimized parameters for each cost function, the simulated force and experimental force are plotted in Fig. 4-5. One can see that for all the 3 sets of parameters, the differences between experimental and simulated force are **not** so apparent. Based on the above two aspects of non-ability (i.e. cannot be selected by comparing the cost function values, and cannot be selected by the difference between experimental and simulated forces), a reasonable way to find the better choice for the cost function is to use the percentage of cost function. The final cost function value is the sum of the expressions after ω_i (included) in Eq. 4-4, where ω_i is assigned as 0.25. So the expressions take percentages in the final cost function, and these values are given in Fig. 4-5 under each curve for each cost function.

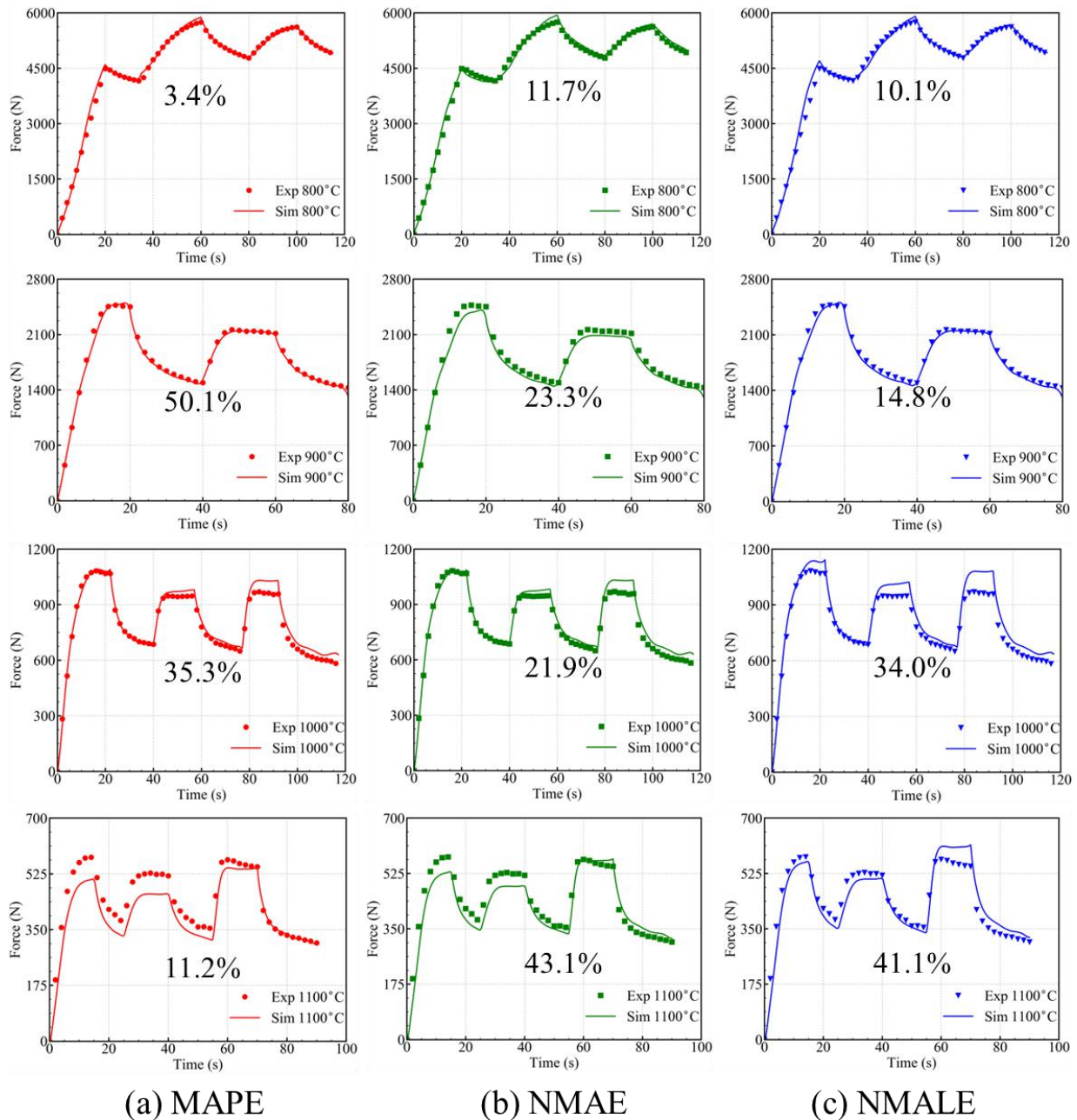


Fig. 4-5 Force comparison between experiments and simulation with optimized parameters on cost function of (a): MAPE, (b) NMAE and (c): NMALE. The cost function percentage of each test is indicated under corresponding curve. The sum of f_c in each column is 100%,

Now, immediately and visually we are able to tell that the appearance of MAPE and the percentages are not “compatible” when we look at the 900°C and 1100°C tests. This is because in MAPE expression, it is very sensitive to local values, especially at the starting period. Looking at the illustration given in Fig. 4-6 for instance, one can see that for the first experimental data point at the sampling point close to 0, the MAPE expressed by Eq. 4-4 will generate a very big value, even though the overall simulated curve and experimental curve match well. That is the reason that in Fig.

4-5 (a), the 900 and 1100°C contribute strange percentage in cost function. Thus, MAPE is not a good choice in this project because in each test the experimental force increases from 0, which could introduce abnormal values at the starting period.

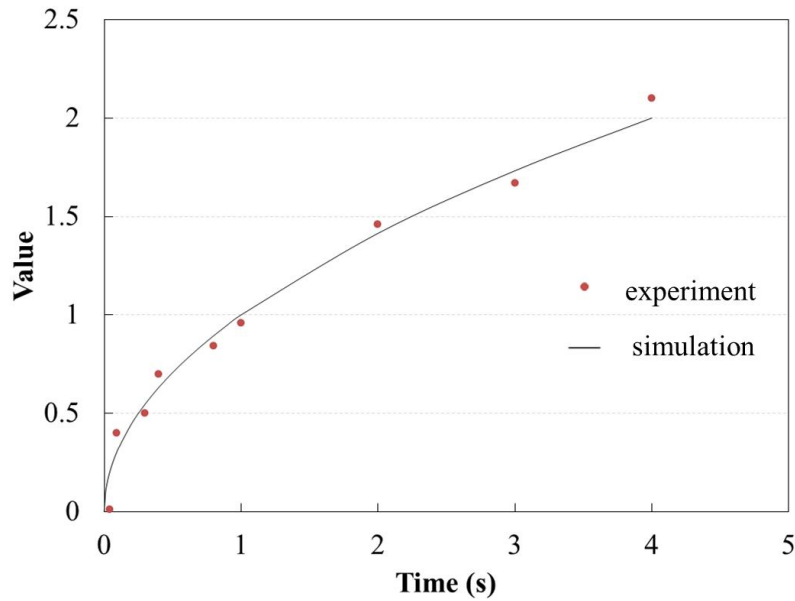


Fig. 4-6 Explanation why MAPE could generate strange values

Then, no obvious advantage can be found based on this figure for the NMAE and NMALE, but the NMAE has a clearer meaning, which is the relative difference of the areas under the experimental curve and the simulated curve.

Based on the above, the NMAE is chosen as the cost function for this work.

4.5.2 Optimization Result with NMAE

The optimization with cost function NMAE is composed of three trials, as listed in Table 4. Trial 2 started with the optimized values found in Trial 1 as initial values, and with a modified relative wider identification domain, which is approximately centered on initial values. Trial 3 uses the same boundaries as Trial 2, but without assigned initial values.

Table 4 Initial, and boundary values of the parameters for 3 trials

Parameter (Unit)	Trial 1			Trial 2				Trial 3		
	Min.	Max.	Opti.	Ini.	Min.	Max.	Opti.	Min.	Max.	Opti.
$\sigma_{Y,ref}$ (MPa)	50	110	110	110	50	170	107	50	170	76
$Q_{r,ref}$ (MPa)	30	100	83	83	53	113	83	53	113	113
b	20	500	371	371	70	670	367	70	670	359
Q_1 (kJ·mol ⁻¹)	140	220	157	157	120	220	157	120	220	155
k_{ref} (MPa)	640	1364	1118	1118	659	1640	1118	659	1640	1537
m	0.1	0.35	0.256	0.256	0.1	0.4	0.252	0.1	0.4	0.285
Q_2 (kJ·mol ⁻¹)	40	110	76	76	46	106	77	46	106	82
$\min(f_c)$			0.0384				0.0382			0.0438

Initial: ini., Minimum: Min., Maximum: Max., Optimum: Opti.

The evolution of the minimum cost function value, $\min(f_c)$, along successive direct simulations, is shown in Fig. 4-7, for the three trials. As the minimum value of the cost function is not systematically decreased at each direct simulation, only characteristic points are indicated on the curves: points at which $\min(f_c)$ is effectively decreased. In between them, direct simulations may contribute to the improvement of the response surface, without necessarily decreasing $\min(f_c)$. In Trial 2, $\min(f_c)$ value starts to converge with the end value of Trial 1, and finally ends with a smaller value than in Trial 1, thanks to the pre-optimized initial values and the modified identification domain. In Trial 3, $\min(f_c)$ converges fast, but does not reach a value as low as in Trial 1. This is because of a wider identification domain. This reveals a kind of correlation between some parameters.

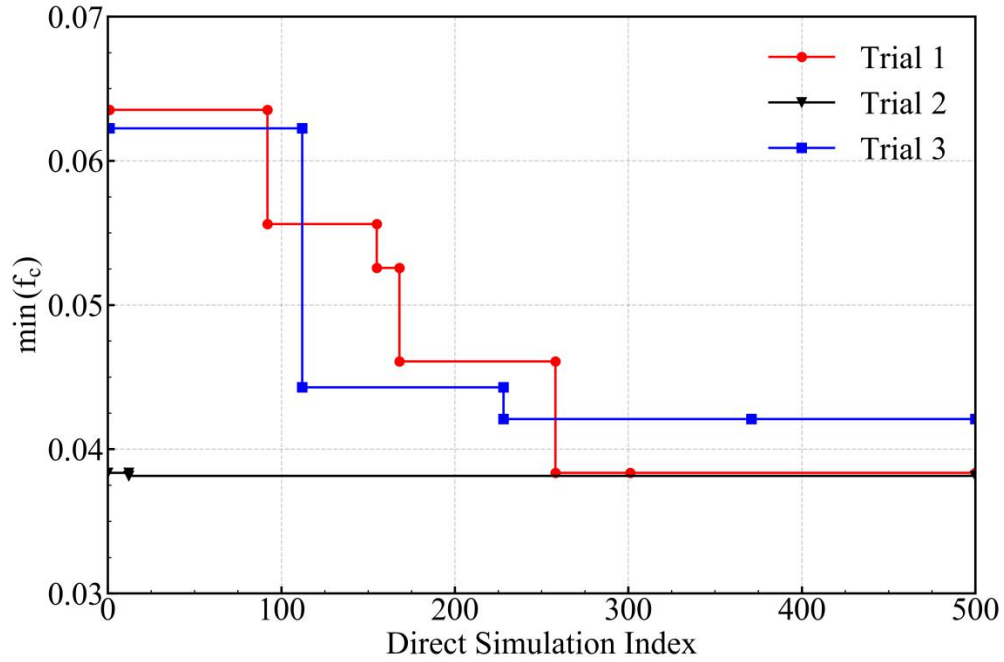


Fig. 4-7 Decrease of $\min(f_c)$ with the number of direct simulations performed in each of the 3 trials

4.5.3 Optimized Parameters and Correlation

4.5.3.1 Q_1 and Q_2

It can be noticed first that the final values of the two activation energies Q_1 and Q_2 are quite different. Q_1 is found to be twice as big as Q_2 . From Eq. 4-6, the temperature sensibility of the overstress ($\sigma_{overstress}$) contribution to the equivalent stress ($\bar{\sigma}$) is smaller than that of the threshold stress (σ_s) contribution due to $Q_1 \approx 2Q_2$. The $\sigma_{overstress}$ and σ_s contribution together with temperature dependency is given in Fig. 4-8, whose values are extracted from numerical sensors at the central portions of meshes at surfaces. At higher temperature levels the overstress becomes the main part of $\bar{\sigma}$. Then, let us remind here, referring to Eqs. 3-47 and 4-6 that it has been assumed that dislocation glide and climb have a similar activation energy: Q_1 , and that the second one, Q_2 , characterizes viscoplastic deformation: $Q_2 = mQ_{vp}$. From the identified values, we get: $Q_g = Q_c = Q_1 = 157\text{kJ}\cdot\text{mol}^{-1}$, and $Q_{vp} = Q_2/m = 77/0.252 \approx 305\text{kJ}\cdot\text{mol}^{-1}$. The value of Q_{vp} found in this work is close to those values of effective activation energy in range of 249 to 310 $\text{kJ}\cdot\text{mol}^{-1}$ for creep behavior [109,110].

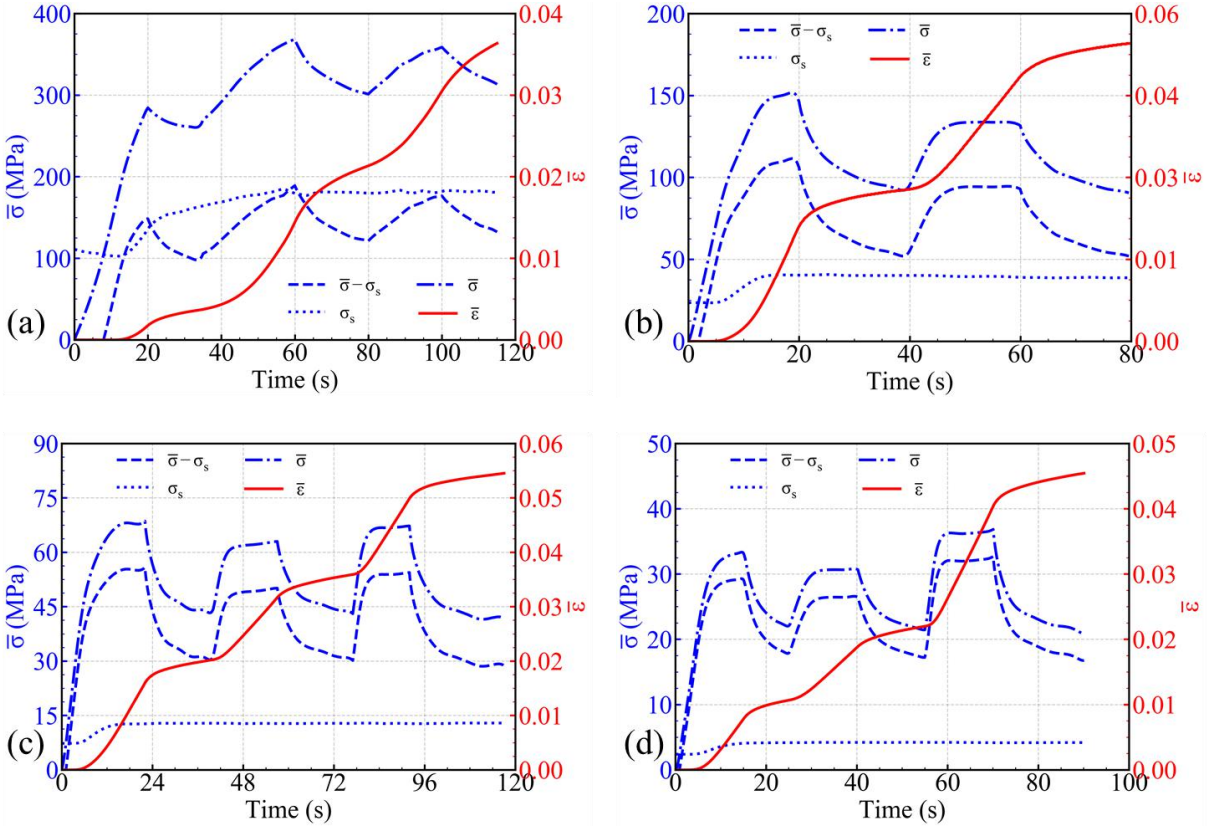


Fig. 4-8 σ_s (blue dotted line), $\bar{\sigma} - \sigma_s$ (i.e. over-stress, blue dashed line) and $\bar{\sigma}$ (blue dash-dotted line), and $\bar{\epsilon}$ (red solid line) from numerical sensors at the mesh surfaces (corresponding center positions at the sample surfaces) in simulation at (a): 800°C, (b) 900°C, (c) 1000°C, and (d)1100°C. These simulations were based on optimized parameters of Trial 2 with temperature field updating.

4.5.3.2 Correlation of $\sigma_{Y,ref}$, $Q_{r,ref}$ and b

A focus on the expression of the hardening function, $Q_{r,ref}(1 - \exp(-b\bar{\epsilon}))$, shows that it is extremely sensitive to b parameter. In the present case, the three identification trials converge to high values of b , always greater than 350. The consequence is that only one percent of plastic deformation is enough to almost saturate this hardening function: $1 - \exp(-350 \times 0.01) = 0.96$, and taking $b = 367$, a 99% saturation is reached at $\bar{\epsilon} = 0.013$. As the tests (from 800 to 1100°C) are performed for plastic strain up to 0.037, 0.053, 0.055 and 0.045, the hardening function is found saturated on a large part of the experimental data base, which is shown in Fig. 4-8. This may cause a tight correlation between the initial yield stress, $\sigma_{Y,ref}$, and the exponential hardening term, $Q_{r,ref}$. Indeed, for any plastic strain exceeding the saturation value 0.013, the threshold stress has the following expression:

$$\sigma_s(T, \bar{\epsilon}) \approx (\sigma_{Y,ref} + Q_{r,ref}) \exp\left(\frac{Q_1}{R_g T} - \frac{Q_1}{R_g T_{ref}}\right) \quad (4-7)$$

Thus, it can be understood that different pairs $(\sigma_{Y,ref}, Q_{r,ref})$ having the same sum can not be discriminated. As a matter of fact, it is worth noticing that the sum $\sigma_{Y,ref} + Q_{r,ref}$ takes similar values in Trial 1, Trial 2, and Trial 3: 193, 190, and 189MPa, respectively. The only possibility for discrimination between such pairs relies on contributions to the cost function provided by the part of the force curves obtained for small plastic deformation (*i.e.* less than 0.013). Note that this may only provide from the first loading of each test. A deconvolution technique – which has not been tested in the present work, due to a lack of time – would consist in affecting an extra weight in the cost function to the beginning of the first load curve of each test.

4.5.3.3 Correlation of k_{ref} and m

Uncoupling these two values requires an extended strain rate range. Table 5 gives the values of the product $k_{ref}\dot{\epsilon}^m$ obtained for different strain rates $\dot{\epsilon}$ with k_{ref} and m values identified in Trial 2 and Trial 3.

Table 5 Analysis of the correlation between parameters k_{ref} and m

Generalized strain rate $\dot{\epsilon}$ (s ⁻¹)	Value of product $k_{ref}\dot{\epsilon}^m$		
	with parameters identified in Trial 1	with parameters identified in Trial 2	with parameters identified in Trial 3
10 ⁻⁵	58.7	61.4	57.8
10 ⁻⁴	105.8	109.8	111.4
10 ⁻³	190.8	196.1	214.7
10 ⁻²	344.0	350.3	413.8

Note that for the first three lower strain rates, the product values differ by less than 10% for the three pairs of k_{ref} and m values. Decorrelation would be more clearly obtained at higher values of $\dot{\epsilon}$ (*e.g.* 10⁻²), for which the product values are less close. This is especially true since this maximum difference is obtained for the high strain rate, which is hardly obtained during the characterization tests. This is illustrated in Fig. 4-9 where the evolution of the zz component of the strain rate $\dot{\epsilon}_{zz}$, as measured by DIC, is plotted (blue dot curves). The $\dot{\epsilon}_{zz}$ component is actually close to $\dot{\epsilon}$ in this quasi-uniaxial configuration, and is extracted at the geometrically central point of the sample surface. Note that this point is not the hottest position, but quite close to it. It is observed that the strain rate is found in between a maximum of 2x10⁻³s⁻¹ during loading, and a minimum of 1.5x10⁻⁵s⁻¹ during relaxation. Longer relaxation steps would give access to lower strain rates, but at a cost of much longer tests, which is problematic regarding surface oxidation of the specimen. An alternative to get low strain rates would consist in proceeding with loading steps at a much slower beam motion, but this cannot be easily controlled on the present Dedimet machine. Nevertheless, it is important to note that the experimental space on which the constitutive equation is identified covers this amplitude: from 1.5x10⁻⁵ to 2x10⁻³s⁻¹, which is fully relevant for further use of the behavior law in the context of numerical simulation of LPBF additive manufacturing.

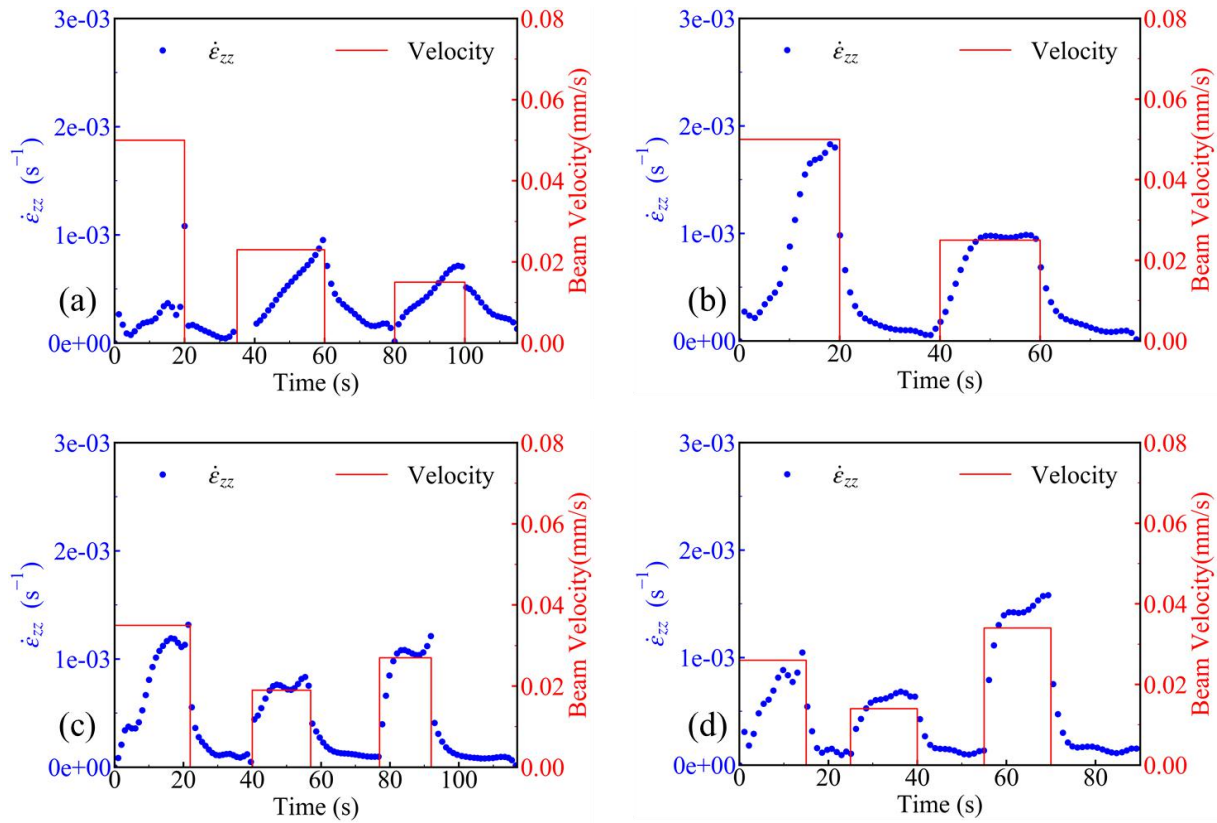


Fig. 4-9 Evolution of beam velocity (red solid lines) and of the experimental strain rate component $\dot{\epsilon}_{zz}$ as measured by DIC at the center of the specimen surface (blue dots) for tests at (a) 800°C, (b) 900°C, (c) 1000°C, and (d) 1100°C.

Despite the preceding remarks, it seems reasonable to consider that the obtained $\min(f_c) = 0.03815$ in Trial 2, is associated with a sound parameter set. In the next section, the obtained results are presented and discussed.

4.5.4 Final Results

The parameters from Trial 2 are taken to run the simulations for the 4 temperature levels with temperature update. Fig. 4- 10 shows the comparison between calculated and measured load curves.

On this chart that encompasses the 4 tests thanks to a unique force scale, it can be seen that the different load and relaxation steps are very well predicted, for various loading velocities and over a 300°C temperature range, from 800 to 1100°C. What is especially striking is the almost perfect agreement upon relaxation steps. This reveals a very good modeling of the viscoplastic parameters, but also their balance with respect to the predefined elastic ones, as it is well known that the slope at relaxation start is governed by the so-called relaxation time, in other words the ratio of the apparent viscosity to the Young modulus. Relaxation at longer times is equally very well described, which means that the modeling of the yield stress (the elastic limit plus the hardening function) is also very accurate, as it is known that the stress asymptotically converges to this yield stress. What's more, in

the simulation no kinematic hardening is used, and this good agreement of force indicates that the kinematic hardening is not necessary for the simulation of the behavior.

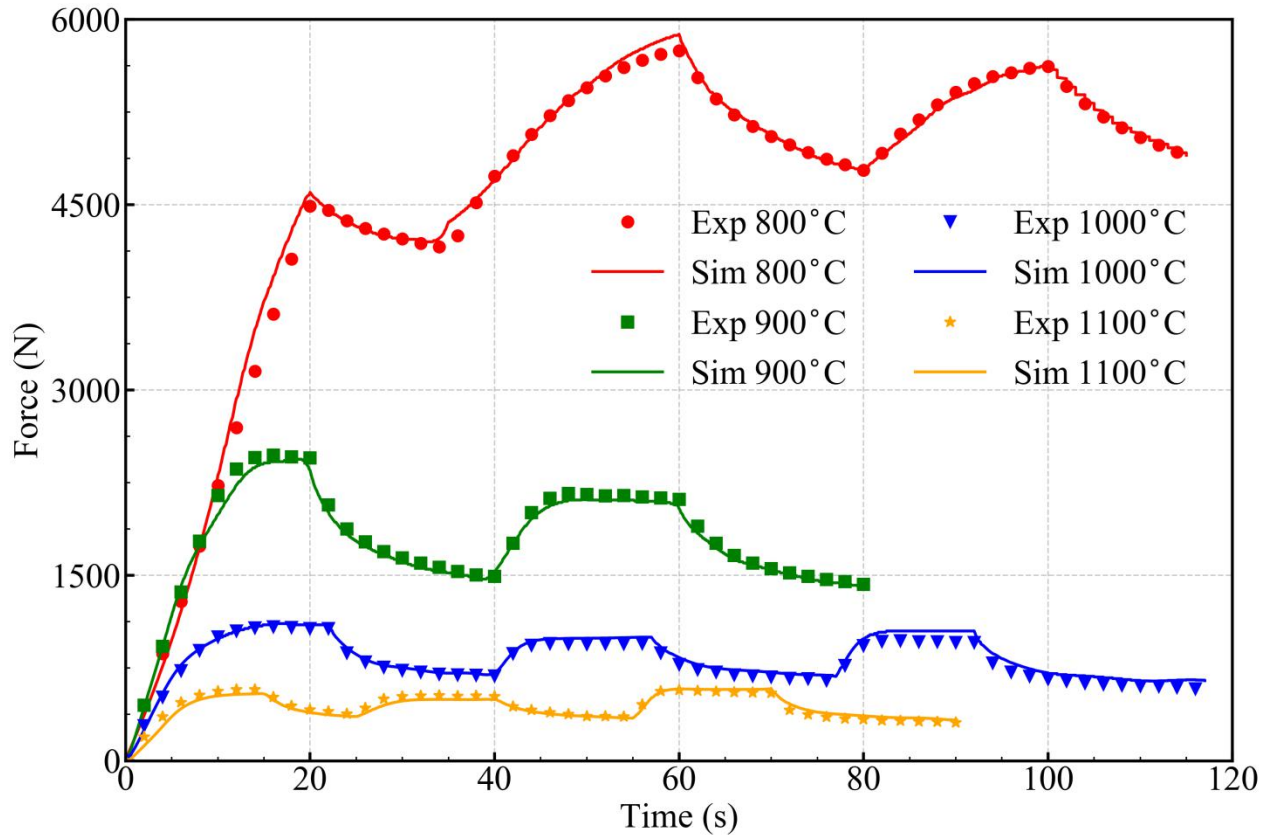


Fig. 4-10 Load comparison between experiments and corresponding simulations with optimized parameters.

The only imperfection can be found during loading steps. This is probably due to the expression of the hardening function which could be improved. However, only minor differences can be observed with respect to the experimental measurements.

These results can be compared with respect to the literature. One can see that the yield strength of IN718 decreases rapidly after 650°C [95,111]. The as-built sample is expected to have a structure close to as-cast or as-solutioned. And it is found that the 0.2% offset yield strength ($R_{0.2p}$) at 650°C under non-aged condition is at a level of about 350MPa [112,113], thus smaller $R_{0.2p}$ is expected at higher temperature of 800°C within short testing duration. In the 800°C simulation, when the equivalent strain reaches 0.2%, the corresponding stress component of σ_{zz} is 284MPa, which is equal to $\bar{\sigma}$ and contains initial yield strength, dynamic hardening and overstress contribution, is reasonable based on the temperature and the material temper state.

Besides, with a value of $b = 367$, it can be proofed that at about 1.3% deformation the stress reaches 99% of the hardening capacity. This fast saturation is found close to some research work carried out at similar temperature and strain rates [114,115,116].

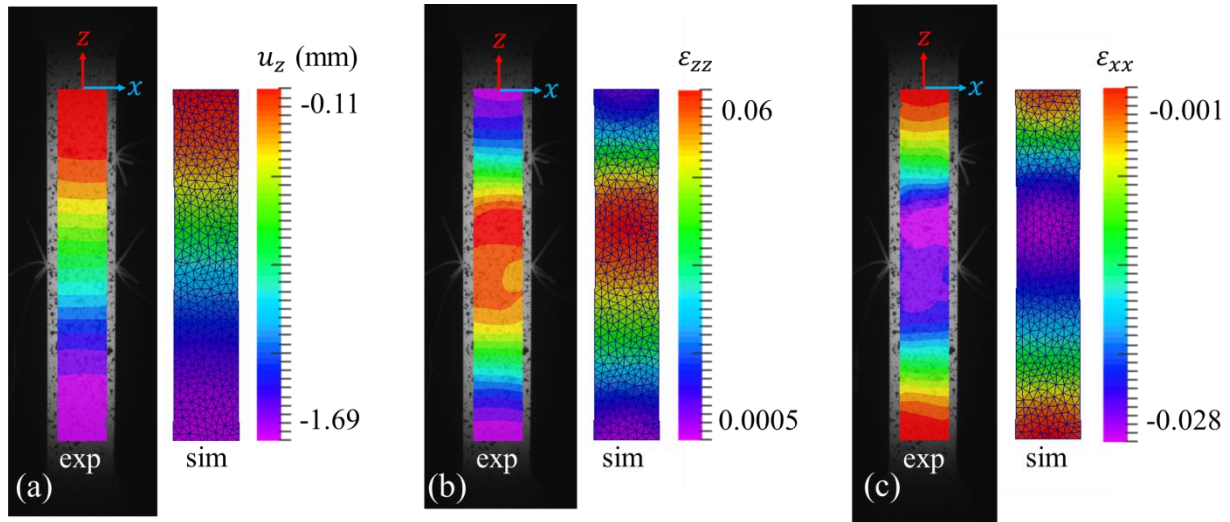


Fig. 4-11 Field comparison of (a): displacement component u_{zz} , (b): deformation component ϵ_{zz} and (c): deformation component ϵ_{xx} , between experiment and simulation of test at 1000°C

What's more, the displacement and deformation information by experiments and simulations is shown in Fig. 4-11. Even though the parameters in the constitutive model were determined by optimizing a cost function built only by force information, the simulated deformation field and the measured experimental ones are quite comparable, which is evidence that the constitutive model is well selected and characterized

4.6 Testing of Characterized Rheological Law

Throughout the previous sections in this chapter, all the parameters are optimized based on temperature fields which do not evolve with time. It is desirable to check if these parameters work well for a test with evolving temperature field.

4.6.1 Verifying Test Design

From Fig. 4-2 one can see that for temperature domain between 900 and 1100°C, the ZOI can be selected with the same length, but for 800°C this length is quite shorter. As a compromised choice, the temperature range of 925 ~ 1130°C is selected.

From a test on Dedimet machine, the cooling rate is higher than $19^{\circ}\text{C}\cdot\text{s}^{-1}$ based on the setting as aforementioned in Chapter 2, and the heating rate can maintain a constant value of $6^{\circ}\text{C}\cdot\text{s}^{-1}$ from room temperature to 1200°C. A verifying test is designed as given in Table 6.

Table 6 Temperature and velocity routines in the verifying test

Time in exp (s)	Time in sim (s)	T (°C)	v (mm·s ⁻¹)
0	—	20	free
180	—	1130	free
360	0	1130	free/0.05
385	25	975	0.05/0
405	45	925	0/0.025
435	75	1025	0.025/0
471	111	1130	0

The verifying test composes of four sections: loadings of different velocities with evolution of temperature at different rates.

4.6.2 Experimental and Simulation Results

The temperature evolution measured at the center of the wide sample surface by IR camera since $t_s = 360s$ in the experiment (*i.e.* from $t = 0$ in simulation) is shown in Fig. 4- 12 (a). It can be seen kept very close to the objective temperature routine. The experimental and simulated forces are shown in Fig. 4- 12 (b). From the figure we can make the following observations in the 4-time sections:

1st loading (0 ~ 25s): the force increases with time as deformation increases. Since about 7s, the force evolution is slowed down since the plastic deformation occurs (refer to the red solid curve in Fig. 4- 12 (b)), and the curve has a convex trend due to the descending temperature. During this second phase in loading 1, the simulation tends to overestimate the force.

1st relaxation (25 ~ 45s): at start of relaxation, the force goes down rapidly because of the viscoplasticity with decreasing strain rate. But at a certain moment - well captured by simulation – that the force increases again due to the descending temperature, which indicates an increase of the stress threshold.

2nd loading (45 ~ 75s): for the starting several seconds the force increases fast thanks to the increasing strain rate, which is again well captured by the simulation. Then, at a certain moment (~50s), again well captured by the simulation that the force goes down as a result of increasing temperature. But once again, the rate of decrease of the force is overestimated by the simulation, and

2nd relaxation (75 ~ 111s): the load decreases continuously, and the force seems to converge to a very low level, which is expected, because the stress threshold at a temperature higher than 1100°C is expected very low.

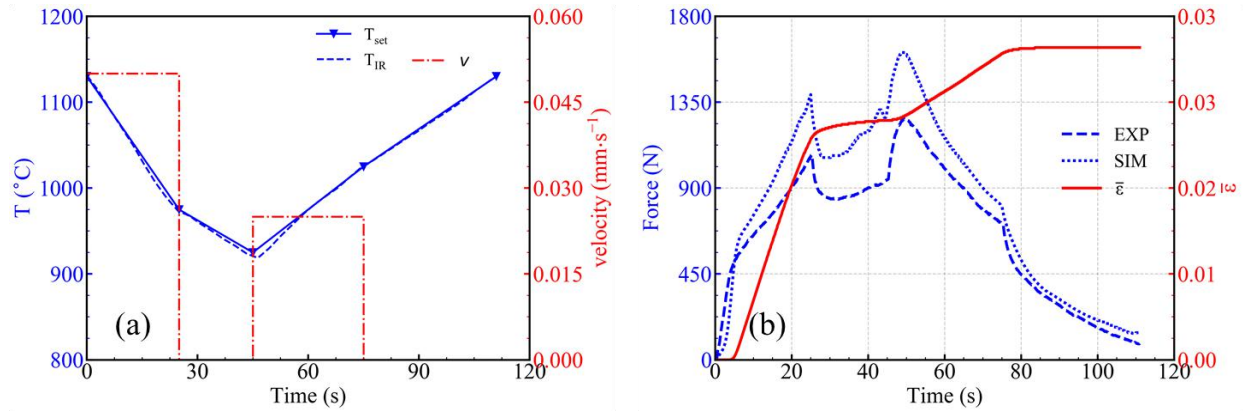


Fig. 4-12 Comparison of (a): measured T by IR camera and set value, (b) measured force and calculated force

The calculated force is systematically higher than the experimental one between ~ 5 and 75s. This bias is partially caused by the temperature measurement error, (which was further caused by IR camera calibration, see Appendix A. 16.1.2): the bigger gap between T_{IR} and T_{set} is, the more bias between experimental and simulated force is found. The NMAE value is 0.245, which is too big compared with the result (0.03815) mentioned at end of Section 4.5.3.3. Aside of the constitutive model selection and the determined parameters, the temperature measurement is the biggest issue that affects the force comparison. After a manual calculation, it is found that if the T_{IR} is increased by 3.18% (i.e. 29 to 36°C, which is in the uncertainty in the error analysis in Appendix A. 16.1.2), the cost function is strongly reduced to 0.0485, and the new comparison of force between experiment and simulation based on the adjusted temperature is given in Fig. 4-13. From this result it is clear that on the one hand, the trend determined by Eq. 4-6 and the determined parameters is quite such as expected, which means the parameters were well determined; on the other hand, the precision of the experimental work is quite important for determining the parameters of the constitutive model. That is also a reason that 100°C was selected as interval for different temperature level tests. Refer to Appendix A. 16.1.2 for more about the error during temperature measurement.

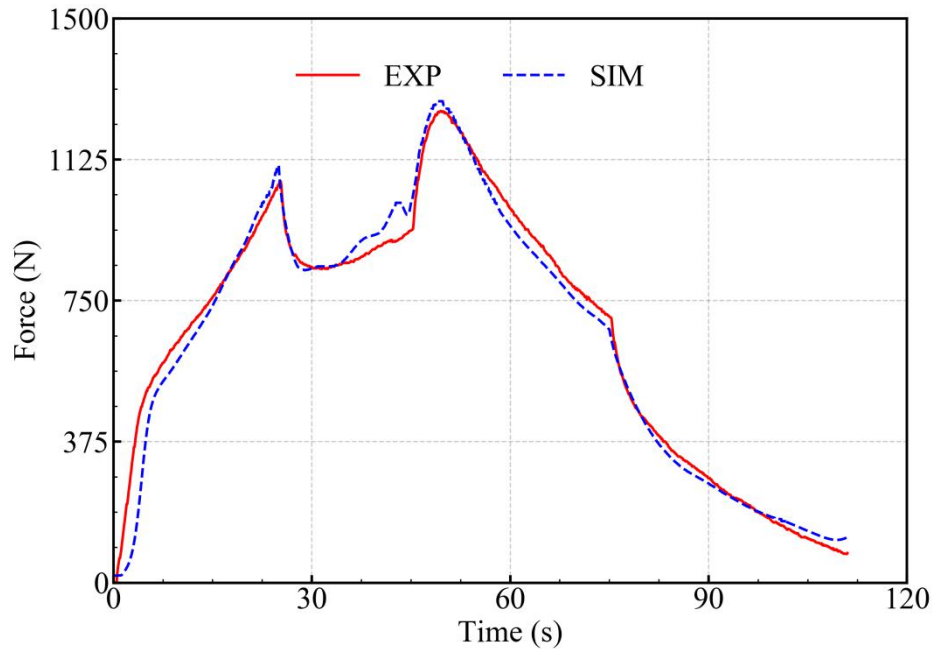


Fig. 4-13 Force comparison with adjusted temperature.

4.7 Chapter Summary

Optimization based on a local strategy is successfully operated on MOOPI, with selected cost function of NMAE. Thanks to the EGO algorithm, the parameters are determined by minimizing the NMAE. The parameters are found close to the values by others' work. Although the parameters are optimized by minimizing a cost function built merely by force, the deformation fields from calculation by the optimized parameters are quite close to the experimental ones, which indicate the rheological law is properly selected and characterized. From the analysis of the correlation of parameters, it is found that the sensitivity analysis of parameters in a rheological law is quite important before determination.

Chapter Reference

100 Buljak, V., 2011. *Inverse analyses with model reduction: proper orthogonal decomposition in structural mechanics*. Springer Science & Business Media.

101 Roux, É., Tillier, Y., Kraria, S. and Bouchard, P.O., 2020. An efficient parallel global optimization strategy based on Kriging properties suitable for material parameters identification. *Archive of Mechanical Engineering*, 67.

102 Koziel, S. and Yang, X.S. eds., 2011. *Computational optimization, methods and algorithms* (Vol. 356). Springer.

103 Dai, Y.H., 2013. A perfect example for the BFGS method. *Mathematical Programming*, 138(1), pp.501-530.

104 Jones DR, Schonlau M, Welch WJ. Efficient global optimization of expensive black-box functions. *Journal of Global optimization*. 1998 Dec 1;13(4):455-92.

105 Haftka, R.T., Villanueva, D. and Chaudhuri, A., 2016. Parallel surrogate-assisted global optimization with expensive functions—a survey. *Structural and Multidisciplinary Optimization*, 54(1), pp.3-13.

106 Jachner, S., Van Den Boogaart, K.G. and Petzoldt, T., 2007. Statistical methods for the qualitative assessment of dynamic models with time delay (R Package qualV).

107 Janik, M., Bossew, P. and Kurihara, O., 2018. Machine learning methods as a tool to analyse incomplete or irregularly sampled radon time series data. *Science of The Total Environment*, 630, pp.1155-1167.

108 Pautrat, A., 2013. Étude expérimentale quantitative de la solidification de l'inconel 718 en fonderie (*Doctoral dissertation*, Paris, ENMP).

109 Chen, W. and Chaturvedi, M.C., 1994. The effect of grain boundary precipitates on the creep behavior of Inconel 718. *Materials Science and Engineering: A*, 183(1-2), pp.81-89.

110 Han, Y. and Chaturvedi, M.C., 1987. Steady state creep deformation of superalloy inconel 718. *Materials Science and Engineering*, 89, pp.25-33.

111 Newell, D.J., 2020. Solution Anneal Heat Treatment to Enhance Mechanical Performance of Additively Manufactured IN718. AIR FORCE INSTITUTE OF TECHNOLOGY WRIGHT-PATTERSON AFB OH WRIGHT-PATTERSON AFB United States. (Fig. 2.3), *Ph.D thesis*.

112 James, W.F., 1985. Mechanical properties of Inconel 718 and Nickel 201 alloys after thermal histories simulating brazing and high temperature service (No. NASA-CR-177940, 19860001845), *NASA contractor report*.

113 Caliari, F.R., Candioto, K.C., Reis, D.A., Couto, A.A., de Moura Neto, C. and Nunes, C.A., 2011. Study of the mechanical behavior of an inconel 718 aged superalloy submitted to hot tensile tests (No. 2011-36-0328). *SAE Technical Paper*.

114 Zhang, P., Hu, C., Ding, C.G., Zhu, Q. and Qin, H.Y., 2015. Plastic deformation behavior and processing maps of a Ni-based superalloy. *Materials & Design* (1980-2015), 65, pp.575-584.

115 Liu, Y., Ning, Y., Yao, Z., Guo, H. and Nan, Y., 2014. Effect of true strains on processing map for isothermal compression of Ni–20.0 Cr–2.5 Ti–1.5 Nb–1.0 Al Ni-base superalloy. *Journal of alloys and compounds*, 612, pp.56-63.

116 Nicolaÿ, A., Fiorucci, G., Franchet, J.M., Cormier, J. and Bozzolo, N., 2019. Influence of strain rate on subsolvus dynamic and post-dynamic recrystallization kinetics of Inconel 718. *Acta Materialia*, 174, pp.406-417.

Chapter 5 Probe into Anisotropy

Résumé

Les éprouvettes préparées par le procédé LPBF ont différentes orientations, et ces orientations entraînent en anisotropie. Dans ce chapitre, deux stratégies (directe et inverse) pour identifier les paramètres de Hill48 sont introduites. La stratégie directe ne fonctionne pas bien. Lorsqu'elle passe à la stratégie inverse, une fonction de coût développée composée de trois éléments, c'est-à-dire la force, la déformation et le coefficient de Lankford, est étudiée. On constate qu'en modifiant les poids des trois éléments, les résultats d'optimisation présentent des variations évidentes. Compte tenu de tous les facteurs, nous avons les résultats d'optimisation finaux, dans lesquels les paramètres liés à l'anisotropie et ceux liés au modèle constitutif sont obtenus via la méthode d'optimisation alternée. L'anisotropie se trouve évoluer avec la température, et la raison possible de l'évolution est analysée à la fin de ce chapitre.

Chapter Introduction

In Chapter 4 the optimization was carried out on the vertical built sample, i.e. O1 in Fig. 5-1. In this chapter all the 5 groups of samples of various orientations are studied.

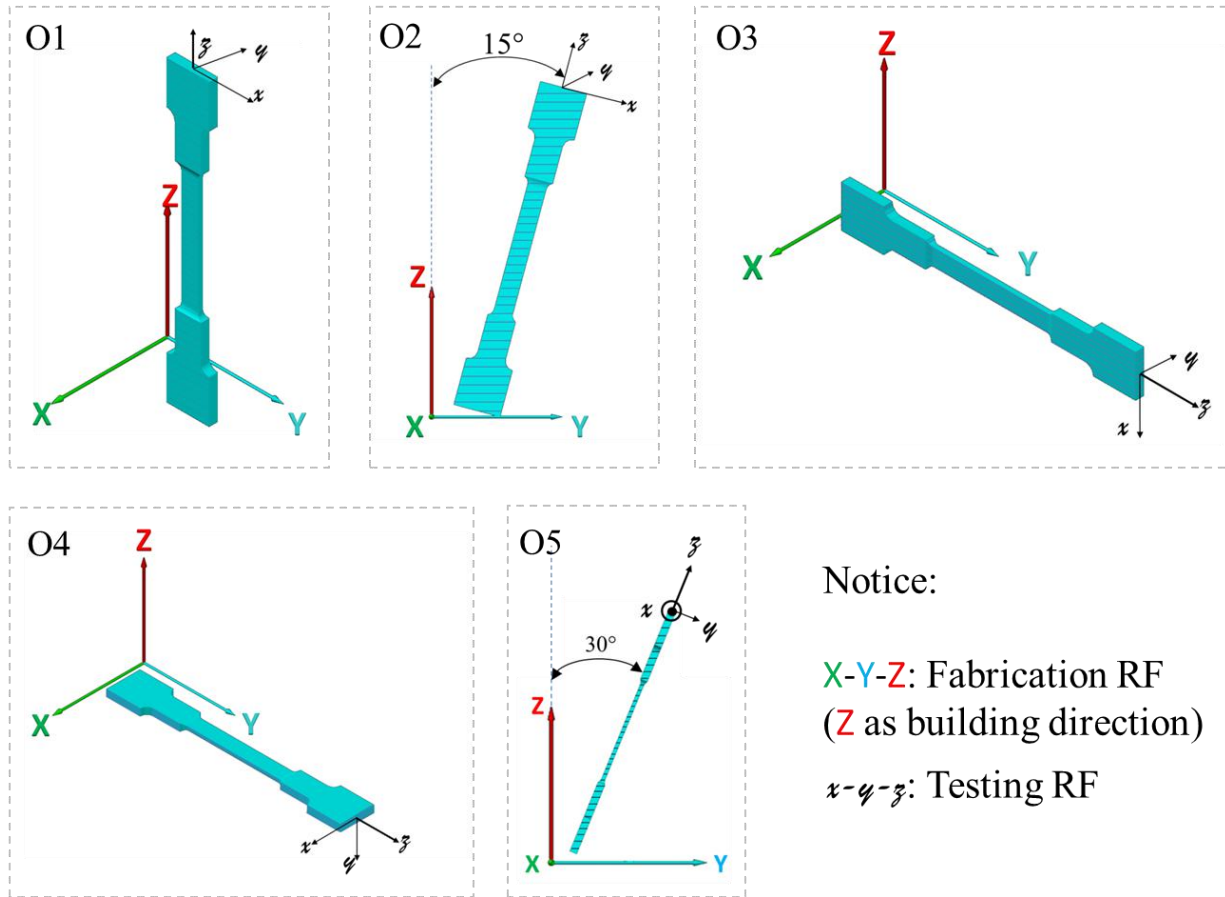


Fig. 5-1 Orientations of the LPBF processed samples mentioned in Table 7. Chapter 4 is based on O1.

The orientations are selected on the possibility of LPBF processing. The main difference is the angle between the building direction (in red arrow with upper-case Z) and the tensile direction of the sample (in black with lower-case z). The reference frame of the colorful upper-case is defined as the RF^M , where M indicates the material, and the black lower-case is defined as the RF^{exp} , where exp indicates the experimental reference frame (Cf Section 3.6.1.1).

With the same optimization method as stated in Chapter 4, 4 additional groups of samples built with different orientations were also tested, and the optimized results based on the von Mises hypothesis are as follows in Table 7 (Noticing, the $T_{ref} = 800^\circ\text{C}$ is used throughout this chapter). The comparison between optimized force and simulated force within each orientation is given in Appendix A. 10. Because the optimizations were done within each orientation, it is thus reasonable to consider that the optimum optimization results on Hill's condition crossing orientations cannot go beyond those inside-orientation optimizations.

Table 7 Optimized parameters based on von Mises hypothesis

Parameter (Unit)	Orientation1	Orientation2	Orientation3	Orientation4	Orientation5
$\sigma_{Y,ref}$ (MPa)	107	126	82	77	80
$Q_{r,ref}$ (MPa)	83	109	50	94	110
b	367	342	116	489	275
Q_1 (kJ·mol ⁻¹)	157	140	145	175	166
k_{ref} (MPa)	1118	1406	1126	1221	1237
m	0.252	0.338	0.223	0.260	0.257
Q_2 (kJ·mol ⁻¹)	77	61	71	60	82

From Table 7 one can get the following information:

- The values of m , k_{ref} , Q_1 , and Q_2 are rather close in all orientations
- The values of $(\sigma_{Y,ref} + Q_{r,ref})$ are quite different in different orientations
- The value of b seems to vary a lot, but it cannot be well identified (Cf Section 4.5.3.2).

It is interesting to find that there is surely anisotropy in this material prepared by LPBF processing, which is revealed by the values of $(\sigma_{Y,ref} + Q_{r,ref})$. This difference is expected to be explained by adjusting the Hill's parameters (F, G, H, L, M, N), which define the anisotropy.

In this chapter, the way to determine the Hill's parameters is introduced. It consists of direct and inverse strategies. In the direct strategy, only the Lankford method (i.e. deformation information) is used to identify the Hill's parameters. In the inverse strategy, both force and deformation are used during the identification of the Hill's parameters. Then, the possible reason for the evolution of anisotropy is analyzed. (In this chapter, $\bar{\epsilon}$ and $\bar{\epsilon}$ are used instead of $\dot{\kappa}$ and κ in the sake of convenience)

5.1 Orientation of the Material

The grain orientations of the as-built samples were examined by EBSD, and the typical orientation 1 and 5 are given in Fig. 5-2, where the surfaces in shadow are the ones examined. The EBSD maps were taken on the centers of the indicated shadowed surfaces. Notice that the $x - y$ coordinate systems marked in this figure are intended for indicating the EBSD map orientations.

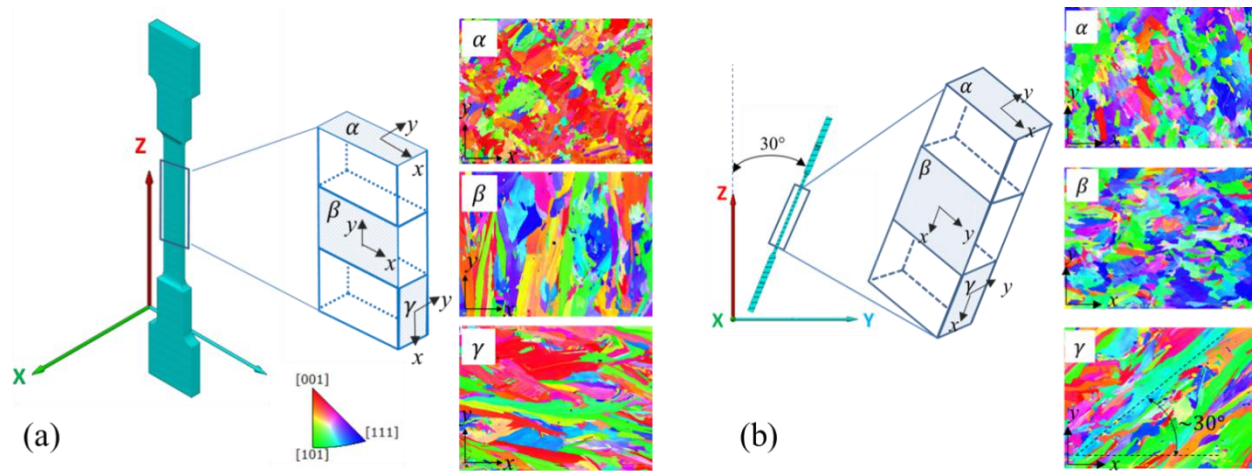


Fig. 5-2 Grain orientations of the as-built sample of (a): O1 and (b): O5

From the above figure, two observations can be found:

- There is a preference tied orientation of grains, which is along the local temperature gradient, and
- The structure presents a transverse symmetry whose axis is along the building direction.

In other words, the material is expected to behave in a transverse isotropy mode around the build direction. The following work is based on this transverse isotropy assumption.

5.2 Two Strategies to Calculate Hill48 Parameters

Basically there are two strategies to calculate the Hill48 parameters, which are the direct strategy and the inverse strategy. In the following sections these two strategies will be introduced.

5.2.1 Direct Strategy

In the direct strategy, two sub-routines are available, which are the Lankford coefficient method (r method) and the yield stress method (σ method). In r method the relations between r value and Hill's parameters are found, similarly in the σ method. They are given in the following sections.

5.2.1.1 r Method

Supposing the unit vector of X axis, Y axis (i.e. the scanning directions) and the Z axis (i.e. building direction) of material reference frame (RF^M) are expressed as $\mathbf{e}_X = (l_1, m_1, n_1)^T$, $\mathbf{e}_Y = (l_2, m_2, n_2)^T$ and $\mathbf{e}_Z = (l_3, m_3, n_3)^T$ in RF^{exp} ($\equiv RF^{sim}$) of xyz , then we consider the matrix \mathbf{M} , composed as:

$$\begin{cases} \mathbf{M} & = [\mathbf{e}_X \ \mathbf{e}_Y \ \mathbf{e}_Z] \\ \mathbf{M}^{-1} = \mathbf{M}^T & = [\mathbf{e}_X \ \mathbf{e}_Y \ \mathbf{e}_Z]^T \end{cases} \quad (5-1)$$

For any vector \mathbf{u} , the following relation is met:

$$\begin{cases} \mathbf{u}|_{xyz} & = \mathbf{M}\mathbf{u}|_{XYZ} \\ \mathbf{u}|_{XYZ} & = \mathbf{M}^T\mathbf{u}|_{xyz} = \mathbf{M}^{-1}\mathbf{u}|_{xyz} \end{cases} \quad (5-2)$$

The theoretical viscoplastic Lankford coefficient defined by the plastic strain rate in RF^{exp} is defined as:

$$r^{theo, vp} = \frac{\dot{\varepsilon}_{xx}^{vp}}{\dot{\varepsilon}_{yy}^{vp}} \quad (5-3)$$

where $\dot{\varepsilon}_{xx}^{vp}$ and $\dot{\varepsilon}_{yy}^{vp}$ are the strain rate component in width direction and thickness direction, respectively. See Fig. 5-1 for checking the RF^{exp} .

To express $r^{theo, vp}$, a constitutive model (EVP) based on Hill48 criterion can be directly used when the testing reference frame and material reference frame are in coincidence. When they are not in this condition, a linear transformation should be done, as shown in Eq. 5-4.

$$\boldsymbol{\sigma}|_{xyz} \xrightarrow{\mathbf{M}^{-1}\boldsymbol{\sigma}|_{xyz}\mathbf{M}} \boldsymbol{\sigma}|_{XYZ} \xrightarrow{\text{Hill48}} \boldsymbol{\varepsilon}^{vp}|_{XYZ} \xrightarrow{\mathbf{M}\boldsymbol{\varepsilon}^{vp}|_{XYZ}\mathbf{M}^{-1}} \boldsymbol{\varepsilon}^{vp}|_{xyz} \rightarrow r^{theo, vp} = \frac{\dot{\varepsilon}_{xx}^{vp}}{\dot{\varepsilon}_{yy}^{vp}} \quad (5-4)$$

The stress tensor in RF^{exp} should be transformed into RF^M , and in RF^M the strain rate is calculated, and finally this strain rate is transformed back to RF^{exp} to calculate Lankford coefficient. In RF^{exp} , the stress tensor can be considered as uniaxial along z direction, at least for small deformation before necking develops:

$$\boldsymbol{\sigma}|_{xyz} = \begin{bmatrix} 0 & 0 & 0 \\ 0 & 0 & 0 \\ 0 & 0 & \sigma_{zz} \end{bmatrix} \quad (5-5)$$

After calculation we obtain:

$$\boldsymbol{\sigma}|_{XYZ} = \mathbf{M}^{-1}\boldsymbol{\sigma}|_{xyz}\mathbf{M} = \sigma_{zz} \begin{bmatrix} n_1^2 & n_1n_2 & n_1n_3 \\ n_2n_1 & n_2^2 & n_2n_3 \\ n_3n_1 & n_3n_2 & n_3^2 \end{bmatrix} \quad (5-6)$$

The plasticity criterion is written as:

$$f(\boldsymbol{\sigma}) = \bar{\sigma} - \sigma_0 \quad (5-7)$$

where, taking Hill48 as the criterion, the equivalent stress $\bar{\sigma}$ may be defined as (quite generally, not taking into account the transverse isotropy yet):

$$\bar{\sigma} = \sqrt{F(\sigma_{YY} - \sigma_{ZZ})^2 + G(\sigma_{ZZ} - \sigma_{XX})^2 + H(\sigma_{XX} - \sigma_{YY})^2 + 2L\sigma_{YZ}^2 + 2M\sigma_{ZX}^2 + 2N\sigma_{XY}^2} \quad (5-8)$$

There are 7 parameters in this expression, i.e. the F, G, H, L, M, N and σ_0 . During an elastic-viscoplastic deformation, we calculate the visco-plastic strain rate tensor as (Cf Section 3.3.1):

$$\begin{aligned} \dot{\boldsymbol{\epsilon}}^{vp}|_{XYZ} &= \frac{\partial \Psi}{\partial \boldsymbol{\sigma}}|_{XYZ} = \frac{\partial \Psi}{\partial \bar{\sigma}} \frac{\partial \bar{\sigma}}{\partial \boldsymbol{\sigma}}|_{XYZ} = \frac{\dot{\bar{\sigma}}}{\bar{\sigma}} \frac{\partial \bar{\sigma}}{\partial \boldsymbol{\sigma}}|_{XYZ} \\ &= \frac{\dot{\bar{\sigma}}}{\bar{\sigma}} \begin{bmatrix} H(\sigma_{XX} - \sigma_{YY}) + G(\sigma_{XX} - \sigma_{ZZ}) & N\sigma_{XY} & M\sigma_{ZX} \\ N\sigma_{XY} & F(\sigma_{YY} - \sigma_{ZZ}) + H(\sigma_{YY} - \sigma_{XX}) & L\sigma_{YZ} \\ M\sigma_{ZX} & L\sigma_{YZ} & G(\sigma_{ZZ} - \sigma_{XX}) + F(\sigma_{ZZ} - \sigma_{YY}) \end{bmatrix} \end{aligned} \quad (5-9)$$

where $\dot{\bar{\sigma}}$ is the anisotropic equivalent strain rate (not explicitly detailed here), see Eqs. 3-48 and 4-6. Injecting Eq. 5-6 into Eq. 5-9, we further get:

$$\dot{\boldsymbol{\epsilon}}^{vp}|_{XYZ} = \frac{\dot{\bar{\sigma}}}{\bar{\sigma}} \sigma_{zz} \begin{bmatrix} G(n_1^2 - n_3^2) + H(n_1^2 - n_2^2) & Nn_1n_2 & Mn_1n_3 \\ Nn_2n_1 & F(n_2^2 - n_3^2) + H(n_2^2 - n_1^2) & Ln_2n_3 \\ Mn_3n_1 & Ln_3n_2 & F(n_3^2 - n_2^2) + G(n_3^2 - n_1^2) \end{bmatrix} = \frac{\dot{\bar{\sigma}}}{\bar{\sigma}} \sigma_{zz} \mathbf{S} \quad (5-10)$$

Then with:

$$\dot{\boldsymbol{\epsilon}}^{vp}|_{xyz} = \mathbf{M} \dot{\boldsymbol{\epsilon}}^{vp}|_{XYZ} \mathbf{M}^{-1} = \frac{\dot{\bar{\sigma}}}{\bar{\sigma}} \sigma_{zz} \mathbf{B} \quad (5-11)$$

with $\mathbf{B} = \mathbf{M} \mathbf{S} \mathbf{M}^{-1}$

The theoretical viscoplastic Lankford coefficient of Eq. 5-3 can be expressed by components of \mathbf{B} as:

$$r^{theo,vp} = \frac{\dot{\epsilon}_{xx}^{vp}}{\dot{\epsilon}_{yy}^{vp}} = \frac{B_{xx}}{B_{yy}} \quad (5-12)$$

where:

$$B_{xx} = (l_2^2 - l_3^2)(n_2^2 - n_3^2)F + (l_1^2 - l_3^2)(n_1^2 - n_3^2)G + (l_1^2 - l_2^2)(n_1^2 - n_2^2)H \\ + 2l_3l_2n_2n_3L + 2l_1l_3n_1n_3M + 2l_1l_2n_1n_2N \quad (5-13)$$

$$B_{yy} = (m_2^2 - m_3^2)(n_2^2 - n_3^2)F + (m_1^2 - m_3^2)(n_1^2 - n_3^2)G + (m_1^2 - m_2^2)(n_1^2 - n_2^2)H \\ + 2m_2n_2m_3n_3L + 2m_3m_1n_3n_1M + 2m_2m_1n_2n_1N \quad (5-14)$$

Consider now transverse isotropy around the building direction (Z axis), we have the following relations:

$$\begin{cases} F & = & G \\ L & = & M \\ F + 2H & = & N \end{cases} \quad (5-15)$$

The first two equations are quite obvious. The demonstration of $F + 2H = N$ is given in Appendix A. 14. So the final expression of the Lankford Coefficient only depends on F , H and L . We write it in the form:

$$r^{theo,vp} = r^{theo,vp}(F, H, L, \mathbf{e}_X, \mathbf{e}_Y, \mathbf{e}_Z) \quad (5-16)$$

One can prove that with the relation of Eq. 5-15, $r^{theo,vp}$ in Eq. 5-16 is no longer \mathbf{e}_X and \mathbf{e}_Y dependent, i.e.:

$$r^{theo,vp} = r^{theo,vp}(F, H, L, \mathbf{e}_Z) \quad (5-17)$$

Based on the expression of Eq. 5-17, given the orientation of \mathbf{e}_Z , the $r^{theo,vp}$ in this orientation $r_{\mathbf{e}_Z}^{theo,vp}$ can be calculated. In this project the orientation number is bigger than the unknown (i.e. F , H and L) number, so the method of least squares is taken. For any test i with $\mathbf{e}_{Z,i}$, define argument:

$$arg_r := \sum_i \left[r_{\mathbf{e}_{Z,i}}^{theo,vp} - r_{\mathbf{e}_{Z,i}}^{exp} \right]^2 = \sum_i \left[\frac{B_{i,xx}}{B_{i,yy}} - r_{\mathbf{e}_{Z,i}}^{exp} \right]^2 \quad (5-18)$$

where $r_{e_{z,i}}^{exp}$ is the Lankford coefficient that measured during the experimental test. The Eq. 5-18 can be resolved by minimization, which will result in a homogeneous equation set. So the final relation of the F , H and L will be in the form of:

$$\begin{bmatrix} F \\ H \\ L \end{bmatrix} = \begin{bmatrix} f \\ h \\ 1 \end{bmatrix} L \quad (5-19)$$

where f and h are the solutions gotten from the homogeneous equation set from Eq. 5-18.

5.2.1.2 σ Method

Let's have a look at the yield point of any test:

$$f(\boldsymbol{\sigma}) = \bar{\sigma} - \sigma_0 = 0 \quad (5-20)$$

i.e.

$$\bar{\sigma}^2 = \sigma_0^2 \quad (5-21)$$

Thus for any test i with orientation e_z , if the uniaxial tensile test returns the yield stress as $\sigma_{zz,i}^{exp}$, the $\bar{\sigma}^2$ can be expressed as:

$$\begin{aligned} \bar{\sigma}_i^2 = & (F(n_2^2 - n_3^2)^2 + G(n_3^2 - n_1^2)^2 + H(n_1^2 - n_2^2)^2 \\ & + 2L(n_2n_3)^2 + 2M(n_1n_3)^2 + 2N(n_1n_2)^2) \sigma_{zz,i}^{exp2} \end{aligned} \quad (5-22)$$

Define an argument of least square to minimize:

$$arg_{\sigma} := \sum_i (\bar{\sigma}_i^{exp2} - \sigma_0^2)^2 \quad (5-23)$$

With constrain of transverse isotropy by Eqs. 5-15, resolve this minimization problem of Eq. 5-23, finally one can get the solution in the following form:

$$\begin{cases} F = k_f \cdot \sigma_0^2 \\ H = k_h \cdot \sigma_0^2 \\ L = k_l \cdot \sigma_0^2 \end{cases} \quad (5-24)$$

where k_f , k_h , and k_l are definitive values, and σ_0^2 is an unknown which can be any positive value. One can assign $L = 1.5$ to calculate all the values of F , H and σ_0 .

5.2.2 Inverse Strategy

In the direct strategy, the Hill's parameters are determined by analytical method, and they are then used as input in the simulations. One problem is that the model is not perfect, and the Hill's parameters calculated by the r method could result in bad simulation output for force, and vice versa [117]. Thus, the inverse strategy is brought up as follows.

From Eqs. in 5-19 and 5-24 one can see that only two independent parameters are found when L is fixed (in our project, $L = 1.5$ is always used hereafter). Immediately it can be seen that one can cast the Hill's parameters in the following relations:

$$\left\{ \begin{array}{l} F = G = fL \\ H = hL \\ N = F + 2H = (f + 2h)L \\ M = L = 1.5 \end{array} \right. \quad (5-25)$$

Then, the parameter vector \mathbf{p} for optimization aforementioned in Section 4.2 is extended with new components f and h . By minimizing the cost function, the anisotropy parameters f and h can be found.

5.3 On Direct Strategy

Firstly, the Hill's parameters are calculated by r method, and then the calculated values are applied as preset ones in FEM simulation to run the optimization for the characterization of the rheological law and then check the force response.

5.3.1 Determination of Hill's Parameters at 1100°C by r Method

In previous section two ways are introduced to calculate the Hill's parameters directly. From Fig. 4-10 in last chapter one can immediately see that the initial yield strength is hard to measure. Thus, the r method is the only way for the determination of Hill's parameters directly for our work at high temperature. But one can use the σ method at room temperature as in reference when the initial yield strength can be easily found [117].

Based on the orientation as shown in Fig. 5-1, one can calculate the theoretical viscoplastic Lankford coefficients ($r^{theo, vp}$), which are given in the third column in Table 8. As a comparison, the averaged experimental Lankford coefficients (\bar{r}^{exp}) are also given in this table, while the way to calculate this \bar{r}^{exp} is detailed in Appendix A. 11.

Table 8 Averaged experimental Lankford coefficients at various temperature levels v.s. theoretical viscoplastic Lankford coefficient expressions for the 5 orientations (refer to A. 11 for detail)

Orientation	\bar{r}^{exp}				$r^{theo, vp}$
	800°C	900°C	1000°C	1100°C	
O1	1.28	1.44	0.89	0.95	1
O2	1.22	1.16	1.2	1.17	$\frac{-0.6875F + 0.0625H - 0.125L}{-0.9330F - 0.0670H}$
O3	1.55	1.27	0.81	0.67	$\frac{F}{H}$
O4	0.65	0.89	1.11	1.29	$\frac{H}{F}$
O5	1.81	1.36	0.75	0.71	$\frac{-0.75F - 0.25H}{-0.0625F + 0.1875H - 0.375L}$

From Table 8 it can be observed the following information:

- For O3 and O4, the product $r_{O3}^{theo, vp} \cdot r_{O4}^{theo, vp} \equiv 1$, and for all temperature levels, the product $\bar{r}_{O3}^{exp} \cdot \bar{r}_{O4}^{exp}$ is found close to 1.
- For O1, the $r_{O1}^{theo, vp} \equiv 1$, which is only observed in experiment at 1100°C level.
- For O3, O4 and O5, there is an obvious temperature dependence, while this dependence is not so obvious in O2, and in O1 it is not so “regular”.

Noticing that the experimental results at 1100°C are in consistence of theoretical analysis, the instant and probably the only choice to use this direct strategy focus on this T level, because the other cases are quite far away from the theoretical value when we look at O1 (in which

$$r^{theo, vp} \equiv 1 \approx 0.95 = \bar{r}^{exp}).$$

By Eqs. 5-15 and 5-18, letting $r_{e_z, i}^{exp} = \bar{r}_{e_z, i}^{exp}$, together with information from Table 8, the independent relations between Hill’s parameters are:

$$\begin{cases} F = 0.217L \\ H = 0.285L \\ L = 1.5 \end{cases} \quad (5-26)$$

The next step is to use those Hill's parameters as preset values to optimize the rheological law by inverse method.

As stated in section 4.4.1, an adjustment of Young's module is adopted for the direct simulation during the identification because of the orientations of the samples. In this chapter, the Young's modulus in each orientation is also adjusted, while the method and values are given in Appendix A. 12. One can see that the elasticity behaves in a close-to transverse isotropic condition from the appendix.

5.3.2 Characterization of Rheological Law on Preset Hill's Parameters

Based on the calculated Hill's parameters in the last section, one optimization of the parameters of the rheological law based on all 5 orientations and 1100°C level is carried out with the boundaries shown in Table 9. It is worth noticing that the boundary for each parameter in Table 9 covers the range of the corresponding optimized parameter at individual case shown in Table 7. The optimization is based on force only.

Table 9 Boundaries of parameters and optimized values based on preset Hill's parameters at 1100°C

Parameter (Unit)	Boundaries		
	Minimum	Maximum	Optimized
$\sigma_{Y,ref}$ (MPa)	60	130	67
$Q_{r,ref}$ (MPa)	45	130	58
b	100	500	395
Q_1 (kJ·mol ⁻¹)	140	180	163
k_{ref} (MPa)	765	1469	1195
m	0.18	0.35	0.245
Q_2 (kJ·mol ⁻¹)	55	85	85

With the optimized parameters, the simulated and experimental force information is given in Fig. 5-3. It is interesting to find that with the preset Hill's parameters, the 5 calculated r coefficients are quite close to the experimental ones, but unluckily the 5 force evolutions are quite far away from "satisfactory". Based on the transverse isotropy, O3 and O4 are supposed to have the similar force response, and this is found in Fig. 5-3: one can see that simulated force in either O3 or O4 is much farther away than the other 3 orientations. And another judgement is when compared with the

corresponding force information in Fig. 7-19, the difference is obvious. This indicates that the optimization routine with pre-set Hills parameters is not a good choice.

From the literature it is seen that this kind of disharmony between force and deformation can be resolved by introducing the non-associated law [117,118,119]. However, in our work the non-associated law is not considered (because of lack of time).

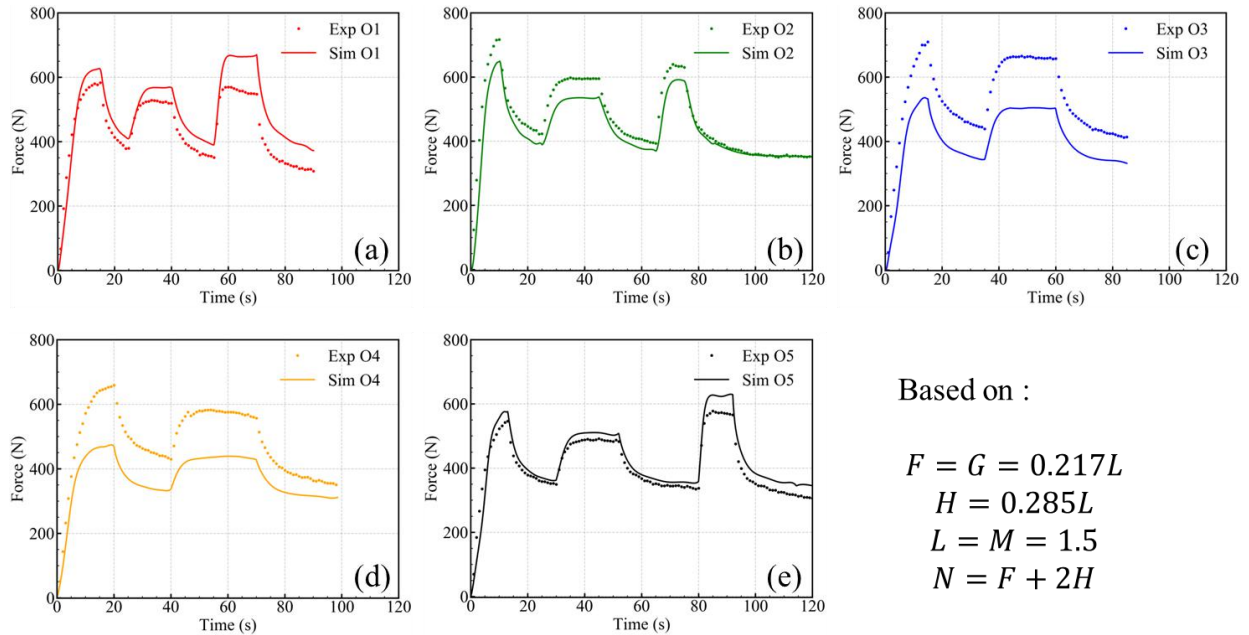


Fig. 5-3 Force comparison between experimental and simulated values for the 5 orientations at T level of 1100°C with pre-set Hill's parameters

Because Hill's parameters are not easily determined by force based on σ method, and the values calculated by Lankford coefficient method do not work well for force, it is reasonable to shift to the inverse strategy.

5.4 On Inverse Strategy

Firstly an alternated optimization method is introduced, and then optimization of the parameters containing rheological law and Hill48 criterion is given.

5.4.1 Alternated Optimization Method

In our optimization work the parameters are organized in vector \mathbf{p} , and MOOPI will update these parameter values in the parameter space. There are 7 parameters in the rheological law (see Table 7), and 2 additional ones in Hill48 (i.e. f and h in Eq. 5-25), so in total 9 parameters. As is known from the EGO algorithm, the initial database is supposed to have parameter points equal or greater than 2^p , where p is the parameter number, or the dimension of the parameter space. It is now

seen that for each experiment, at least 512 direct simulations are needed for initialization. Given 20 experiments in total, the direct simulation will be a very, very heavy task.

In order to avoid this heavy initialization, an alternated optimization method is applied based on the EGO algorithm. In this alternated optimization, the parameters to be optimized are grouped into 2 or more sub-groups. In our project two sub-groups are selected, so \mathbf{p} is divided into \mathbf{p}_1 and \mathbf{p}_2 , and the dimension of \mathbf{p}_1 and \mathbf{p}_2 should be close so that the initialization size can be efficiently reduced. $\mathbf{p}_1^T = [f, h, \sigma_{Y,ref}, Q_{r,ref}, b]$ and $\mathbf{p}_2^T = [k_{ref}, m, Q_1, Q_2]$ are chosen, because \mathbf{p}_1 can be deemed as parameters controlling anisotropy and strain hardening, and \mathbf{p}_2 deemed as the ones controlling viscoplasticity and thermal softening. The way to conduct this alternated optimization is as follows:

- Step 1, optimize the parameters of \mathbf{p}_1 with pre-set reasonable \mathbf{p}_2
- Step 2, optimize the parameters of \mathbf{p}_2 with pre-set \mathbf{p}_1 gotten from Step 1
- Step 3, optimize the parameters of \mathbf{p}_1 with pre-set \mathbf{p}_2 gotten from Step 2
- Step 4, optimize the parameters of \mathbf{p}_2 with pre-set \mathbf{p}_1 gotten from Step 3
- And going on...

For each of the steps, the boundaries for the parameters should be adjusted. After several steps, the optical values of \mathbf{p} by \mathbf{p}_1 and \mathbf{p}_2 are obtained.

5.4.2 Cost Function by Both Force and Deformation

The notation in this section has no relation with Hill's criterion.

As previously shown in Eq. 4-4 (a), only force was used in building the cost function. Here a cost function composed both force and deformation is introduced based on NMAE, given in Eq. 5-27.

$$f_c = \sum_{i=0}^{N-1} \omega_i \cdot (\alpha_i \cdot A_i + \gamma_i \cdot C_i) \quad (5-27)$$

where:

- N is the total test number, and each test having an identity number i ($i = 0, 1, \dots, N - 1$), and an assigned weight ω_i . The test weights are such that $\sum_{i=0}^{N-1} \omega_i \equiv 1$. (Notice that the sum of unity is not mandatory, but the ratios between ω_i)
- For each laboratory test i , the load information in the i^{th} test has a weight α_i , and the overall deformation information in the i^{th} test has a weight γ_i . In this project their relation is: $\alpha_i + \gamma_i \equiv 1$.

The expressions of A_i and C_i are given in Eq. 5-28.

$$\begin{cases} A_i = \frac{\sum_{j=0}^{M_i-1} |F_{ij}^{exp} - F_{ij}^{sim}| \cdot \theta_{ij}}{\sum_{j=0}^{M_i-1} |F_{ij}^{exp}| \cdot \theta_{ij}} & \dots \quad (a) \\ C_i = \frac{1}{2} \left(\frac{\sum_{j=0}^{M_i-1} |\varepsilon_{xx}^{exp} - \varepsilon_{xx}^{sim}| \cdot \theta_{ij}}{\sum_{j=0}^{M_i-1} |\varepsilon_{xx}^{exp}| \cdot \theta_{ij}} + \frac{\sum_{j=0}^{M_i-1} |\varepsilon_{zz}^{exp} - \varepsilon_{zz}^{sim}| \cdot \theta_{ij}}{\sum_{j=0}^{M_i-1} |\varepsilon_{zz}^{exp}| \cdot \theta_{ij}} \right) & \dots \quad (b) \end{cases} \quad (5-28)$$

where F_{ij}^{exp} and F_{ij}^{sim} are the force value at j^{th} sampling instant in i^{th} test from experiment and simulation, respectively, M_i is the total sampling instants in the i^{th} test, ε_{zz}^{exp} and ε_{xx}^{exp} are deformation component information from the sensor selected at the sample center at the j^{th} sampling instant in the i^{th} test from experiment, and ε_{zz}^{sim} and ε_{xx}^{sim} are from the projected sensor in the corresponding simulations. The temporal weight θ_{ij} with the same expression as in Eq. 4-3 is used. In the i^{th} test, the load is global information; see Eq. 5-28 (a). But the deformation information has two experimentally measured components (ε_{zz} and ε_{xx}), and they are of equal importance. That is why there is $\frac{1}{2}$ in right part of Eq. 5-28 (b).

The cost function parameters are $N = 20$, $\omega_i = 0.05$, $\alpha_i = \beta_i = 0.5$, i.e. the experiments are equally considered, and the deformation and the force within each test have the same weight.

5.4.3 On Inverse Strategy at All Temperature Levels and All Orientations

From Table 8, if the method of least squares is whatever used to calculate the values of f and h at each temperature level on O2~O5, one can get Fig. 5-4.

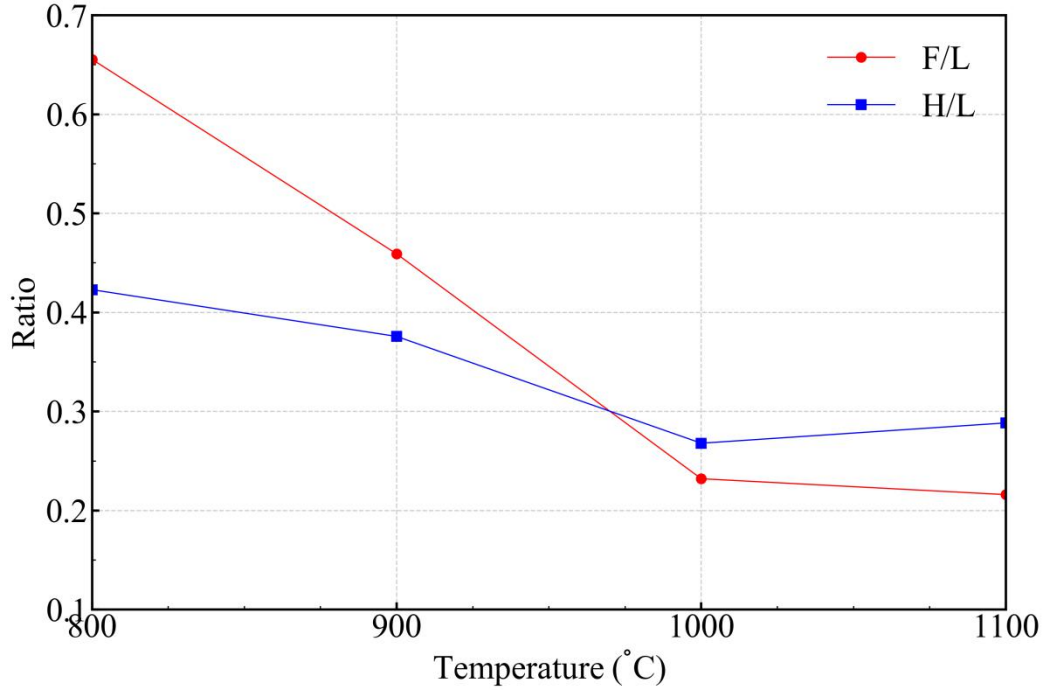


Fig. 5-4 Evolution of f and h calculated from least square method by $r^{theo,vp}$ and \bar{r}^{exp} from Table 8

It can be seen that f and h generally decrease with T . A linear relation or quadratic relation can be used for describing this temperature dependence when considering all the 4 temperature levels. From the side of simplification, linear relation is preferred. Then, considering the crossing of f and h at T_{cross} (at about 950°C), a relation of f and h as function of temperature in unit of K (because of the FEM unit system) is given as:

$$\begin{cases} h = h_0 + h_1 T & \dots (a) \\ f = h_0 + h_1 T_{cross} + f_1 (T - T_{cross}) & \dots (b) \end{cases} \quad (5-29)$$

So the f depends on f_1 and T_{cross} , and h depends on h_0 and h_1 . It is obvious that $0 > h_1 > f_1$, and the parameter array \mathbf{p} is extended to 11 components.

$$\mathbf{p} = [T_{cross}, f_1, h_0, h_1, \sigma_{Y0}, Q_{r0}, b, k, m, Q_1, Q_2]^T \quad (5-30)$$

\mathbf{p} is re-grouped into new sub-vectors $\mathbf{p} = \mathbf{p}_3 + \mathbf{p}_4$, i.e.:

$$\mathbf{p} \rightarrow \begin{cases} \mathbf{p}_3 = [T_{cross}, f_1, h_0, h_1, \sigma_{Y,ref}, Q_{r,ref}]^T \\ \mathbf{p}_4 = [b, k_{ref}, m, Q_1, Q_2]^T \\ L = 1.5 \end{cases} \quad (5-31)$$

This time parameter b is put into vector \mathbf{p}_4 from \mathbf{p}_2 , because the b value is supposed to be in range of (100, 500), where the saturation is fast, thus it has weak influence on anisotropy. The alternated optimization is used to optimized \mathbf{p}_3 and \mathbf{p}_4 .

5.4.4 Optimization Results

In the previous section a crossing relation of f and h is defined. Based on this preset constraint on f and h , with the cost function of Eq. 5-27, the parameters of \mathbf{p} obtained via the alternated optimization given in Table 10

Table 10 Characterized constitutive parameters by minimizing a cost function composed of both force and deformation under transverse anisotropy condition by alternated optimization strategy (underlined parameters are the optimized ones in each column)

Parameters	Step 1 on \mathbf{p}_3	Step 2 on \mathbf{p}_4	Step 3 on \mathbf{p}_3	Step 4 on \mathbf{p}_4
T_{cross} (K)	<u>1243</u>	1243	<u>1243</u>	1243
f_1	<u>-0.0004651</u>	-0.0004651	<u>-0.0005067</u>	-0.0005067
h_0	<u>0.6648</u>	0.6648	<u>0.6248</u>	0.6248
h_1	<u>-0.0003119</u>	-0.0003119	<u>-0.0002860</u>	-0.0002860
$\sigma_{Y,ref}$ (MPa)	<u>64</u>	64	<u>67</u>	67
$Q_{r,ref}$ (MPa)	<u>91</u>	91	<u>84</u>	84
b	418	<u>362</u>	362	<u>399</u>
k_{ref} (MPa)	1673	<u>1771</u>	1771	<u>1626</u>
m	0.2819	<u>0.2844</u>	0.2844	<u>0.2757</u>
Q_1 (kJ·mol ⁻¹)	157.0	<u>151.0</u>	151.0	<u>150.0</u>
Q_2 (kJ·mol ⁻¹)	84.8	<u>90.5</u>	90.5	<u>90.7</u>
min (fc)	0.10606	0.10488	0.10416	0.10407

From Table 10 it can be seen that T_{cross} is unchanged in Step 3 compared with Step 1, because it reaches the maximum boundary. It was observed, but not reported here, that T_{cross} go to higher temperatures, so that f values are always bigger than h values, i.e. no cross of f and h within the studied temperature range. In order to avoid this loss-of-control, the maximum boundary of T_{cross} was fixed at 1243K.

The Lankford coefficients in all simulations based on parameters in Table 10 are given in Table 11. Most of the averaged Lankford coefficients from experiments and simulations are close to each other except the ones underlined.

Table 11 Averaged simulated Lankford coefficient (\bar{r}^{sim}) from simulations with optimized values in Table 10 at all temperature levels, and the averaged experimental Lankford coefficient (\bar{r}^{exp}).

	800°C		900°C		1000°C		1100°C	
	\bar{r}^{exp}	\bar{r}^{sim}	\bar{r}^{exp}	\bar{r}^{sim}	\bar{r}^{exp}	\bar{r}^{sim}	\bar{r}^{exp}	\bar{r}^{sim}
O1	<u>1.28</u>	<u>0.98</u>	<u>1.44</u>	<u>1.02</u>	0.89	0.98	0.95	1.01
O2	<u>1.22</u>	<u>0.93</u>	1.16	1.05	1.20	1.19	1.17	1.26
O3	<u>1.55</u>	<u>1.07</u>	1.27	1.10	0.81	0.98	0.67	0.87
O4	0.65	0.88	0.89	0.91	1.11	1.05	1.29	1.12
O5	<u>1.81</u>	<u>0.89</u>	<u>1.36</u>	<u>0.90</u>	0.75	0.74	0.71	0.62

The reason that the T_{cross} tends to go to higher temperatures can be explained by the “deformation direction”, which is linked to Lankford coefficient. As shown in Fig. 5-5, the expressions of corresponding deformation components are preset as given in Eq. 5-32. One can easily calculate that the area between curves ε_{zz}^- and ε_{zz}^0 , and area between curves ε_{zz}^+ and ε_{zz}^0 are the same, similarly for the curves of ε_{xx}^- , ε_{xx}^0 and ε_{xx}^+ . However, if the averaged Lankford coefficients are calculated, one can see that the difference is quite surprising: $\bar{r}^{--} = 0.96$, $\bar{r}^{00} = 0.67$, and $\bar{r}^{++} = 0.49$. The first sign exponent indicates which ε_{xx} is used, and the second sign exponent indicates which ε_{zz} is used. This example indicates that the deformation-related part in the cost function as expressed in Eq. 5-27 is not adequate to identify anisotropy.

$$\left\{ \begin{array}{l} \varepsilon_{zz}^+ = +0.000110t \\ \varepsilon_{zz}^0 = +0.000100t \\ \varepsilon_{zz}^- = +0.000090t \\ \varepsilon_{xx}^+ = -0.000036t \\ \varepsilon_{xx}^0 = -0.000040t \\ \varepsilon_{xx}^- = -0.000044t \end{array} \right. \quad (5-32)$$

On the other side, if only Lankford coefficient is considered, a similar problem can be encountered. One can calculate $\bar{r}^{-+} = 0.67$, and $\bar{r}^{+-} = 0.67$, while there is a significant difference between the deformation components, as shown in Fig. 5-5.

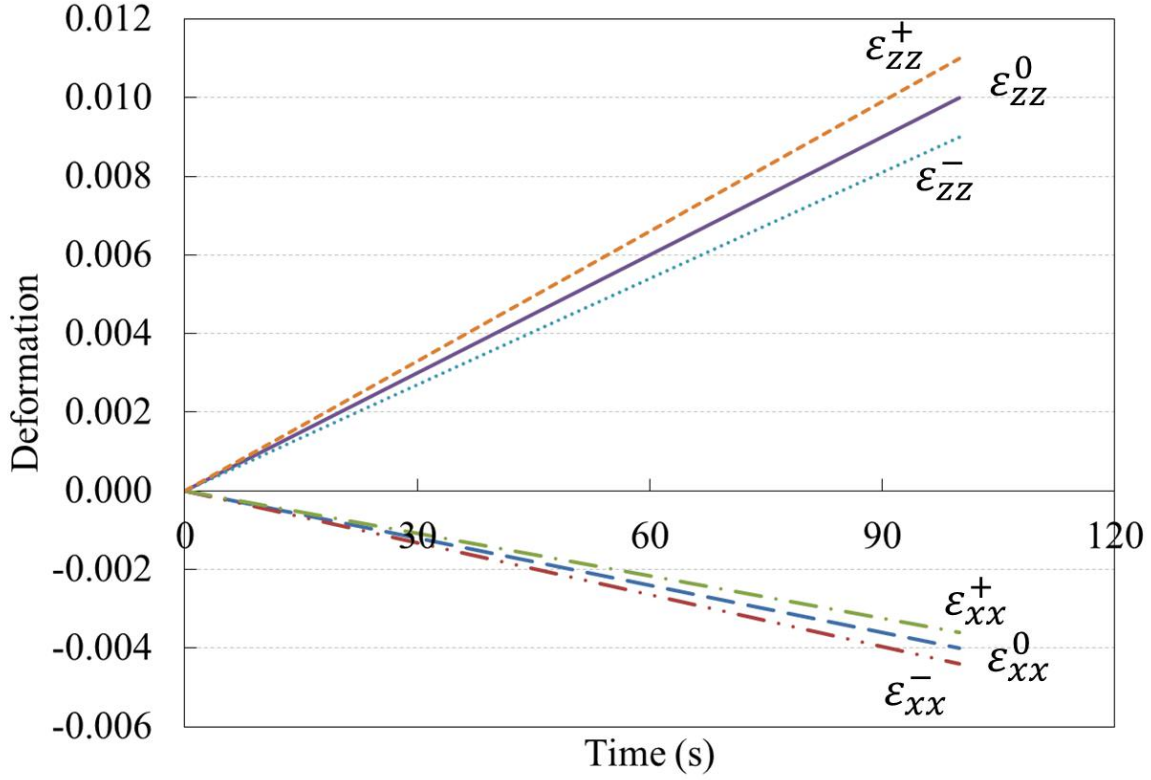


Fig. 5-5 Explanation for direction of deformation difference

Based on the discussion above, it appears natural to introduce a cost function which can avoid those drawbacks. In fact, just an additional part is added in the previous Eq. 5-27 to get Eq. 5-33.

$$\left\{ \begin{array}{l}
 f_c = \sum_{i=0}^{N-1} \omega_i \cdot (\alpha_i \cdot A_i + \beta_i \cdot B_i + \gamma_i \cdot C_i) \quad \dots (a) \\
 A_i = \frac{\sum_{j=0}^{M_i-1} |F_{i,j}^{exp} - F_{i,j}^{sim}| \cdot \theta_{i,j}}{\sum_{j=0}^{M_i-1} |F_{i,j}^{exp}| \cdot \theta_{i,j}} \quad \dots (b) \\
 B_i = \left| \frac{\frac{\sum_{j=0}^{M_i-1} \varepsilon_{xx,i,j}^{exp} \cdot \theta_{i,j}}{-\sum_{j=0}^{M_i-1} \varepsilon_{xx,i,j}^{exp} \cdot \theta_{i,j} - \sum_{j=0}^{M_i-1} \varepsilon_{zz,i,j}^{exp} \cdot \theta_{i,j}} - \frac{\sum_{j=0}^{M_i-1} \varepsilon_{xx,i,j}^{sim} \cdot \theta_{i,j}}{-\sum_{j=0}^{M_i-1} \varepsilon_{xx,i,j}^{sim} \cdot \theta_{i,j} - \sum_{j=0}^{M_i-1} \varepsilon_{zz,i,j}^{sim} \cdot \theta_{i,j}}}{\frac{\sum_{j=0}^{M_i-1} \varepsilon_{xx,i,j}^{exp} \cdot \theta_{i,j}}{-\sum_{j=0}^{M_i-1} \varepsilon_{xx,i,j}^{exp} \cdot \theta_{i,j} - \sum_{j=0}^{M_i-1} \varepsilon_{zz,i,j}^{exp} \cdot \theta_{i,j}}} \right| \quad \dots (c) \\
 C_i = \frac{1}{2} \left(\frac{\sum_{j=0}^{M_i-1} |\varepsilon_{xx,i,j}^{exp} - \varepsilon_{xx,i,j}^{sim}| \cdot \theta_{i,j}}{\sum_{j=0}^{M_i-1} |\varepsilon_{xx,i,j}^{exp}| \cdot \theta_{i,j}} + \frac{\sum_{j=0}^{M_i-1} |\varepsilon_{zz,i,j}^{exp} - \varepsilon_{zz,i,j}^{sim}| \cdot \theta_{i,j}}{\sum_{j=0}^{M_i-1} |\varepsilon_{zz,i,j}^{exp}| \cdot \theta_{i,j}} \right) \quad \dots (d)
 \end{array} \right. \quad (5-33)$$

In the new cost function, the “deformation direction” is considered in the B_i part, which is named as “variant Lankford coefficient” hereafter (not in the conventional expression of Lankford coefficient). In the following optimization, weights of $\omega_i = 0.05$ remains, while α_i , β_i and γ_i will be adjusted to check their influence on optimization results.

5.4.5 Influence of Cost Function Components

From Eq. 5-33 one can choose the relative weight of force, of deformation error and of “variant Lankford coefficient”. Several trials are given in Table 13 to show the influence of the cost function components. The values of \mathbf{p}_4 are fixed as: $k_{ref} = 1771\text{MPa}$, $m = 0.2844$, $Q_1 = 151.0\text{kJ}\cdot\text{mol}^{-1}$, $Q_2 = 90.5\text{kJ}\cdot\text{mol}^{-1}$, and $b = 362$, which are the results of Step 2 in Table 10. The boundaries of the parameters of \mathbf{p}_3 are given in Table 12

Table 12 Parameter boundaries of \mathbf{p}_3 for Table 13

	minimum	maximum
T_{cross} (K)	1073	1373
f_1	-10^{-3}	-4×10^{-4}
h_0	0.42475	1
h_1	-3.9×10^{-4}	-10^{-4}
$\sigma_{Y,ref}$ (MPa)	59	79
$Q_{r,ref}$ (MPa)	75	95

From Table 13 it is found that:

- when the weight of “variant Lankford coefficient” increases, the T_{cross} trends to go towards 1240K, i.e. 967°C (Trials 1~5);
- when the none of β_i or γ_i is zero, the T_{cross} is within 1241 and 1281K (Trials 2~5);
- when only force is considered in the cost function, the T_{cross} trends to go to the maximum of the temperature range, which makes the F and H almost not crossed (Trial 1);
- when no “variant Lankford coefficient” is considered, i.e. $\beta_i = 0$ (Trials 1, 5 and Table 10), the slope of F has smaller magnitude compared with the considered cases (Trials 2~4);
- when force is considered but “variant Lankford coefficient” is not considered (Trial 1 and Table 10), the H decreases with temperature fast, with big starting h_0 , and
- the sum of $\sigma_{Y,ref}$ and $Q_{r,ref}$ is around 150MPa, and $\sigma_{Y,ref}$ is a little smaller than $Q_{r,ref}$ (Table 12 and Table 13).

Table 13 Influence of weights of the cost function components

	Trial 1	Trial 2	Trial 3	Trial 4	Trial 5	
Parameters	$\alpha_i = 1$	$\alpha_i = 0.50$	$\alpha_i = 0$	$\alpha_i = 0$	$\alpha_i = 0$	
	$\beta_i = 0$	$\beta_i = 0.25$	$\beta_i = 0.5$	$\beta_i = 1$	$\beta_i = 0$	
	$\gamma_i = 0$	$\gamma_i = 0.25$	$\gamma_i = 0.5$	$\gamma_i = 0$	$\gamma_i = 1$	
T_{cross} (K)	1352	1280	1260	1241	1281	
f_1	-4.850×10^{-4}	-8.167×10^{-4}	-9.586×10^{-4}	-9.476×10^{-4}	-6.658×10^{-4}	
\mathbf{p}_3	h_0	0.6331	0.4313	0.4327	0.4490	0.4334
	h_1	2.964×10^{-4}	-1.402×10^{-4}	-1.254×10^{-4}	-1.202×10^{-4}	-1.415×10^{-4}
	$\sigma_{Y,ref}$ (MPa)	67	75	62	64	63
$Q_{r,ref}$ (MPa)	92	76	94	81	82	

5.4.6 Final Optimized Parameters

To make final decision, $T_{cross}=1241\text{K}$ is selected based on Trial 4 in Table 13, and then $\alpha_i=0.5$, $\beta_i=0$, and $\gamma_i=0.5$ is taken. Again the alternated optimization method is adopted, and the results are given in Table 14.

Then, those parameters in Table 14 are used in the simulations, and the simulated force and deformation components are plotted in the same figure with the counterpart information from corresponding experiment, in Fig. 5-6 ~ Fig. 5-9. The curves entitled with “Ulti” are the forces from Fig. 7-19, which are obtained by optimization within individual orientation. The curves entitled with “Hill” are from the simulations using parameters in Table 14. When comparing the force curves of “Ulti” and “Hill” one can see the matching is not bad.

Table 14 Final optimized parameters of p_3 , and p_4 , where T_{cross} in p_3 is preset, and the underlined parameters are the optimized ones in each column

Parameters	Step 1 on p_3	Step 2 on p_4	Step 3 on p_3	Step 4 on p_4
T_{cross} (K)	<u>1241</u>	<u>1241</u>	<u>1241</u>	<u>1241</u>
f_1	<u>-0.00058702</u>	-0.00058702	<u>-0.00057687</u>	-0.00057687
h_0	<u>0.68217</u>	0.68217	<u>0.66229</u>	0.66229
h_1	<u>-0.00032791</u>	-0.00032791	<u>-0.00031620</u>	-0.00031620
$\sigma_{Y,ref}$ (MPa)	<u>79</u>	79	<u>75</u>	75
$Q_{r,ref}$ (MPa)	<u>76</u>	76	<u>84</u>	84
b	362.6	<u>477.1</u>	477.1	<u>515.5</u>
k_{ref} (MPa)	1771	<u>2120</u>	2120	<u>2249</u>
m	0.28443	<u>0.30647</u>	0.30647	<u>0.31604</u>
Q_1 (kJ·mol ⁻¹)	151.0	<u>143.4</u>	143.4	<u>136.1</u>
Q_2 (kJ·mol ⁻¹)	90.5	<u>95.5</u>	95.5	<u>96.8</u>
min (fc)	0.10312	0.10265	0.10213	0.10200

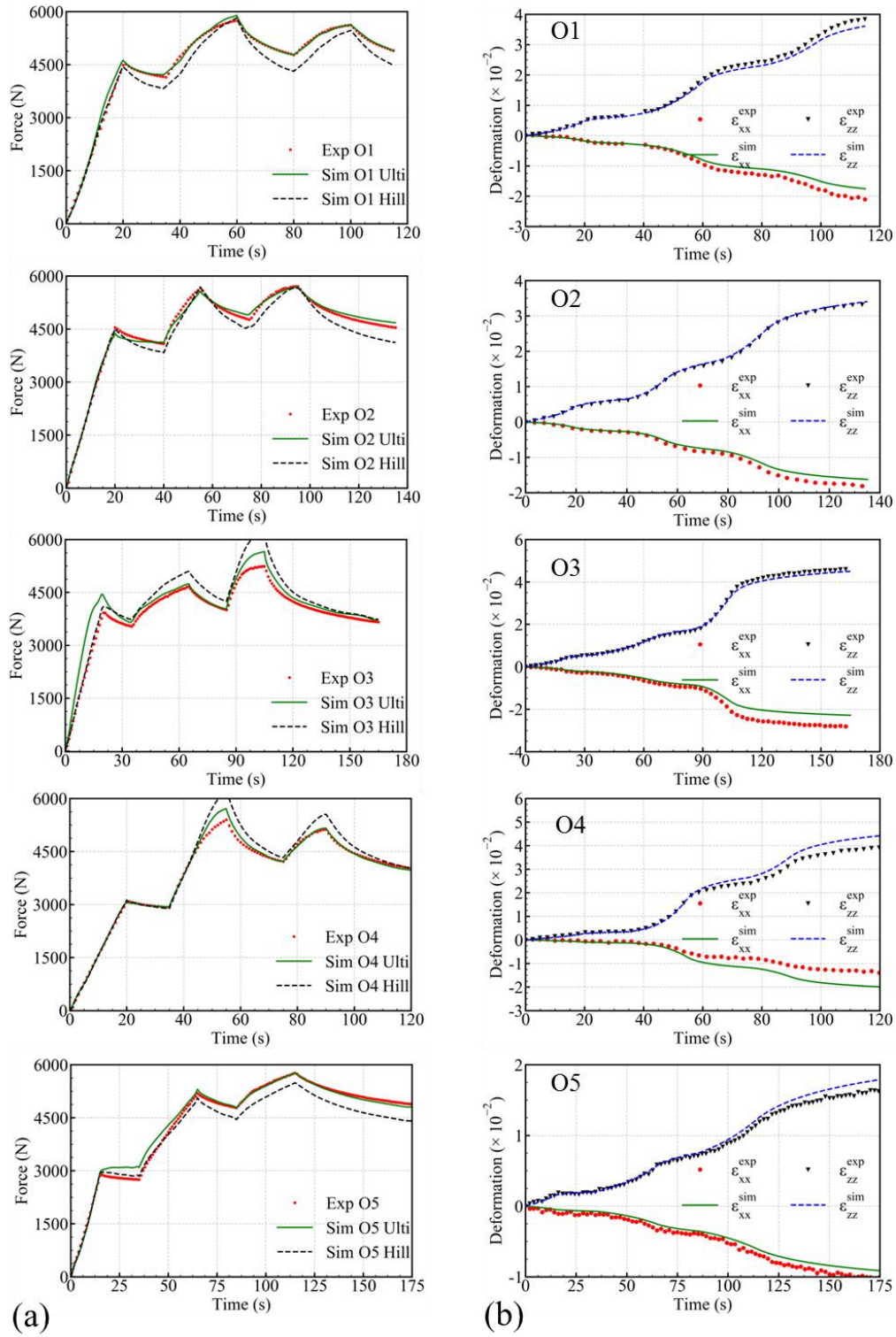


Fig. 5-6 Experimental force v.s. simulated force, experimental deformation v.s. simulation deformation for all the 5 orientations at temperature level 800°C

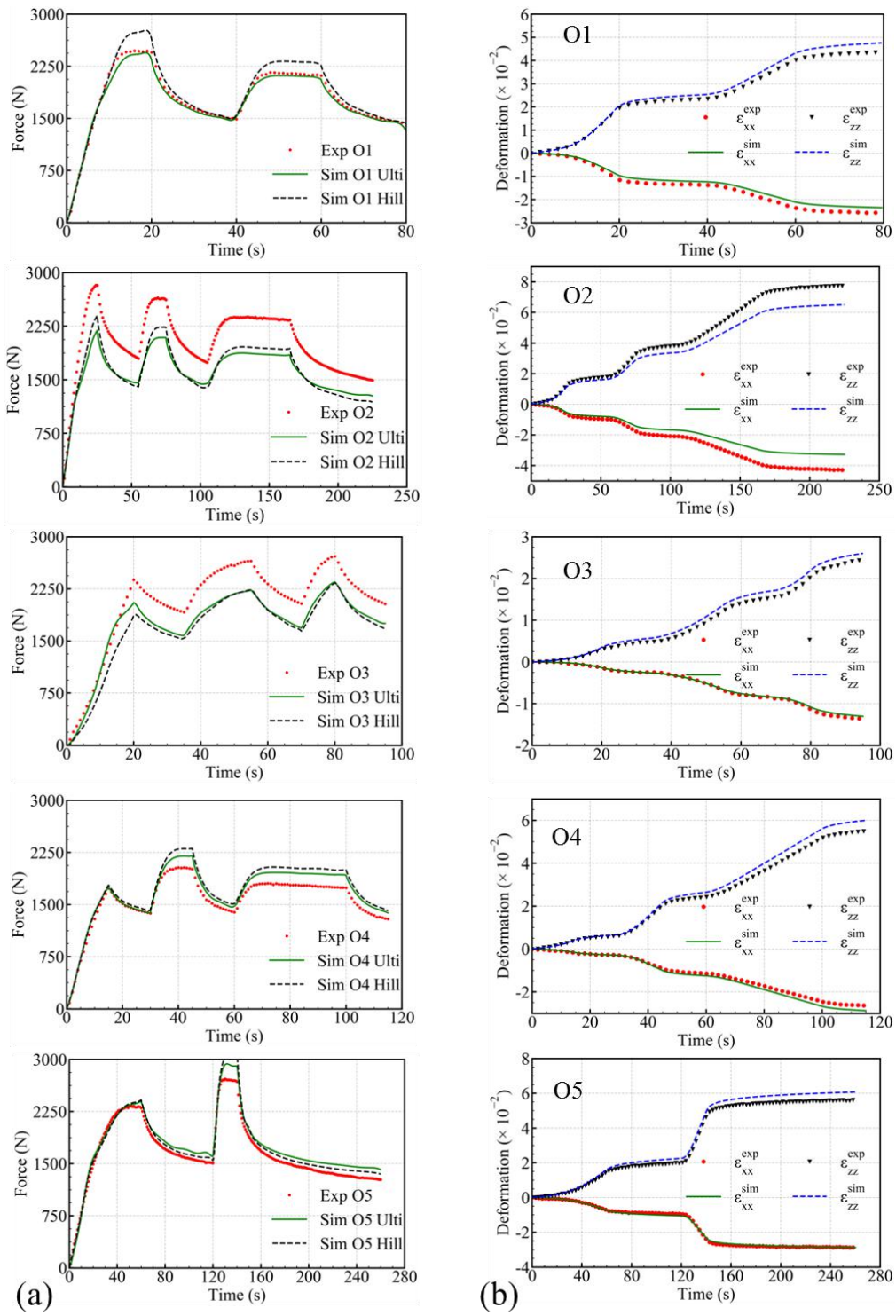


Fig. 5-7 Experimental force v.s. simulated force, experimental deformation v.s. simulation deformation for all the 5 orientations at temperature level 900°C

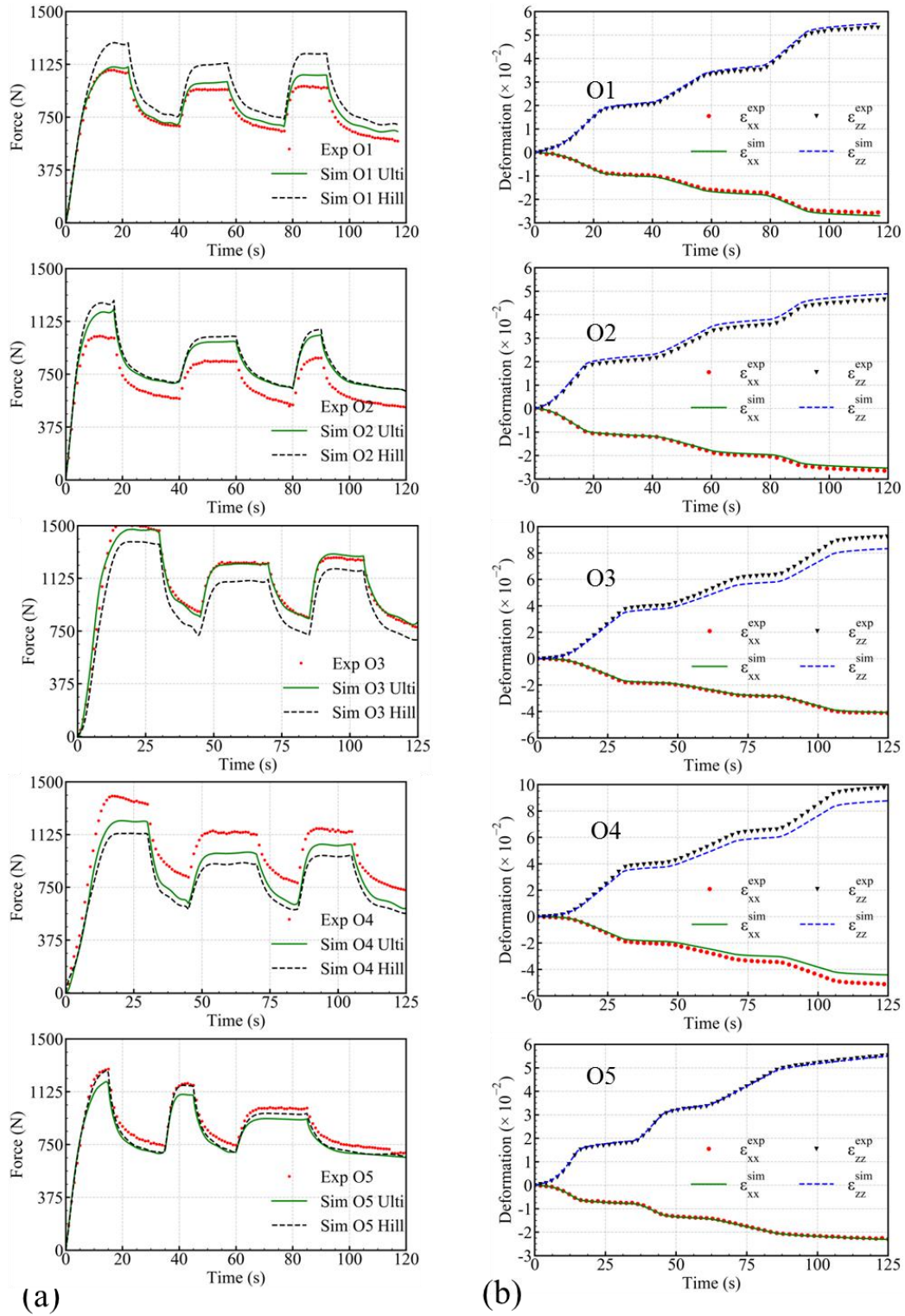


Fig. 5-8 Experimental force v.s. simulated force, experimental deformation v.s. simulation deformation for all the 5 orientations at temperature level 1000°C

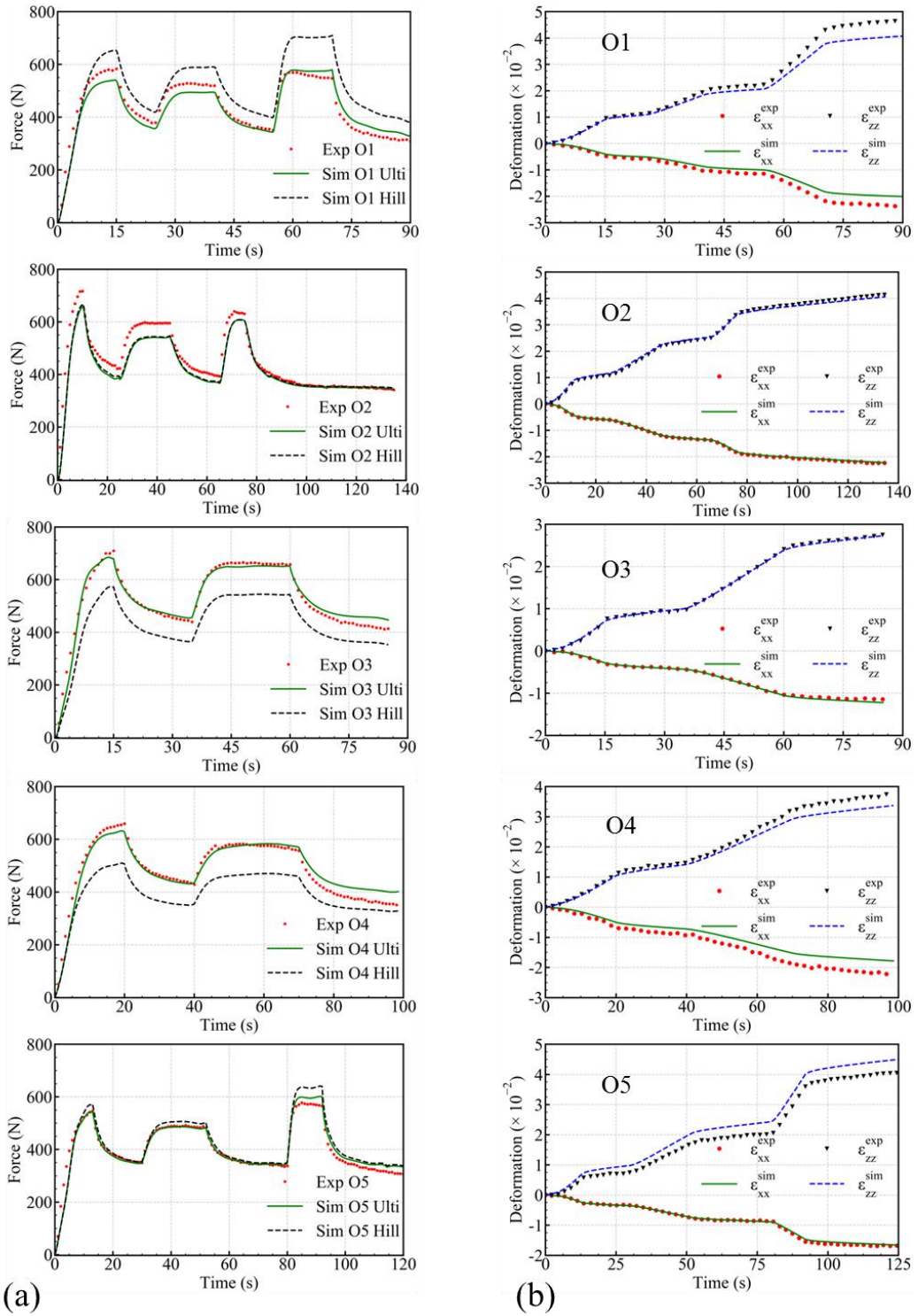


Fig. 5-9 Experimental force v.s. simulated force, experimental deformation v.s. simulation deformation for all the 5 orientations at temperature level 1100°C

5.5 Exploration of the Source of the Anisotropy Evolution

In the last section, a description of the temperature dependence of the anisotropy coefficients has been studied on the as-built samples by inverse analysis. This conducted to an acceptable modelling of the anisotropic behavior of the material, with a reasonable agreement with the measurements.

However, the origin and the physical phenomena governing this dependency to temperature are not understood yet. From view of the LPBF process, residual stress and back stress may be introduced. And during the test for characterization, the microstructure may evolve. All those factors can contribute to the evolution of anisotropy. They will be analyzed hereafter in the hope of explaining source of the anisotropy evolution.

5.5.1 Residual Stress

Residual stress is introduced or modified mainly during three steps: during manufacturing of LPBF, during removal of the supporting of the as-built samples, and during sand blasting before test. Those determine the stress state of Dedimet samples before their test processing, i.e. the initial stress state. That “initial” stress state is then non-uniform. The reason that it may impact the anisotropy response of samples at different temperature is because the stress state will evolve during Dedimet tests: evolution during heating and temperature maintaining before loading.

The evolution of residual stress due to heat exposure can be estimated by Zener-Wert-Avrami relation [120,121], as:

$$\frac{\sigma_{T,t}^{RS}}{\sigma_{start}^{RS}} = \exp\left(-\left(C_{RS}\exp\left(-\frac{\Delta H_{RS}}{\kappa_B T}\right)t\right)^{m_{RS}}\right) \quad (5-34)$$

where σ_{start}^{RS} is the residual stress at the start of stress releasing by heating, C_{RS} and m_{RS} are two material constants, ΔH_{RS} is the activation enthalpy for the relaxation process, κ_B is the Boltzmann's constant, T is the exposure temperature in unit of K, t is the exposure duration under T , and $\sigma_{T,t}^{RS}$ is the residual stress after exposure to heat at T and a duration t . From literature [121], $C_{RS} \approx 3.633 \times 10^{10} \text{s}^{-1}$, $\Delta H_{RS} \approx 332.88 \text{kJ} \cdot \text{mol}^{-1}$, and $m_{RS} \approx 0.77$.

For any Dedimet test the thermal routine contains (180s') heating and (180s') maintaining before loading, and there are 4 temperature levels for each orientation. An instant reflection is to check if the 360s' thermal routine is enough to remove residual stress from theoretical calculation based on Eq. 5-34. As a solid complementation, Dedimet tests on anneal solution treated samples should be also run to check the impact of residual stress on tensile strengths.

The analysis of this section is carried on samples of O5 in Fig. 5- 1.

5.5.1.1 Residual Stress Removal during Heating with Free Expansion

As aforementioned in Section 2.6, the Dedimet samples undergo 360s heating without force constraint. It is thus necessary to check if this duration of heating could remove part or all of the residual stress. The calculation result at the temperature control point of the 4 temperature levels of O5 is given in Fig. 5-10, calculated based on Eq. 5-34.

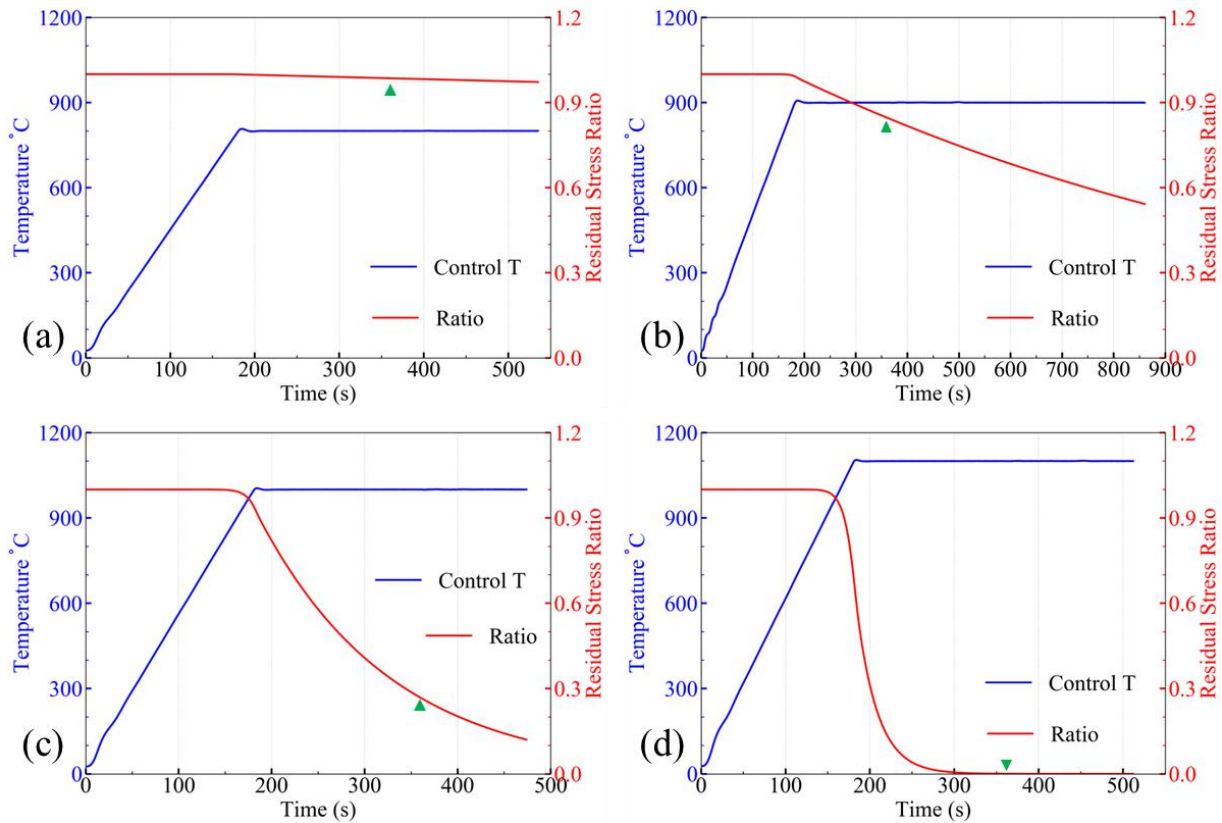


Fig. 5-10 residual stress ratio evolution (red curve) with time under experimental temperature routine for the experimental tests at (a): 800°C, (b): 900°C, (c): 1000°C and (d): 1100°C. The green triangle indicates when the first loading is imposed (after 360s).

From Fig. 5-10 it can be seen that only the 1100°C test shows a full release of the potential residual stress at the 360s, i.e. the instant at which the first loading is imposed. Thus, it is necessary to check if a solution treatment has an influence on the tensile tests.

5.5.1.2 Tensile Tests on Samples with/without Solution Treatment

With Eq. 5-34, one can calculate that when T is selected as 982°C and after an exposure of 30min, the residual stress will be only 0.014% of the initial state. Thus, solution treatment at 982°C for 30 min is selected as the routine for residual stress releasing treatment, which is also found in experimental literature [122]. The solution treatment (ST) aforementioned is used to release the residual stress. The heat-treated samples were air cooled down to room temperature. Then, at as-

built samples and the solution treated samples undergo the same testing routine to check the force responses. The experimental results are shown in Fig. 5-11.

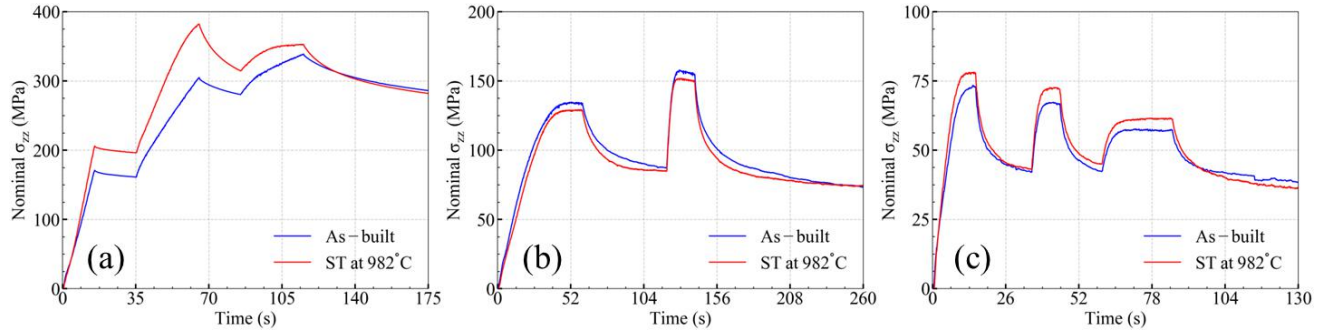


Fig. 5-11 Nominal stress component σ_{zz} on the as-built and solution treated samples, where the tensile tests are taken at (a) 800°C, (b): 900°C and (c): 1000°C

From Fig. 5-11 one can see that for the test at 800°C, the sample with ST has a higher force response compared with the sample without ST. For tests at 900 and 1000°C, the ST does not have an obvious influence on the force responses.

One possible reason could be that the residual stress no longer has strong influence on the force response at 900°C and over. The residual stress in the as LPBFed sample is not zero in O5, according to an XRD measurement. At room temperature, the residual stress component of σ_{zz} is around 80MPa at the surface in one or two decades of micrometers. One can find that when there is such a residual stress distribution, the tensile test will return a smaller force response, which is explained hereafter through the following simple model as shown in Fig. 5-12.

Consider a material whose Young's modulus and initial yield stress are E_0 and σ_y , respectively, under linear elastic and bilinear strain hardening elasto-plastic behavior. When the material free of residual stress goes into plasticity domain, the slope of $\sigma - \varepsilon$ curve will become smaller, and it is marked as H_1 ($E_0 > H_1 > 0$). The strain at the yield stress is thus σ_y/E_0 , as shown in Fig. 5-12 (a).

Now consider a system with residual stress, as shown in Fig. 5-12 (b). It is supposed that the outer two bars are in tensile condition, and the inner two bars are in compressive condition, and with force balance one can find the sum of the elastic strain should be zero. For simplification, the magnitude of the residual strain is assumed to be $\sigma_y/(2E_0)$, and immediately the inner stress within each bar can be calculated as $\sigma_y/2$, and they are marked in the figure in balanced state. With Hook's law, the initial lengths of the bars free of stress can be calculated given the system length at this moment t_0 as $l_{sys}^{t_0}$ under charged residual stress:

$$\begin{cases} l_{out}^r = \frac{2E_0}{2E_0 + \sigma_y} l_{sys}^{t_0} \\ l_{in}^r = \frac{2E_0}{2E_0 - \sigma_y} l_{sys}^{t_0} \end{cases} \quad (5-35)$$

where l_{out}^{fr} and l_{in}^{fr} are the initial lengths of the outer bars and inner bars when free of stress, respectively.

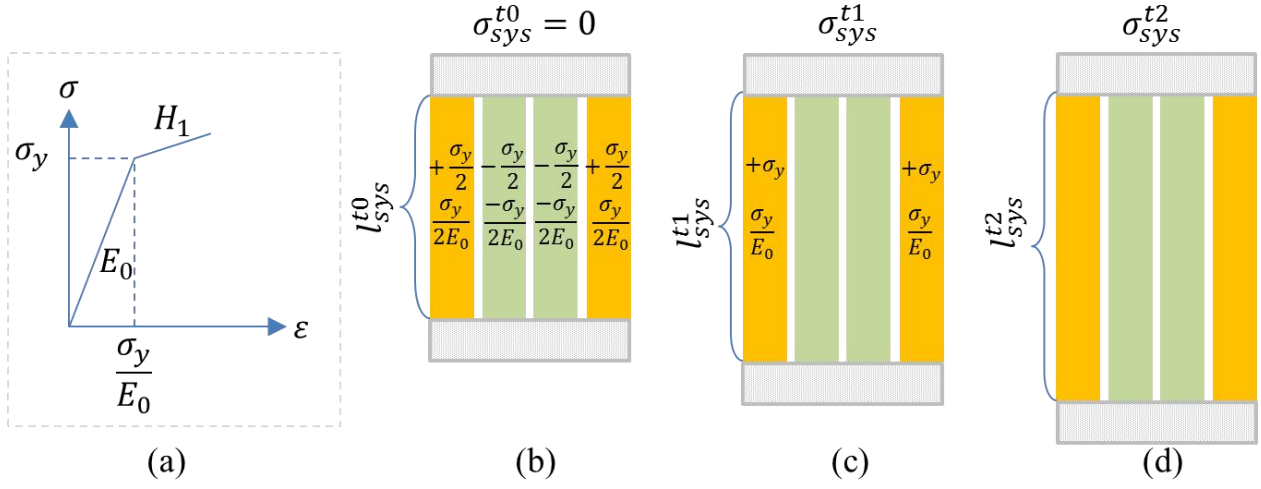


Fig. 5-12 Explanation why with residual stress the apparent yield stress is lower

Then, start to stretch the system. When the system goes into one critical state, i.e. the outer two tensile bars are at the yield point, as shown in Fig. 5-12 (c), relations can be found as Eq. 5-36:

$$\left\{ \begin{array}{l} \varepsilon_{out}^{t1} = \frac{\sigma_y}{E_0} \\ l_{sys}^{t1} = \frac{2E_0 + 2\sigma_y}{2E_0 + \sigma_y} l_{sys}^{t0} \\ \varepsilon_{in}^{t1} = \frac{-\sigma_y^2}{E_0(2E_0 + \sigma_y)} \\ \varepsilon_{sys}^{t1} = \frac{\sigma_y}{2E_0 + \sigma_y} \end{array} \right. \quad (5-36)$$

where ε_{out}^{t1} and ε_{in}^{t1} are the strains of the outer and inner bars at moment $t1$, respectively. It should be mentioned that the reference of local strains is related to the stress-free state, while the reference of the system is related to $t0$. At this stage, the system stress is found to be:

$$\sigma_{sys}^{t1} = \frac{1}{4}(2E_0\varepsilon_{out}^{t1} + 2E_0\varepsilon_{in}^{t1}) = \frac{\sigma_y E_0}{2E_0 + \sigma_y} \quad (5-37)$$

Checking Hook's law for the system, one can find:

$$k_{sys} = \frac{\sigma_{sys}^{t1}}{\varepsilon_{sys}^{t1}} = E_0 \quad (5-38)$$

That is to say, as long as all the material is in elastic domain, the Hook's law for the system still works.

Now, continue stretching the system as shown in Fig. 5-12 (d), until it comes at the expected "yield strain", i.e.

$$\varepsilon_{sys}^{t2} = \frac{\sigma_y}{E_0} \quad (5-39)$$

It can be calculated based on Eq. 5-35 that:

$$\begin{cases} l_{sys}^{t2} &= \left(1 + \frac{\sigma_y}{E_0}\right) l_{sys}^{t0} \\ \varepsilon_{out}^{t2} &= \frac{3E_0\sigma_y + \sigma_y^2}{2E_0^2} \\ \varepsilon_{in}^{t2} &= \frac{E_0\sigma_y - \sigma_y^2}{2E_0^2} \end{cases} \quad (5-40)$$

At this moment, the outer bar in the stage of plastic evolution (with hardening modulus H_1) under total strain $\frac{3E_0\sigma_y + \sigma_y^2}{2E_0^2} \left(> \frac{\sigma_y}{E_0}\right)$, while the internal bars are still in the elastic domain $\left(\frac{E_0\sigma_y - \sigma_y^2}{2E_0^2} < \frac{E_0\sigma_y}{2E_0^2} = \frac{\sigma_y}{2E_0} < \frac{\sigma_y}{E_0}\right)$.

Now the system stress will be:

$$\begin{aligned} \sigma_{sys}^{t2} &= \frac{1}{4} \left\{ 2 \left(\sigma_y + \left(\varepsilon_{out}^{t2} - \frac{\sigma_y}{E_0} \right) H_1 \right) + 2 \varepsilon_{in}^{t2} E_0 \right\} \\ &= \frac{3}{4} \sigma_y + \frac{H_1}{4E_0} \sigma_y + \frac{(H_1 - E_0)}{4E_0^2} \sigma_y^2 < \sigma_y \end{aligned} \quad (5-41)$$

Obviously, the apparent stress at the "expected yield strain", i.e. the system stress is smaller when there is residual stress. That is the explanation of Fig. 5-11 (a) from view of mechanical behavior, that the residual stress released sample behaves stronger than the one with residual stress.

The evolution of the potential residual stress is not taken into account in this work, while its influence is inherited in the optimized rheological parameters.

5.5.2 Back Stress

As aforementioned in Section 1.2.4, during the AM process there is cyclic heating, thus cyclic stress is introduced. In the vicinity of the melt pool the material is in plastic state. No doubt that the

cyclic stress could introduce back stress in the material. The following simulation can show that when there is back stress, the Lankford coefficient will change.

The parameters of rheological law are directly taken from Table 14, as shown in the first column in Table 15, with $T_{ref} = 1073\text{K}$ (800°C). The Hill48 parameters expressed in Eq. 5-26 are selected, which are shown in the second column in Table 15. The back stress preset in material reference frame does not evolve, and Orientation 5 is selected for the analysis. With respect to the no back stress situation, three different cases are considered: BS1, BS2 and BS3. The constant back stress tensor \mathbf{X} in material reference frame is here taken as a diagonal deviatoric tensor, characterized by its three diagonal items, the sum of which is zero. The X_{XX} magnitude is differently selected from that of X_{YY} , since the width and thickness values are not the same. The transformation of \mathbf{X} from material reference frame to testing reference frame is not detailed, and one can refer to Section 5.2.1.1 or Appendix A. 12.1 for the solution by himself.

Table 15 Parameters in simulation to check the influence of back stress

Rheological law		Hill48		Back Stress (MPa)				
				No BS	BS 1	BS 2	BS 3	
$\sigma_{Y,ref}$ (MPa)	75	F	0.3255	X_{XX}	0	+9.5	+19	+28.5
$Q_{r,ref}$ (MPa)	84	G	0.3255	X_{YY}	0	+7	+14	+21
b	515.5	H	0.4275	X_{ZZ}	0	-16.5	-33	-49.5
Q_1 (kJ·mol ⁻¹)	136.1	L	1.5	X_{YZ}	0	0	0	0
k_{ref} (MPa)	2249	M	1.5	X_{ZX}	0	0	0	0
Q_2 (kJ·mol ⁻¹)	96.8	N	1.1805	X_{XY}	0	0	0	0
m	0.316	r_{vp}^{theo}	0.698	Slope	0.689	0.73	0.77	0.81

The testing temperature is prescribed at 800°C for all elements, and the boundary conditions of $v_z^{up} = 0$ and $v_z^{low} = -0.004\text{mm}\cdot\text{s}^{-1}$ are imposed to a cuboid mesh of $8.02 \times 2.22 \times 40.3\text{mm}$ during 134s. Then, the ε_{xx} as function of $(-\varepsilon_{zz} - \varepsilon_{xx})$ is plotted, as shown in Fig. 5-13.

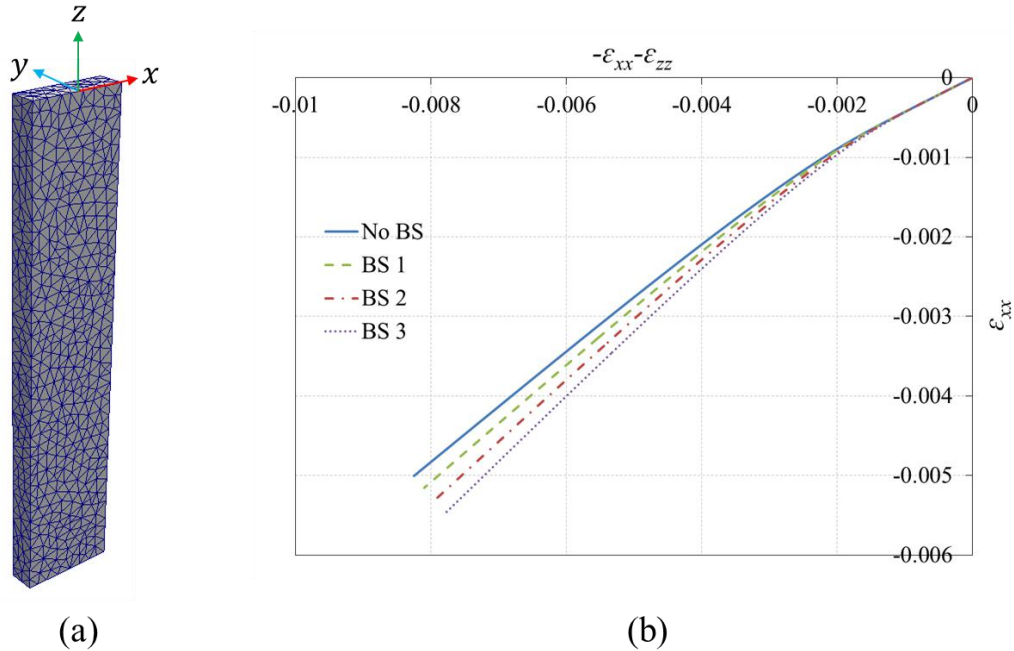


Fig. 5-13 (a): the cuboid mesh with reference frame, and (b): influence of back stress (BS) on the values of Lankford coefficient

The slopes of the four curves in Fig. 5-13 (b) within ranges of $-\varepsilon_{zz} - \varepsilon_{xx} < -0.004$ are given in Table 15. The theoretical plastic Lankford coefficient r_{vp}^{theo} is also given in Table 15. From the table and the figure, it can be found that:

- In absence of backstress, the slope of the chart in Fig. 5-13 is found close to the expected theoretical value r_{vp}^{theo} , which is as expected and quite acceptable considering that the computed Lankford coefficient in an “averaged” one (slope) and that it is evaluated based on the total strain components (instead of the viscoplastic ones)
- The slope deviation of the curves increases with the magnitude of back stress. The second observation is interesting, because it means that if there is back stress introduced during the AM process, the Lankford coefficient during the afterwards tensile test will change.

One natural expectation is that the back stress introduced during the AM process would degrade when the sample is re-heated to a moderate to high temperature, because when the sample is at its solidus, no back stress exists (such kind of evolution was observed in polycarbonate material [123]). Considering the elevated testing temperature levels in this project, the back stress degrades, thus at 1100°C it can be expected that there is no back stress in the material. That could be the reason that the Lankford coefficients at 1100°C in Table 8 are close to the theoretical value. In present work the back stress is not considered during the characterization, thus its potential influence is embedded in the optimized parameters.

From sections 5.5.1 and 5.5.2 one can see that knowing σ_{res} and/or \mathbf{X} in the Dedimet samples is possible, but that requires some conditions not fully easy to reach:

- The analysis of the built-up of σ_{res} and/or \mathbf{X} should be conducted from the LPBF process, through a macroscopic thermos-mechanical simulations of LPBF process, followed by cutting process, and sand blasting process.
- Then, to follow σ_{res} and/or \mathbf{X} evolution in the ZOI during heating, it is not obvious that the analysis could be conducted on the ZOI only. Maybe it would be necessary to calculate the whole sample. and finally
- The need of a constitutive model from room temperature to testing temperature.

5.5.3 Microstructure Evolution

The microstructure evolution at different temperature levels could also contribute to the evolution of anisotropy. In this work the precipitation of γ' during the test is considered not to happen, which is shown in Appendix A. 15. Considering the common phases in IN718 (γ , γ' , γ'' , δ , Laves, M_6C [124]), the γ' and γ'' are not believed to link with the evolution of anisotropy, since their lattice constants are close to the γ matrix. For the M_6C phase, at the temperature levels (800 – 1100°C) they are not supposed to be dissolved [125], so they are not suspected. It is thus time to consider only δ and Laves phases. Some basic information of δ and Laves phases are gathered below.

- δ : It can be deemed as Nb_3Ni [126,127] with cubic structure of $a \approx 0.4046$ [128], and starts to dissolve since about 1100°C [127,129]. It is also found that solution of δ phase can happen since 2 min at 1020°C and this solution can cut the strip-shaped Laves phase into small non-continuous particles[130].
- Laves: A_2B (Fe+Cr+Ni), (Ti+Nb+Mo) [124,131], hexagonal crystal structure with $a \approx 0.487nm$, and $c \approx 0.753nm$ [127,132]. Laves phase is found to precipitate along the interdendritic regions [133,134,135], which might define the anisotropy together with the dendrite orientations.

Based on the above information from literature, one hypothesis can be formulated, which is:

At temperature lower than 1020°C, the anisotropy is defined by both Laves phase and the dendrites of γ phase; at temperature higher than this value, the Laves phase is cannibalized by the solution of δ phase, and only γ dendrites define the anisotropy.

The following Fig. 5-14 presents the microstructure of the sample of O5 that is taken under SEM. The sample was polished and etched by waterless Kalling's reagent.

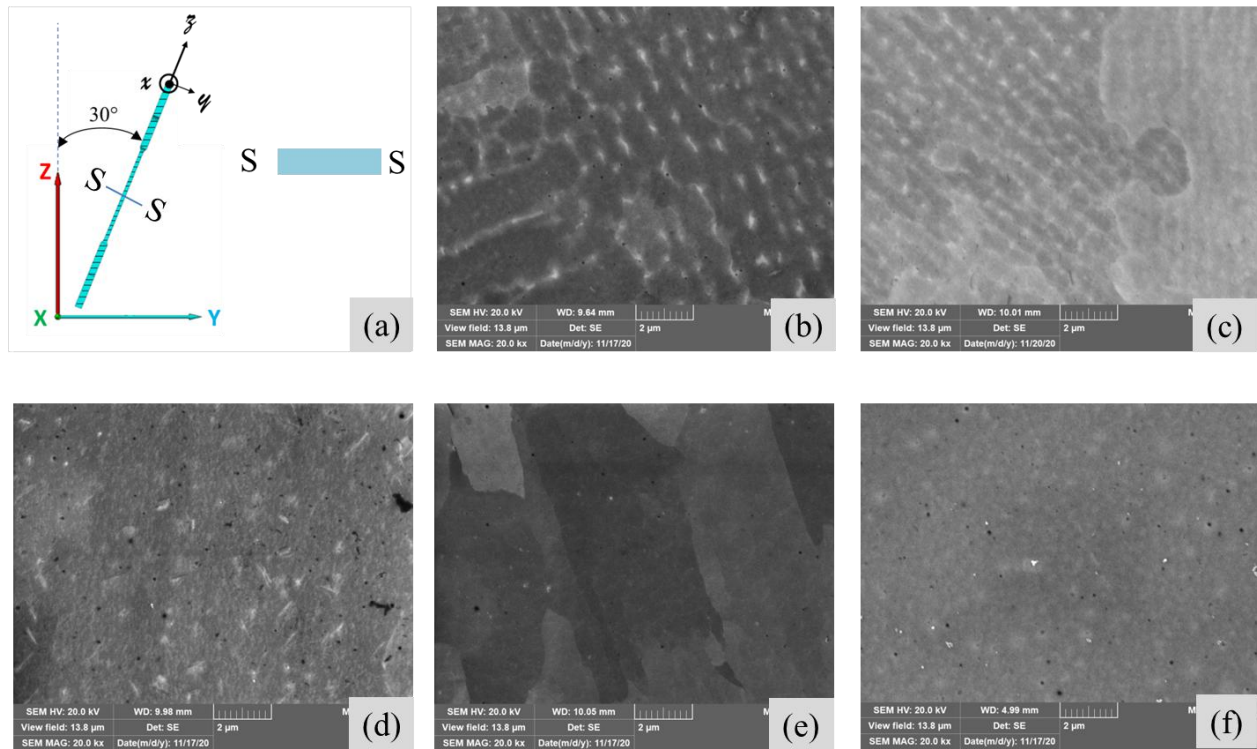


Fig. 5-14 (a): Observation direction along z (normal of S-S) of O5 samples, (b): as-built sample, (c): tested sample at 800°C , (d): tested sample at 900°C , (e): tested sample at 1000°C , and (f): tested sample at 1100°C

The microstructure as shown in Fig. 5-14 (a) and (b) is also found by others' work [136]. The morphology is formed by phases which are mainly composed of Laves and δ . It can be seen that both phases are still present after the specimen has been tested and deformed at 800°C , and then cooled down. Then, following a test at 900°C the pattern becomes less clear. At 1000°C the bright pattern cannot be almost seen, and at 1100°C the morphology is totally missing. Thus, it could be inferred that the evolution of the microstructure has an influence on the anisotropy.

5.6 Chapter Summary

The anisotropy of the as-built LPBF samples is studied by minimizing a cost function that is composed of both force and deformation. At the same time, the evolution of the indicator of anisotropy, i.e., the evolution of Hill48 parameters is also found. The potential reasons (residual stress, back stress and microstructure evolution) for the evolution of the anisotropy are analyzed. It is found that the back stress has certain influence of the Lankford coefficient, but a little weak. Microstructure evolution is thus considered the strongest source of anisotropy evolution. It is found that only Lankford coefficient is not sufficient to check the anisotropy: the deformation comparison between experiments and simulation should be accompanied with Lankford coefficient for a convincing identification. What's more, an alternated optimization method is used to avoid heavy computing of FEM simulations.

Chapter Reference

- 117 Lian, J., Shen, F., Jia, X., Ahn, D.C., Chae, D.C., Münstermann, S. and Bleck, W., 2018. An evolving non-associated Hill48 plasticity model accounting for anisotropic hardening and r-value evolution and its application to forming limit prediction. *International Journal of Solids and Structures*, 151, pp.20-44.
- 118 Taherizadeh, A., Green, D.E., Ghaei, A. and Yoon, J.W., 2010. A non-associated constitutive model with mixed iso-kinematic hardening for finite element simulation of sheet metal forming. *International journal of plasticity*, 26(2), pp.288-309.
- 119 Pacheco, M., García-Herrera, C., Celentano, D. and Ponthot, J.P., 2020. Mechanical Characterization of the Elastoplastic Response of a C11000-H2 Copper Sheet. *Materials*, 13(22), p.5193.
- 120 Chin, K.S., Idapalapati, S. and Ardi, D.T., 2020. Thermal stress relaxation in shot peened and laser peened nickel-based superalloy. *Journal of Materials Science & Technology*, 59, pp.100-106.
- 121 Zhou, Z., Bhamare, S., Ramakrishnan, G., Mannava, S.R., Langer, K., Wen, Y., Qian, D. and Vasudevan, V.K., 2012. Thermal relaxation of residual stress in laser shock peened Ti-6Al-4V alloy. *Surface and Coatings Technology*, 206(22), pp.4619-4627.
- 122 Amato, K.N., Gaytan, S.M., Murr, L.E., Martinez, E., Shindo, P.W., Hernandez, J., Collins, S. and Medina, F., 2012. Microstructures and mechanical behavior of Inconel 718 fabricated by selective laser melting. *Acta Materialia*, 60(5), pp.2229-2239.
- 123 Negahban, M., Strabala, K., Delabarre, P., Goel, A., Feng, R. and Grene, J., 2007, November. Temperature Dependence of the Back-Stress in Shear for Glassy Polycarbonate. *In Macromolecular symposia* (Vol. 258, No. 1, pp. 142-151). Weinheim: WILEY-VCH Verlag.
- 124 Keiser, D.D. and Brown, H.L., 1976. *Review of the physical metallurgy of Alloy 718* (No. ANCR-1292). Idaho National Engineering Lab., Idaho Falls (USA).
- 125 Radavich, J.F., 1989. The physical metallurgy of cast and wrought alloy 718. *Superalloy*, 718(33), pp.229-240.

126 Mostafa, A., Picazo Rubio, I., Brailovski, V., Jahazi, M. and Medraj, M., 2017. Structure, texture and phases in 3D printed IN718 alloy subjected to homogenization and HIP treatments. *Metals*, 7(6), p.196.

127 Zhou, L., Mehta, A., McWilliams, B., Cho, K. and Sohn, Y., 2019. Microstructure, precipitates and mechanical properties of powder bed fused inconel 718 before and after heat treatment. *Journal of Materials Science & Technology*, 35(6), pp.1153-1164.

128 <https://materialsproject.org/materials/mp-999437/>, mp-999437: Nb₃Ni (cubic, Pm-3m, 221), visited Apr. 28th, 2021

129 Azadian, S., Wei, L.Y. and Warren, R., 2004. Delta phase precipitation in Inconel 718. *Materials characterization*, 53(1), pp.7-16.

130 Liu, F., Lyu, F., Liu, F., Lin, X. and Huang, C., 2020. Laves phase control of inconel 718 superalloy fabricated by laser direct energy deposition via δ aging and solution treatment. *Journal of Materials Research and Technology*, 9(5), pp.9753-9765.

131 Radhakrishna, C.H. and Rao, K.P., 1997. The formation and control of Laves phase in superalloy 718 welds. *Journal of Materials Science*, 32(8), pp.1977-1984.

132 Knorovsky, G.A., Cieslak, M.J., Headley, T.J., Romig, A.D. and Hammett, W.F., 1989. Inconel 718: a solidification diagram. *Metallurgical transactions A*, 20(10), pp.2149-2158.

133 Nagahari, T., Nagoya, T., Kakehi, K., Sato, N. and Nakano, S., 2020. Microstructure and Creep Properties of Ni-Base Superalloy IN718 Built up by Selective Laser Melting in a Vacuum Environment. *Metals*, 10(3), p.362.

134 Hilaire, A., Andrieu, E. and Wu, X., 2019. High-temperature mechanical properties of alloy 718 produced by laser powder bed fusion with different processing parameters. *Additive Manufacturing*, 26, pp.147-160.

135 Tao, P., Li, H., Huang, B., Hu, Q., Gong, S. and Xu, Q., 2019. The crystal growth, intercellular spacing and microsegregation of selective laser melted Inconel 718 superalloy. *Vacuum*, 159, pp.382-390.

136 Tucho, W.M., Cuvillier, P., Sjolyst-Kverneland, A. and Hansen, V., 2017. Microstructure and hardness studies of Inconel 718 manufactured by selective laser melting before and after solution heat treatment. *Materials Science and Engineering: A*, 689, pp.220-232.

Chapter 6 Conclusions and Prospects

6.1 Conclusions

In the present work, a comprehensive methodology has been developed for the characterization of the behavior law and anisotropy of the as-built IN718 prepared by LPBF process. As three bricks of this strategy, experimental, simulation and optimization yield the following main outputs.

- Field measurements at very high temperature are key points that have been successfully addressed. First the temperature field was successfully measured by bichromatic infrared camera, and the calibration method was also given. Regarding the displacement field, a self-emitting method was proposed to measure it at high temperature, which is original with respect to the present literature. The compromises associated with this self-emitting method, together with its complementarity with respect to standard method were presented and discussed. With the measured displacement field, the deformation field and velocity field could be accessed. In such thermal-mechanical behavior tests, a precise temperature measurement requires the most important consideration, as temperature has an exponential sensitivity effect, from the error analysis.

- The design of the numerical simulation, and especially the choice to restrict the computational domain to the central zone of samples was another key point of the study. In view of inverse identification, instead of embarking a complex multi-physical calculation operated on the full sample, with an uncertain knowledge and control of boundary conditions, the choice which was done to develop the concept of Zone Of Interest was quite fruitful. Based on the experimental temperature and displacement fields, the ZOI is selected in a localized part of each sample, with an assigned mesh and associated boundary conditions issued from the DIC. This offered a sound terrain for the identification of the mechanical behavior. An important point in this approach was the definition of sound mechanical boundary conditions through a master-slave fitting method which was proposed to efficiently smooth the boundary conditions without losing much information. In this ZOI context, reference frame transformations among different data sources were detailed. In total, the ZOI inverse approach proved to work well, from different points of view: time savings, efficiency, robustness.

- In the optimization step, basic cost function candidates were firstly tested for a reasonable choice. In this work the normalized mean absolute error (NMAE) was finally selected, for both a simple optimization built only by force and a complex optimization built by force and deformation. Before conducting the optimization with EGO algorithm, it is valuable to estimate the sensitivity of the parameters. With respect to initialization of database for the EGO algorithm, an alternated method was proposed to reduce the size of the initial direct simulations.

With the above three bricks, we were able to analyze the anisotropy of as-built IN718 alloy, with the following results.

- A theoretical transverse isotropy elasticity tensor was obtained starting from the single crystal data. It was found that for samples built along different directions, the Young's modulus along the loading direction is varying based on the transverse isotropy hypothesis. MOOPI is used to identify the Young's modulus of the as built IN718 material in selected orientations. Young's modulus varying with building direction in real material is found to have similar trend as that of theoretical transverse isotropy. It is a proof that the as-built material is close to a transverse isotropy condition from view of elasticity.

- In the step of searching transverse isotropy in viscoplasticity domain, Hill48 based associated law was used and characterized. Inverse strategy was proved a better choice for calculating Hill48 parameters compared with direct strategy. In the light of literature, and according to the microstructural characterization we did, showing γ -grains preferably aligned along the build direction, transverse isotropy was anticipated. However, our measurements of Lankford coefficients, issued from DIC at the surface of the samples, didn't allow us to validate this hypothesis. Actually, Lankford values that would express transverse isotropy were found only on specimens deformed at the highest temperature: 1100°C. For lower test temperatures, the measured values were not consistent with transverse isotropy. The temperature dependence of the Hill parameters was identified by our inverse analysis technique. To better understand the origin of this phenomenon, two possible reasons for this discrepancy were investigated. First, the existence of residual stress and possibly back stress, issued from the LPBF process (and resulting from a constitutive model including kinematic hardening) that would affect the measured Lankford, despite the effective orientation of γ -grains. A second hypothesis was that the Laves phase and δ phase – which precipitate in the interdendritic regions during the LPBF process – could determine the anisotropy, in addition to γ -grains orientation. At lower test temperature, the departure from transverse isotropy would be significant, while at higher test temperature, because of the solution process affecting Laves phase and δ phase, transverse isotropy would be retrieved. Our conclusion was that the explanation through residual stress or back stress could not explain the amplitude of the discrepancy. At this stage, the microstructural explanation seems the more relevant, but this will need in-depth study in the future.

6.2 Prospects

In view of experimental work:

First, let us mention here that this study is the first one carried out on the Dedimet set-up, compared with the pioneer set-up named Taboo, which was operated by Christophe Pradille. Dedimet allows us to proceed to tests under a certain control of the atmosphere and vacuum, which was a real step forward. But this new equipment presented its own weaknesses and limitations. During this work, we spent a significant time trying to overcome some practical obstacles, as

reported in the manuscript. As Dedimet is currently used for the characterization of mechanical behavior of single crystals (ongoing PhD work of Emile Hazemann), and could be used again in connection with additive manufacturing, some interesting or necessary developments of the set-up and the experimental techniques can be listed.

Regarding the machine, a better control of the beam motion at very low velocity is required, together than a better mechanical alignment of the tensile line. Besides, a deeper vacuum would be better for similar high temperature thermo-mechanical tests. First, K type thermocouples can work at about 1200°C when vacuum is high. Second, and more important, the surface state of the samples will change less during tests, which means emissivity will change less too, thus the temperature control by bichromatic pyrometer and measurement by bichromatic infrared camera will be more stable and precise.

Displacement field measurement by the present self-emitting method worked well in the present project, but it has certain drawbacks. The first one is the preparation of the ceramic speckle, which is quite experience dependent, and should be developed (such as spay gun). What's more, if the ceramic points are too dense at certain position, the local heat generated in the sample cannot be outlet, which can induce the local fusion (which was found in an additional test at 1200°C in this project, but not reported in this manuscript). The second one is about the three compromises for the self-emitting method. They probably reduce the measurement precision. As a consequence, the DIC method relying on laser interferometry – based on a virtual speckle, and as developed by Pradille [70] – might be a better choice, provided it is proved unaffected by window glass.

In view of constitutive model and simulations:

The present work characterized the selected rheological law only in temperature range of 800 ~ 1100°C at low strain rates. In a future work the temperature should reach room temperature downwards and reach the solidus upwards, and the strain rate should extend to wider range. Only by this it is possible to simulate the whole chain, from the additive manufacturing to the testing of fabricated samples. Such extra-wide-temperature-range constitutive models raise some questions, as the background physics of plastic deformation is quite different according to the temperature domain, but they will be necessary as inputs of process simulation at different scales, to efficiently predict potential defects. In a more global perspective, they will be also required to develop numerical twins of AM-fabricated alloys that could be used to simulate their whole life span: AM processing, heat treatment, post treatments like milling, surface treatments, in-service solicitation, life span prediction, recycling.

Static recovery was simply introduced in the present model, but it was not used in the characterization work. What's more, the introduction of static recovery was realized by reducing the initial yield strength, which is not so “reasonable”. In the further work this static recovery could be conducted by reducing the contribution of the equivalent strain value to the isotropic hardening.

Residual stress and back stress is found in the as-built samples by LPBF process, and, so far, it is difficult to have a clear analysis on them. It can be seen that if the manufacturing-testing chain would be wholly simulated, i.e. the simulation of LPBF process, of supports cutting, of sand blasting, and finally of Dedimet test, then the analysis and discussion of the residual and back stress influence could be conducted in a more quantitative and convincing manner.

Chapter 7 Appendices

A. 1 How to well weld a thermocouple

Generally speaking when we need to weld a thermocouple on to the sample, we can simply weld the two wires together and then weld the joint on to the sample surface. However, there is something that we need to pay much attention when we do this in our project, because our sample is heated by Joule effect. We will discuss it in this section.

The thermocouple generates electrical potential under some temperature in the measuring range. Let's take the K type into consideration. Each degree increase will raise the thermoelectric voltage for 0.032~0.039mV [137].

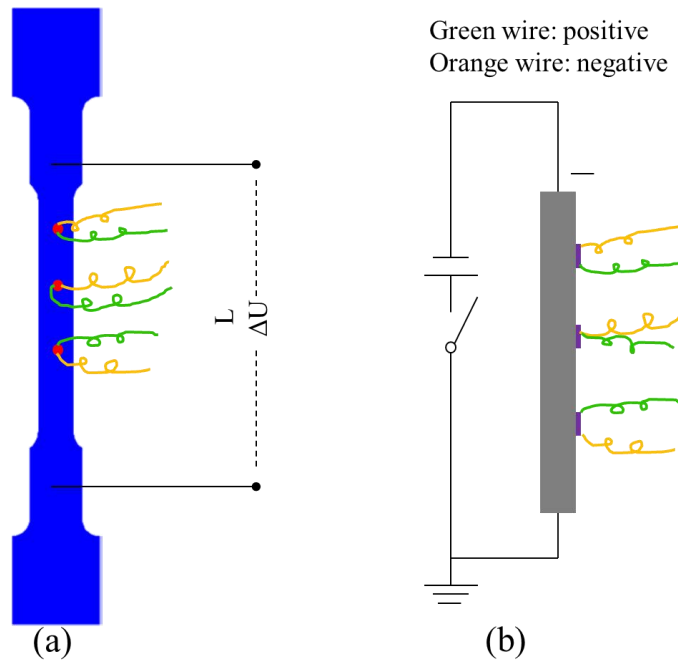


Fig. 7-1 schematic drawing for welding thermocouples in this project

When we weld the joint thermocouple, i.e. the ball formed from the melt wires onto the sample surface we can have three configurations, see Fig. 7-1. The sample is heated by direct current and we can simplify the Fig. 7-1 (a) to (b). From Fig. 7-1 (b) we can see that the joint balls of the thermocouple have a certain diameter, and this diameter will take partial of the voltage that we impose on the sample, and we mark this potential from the imposed voltage is $E^{extrenal}$. At the same time, the thermocouple will generate thermoelectric potential, which is connected in series in the current, and we mark this thermoelectric part as $E^{thermal}$. Obviously the voltage got from the

thermocouple is actually the sum of the potential section distributed on the joint ball of the thermocouple and the thermoelectric potential, i.e.

$$E = E^{extrenal} + E^{thermal} \quad (7-1)$$

Thus in the three configurations, the values introduced by the $E^{extrenal}$ should be different, and the upper one should have an opposite trend of the lower one, and the middle one should be influenced least.

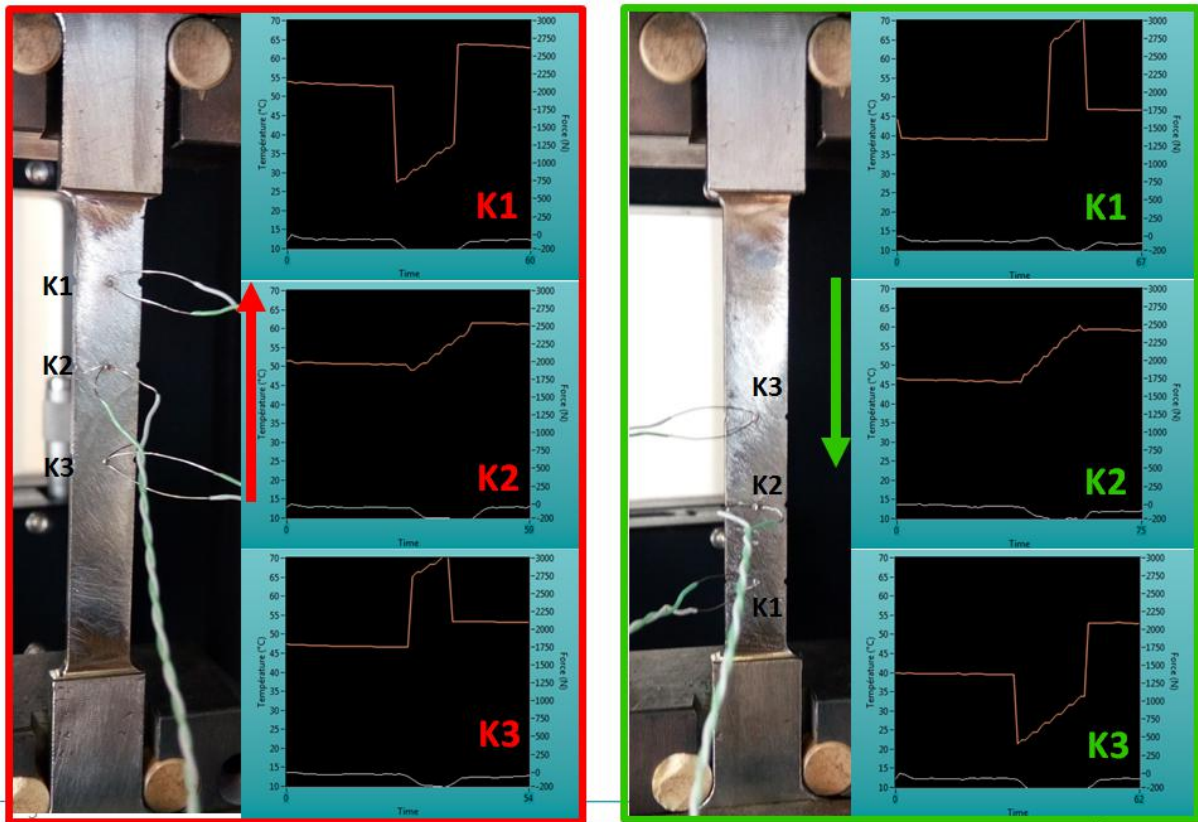


Fig. 7-2 signal jump when we impose 150A, imposing electrical current and cut off current (white wire: negative, green wire: positive).

At one test the measured potential during the ΔU is about $0.8V$ when we impose $150A$ current, and L being about $100mm$, so we could get a rather rough potential distribution of $8mV/mm$. Let's consider the joint ball diameter (in precise the distance between the two wires that are welded on the joint ball) as $0.1\sim 0.2mm$, and we have an $E^{extrenal} = 0.8\sim 1.6mV$, corresponding temperature jump at about $21 \sim 42^{\circ}C$. The Fig. 7-2 shows the trends and magnitudes, which is in accordance with the analysis, and the K2 in Fig. 7-2 has a relatively better response of electrical charge.

Based on the previous analysis we know that when we weld thermocouple onto the sample surface we should avoid both case K1 and case K3 in Fig. 7-2.

A. 2 How to Apply the Speckle onto the Sample Surface

To apply speckle onto the sample surface we need 2 main steps: the first is to sand-blast the sample surface to get a relative smooth and fresh surface, and the second is to apply the paint solution on the sample surface.

A. 2.1 Pre-treatment by Sand-blasting

We put the sample that have been geometry amended (i.e. after being removed of the additional part and amended the fillets so that they can be mounted in the fixtures in Dedimet) into the sand blaster. Start the machine and use the blasted sand to blow the sample surface with uniform speed several passes until the sample surface are all new, i.e. we can no longer see the original color of the sample. Then the sample is cleaned with compressed air to remove the residual sand on its surface.



There are many ways to apply the speckle, such as roller, spray painting, printed paper... In our project the solution (NaAlO_2 , HNO_3) that we use has erosion effect on the spray gun, so we decided finally not to use spray painting, but brush spattering.

A. 2.2 Brush spattering

S1: cut the brush filaments short so that they are more rigid

S2: transfer a little amount of solution into a flat container, and then brush the transported solution with the cut brush for several times to spread the solution uniformly in the filaments of the brush

S3: spatter the brush towards an empty container for 1 or 2 times to get rid of the big droplets

S4: spatter the brush towards the sample 1 or 2 times to get the speckle

S5: repeat S2, S3 and S4 for several times until the sample surface is covered with uniform dense speckle.

A. 3 Method to Calculate the Dot Areas in a Speckle

The analysis of the dot areas is done by means of ImageJ software.

As shown in Fig. 7-3 (a), firstly the central portion of the image is selected for the analysis, because this portion has the strongest contrast. Then in Fig. 7-3 (b) a scale is added for transforming pixel to millimeters. In Fig. 7-3 (c), all the dots (in fact deemed as particles in software ImageJ) are transformed into binary condition, which is either 0 (black) or 255 (white). Finally ImageJ can calculate the area of each dot in the speckle.

The analyzed data is plotted in Fig. 7-3 (d), with x axis the areas of the dots from the minimum to maximum, and y axis the number of dots in corresponding areas of dots.

It must be mentioned that theoretically a normal-distribution-like curve is expected. However, the DIC camera do not has such a high image resolution and the light blocking by the small dots is weak too, which induces that the distribution in the small half of the normal-distribution-like curve is missing.

The speckle areas are found mainly in range of 0.004 and 0.27mm² for this figure. Assuming a round shape, the diameters are in the range 70 to 600μm.

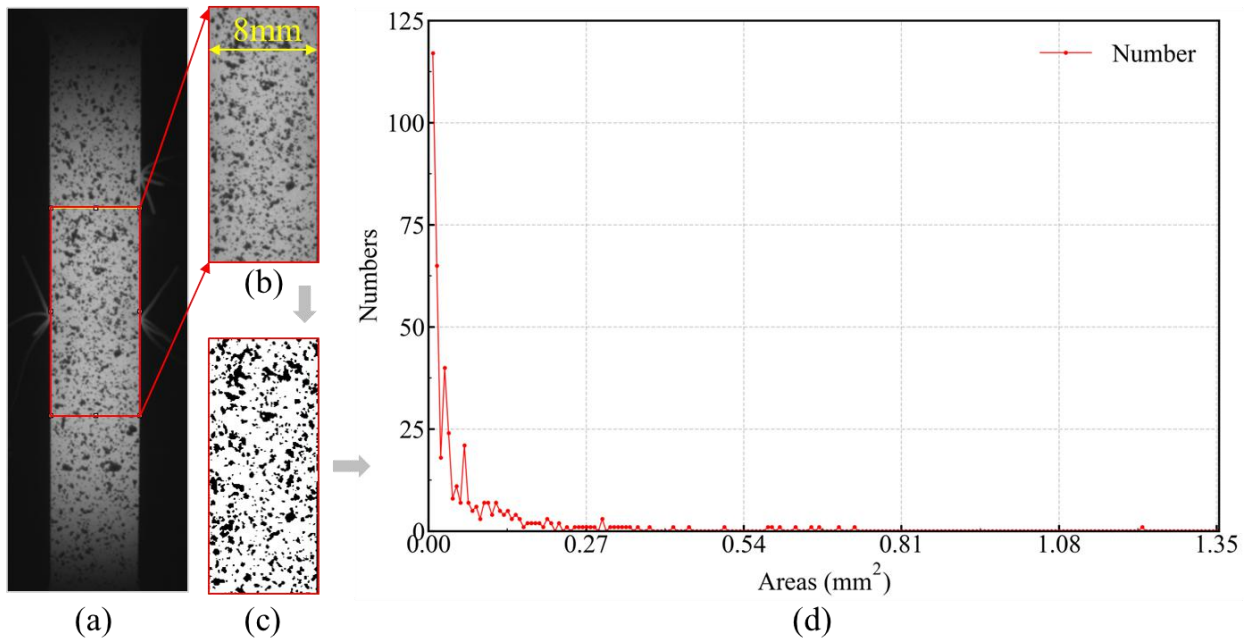


Fig. 7-3 Steps to summarize the dots areas in speckle, where (a): as-recorded image by DIC camera, (b): selected portion of the image of (a), (c) binary image of (b), and (d): number of dots in the speckle w.r.t. the dot areas.

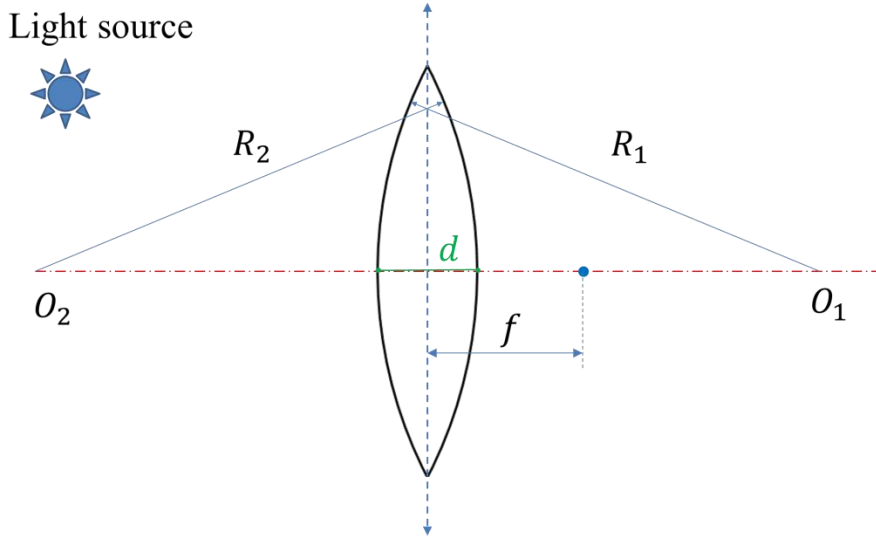
A. 4 Influence of Wavelength on a Shape Image for the Post-calibration

A. 4.1 Focal Length as a Function of Refractive Index

First of all, a short introduction of the focal length of a lens is given as the first brick. For simplicity, hemispherical lens is used for the explanation. Its focal length can be expressed by the lensmaker's equation expressed [138] as:

$$\frac{1}{f} = (n - 1) \left[\frac{1}{R_1} - \frac{1}{R_2} + \frac{(n-1)d}{nR_1R_2} \right] \quad (7-2)$$

where R_1 is the radius of curvature of the lens surface closer to the light source, R_2 is the radius of curvature of the lens surface farther from the light source, d is the thickness of the lens (the distance along the lens axis between the two surface vertices), n is the refractive index of the lens material, and f is the focal length of the lens at the side away from the light



source.

Fig. 7-4 Schematic illustration of hemispherical lens

From Eq. 7-2 it is very clear that when the refractive index increases, the focal length degrades.

A. 4.2 Refractive Index as Function of Wavelength

The refractive index depends on materials, but it is also a function of wavelength of the light for a given material, and this relation is modeled by the empirical Cauchy's equation:

$$n = A + \frac{B}{\lambda^2} + \frac{C}{\lambda^4} + \dots \quad (7-3)$$

Keeping only the first two items at the right hand side:

$$n = A + \frac{B}{\lambda^2} \quad (7-4)$$

It can be found that both A and B in Eq. 7-4 are positive [139]. Together with lots of experimental works it is quite clear that when the wavelength increases, the refractive index decreases [140]. When Eqs. 7-2 and 7-4 are considered at the same time, one can immediately see that when the wavelength increases, the focal length increases.

A. 4.3 Focusing Influenced by Wavelength

A basic optical background is that when an incident light is parallel to the optical axis, the refracted light always goes through the focal position. When the incident light goes through the lens center it does not change its direction.

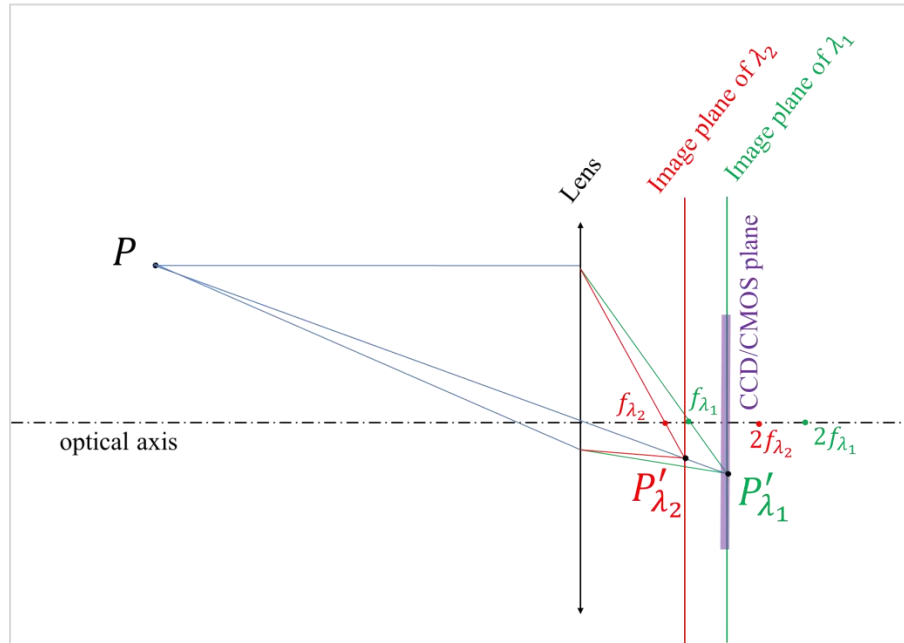


Fig. 7-5 Light path diagram at focusing state of a digital camera

A brief light path diagram for camera focusing is given in Fig. 7-5. Initially, the point P has an image at P'_{λ_1} when the light wavelength is λ_1 . And the CCD/CMOS of a digital camera is put at the image plane of λ_1 . When the wavelength is then changed to λ_2 with $\lambda_2 < \lambda_1$, the image point of P will be found in position of P'_{λ_2} , where the image plane of λ_2 is different from that of λ_1 (the focal distance f_{λ_2} is lower than f_{λ_1}).

Now let's come to Dedimet testing condition. The DIC cameras are focused at high temperature, which corresponds to the image plane of λ_1 . Because self-emitting is used, the emitted light is mainly red and orange: wavelengths are big. During the calibration, another light is used, and its wavelength is smaller than that of the self-emitted one, which corresponds to the image plane of λ_2 . That is why the focused DIC camera at testing condition loses its focusing at the calibration condition (at room temperature).

A. 4.4 Small Aperture Influences

Considering the condition in Fig. 7-5, we introduce Fig. 7-6, where we let CCD/CMOS at the image plane of λ_1 . When the point P is under light condition of λ_2 , if an aperture A-A is used, the image of P will be in range of P'_{λ_2} on image plane of λ_1 ; if a reduced aperture B-B is used, the image

of P will be in range of $P_{\lambda_2}^B$ on image plane of λ_1 . That's why when we use a smaller aperture, DIC camera can record clear images of grid for calibration.

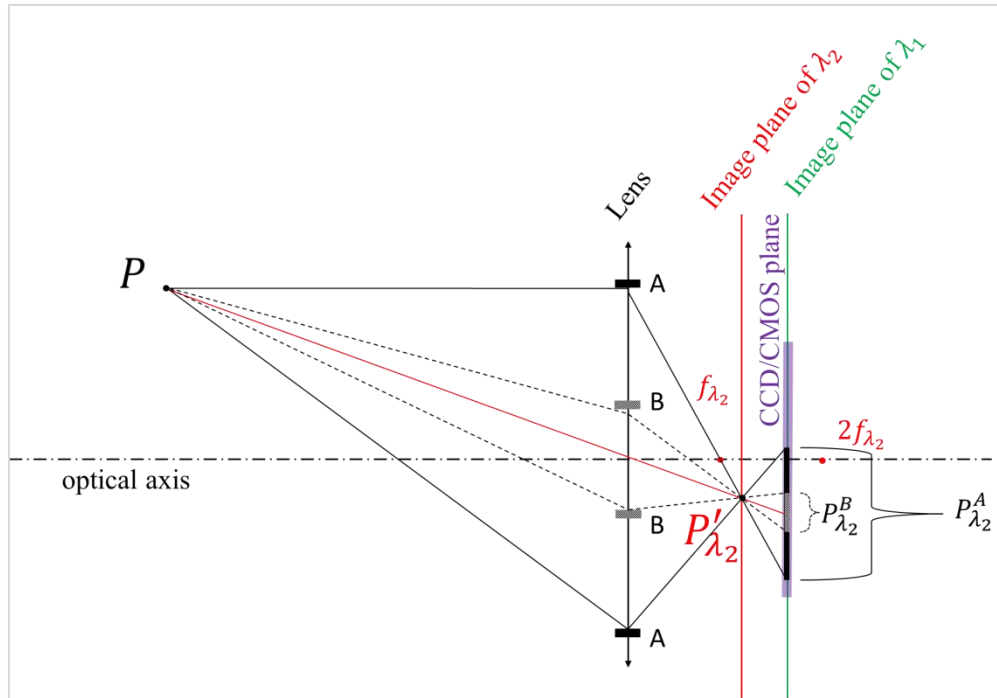


Fig. 7-6 aperture influence of clear image

That's why during the post calibration very small aperture must be used.

A. 5 Typical Temperature Variation during Test

Fig. 7-7 shows the temperature evolution of K3 when the center-positioned thermal couple K1 is used for controlling measured material point stable at 900°C with three pairs of loading and relaxation with various velocities and durations. It shows that the temperature variation at position measured by K3 is about 15°C , and this span is almost the measuring precision of the IR camera. Thus, it is reasonable not to impose the temperature field time step by time step.

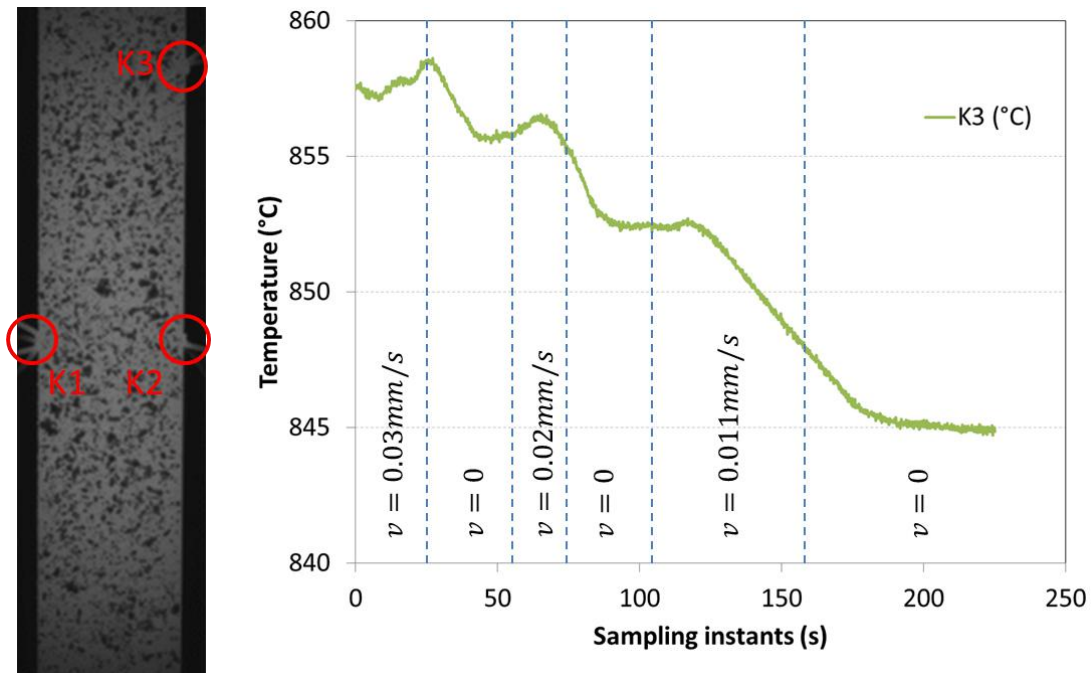


Fig. 7-7 Temperature variation at different loading velocities and durations when central point (K1) is controlled as constant 900°C

There are two advantages if T field is not updated step by step: firstly, the time-costing file-reading is avoided, which will save quite a little time for the direct simulation, and secondly, temperature field variation between two time steps could cause a sudden jump of simulation input, which makes the simulation consume more time for convergence.

If the thermal expansion is nevertheless considered, it could be found that the thermal strain component is about $17 \times 10^{-6} \text{K}^{-1} \times (15\text{K}) = 2.55 \times 10^{-4}$, which is negligible compared with the strain induced by the imposed velocity, refer to Fig. 4-8, and this is also good reason not to consider the updates of temperature field.

A. 6 Why We Can Deem That through the Thickness the Temperature Is Uniform

In the whole project we make an assumption that throughout the thickness of the sample the temperature is homogenous. This assumption is based on the following calculation as shown in the figure and by mathematical relations.

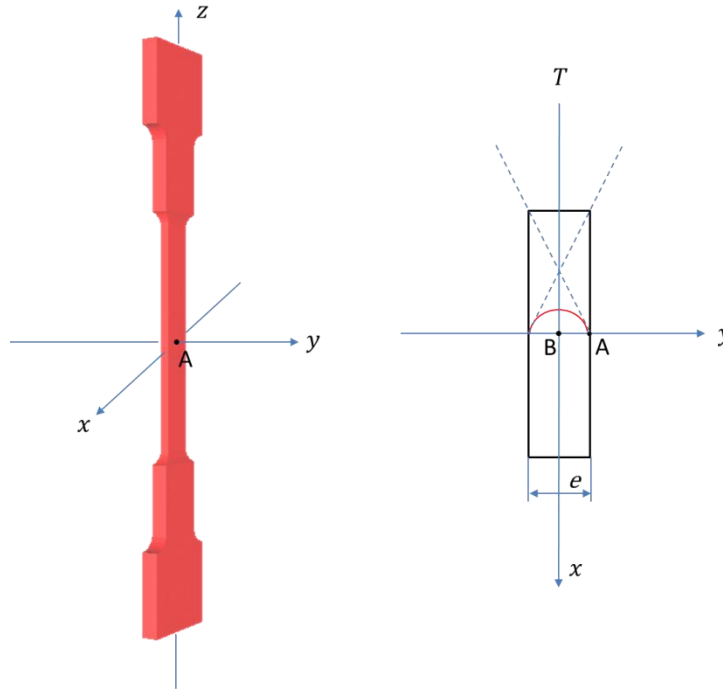


Fig. 7-8 Schematic image for explaining temperature gradient along thickness direction, where the thickness along y direction is $e = 2mm$

If we take a longitudinal cross section (x, y) of the sample, we have a rectangle as shown in Fig. 7-8, where the origin of the reference frame is set at the section center. So at point A we have the heat flux density by Fourier's law:

$$\mathbf{q} = -k_c \nabla T = -k_c \left(\frac{\partial T}{\partial x} \mathbf{i} + \frac{\partial T}{\partial y} \mathbf{j} + \frac{\partial T}{\partial z} \mathbf{k} \right) \quad (7-5)$$

where \mathbf{q} is the local heat flux density with unit of $W \cdot m^{-2}$, k_c is the conductivity of the material with unit of $W \cdot m^{-1} \cdot K^{-1}$, ∇T is the temperature gradient with unit of $K \cdot m^{-1}$, At point A (at the surface), and along y axis this leads to:

$$q = k_c \left. \frac{dT}{dy} \right|_{surface} \quad (7-6)$$

The flux exchanged with the environment is composed of two parts: the heat convection and heat radiation. The heat transfer by convection from the solid surface to the fluid (gas) can be modeled by:

$$q_{conv} = h_c (T - T_{gas}) \quad (7-7)$$

where h_c is the heat transfer coefficient, T_{gas} is the temperature of the surrounding fluid

Regarding radiation, we simply consider the specimen surface as a gray body:

$$q_{rad} = \sigma_{SB}\epsilon(T_{sur}^4 - T_{ext}^4) \quad (7-8)$$

where σ_{SB} is the Stefan–Boltzmann constant whose value is $5.670367 \times 10^{-8} \text{W} \cdot \text{m}^{-2} \cdot \text{K}^{-4}$, ϵ is the emissivity, T_{ext} is the temperature of Dedimet chamber walls.

Based on the heat flux through the surface should be equilibrium, instantly we have:

$$q = q_{conv} + q_{rad} \quad (7-9)$$

So

$$\left. \frac{dT}{dy} \right|_{surface} = \frac{1}{k_c} [h_c(T - T_{gas}) + \sigma_{SB}\epsilon(T^4 - T_{ext}^4)] \quad (7-10)$$

Taking $T = 1273\text{K}$ (1000°C) and $T_{ext} = T_{gas} = 298\text{K}$ (25°C) for example, from literature [93,141,142], we can take the following values:

$$k_c = 26 \text{W} \cdot \text{m}^{-1} \cdot \text{K}^{-1}$$

$$h_c = 25 \text{W} \cdot \text{m}^{-2} \cdot \text{K}^{-1}$$

$$\epsilon = 0.85$$

It can be calculated:

$$\left. \frac{dT}{dy} \right|_{surface} = \left. \frac{dT}{dy} \right|_{y=0.001} \approx 5800 \text{K} \cdot \text{m}^{-1} \quad (7-11)$$

The heat equation is:

$$\rho c_p \frac{\partial T}{\partial t} - \nabla \cdot (k_c \nabla T) = \dot{q}_V \quad (7-12)$$

where $\rho = 8190 \text{kg} \cdot \text{m}^{-3}$, $c_p = 435 \text{J} \cdot \text{kg}^{-1} \cdot \text{K}^{-1}$, and \dot{q}_V is the volumetric heat source with unit of $\text{J} \cdot \text{m}^{-3} \cdot \text{s}^{-1}$, in this case it is the Joule heat input. If the quasi-steady state ($\partial T / \partial t = 0$) and $1D$ along y is further considered, immediately it can be obtained:

$$\frac{\partial^2 T}{\partial y^2} = C_0 \quad (7-13)$$

where C_0 is an unknown constant. With boundary conditions:

$$\begin{cases} T|_{y=0.001} = 1273K \\ \frac{\partial T}{\partial y}|_{y=0} = 0 \\ \frac{\partial T}{\partial y}|_{y=0.001} = 5800K \cdot m^{-1} \end{cases} \quad (7-14)$$

Then within the material along the y direction the temperature is expressed as (i.e. the special solution of Eq. 7-13):

$$T = -2.90 \times 10^6 y^2 + 1276 \quad (7-15)$$

A temperature difference of 3.0°C is found between the surface and the center. Note that we took $\epsilon = 0.85$, which is a high emissivity value. It can be thought that this 3.0°C estimation is an upper bound for the temperature difference.

In our test we use the K type thermocouple to measure the temperature. This kind of thermocouple has a precision of $\pm 2.2^\circ\text{C}$ or $\pm 0.75\%$, whichever is greater. The testing temperature is at 1000°C and the measuring bias would be about 7.5°C which is bigger than the calculated 3.0°C . Besides, the temperature measured by the infrared camera has even a bigger bias. Thus we could consider that through the thickness the temperature is uniform.

A. 7 Data Smoothing Method for Displacement

From experiments analyzed by DIC method (VIC-3D), the displacement field along the surface of the sample can be obtained. Then, at a considered material point (from DIC sensor), the velocity can be derived from the displacement fields by function:

$$\mathbf{v}_i = \frac{\mathbf{u}_i - \mathbf{u}_{i-1}}{t_i - t_{i-1}} \quad (7-16)$$

where \mathbf{v}_i is the velocity of a material point at sampling instant i , \mathbf{u}_i and \mathbf{u}_{i-1} are the displacements of a material point at sampling instant i and $i - 1$, and t_i and t_{i-1} are the time at sampling instant i and $i - 1$, respectively.

It can be obviously known that during sampling the displacement field there is measurement error (we take only precision error into account) which could be deemed as a fix range. If we simply

use Eq. 7-16 for calculating the velocity from raw data of displacement from Fig. 7-9 (a) we find that velocity evolves with time as shown in Fig. 7-10 (red triangles).

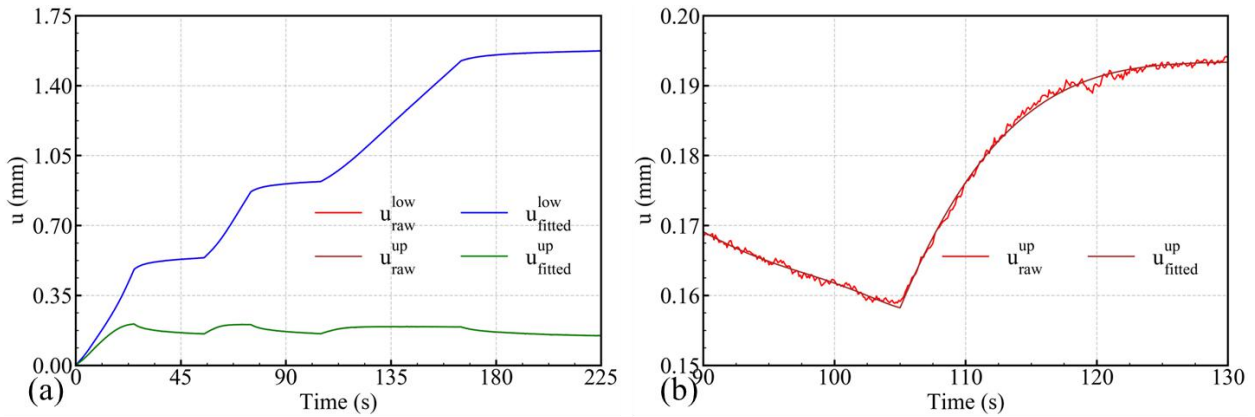


Fig. 7-9 Test at nominal temperature of 900°C: (a) fitted and raw displacement of up and low boundaries of ZOI along loading direction, and (b): the zoom in time domain of 90 – 130s for upper boundary of ZOI

It can be seen from Fig. 7-9 (a) that even though the displacement along the loading direction seems smooth, the velocity in Fig. 7-10 is definitely not smooth. The reason for this kind of strong oscillation is that the displacement is not really smooth, as shown in Fig. 7-9 (b). Imposing such a velocity boundary condition into the simulation would induce severe oscillations in terms of strain rate and possible non-convergence. The frequent jumping of the velocity will also reduce the simulation speed, i.e. costing more time for convergence. No doubt that for an efficient optimization the displacement should be smoothed to generate smoother velocity boundary conditions. On this objective, the following method has been developed.

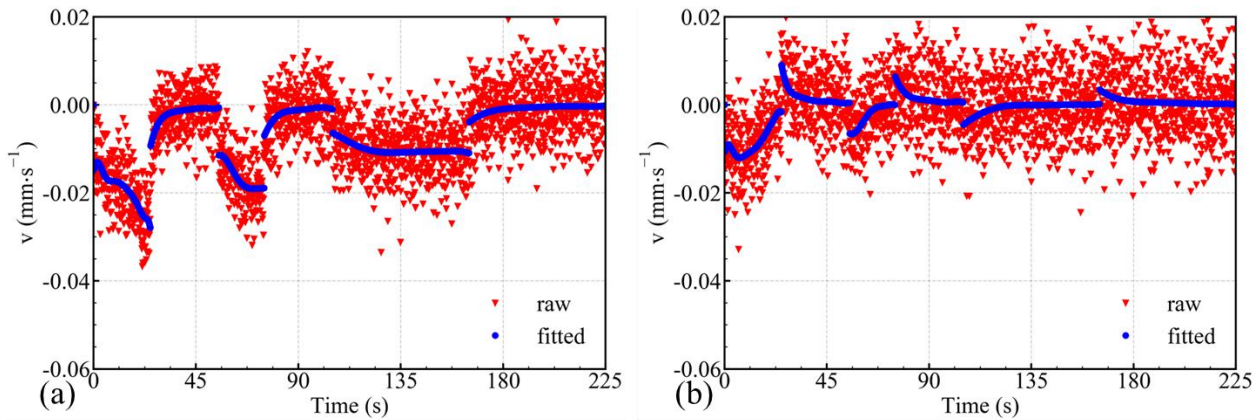


Fig. 7-10 Comparison of velocity component along loading direction using Eq. 7-16 based on raw (red triangles) and fitted (blue dots) displacement data at (a): upper boundary, and (b): lower boundary of the ZOI shown in Fig. 2-17.

Two series of raw data are obtained from DIC result, which are the z component of the displacement of the lower boundary (u_z^{low}), z component of the displacement of the upper boundary (u_z^{up}). It is reminded here that those two quantities u_z^{low} and u_z^{up} result from an average operated on a

certain number (generally 7) of sensors belonging to two lines: one line at the top of the ZOI and one line at the bottom. Then, at any sampling time, the length of ZOI (Δl^{ZOI}) can be calculated as:

$$\Delta l^{ZOI} = u_z^{low} - u_z^{up} \quad (7-17)$$

We could fit any of the two. Then how do we select the to-be-fitted data? Firstly and most important, from analysis one can see that the temporal evolution of Δl^{ZOI} is the real boundary condition, and the velocities extracted from u_z^{low} and u_z^{up} are in fact the way to realize this evolution of Δl^{ZOI} , so Δl^{ZOI} must be fitted. Besides, we select the other one based on the relative measuring error. As we discussed before, the precision measurement error could be somewhat a constant range. Thus when the displacement is big, the relative error is small, and on the contrary, when the displacement is small, the relative error is big. Fig. 7-9 (a) presents the displacement components of the upper boundary and lower boundary along the loading direction. Clearly, the lower boundary moves much more than the upper boundary. From the view of measuring error, the lower boundary will give a better relative precision and should be chosen as the second to-be-fitted data.

With the above analysis, for any sampling instant indexed with i , using u and v rather than u_z and v_z to simplify the expression, the master-slave fitting method is organized as follows:

S1 – extract u_i^{up} , u_i^{low} and t_i , and calculate Δl_i^{ZOI} by Eq. 7-17

S2 - fit u_i^{low} and Δl_i^{ZOI} separately, to get \hat{u}_i^{low} and $\hat{\Delta l}_i^{ZOI}$

S3 - calculate $\hat{u}_i^{up} = \hat{u}_i^{low} - \hat{\Delta l}_i^{ZOI}$

S4 - derive v_i^{up} and v_i^{low} based on \hat{u}_i^{up} and \hat{u}_i^{low} , separately via Eq. 7-16.

Fig. 7-10 shows that there are several sections within one test, which are loading 1, 2, 3 and relaxation 1, 2, 3. No doubt that the fitting should be done section by section, with a constraint of continuity at section junctions.

For each section, an M-ordered polynomial fitting is taken as estimator for Step 2:

$$\hat{u}_i = \sum_{m=0}^{M-1} p_m \cdot t_i^m \quad (7-18)$$

The parameters p_m in the expression are determined by a constrained Least Squares Methods (LSM) with L2 regularization and Lagrange multipliers, i.e.

$$arg_{min} := \underbrace{\sum_{i=0}^{l-1} (\hat{u}_i - u_i)^2}_{part1} + \underbrace{\mu \cdot \sum_{m=0}^{M-1} p_m^2}_{part2} + \underbrace{2 \cdot \lambda_0 \cdot (\hat{u}_0 - u_0) + 2 \cdot \lambda_1 \cdot (\hat{u}_{l-1} - u_{l-1})}_{part3} \quad (7-19)$$

where I is the number of time steps considered.

On the right side of Eq. 7-19, the first part is the LSM component to be minimized, the second part is the L2 regularization to avoid over-fitting with a prescribed positive parameter μ , and the part 3 are for the continuity at the junction positions with Lagrange multipliers.

By calculating:

$$\begin{cases} \frac{\partial arg_{min}}{\partial p_m} = 0 \\ \frac{\partial arg_{min}}{\partial \lambda_0} = 0 \\ \frac{\partial arg_{min}}{\partial \lambda_1} = 0 \end{cases} \quad (7-20)$$

The parameters can be determined by resolving this linear function set. All the functions were coded via Python. The comparison between the raw velocity and the fitted velocity is shown in Fig. 7-10, in blue dots.

A. 8 Improvement Work since the Beginning of the Project

A. 8.1 Automatic Changing of Temperature Control Signal

On Dedimet we have different channels for temperature measurement. For example, we have channels for K type thermo-couple, we have channels for R type thermo-couple, and we have also a channel for the bichromatic pyrometer (BP). At any moment we need to select a channel as the signal to control the temperature routine when we heat the sample loaded in the Dedimet chamber, and this signal is put into a PID algorithm as the feedback.

Generally, at any instant, only one of the temperature signals should be used for temperature control, because in our case we do not need to control the temperature distribution, but just at a selected location of interest. For practical reasons we weld the K type thermo-couple directly on the sample to measure the temperature, because this generates a good measurement thanks to the good heat conductivity at the welding position (noticing that there are some other factors that could influence the temperature measurement, e.g. the potential on the welding point, but it is not discussed here). And the K type has a measuring range that varies from room temperature (RT) till 1200°C. This kind of thermo-couple will deteriorate when the temperature is higher than 1250°C. So we just use it for the measurement in the range of RT to 1200°C. Then what should we do when the temperature is higher than 1200°C?

With R type thermo-couple we can carry out the measurement at a temperature higher than 1200 °C, but R type thermo-couple is very expensive and we cannot use it in the way that we mention before, i.e. welding it onto the sample, because each time when the test is accomplished we

need to remove the thermo-couple and this will cause a severe loss of money. The solution is to use the BP, which is designed to measure elevated temperatures, for example from 700 °C to 1400°C.

The BP with two working wave lengths is considered not to be influenced by the emissivity but there is yet a variable coefficient, the " $\frac{\epsilon_{\lambda_2}}{\epsilon_{\lambda_1}}$ " in Eq. 2- 15, so that the measuring could be compared and calibrated with respect to other methods, for example , the thermo-couple. Let's see an example on CRES340 alloy, when the sample temperature at the control point is read 900°C on the thermo-couple, the reading on the BP is 870°C, and we must adjust the coefficient so that the reading by the BP is 900°C, too. However, when we measure another sample made of Inconel 718, the calibration coefficient could be a different value. The method proposed hereafter resolves this problem by avoiding adjusting this coefficient.

By the electronical design, what we finally get in Dedimet is the voltage on the resistance which is connected to the current output of BP in series. If we plot the temperature measured by thermo-couple as a function of the voltage of the BP, we get a rather good linear relation, which gives a way to fix the problem.

The idea is as follows, at any moment i:

- when the temperature measured by thermo-couple (T_{tc}^i) is lower than a value (T_{start} , e.g. 900°C), we use the thermo-couple signal for controlling;
- when the $T_{tc}^i > T_{start}$, we start to record the T_{tc}^i and the voltage of BP (U_{bp}^i) into two arrays, we still use the thermo-couple signal for controlling;
- when the temperature measured by thermo-couple (T_{tc}^i) is higher than a value (T_{end} , e.g. 1200°C), we stop recording T_{tc}^i and U_{bp}^i , and we fit these two data array in the way that T_{tc}^i is a linear function of U_{bp}^i , and we obtain the relation. Then we calculate the temperature with the U_{bp}^i based on the fitted relation. Now we use the BP signal for the controlling;
- for the rest of the test, temperature will all be controlled by BP signal, whatever the temperature is.

By the above four steps, we now do not need to adjust the coefficient every time. What is better is that the control signal is changed to the wanted one automatically. If we conduct a test from RT to 1300°C, for example, we can simply take the test, and from RT to 1200°C temperature is controlled by thermo-couple, and from 1200 to 1300 it is controlled by the BP.

Noticing: we need to select a start temperature not too low. Generally speaking it would be good to select this temperature value greater 900°C, because at this temperature the surface state of the sample is stable. In other words, the oxidation surface state is stable, which makes the measurement more precise.

A. 8.2 Water Cooling System

We introduce the water cooling system in order to get more precise temperature measurement as well as better protection of the force sensor.

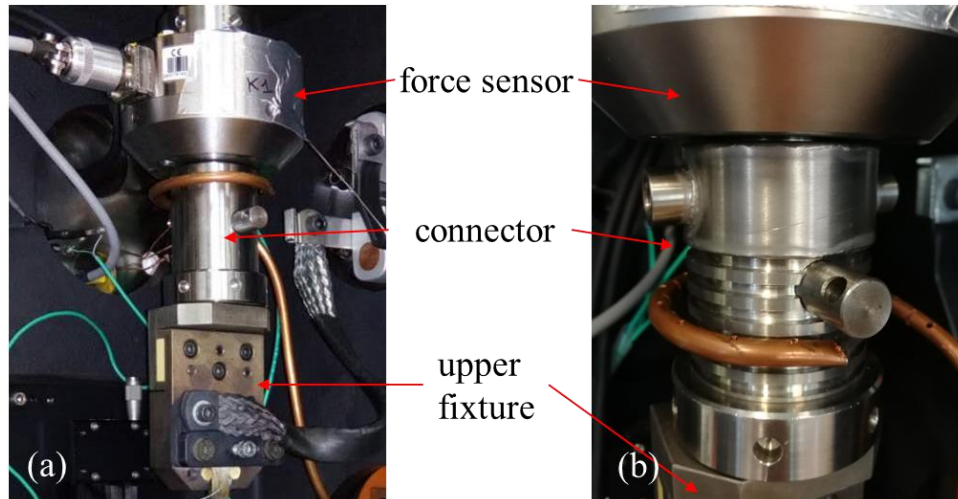


Fig. 7-11 Original connector (a) and water-cooling connector (b) for force sensor in Dedimet

The original connector between the force sensor and the upper fixture (Fig. 7-11 a) was of smooth surface, and we used only a curved copper tube with holes to cool down the connector so that the force sensor is not overheated by the sample. The testing result revealed that the smooth connector didn't work well, so the connector was machined to a fin-bar shape, which is a passive heat sink (Fig. 7-11 b). With this kind of fin-shape the cooling became a little better, however we still have a severe problem of the precise temperature control: the temperature of the sample became very un-stable because of the convection introduced by the injected compressed air onto the fin-shape connector. In Fig. 7-12, it can be seen that the oscillation introduced by the convection is quite important. Thus the water cooled connector was finally chosen as the solution.

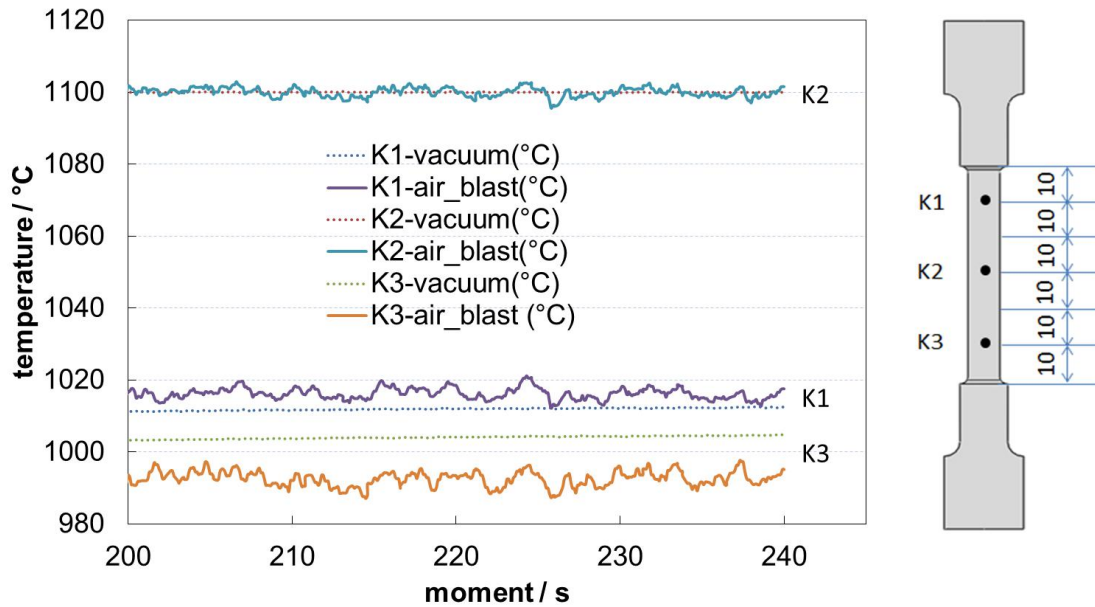


Fig. 7-12 Measured temperature at different positions with air blasting or with vacuum within one test

A. 8.3 Blue Lighting System

The blue lighting system is used to measure the displacement field of the sample at high temperature according to the literatures. With this light source together with band-pass filter we can measure displacement field from room temperature until 1400°C.

If we do not use the blue light, when the temperature reaches 800°C the correlation calculation fails because the contrast between the base and the speckle is fading, as is shown in Fig. 7-13

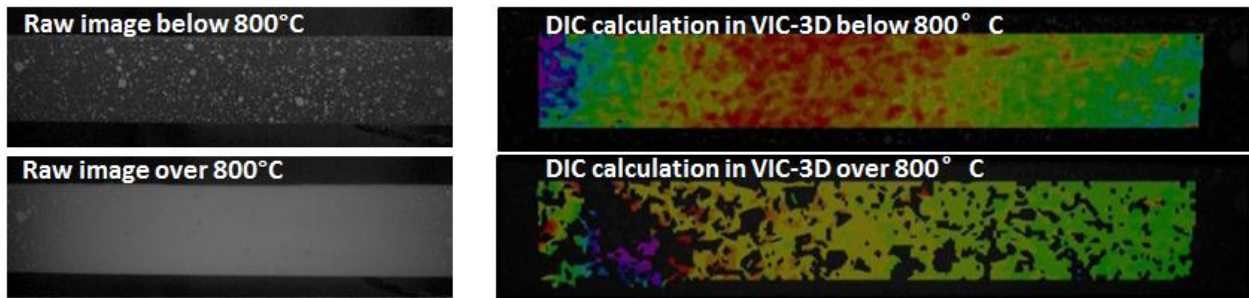


Fig. 7-13 DIC results analyzed by VIC-3D for temperatures under and over 800°C without a blue lighting system

It is obvious that in Fig. 7-13 the speckle cannot be seen, which induces the correlation failure. One way to resolve the afore-mentioned problem is to use the laser speckle technique [143], which was proved to be reasonable for high temperature measuring in previous work in Cemef [70]. A possible alternative is to use monochromatic lighting source with a wave length which is much shorter than the peak wave length of the spectrum radiated from the sample together with a band-pass filter of the same wave length of the lighting source [60,61,62]. Fig. 7-14 shows the

monochromatic emissive power of black body, and for the gray body it has the same shape but lower amplitude [144,145]. A LED matrix provides a peak wave length of 430 nm for lighting, and a band-pass filter with a peak wave length of 432 nm is used to filter down the un-wanted wave length, and the wave length position is shown in the blue band in Fig. 7-14. With all being setup, the camera is able to capture the speckle on the sample as if it didn't emit any light, making it possible for the DIC analysis, at least from a theoretical part of view.

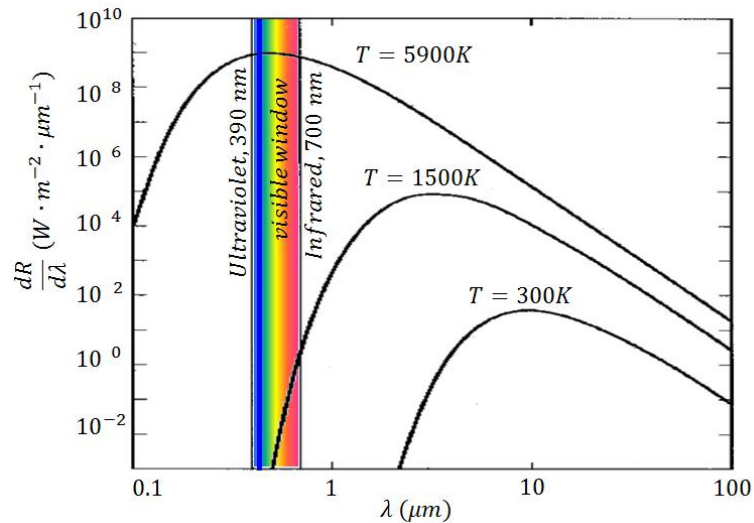


Fig. 7-14 Selected wave length (blue band) in the monochromatic emissive power of black body

All the above are from literature. However when we took all these into consideration, and we set up the blue LED system with band-pass filters, we found that the measurement of the displacement was not so good as presented in the literature, i.e. with the blue light system we can extend measuring the displacement up to 900 °C which is better than the previous 800°C limitation, but when the temperature is higher than 900°C, again we encountered the same problem as if we do not had the blue lighting system. Then when the temperature is higher than 900°C we simply use the light emitted from the sample as the lighting source, which turned to be a good solution.

A. 9 Infrared Camera Coordinates, from Pixels to Millimeters

The bichromatic infrared camera records the temperature field in the unit of pixel for the coordinates. But in our simulation it is in unit of millimeters. In this section we discuss how to convert pixels into millimeters. The infrared camera records in a 2D form, so we need to get the two factors of the transformation. The calibration target used in DIC calibration is used here.

Step 1, a sample is loaded, and then adjustment of the infrared camera is taken so that the axis of the camera is along the normal direction of the sample center, as shown in Fig. 7-15 (a). Then, rotate the camera to ensure that the sample is vertically seen in the IR camera client, as shown in Fig. 7-15 (b).

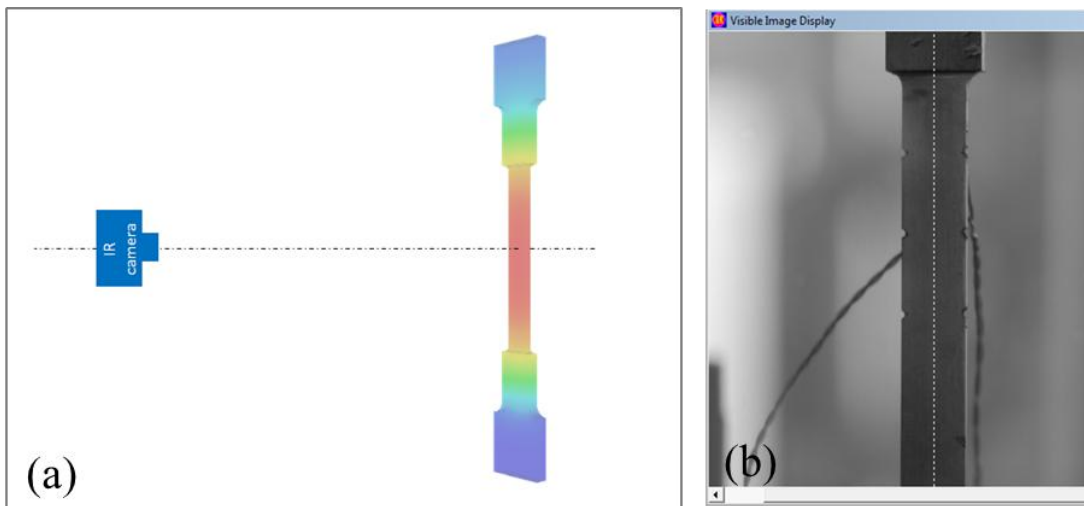


Fig. 7-15 Infrared camera positioning: (a) normality, and (b) alignment

Step 2, the DIC target is flatly set on the sample, making sure that the point matrix is horizontal and vertical. Then an image is recorded by the visible light signal in the infrared camera, as seen in Fig. 7-16.

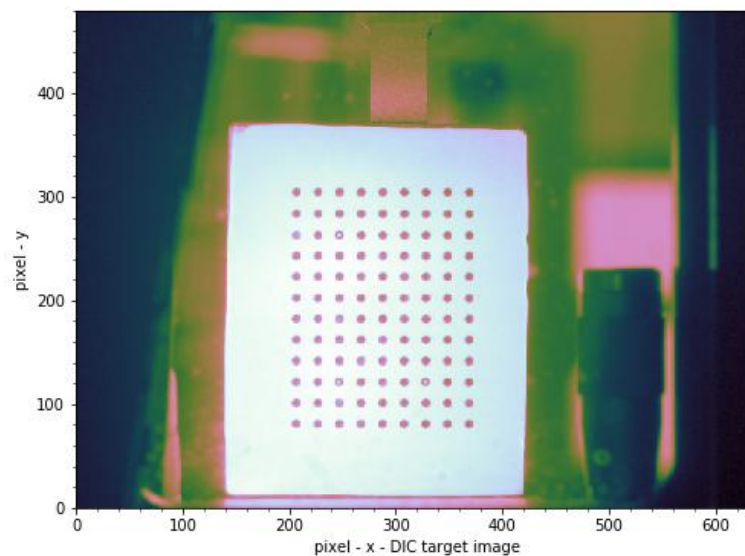


Fig. 7-16 Image of the target

Step 3, the points are extracted from the target as shown in Fig. 7-17, and the left and right pixel boundaries of the points are found, refer to Fig. 7-18. With the up-low and left-right boundaries a series of rectangles can be defined, as shown in Fig. 7-18.

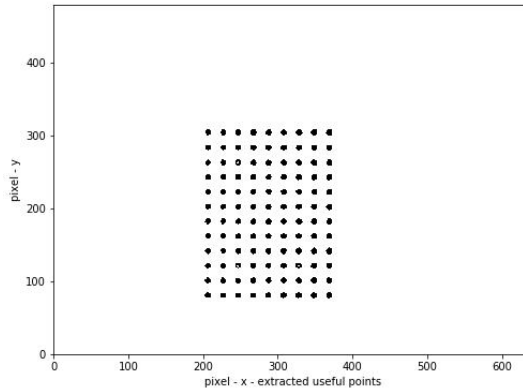


Fig. 7-17 Extracted image of the points in the target

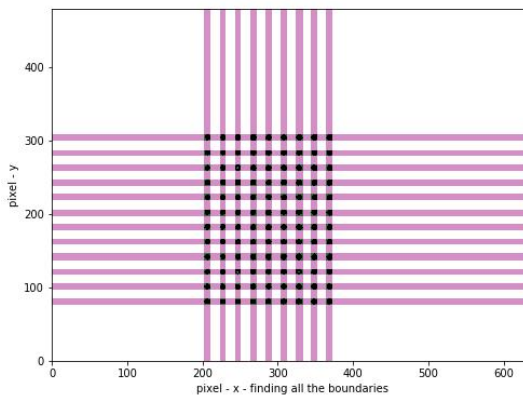


Fig. 7-18 Up-low and left-right boundaries of all the points in the target

Finally the central positions of the rectangles are calculated, and the horizontal and vertical distances between neighboring points are calculated, and then wholly averaged in unit of pixels. Then by using the known distance between each points of the target (for example, 3mm), we can calculate the ratio between pixel and millimeters.

A. 10 Optimization within Orientation Based on von Mises

In Chapter 4 a comparison of experimental and simulated forces in orientation 1 is already given, but in one unique chart. Here all the 5 orientations are given, for each temperature level the scale is adjusted so that one can see clearly the difference between experimental and simulated values. The parameters used in the simulations are determined by optimization based on force only. The optimizations were based on von Mises hypothesis, and were carried out within each orientation at all 4 temperature levels.

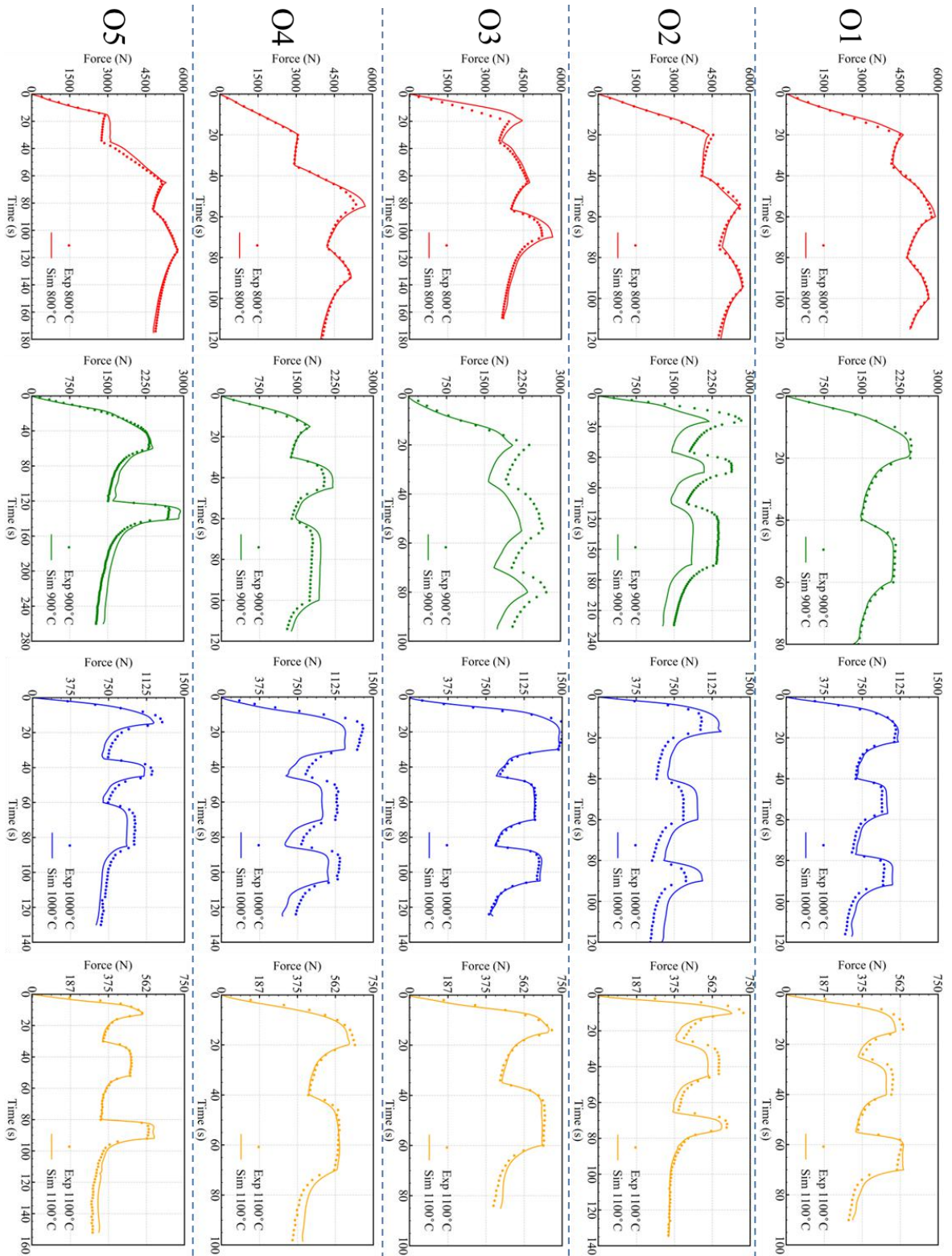


Fig. 7-19 Experimental (dots) and simulated (solid line) force of orientations 2, 3, 4 and 5 at 4 temperature levels

A. 11 Calculating Lankford Coefficient

The experimental Lankford Coefficient in this work is defined as:

$$r^{exp} = \frac{\varepsilon_{xx}^{exp}}{-\left(\varepsilon_{xx}^{exp} + \varepsilon_{zz}^{exp}\right)} \quad (7-21)$$

where ε_{xx}^{exp} and ε_{zz}^{exp} are the overall strain components along width direction and length direction, respectively, with reference frame as shown in Fig. 3-5 (c).

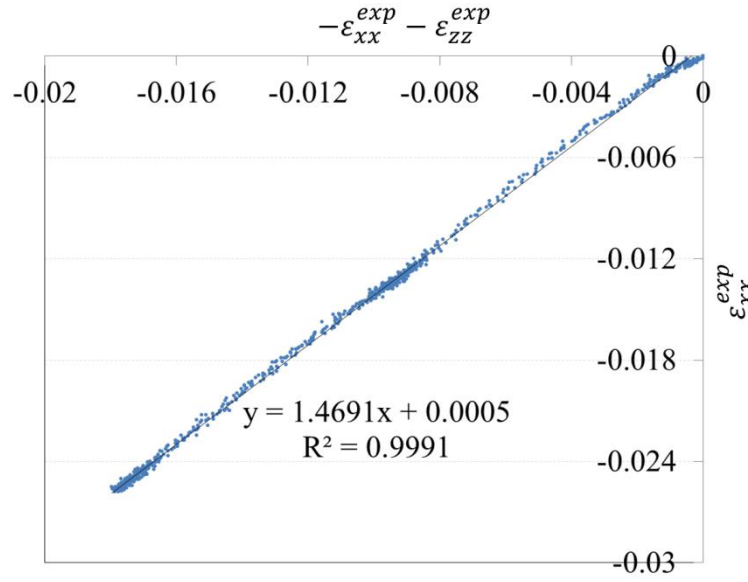


Fig. 7-20 Plotting of ε_{xx}^{exp} as function of $(-\varepsilon_{xx}^{exp} - \varepsilon_{zz}^{exp})$ of Orientation 1 at 900°C

Fig. 7-20 presents a typical experimental plot of the relation between ε_{xx}^{exp} and $(-\varepsilon_{xx}^{exp} - \varepsilon_{zz}^{exp})$. One can see that the global relation is linear, only at the beginning there is deviation from the global linear trend where pure elastic deformation happens. Taking the linear fitting, one can get the averaged experimental Lankford coefficient \bar{r}^{exp} . For the case in Fig. 7-20, $\bar{r}^{exp} = 1.47$.

When plastic deformation is not too small, i.e. the elastic deformation is negligible compared with plastic deformation, i.e. $\varepsilon_{xx}^{exp} \approx \varepsilon_{xx}^{exp,vp}$, $\varepsilon_{yy}^{exp} \approx \varepsilon_{yy}^{exp,vp}$ and $\varepsilon_{zz}^{exp} \approx \varepsilon_{zz}^{exp,vp}$, one can use the volume conservation relation of plasticity to estimate ε_{yy}^{exp} as:

$$-\left(\varepsilon_{xx}^{exp} + \varepsilon_{zz}^{exp}\right) \approx \varepsilon_{yy}^{exp} \quad (7-22)$$

Injecting Eq. 7-22 into Eq. 7-21, together with Eq. 5-3, we will have:

$$r^{exp} = \frac{\epsilon_{xx}^{exp}}{-(\epsilon_{xx}^{exp} + \epsilon_{zz}^{exp})} \approx \frac{\epsilon_{xx}^{exp}}{\epsilon_{yy}^{exp}} \approx \frac{\epsilon_{xx}^{exp,vp}}{\epsilon_{yy}^{exp,vp}} = \frac{\dot{\epsilon}_{xx}^{exp,vp}}{\dot{\epsilon}_{yy}^{exp,vp}} = r^{exp,vp} \quad (7-23)$$

Eq. 7-23 shows that the experimental Lankford coefficient (r^{exp}) and experimental viscoplastic Lankford coefficient ($r^{exp,vp}$) should be close but different, and should be close to the theoretical one ($r^{theo,vp}$).

The experimental Lankford coefficient field is calculated by two steps:

- Select the point matrix in the DIC result image, and output the strain components;
- For each point, the strain information is used to calculate the averaged experimental Lankford coefficient \bar{r}^{exp} , as prescribed just above (Fig. 7-20). Then interpolation of the values in a 2D map is carried out.

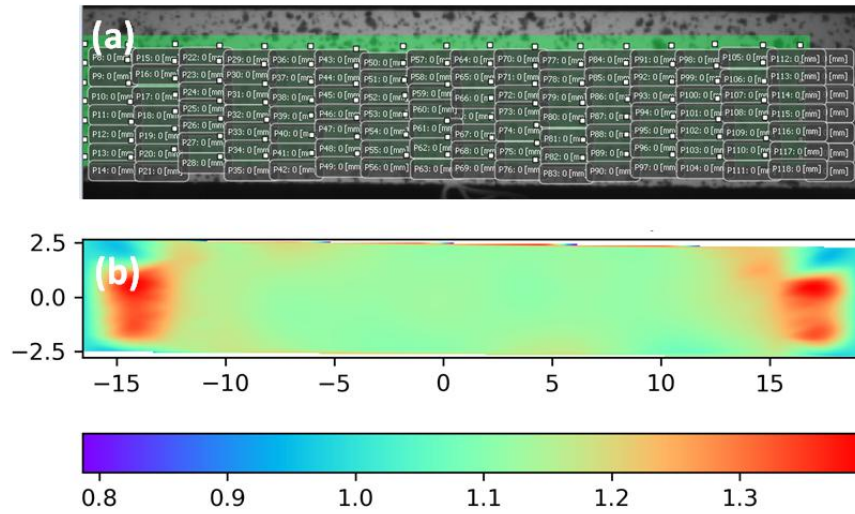


Fig. 7-21 (a): Selected points to calculate \bar{r}^{exp} values, and (b): interpolated 2d \bar{r}^{exp} map

In the DIC result, a matrix of points can be selected, as shown in Fig. 7-21 (a). Also in Fig. 7-21(a) a minimum rectangle to cover all the points can be found, and this rectangle is the plotting boundary in Fig. 7-21(b). The way to interpolate the information is based on the Python package ‘scipy.interpolate.griddata’, with the method ‘cubic’ [146]. In precise introduction: for each point, the \bar{r}^{exp} value is defined as 1 as initial value. When the linear regression is finished, if the regression coefficient is greater than 0.99, the \bar{r}^{exp} at the point is assigned with the slope of the linear regression, if not, the \bar{r}^{exp} value remains 1. Afterwards comes the interpolation. Then the \bar{r}^{exp} map is obtained.

Similarly, the simulated Lankford coefficient is defined as:

$$r^{sim} = \frac{\epsilon_{xx}^{sim}}{-(\epsilon_{xx}^{sim} + \epsilon_{zz}^{sim})} \quad (7-24)$$

The corresponding averaged simulated Lankford coefficient is noted as \bar{r}^{sim} .

As database, the averaged experimental Lankford coefficients of all the orientations at all temperature levels are given below:

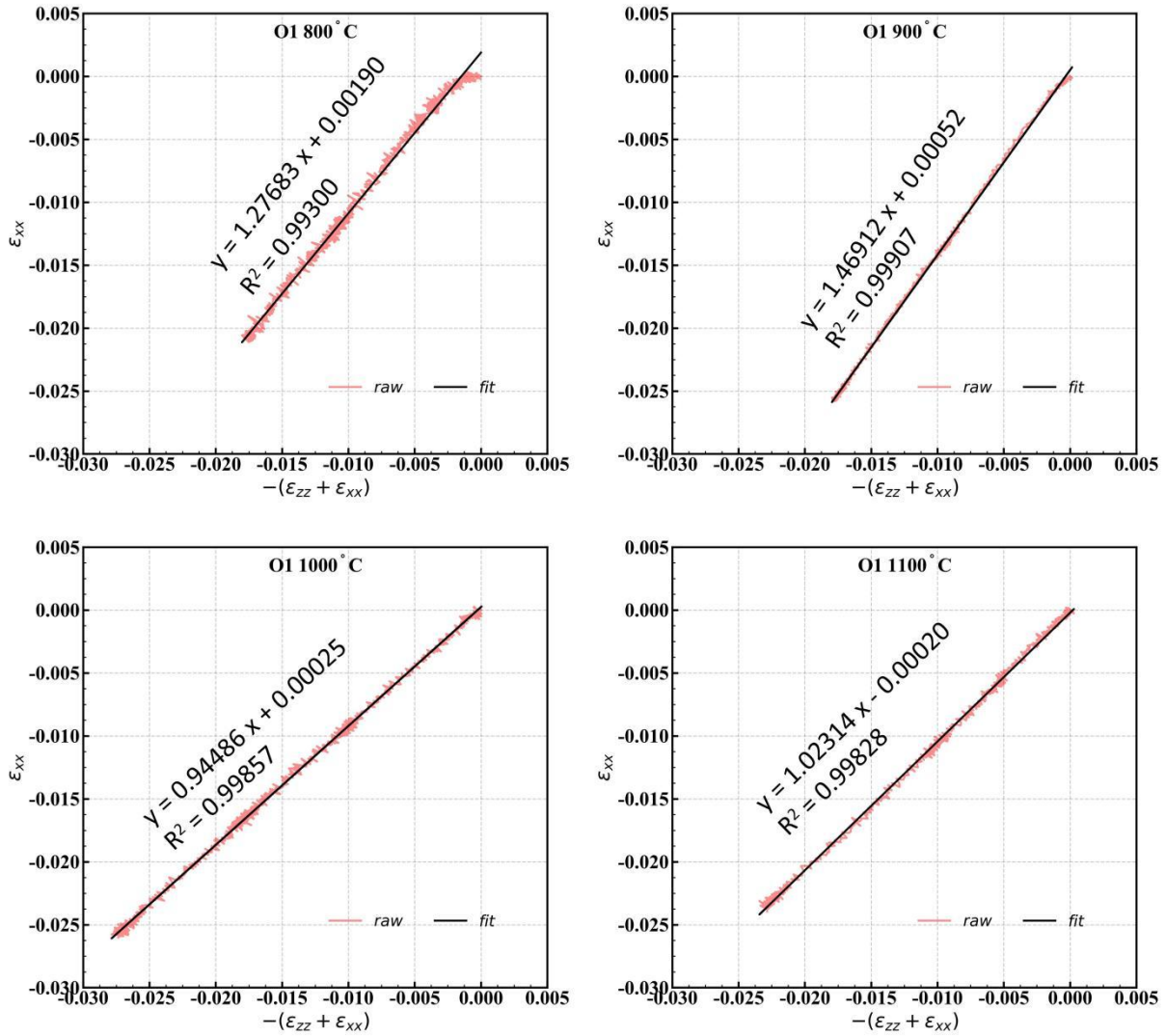


Fig. 7-22 Plotting of ϵ_{xx}^{exp} as function of $(-\epsilon_{zz}^{exp} - \epsilon_{xx}^{exp})$ of Orientation 1 at the four temperature levels (in red) v.s. the fitted straight curve with slope, i.e. the averaged Lankford coefficient (in black)

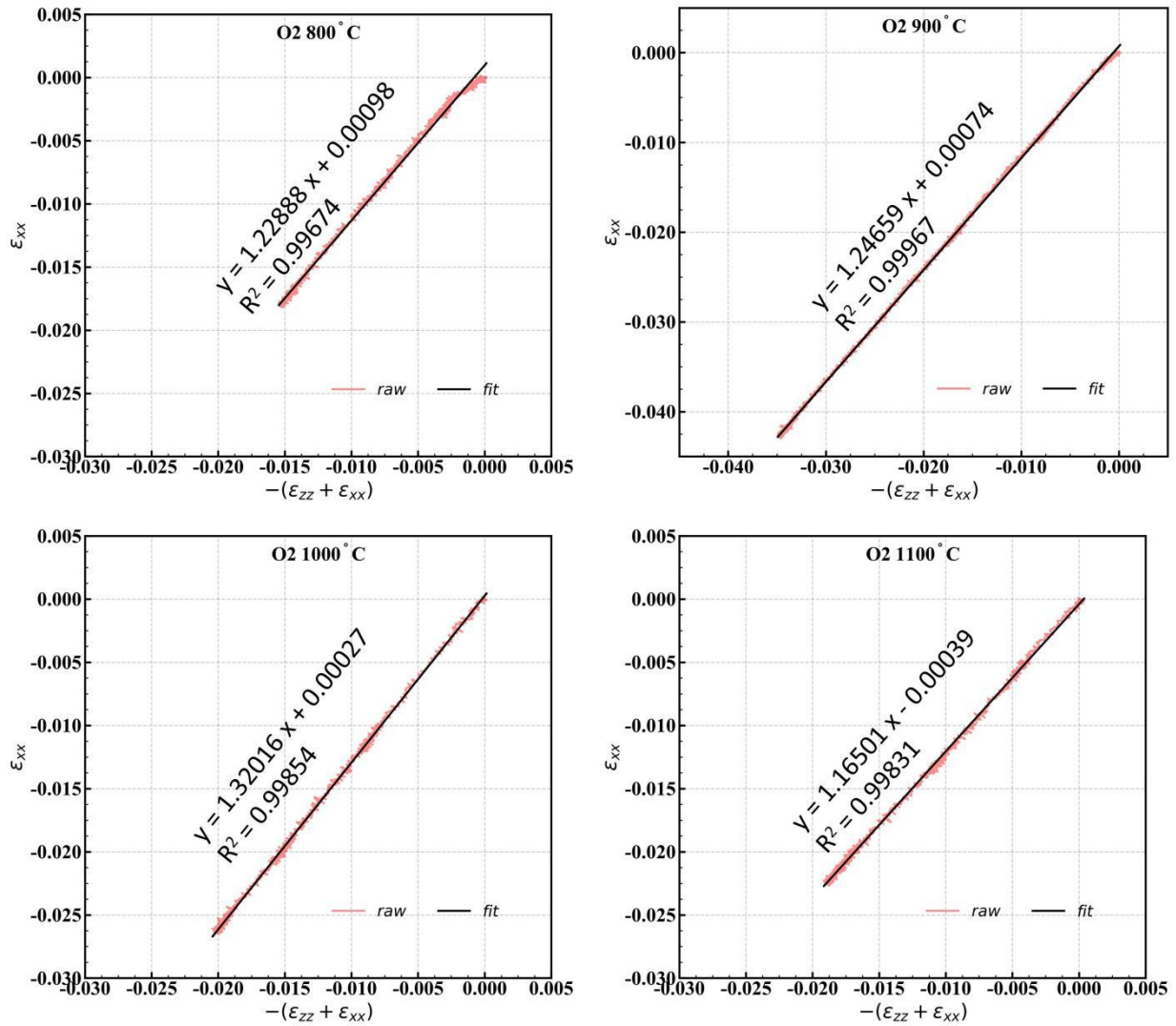


Fig. 7- 23 Plotting of ϵ_{xx}^{exp} as function of $(-\epsilon_{xx}^{exp} - \epsilon_{zz}^{exp})$ of Orientation 2 at the four temperature levels (in red) v.s. the fitted straight curve with slope, i.e. the averaged Lankford coefficient (in black)

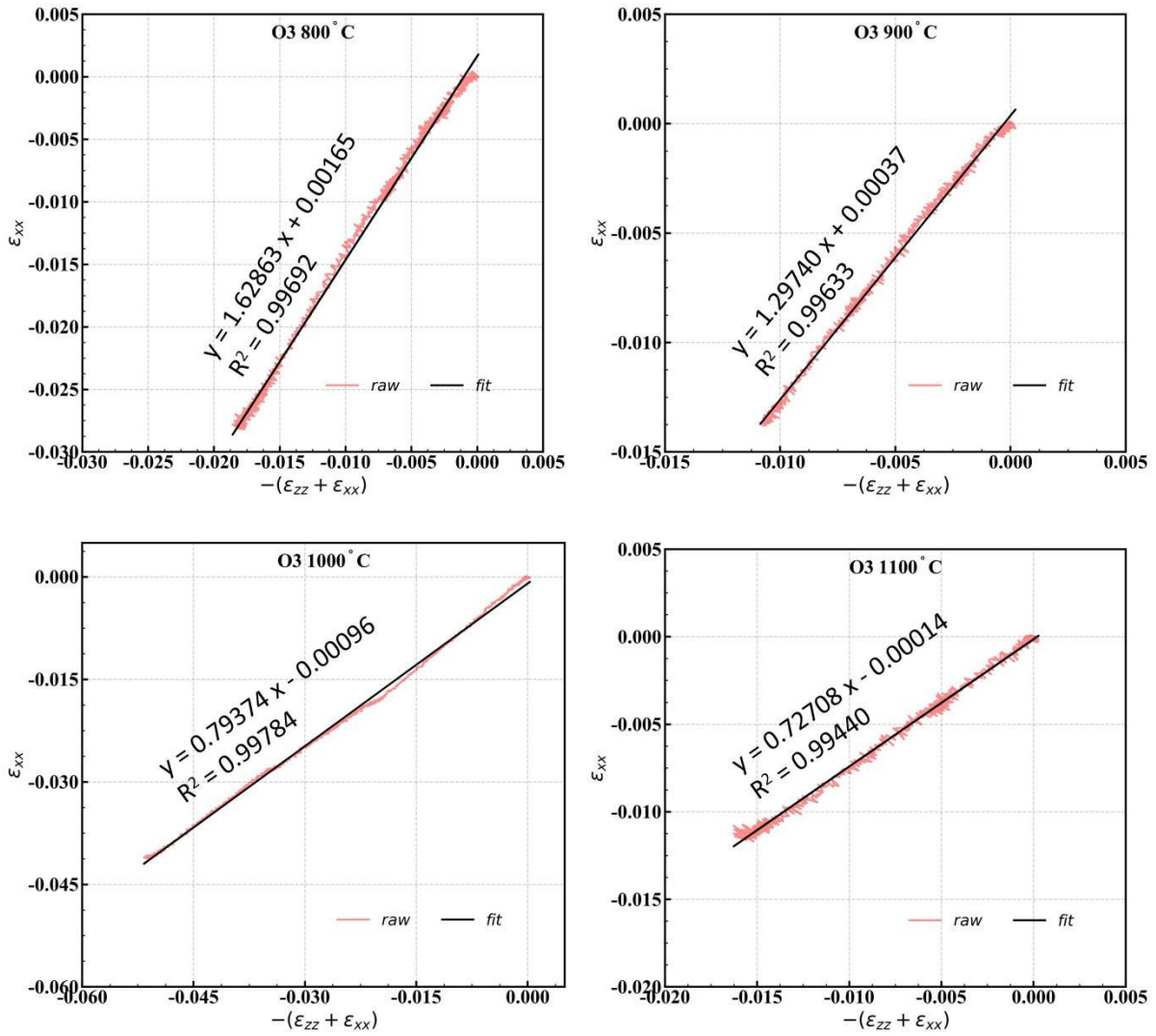


Fig. 7-24 Plotting of ϵ_{xx}^{exp} as function of $(-\epsilon_{xx}^{exp} - \epsilon_{zz}^{exp})$ of Orientation 3 at the four temperature levels (in red) v.s. the fitted straight curve with slope, i.e. the averaged Lankford coefficient (in black)

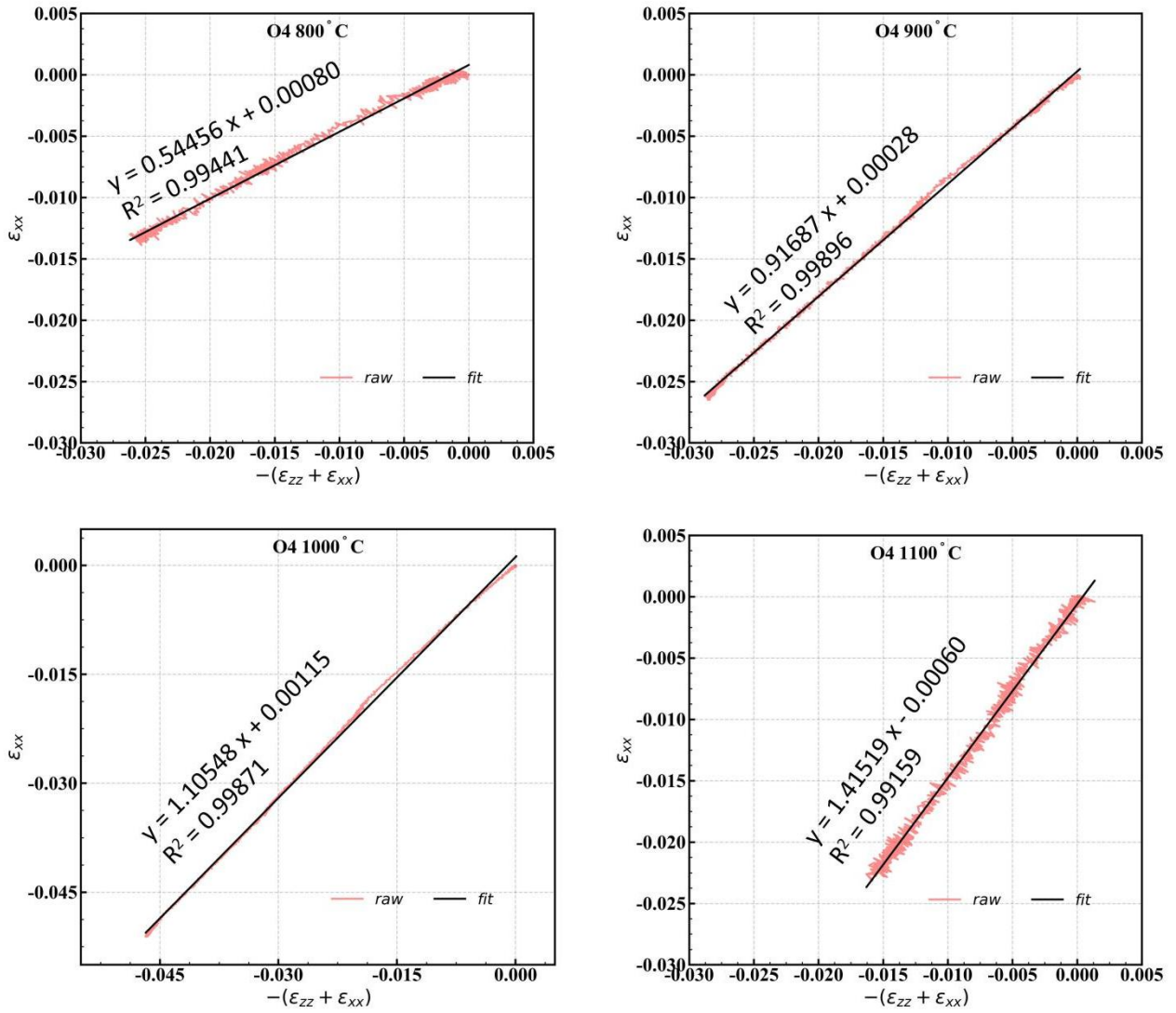


Fig. 7- 25 Plotting of ϵ_{xx}^{exp} as function of $(-\epsilon_{xx}^{exp} - \epsilon_{zz}^{exp})$ of Orientation 4 at the four temperature levels (in red) v.s. the fitted straight curve with slope, i.e. the averaged Lankford coefficient (in black)

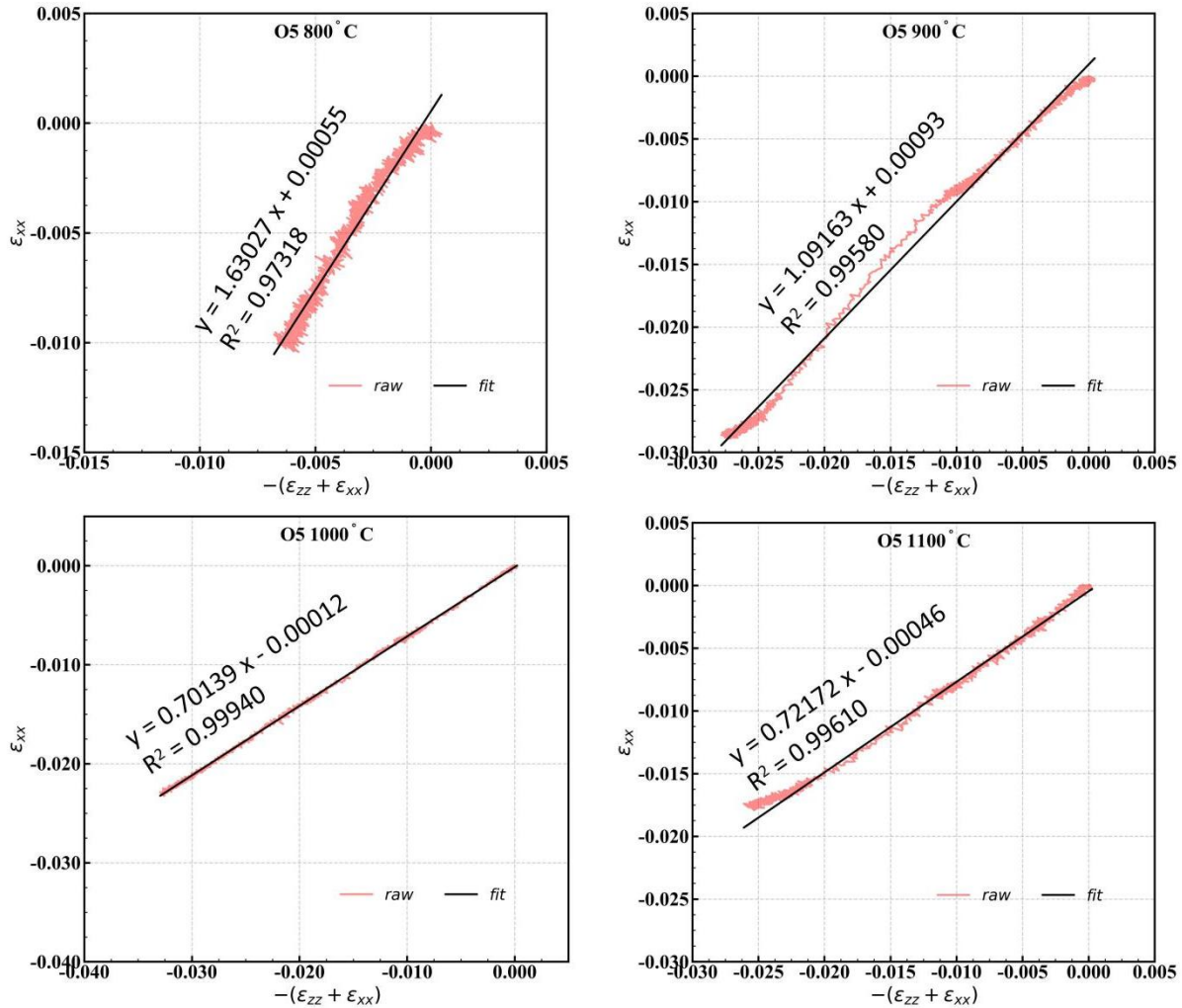


Fig. 7-26 Plotting of ϵ_{xx}^{exp} as function of $(-\epsilon_{xx}^{exp} - \epsilon_{zz}^{exp})$ of Orientation 5 at the four temperature levels (in red) v.s. the fitted straight curve with slope, i.e. the averaged Lankford coefficient (in black)

It is worth noticing that the averaged experimental Lankford coefficients in the above figures (7-22 ~ 7-26) are of slight difference with those in Table 8. The reason is that the raw data were not treated on the same days, and the subsizes of DIC analysis were not exactly the same. Besides, the $\bar{\tau}^{exp}$ of O5 at 900°C in Table 8 were based on the range of about -0.0225 ~ -0.0125 of $(-\epsilon_{xx}^{exp} - \epsilon_{zz}^{exp})$ of the O5 at 900°C in Fig. 7-26.

Although there are some experimental curves and fitted straight lines not in good accordance, it will not influence the optimization result in Chapter 5, because in section 5.4.4 the variant Lankford coefficient is adopted, which does not consider the shape of the fitting curve.

A. 12 Calculation of Young's Modulus for Transverse Isotropy

This work is given in three steps:

- Reference frame transformation for strain and stress tensors;
- Application of the transformation;
- Apparent Young's modulus in given direction

A. 12.1 FR transformation for Strain and Stress Tensors

Consider two reference frames (RFs) of $X_1X_2X_3$ and $x_1x_2x_3$ as shown in Fig. 7-27, where the lower-case letters stand for the testing RF, and upper-case letters stand for the material (i.e. anisotropy) RF. Supposing the base vectors of RF $X_1X_2X_3$ are expressed by the base vectors of RF $x_1x_2x_3$ in the following relation:

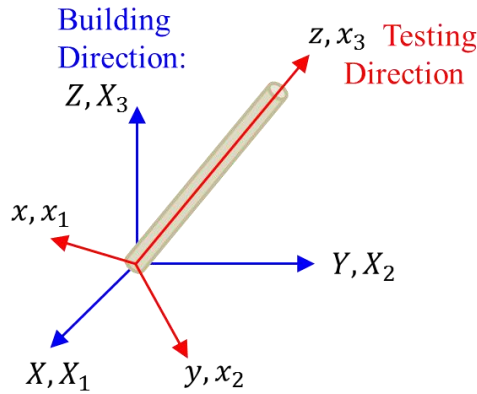


Fig. 7-27 Schematic image for RF transformation

$$\begin{cases} X_1 = l_1x_1 + m_1x_2 + n_1x_3 \\ X_2 = l_2x_1 + m_2x_2 + n_2x_3 \\ X_3 = l_3x_1 + m_3x_2 + n_3x_3 \end{cases} \quad (7-25)$$

For any vector (e.g. displacement, velocity) expressed in two RFs:

$$\mathbf{x} = \begin{bmatrix} x_1 \\ x_2 \\ x_3 \end{bmatrix} \quad \text{and} \quad \mathbf{X} = \begin{bmatrix} X_1 \\ X_2 \\ X_3 \end{bmatrix} \quad (7-26)$$

The relation of their components is:

$$\begin{bmatrix} X_1 \\ X_2 \\ X_3 \end{bmatrix} = \begin{bmatrix} l_1 & m_1 & n_1 \\ l_2 & m_2 & n_2 \\ l_3 & m_3 & n_3 \end{bmatrix} \begin{bmatrix} x_1 \\ x_2 \\ x_3 \end{bmatrix} \quad (7-27)$$

One can get the following relations from Eq. 7-27:

$$\begin{cases} \frac{\partial X_1}{\partial x_1} = l_1 & \frac{\partial X_1}{\partial x_2} = m_1 & \frac{\partial X_1}{\partial x_3} = n_1 & \dots & (a) \\ \frac{\partial x_1}{\partial X_1} = l_1 & \frac{\partial x_2}{\partial X_1} = m_1 & \frac{\partial x_3}{\partial X_1} = n_1 & \dots & (b) \end{cases} \quad (7-28)$$

The strain tensor is given in Voigt notation as:

$$\begin{aligned} \tilde{\epsilon} &\equiv (\epsilon_{xx}, \epsilon_{yy}, \epsilon_{zz}, 2\epsilon_{yz}, 2\epsilon_{zx}, 2\epsilon_{xy})^T \\ &\equiv (\epsilon_{11}, \epsilon_{22}, \epsilon_{33}, 2\epsilon_{23}, 2\epsilon_{31}, 2\epsilon_{12})^T \\ &\equiv (\epsilon_{11}, \epsilon_{22}, \epsilon_{33}, \gamma_{23}, \gamma_{31}, \gamma_{12})^T \end{aligned}$$

For small deformation, the strain tensors in the two RFs are defined as:

$$\begin{cases} \epsilon_{ij} = \frac{1}{2} \left(\frac{\partial u_i}{\partial x_j} + \frac{\partial u_j}{\partial x_i} \right) \\ E_{ij} = \frac{1}{2} \left(\frac{\partial U_i}{\partial X_j} + \frac{\partial U_j}{\partial X_i} \right) \end{cases} \quad (7-29)$$

For the first component of $\tilde{\epsilon}$ in material RF, E_{11} , using relation of 7-27:

$$E_{11} = \frac{\partial U_1}{\partial X_1} = \frac{\partial(l_1 u_1 + m_1 u_2 + n_1 u_3)}{\partial X_1} = \underbrace{l_1 \frac{\partial u_1}{\partial X_1}}_{(a)} + \underbrace{m_1 \frac{\partial u_2}{\partial X_1}}_{(c)} + \underbrace{n_1 \frac{\partial u_3}{\partial X_1}}_{(d)} \quad (7-30)$$

with the chain rule to deal with the indicated (a) part in Eq. 7-30:

$$\frac{\partial u_1}{\partial X_1} = \frac{\partial u_1}{\partial x} \frac{\partial x}{\partial X_1} = \frac{\partial u_1}{\partial x_1} \frac{\partial x_1}{\partial X_1} + \frac{\partial u_1}{\partial x_2} \frac{\partial x_2}{\partial X_1} + \frac{\partial u_1}{\partial x_3} \frac{\partial x_3}{\partial X_1} \quad (7-31)$$

by the relation in Eq. 7-28 (b), Eq. 7-31 can be written as:

$$\frac{\partial u_1}{\partial X_1} = \frac{\partial u_1}{\partial x_1} l_1 + \frac{\partial u_1}{\partial x_2} m_1 + \frac{\partial u_1}{\partial x_3} n_1 \quad (7-32)$$

The indicated part (b) in Eq. 7-30 can be expressed as:

$$l_1 \frac{\partial u_1}{\partial X_1} = \frac{\partial u_1}{\partial x_1} l_1 l_1 + \frac{\partial u_1}{\partial x_2} m_1 l_1 + \frac{\partial u_1}{\partial x_3} n_1 l_1 \quad (7-33)$$

Similarly, we can deal with the (c) and (d) parts in Eq. 7-30 to get:

$$\begin{cases} m_1 \frac{\partial u_2}{\partial X_1} = \frac{\partial u_2}{\partial x_1} l_1 m_1 + \frac{\partial u_2}{\partial x_2} m_1 m_1 + \frac{\partial u_2}{\partial x_3} n_1 m_1 \\ n_1 \frac{\partial u_3}{\partial X_1} = \frac{\partial u_3}{\partial x_1} l_1 n_1 + \frac{\partial u_3}{\partial x_2} m_1 n_1 + \frac{\partial u_3}{\partial x_3} n_1 n_1 \end{cases} \quad (7-34)$$

Inject Eqs. 7-33 and 7-34 into Eq. 7-30:

$$\begin{aligned} E_{11} = & \frac{\partial u_1}{\partial x_1} l_1 l_1 & + \frac{\partial u_2}{\partial x_2} m_1 m_1 & + \frac{\partial u_3}{\partial x_3} n_1 n_1 \\ & + \left(\frac{\partial u_2}{\partial x_3} + \frac{\partial u_3}{\partial x_2} \right) m_1 n_1 & + \left(\frac{\partial u_1}{\partial x_3} + \frac{\partial u_3}{\partial x_1} \right) l_1 n_1 & + \left(\frac{\partial u_2}{\partial x_1} + \frac{\partial u_1}{\partial x_2} \right) m_1 l_1 \end{aligned} \quad (7-35)$$

i.e.:

$$E_{11} = l_1 l_1 \varepsilon_{11} + m_1 m_1 \varepsilon_{11} + n_1 n_1 \varepsilon_{11} + m_1 n_1 \gamma_{23} + l_1 n_1 \gamma_{31} + m_1 l_1 \gamma_{12} \quad (7-36)$$

Similarly the rest 5 components of the strain tensor in material RF can be calculated, and the final relation is:

$$\begin{bmatrix} E_{11} \\ E_{22} \\ E_{33} \\ \Gamma_{23} \\ \Gamma_{31} \\ \Gamma_{12} \end{bmatrix} = \begin{bmatrix} l_1 l_1 & m_1 m_1 & n_1 n_1 & m_1 n_1 & n_1 l_1 & l_1 m_1 \\ l_2 l_2 & m_2 m_2 & n_2 n_2 & m_2 n_2 & n_2 l_2 & l_2 m_2 \\ l_3 l_3 & m_3 m_3 & n_3 n_3 & m_3 n_3 & n_3 l_3 & l_3 m_3 \\ 2l_2 l_3 & 2m_2 m_3 & 2n_2 n_3 & m_2 n_3 + m_3 n_2 & n_2 l_3 + n_3 l_2 & l_2 m_3 + l_3 m_2 \\ 2l_3 l_1 & 2m_3 m_1 & 2n_3 n_1 & m_3 n_1 + m_1 n_3 & n_3 l_1 + n_1 l_3 & l_3 m_1 + l_1 m_3 \\ 2l_1 l_2 & 2m_1 m_2 & 2n_1 n_2 & m_1 n_2 + m_2 n_1 & n_1 l_2 + n_2 l_1 & l_1 m_2 + l_2 m_1 \end{bmatrix} \begin{bmatrix} \varepsilon_{11} \\ \varepsilon_{22} \\ \varepsilon_{33} \\ \gamma_{23} \\ \gamma_{31} \\ \gamma_{12} \end{bmatrix} \quad (7-37)$$

In short expression:

$$\tilde{\mathbf{E}} = \mathbf{R}_e^{G2M} \tilde{\boldsymbol{\varepsilon}} \quad (7-38)$$

where \mathbf{R}_e^{G2M} stands for the 6x6 matrix, the upper index indicates “global to material”, and lower index indicates “epsilon”.

When go to the stress relation, work conservation in the two RFs is used:

$$\underbrace{\tilde{\boldsymbol{\Sigma}} \cdot \delta \tilde{\mathbf{E}} = \tilde{\boldsymbol{\sigma}} \cdot \delta \tilde{\boldsymbol{\epsilon}}}_{\text{inner product}} \Leftrightarrow \underbrace{\tilde{\boldsymbol{\Sigma}}^T \delta \tilde{\mathbf{E}} = \tilde{\boldsymbol{\sigma}}^T \delta \tilde{\boldsymbol{\epsilon}}}_{\text{matrix multiplication}} \quad (7-39)$$

We have:

$$\tilde{\boldsymbol{\Sigma}}^T \delta \tilde{\mathbf{E}} = \tilde{\boldsymbol{\Sigma}}^T (\mathbf{R}_e^{G2M} \delta \tilde{\boldsymbol{\epsilon}}) = (\tilde{\boldsymbol{\Sigma}}^T \mathbf{R}_e^{G2M}) \delta \tilde{\boldsymbol{\epsilon}} = \tilde{\boldsymbol{\sigma}}^T \delta \tilde{\boldsymbol{\epsilon}} \quad (7-40)$$

And immediately:

$$\left\{ \begin{array}{l} \tilde{\boldsymbol{\Sigma}}^T \mathbf{R}_e^{G2M} = \tilde{\boldsymbol{\sigma}}^T \quad \dots \quad (a) \\ \mathbf{R}_e^{G2M^T} \tilde{\boldsymbol{\Sigma}} = \tilde{\boldsymbol{\sigma}} \quad \dots \quad (b) \\ \tilde{\boldsymbol{\Sigma}} = \mathbf{R}_e^{G2M^{-T}} \tilde{\boldsymbol{\sigma}} \quad \dots \quad (c) \end{array} \right. \quad (7-41)$$

i.e.:

$$\mathbf{R}_s^{G2M} = \mathbf{R}_e^{G2M^{-T}} \quad (7-42)$$

where the lower index of “s” indicates “stress”.

Up to now, the transformation of stress and strain in two RFs is done.

A. 12.2 Application of Transverse Isotropy of Young’s Module

This section will introduce how to calculate transverse isotropy elasticity tensor from mono-crystal data.

For monocrystal FCC metal, the elasticity tensor \mathbf{C}^M in material RF can be determined by three components: C_{11}^M , C_{12}^M and C_{44}^M [44,147]. The Hook’s law is then expressed as:

$$\tilde{\boldsymbol{\Sigma}} = \mathbf{C}^M \tilde{\boldsymbol{\epsilon}} \quad (7-43)$$

Injecting Eqs. 7-38 and 7-41 (c) into Eq. 7-43 to get:

$$\tilde{\sigma} = \underbrace{\mathbf{R}_e^{G2M^T} \mathbf{C}^M \mathbf{R}_e^{G2M}}_{\mathbf{C}^G} \tilde{\epsilon} \quad (7-44)$$

So with Eq. 7-44, the elasticity tensor in testing RF (\mathbf{C}^G) can be found. Here comes the algorithm to find the transverse isotropy elasticity tensor.

As shown in Fig. 7-28, the following 5 steps are carried out:

- Step 1: put the material RF(XYZ) and the testing RF (xyz) in coincidence;
- Step 2: rotate the material round z axis a small angle δa , with $X \rightarrow X', Y \rightarrow Y'$;
- Step 3: calculate $\mathbf{C}_{(1)}^G$;
- Step 4: repeat Step 2 to position $X''Y''Z''$ to get $\mathbf{C}_{(2)}^G$, similar get $\mathbf{C}_{(3)}^G, \dots, \mathbf{C}_{(n)}^G$, where $\delta a \cdot n = \pi/2$;
- Step 5: calculate $\mathbf{C}^G = \lim_{n \rightarrow \infty} \frac{1}{n} \sum_{i=1}^n \mathbf{C}_{(i)}^G$.

In fact, when $n \geq 1000$, a good convergence is found.

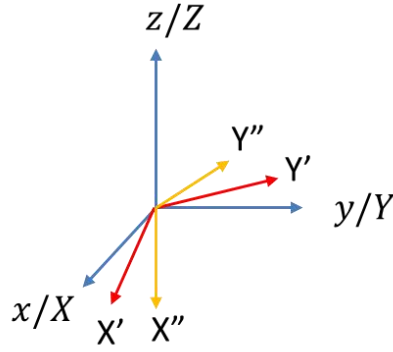


Fig. 7-28 Schematic image to show the way to find the transverse isotropy elasticity tensor

Take the averaged values of C_{11}^M , C_{12}^M and C_{44}^M in reference [44] and [147], we can apply the aforementioned 5 steps to get the following elasticity tensor in testing RF:

$$\mathbf{C}^G = \begin{bmatrix} 262.9 & 135.9 & 154.9 & 0 & 0 & 0 \\ 135.9 & 262.9 & 154.9 & 0 & 0 & 0 \\ 154.9 & 154.9 & 243.9 & 0 & 0 & 0 \\ 0 & 0 & 0 & 110.8 & 0 & 0 \\ 0 & 0 & 0 & 0 & 110.8 & 0 \\ 0 & 0 & 0 & 0 & 0 & 63.5 \end{bmatrix} = \mathbf{C}_z^M \quad (7-45)$$

The \mathbf{C}^G in Eq. 7-45 is in turn the new \mathbf{C}_z^M expressing the transverse isotropy around the z (Z) axis. A similar elasticity tensor is found in reference [44], which indicates that our algorithm works well.

Likely, based on \mathbf{C}_z^M , re-do Steps 1-5 around x axis to get \mathbf{C}_{zx}^M , then around y axis to get \mathbf{C}_{zxy}^M ... Repeat several times (5 times is good enough) to get the isotropic elastic tensor as:

$$\mathbf{C} = \begin{bmatrix} 277 & 138 & 138 & 0 & 0 & 0 \\ 138 & 277 & 138 & 0 & 0 & 0 \\ 138 & 138 & 277 & 0 & 0 & 0 \\ 0 & 0 & 0 & 69.4 & 0 & 0 \\ 0 & 0 & 0 & 0 & 69.4 & 0 \\ 0 & 0 & 0 & 0 & 0 & 69.4 \end{bmatrix} \quad (7-46)$$

The Young's modulus for isotropic material is found to be $E_{iso}=185\text{GPa}$, and Poisson's ratio $1/3$.

A. 12.3 Find Apparent Young's Modulus in a Given Direction

As shown in Fig. 7-29 (a), for a tensile test along a direction with an angle θ (in degree) w.r.t. to the building direction, with the elasticity tensor in transverse isotropy condition (Eq. 7-45), it is possible to calculate the apparent Young's modulus (E_θ) in this selected direction, whose evolution with θ is given in Fig. 7-29 (b).

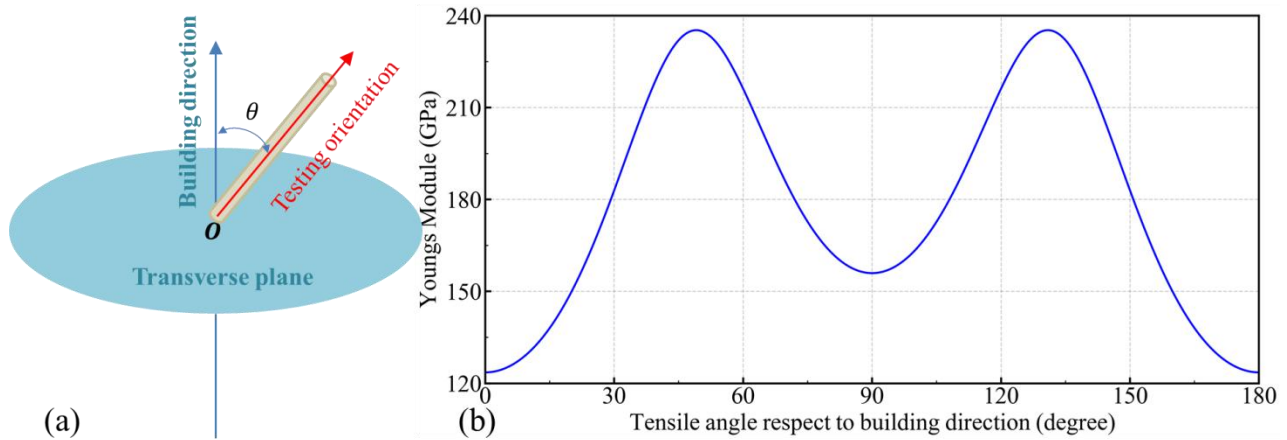


Fig. 7-29 (a) Schematic of orientation, and (b) the apparent Young's modules at the angle θ

It can be seen that the isotropic Young's module calculated in A. 12.2 (185GPa) is smaller than the values that are mostly found in literature ($\sim 200\text{GPa}$). Thus, we cannot compare the computed values directly with the values from the reference of Safran, because the base is not the same. However, we can compare the ratios. The theoretical ratios are shown in Fig. 7-30 in blue curve.

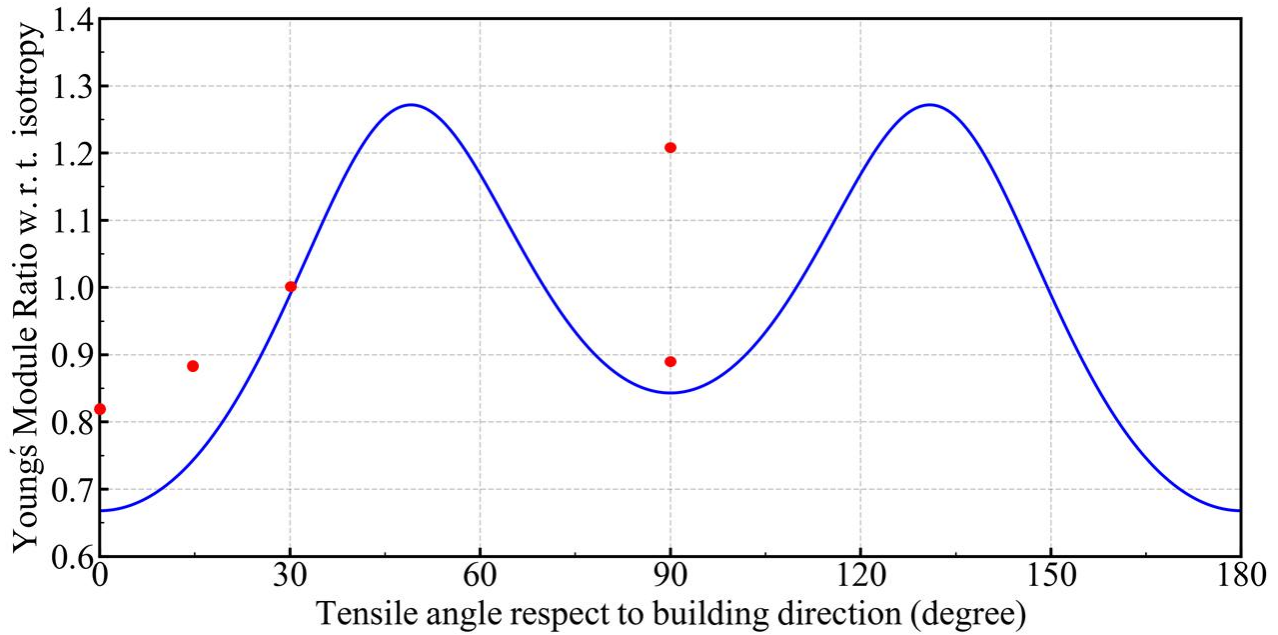


Fig. 7-30 Theoretical values of E_{θ}/E_{iso} for θ in range (0,180°) in blue curve, and optimized ratio in red points for the samples in this project by inverse method on MOOPI

The θ angles for the 5 orientations are given in Table 16, and their theoretical ratios are also given in the same table. The corresponding orientations of the samples in our project as shown in Fig. 5-1 are also noted. However, the real as-built material is close to transverse isotropy state, not perfectly in this state. To find the ratio of the real material, MOOPI is used. The Young's modules of IN718 as function of temperature from Safran are used as the isotropic ones. Force information is used for building the cost function. Within each orientation for all 4 temperature levels, direct simulations are constructed for initial several seconds. The optimized ratios by MOOPI are also given in Table 16, and plotted in red points in Fig. 7-30.

Table 16 Comparison between theoretical and optimized ratio of Young's module

θ	0° (O1)	15° (O2)	30° (O5)	90° (O3)	90° (O4)
Theoretical	0.67	0.75	0.99	0.84	0.84
MOOPI	0.82	0.87	1.00	(1.21) 0.89	0.89

One can see that the optimized trend and the theoretical trend of the Young's module ratio are in accordance, except the O3 case. This "abnormal" value could be caused by the uncertainty of experimental measurement, thus it is replaced by the value of 0.89. This comparison between theoretical ratio and optimized ratio demonstrates that the as-built IN718 material by LPBF process is close to the transverse isotropic condition in elasticity.

Now the adjustment of Young's modulus for each orientation is finished.

A. 13 Why Only Exponential Part of Rheological Law Is Enough

In Eq. 3-49 there are two isotropic hardening parts, i.e. the power law part (also called Ludwick-Holloman Law) and the exponential law part (also called Voce equation). For the tests of the 4 temperature levels, optimizations were carried out based on three isotropic hardening cases:

- Only with power law;
- Only with exponential law;
- Mixed power and exponential law.

The minimum, maximum, optimized parameters are given in Table 17.

Table 17 Boundaries and optimized values of the parameters of the three trials with only power relation, only exponential relation and mixed relation in the rheological law

Parameter (Unit)	Power			Exponential			Mixed		
	min	max	opti	min	max	opti	min	max	opti
$\sigma_{Y,ref}$ (MPa)	50	170	55	50	110	110	50	120	114
H_{ref} (MPa)	500	1200	859	—	—	—	1	700	18
n	0.1	0.5	0.49	—	—	—	0.1	0.6	0.53
$Q_{r,ref}$ (MPa)	—	—	—	30	100	83	1	110	47
b	—	—	—	20	500	372	50	400	292
Q_1 (kJ·mol ⁻¹)	120	220	174	140	220	157	150	170	166
Q_2 (kJ·mol ⁻¹)	46	106	88.1	40	110	76.3	65	90	82.5
k_{ref} (MPa)	659	1640	1453	640	1364	1118	967	1573	991
m	0.1	0.4	0.253	0.1	0.35	0.256	0.2	0.3	0.217
$min(fc)$	0.05883			0.03836			0.04087		

From Table 17 one can see that the optimization on power law returns the biggest $min(fc)$ value, while the exponential law returns the minimum $min(fc)$. Although theoretically the mixed law is expected to return an even smaller value of $min(fc)$ than the case of only exponential, the 9 parameters in the mixed case has difficulty in converging well. With the optimized values given in Table 17, the simulated and experimental forces at 4 temperature levels are given in Fig. 7-31.

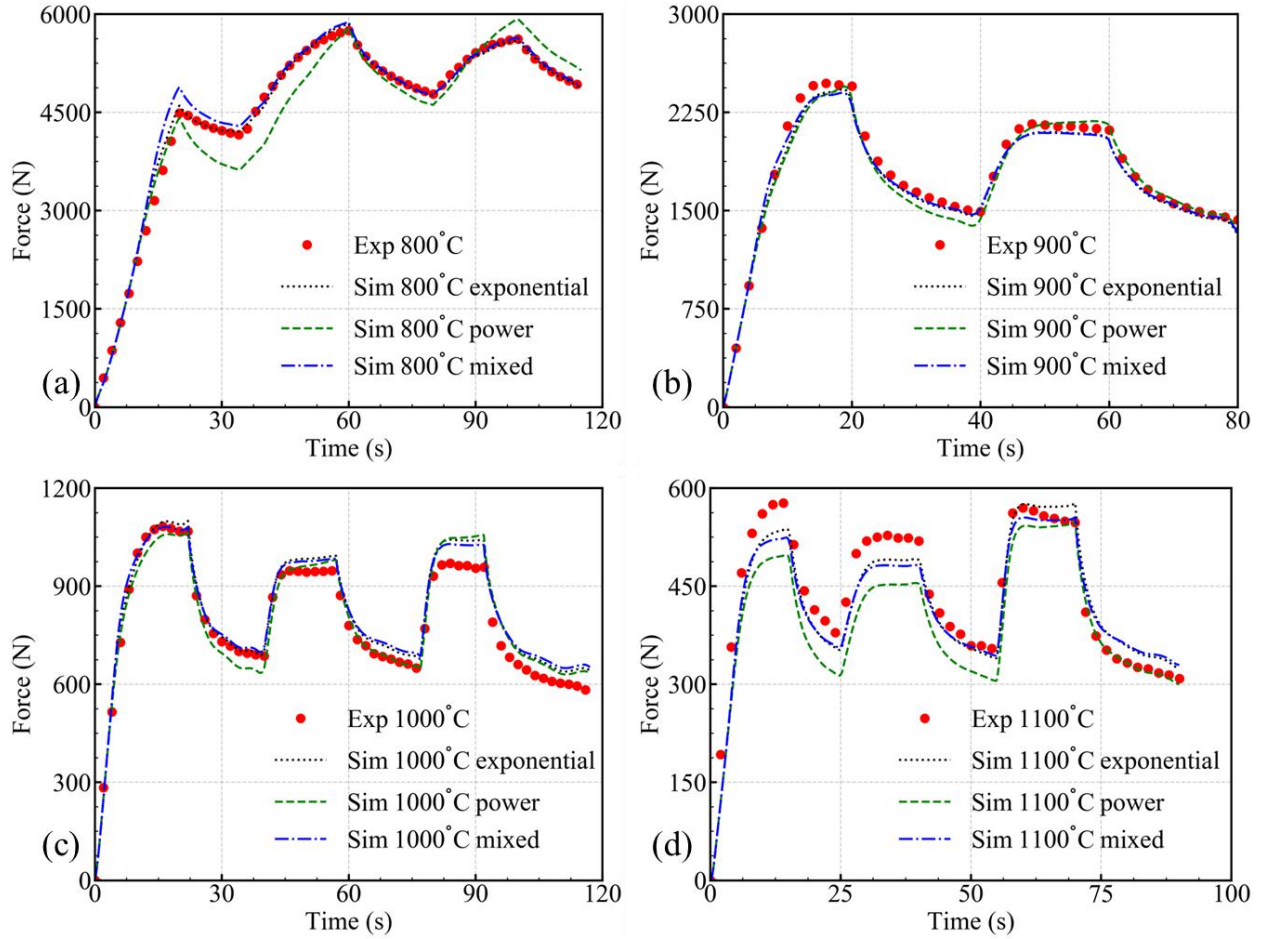


Fig. 7-31 Comparison of force in three optimizations based on rheological law of only exponential (black dotted line), only power law (green dashed line) and mixed (blue dash dotted line)

It can be seen in Fig. 7-31 that with only exponential relation used in the rheological law, the final optimization is good enough. In the view of time saving in optimization, rheological law with only exponential relation is selected.

A. 14 Demonstration of $F + 2H = N$

The transverse isotropy is around the Z axis. Based on Eq. 5-9, write it in Voigt notation as:

$$\begin{bmatrix} \dot{\epsilon}_{XX} \\ \dot{\epsilon}_{YY} \\ \dot{\epsilon}_{ZZ} \\ \dot{\gamma}_{YZ} \\ \dot{\gamma}_{ZX} \\ \dot{\gamma}_{XY} \end{bmatrix} \equiv \begin{bmatrix} \dot{\epsilon}_{XX} \\ \dot{\epsilon}_{YY} \\ \dot{\epsilon}_{ZZ} \\ 2\dot{\epsilon}_{YZ} \\ 2\dot{\epsilon}_{ZX} \\ 2\dot{\epsilon}_{XY} \end{bmatrix} = \frac{\dot{\epsilon}}{\sigma} \begin{bmatrix} F + H & -H & -F \\ -H & H + F & -F \\ -F & -F & F + F \end{bmatrix} \begin{matrix} 2L \\ 2L \\ 2N \end{matrix} \begin{bmatrix} \sigma_{XX} \\ \sigma_{YY} \\ \sigma_{ZZ} \\ \sigma_{YZ} \\ \sigma_{ZX} \\ \sigma_{XY} \end{bmatrix} \quad (7-47)$$

Consider a pure shear stress “tensor” in $X - O - Y$ plan:

$$\boldsymbol{\sigma}_{XOY} = \begin{bmatrix} \sigma_{XX} & \sigma_{XY} \\ \sigma_{YX} & \sigma_{XX} \end{bmatrix} = \begin{bmatrix} 0 & \tau \\ \tau & 0 \end{bmatrix} \quad (7-48)$$

With relation of Eq. 7-47, the strain rate “tensor” in the same plane will be:

$$\dot{\boldsymbol{\epsilon}}_{XOY} = \begin{bmatrix} \dot{\epsilon}_{XX} & \dot{\epsilon}_{XY} \\ \dot{\epsilon}_{YX} & \dot{\epsilon}_{XX} \end{bmatrix} = \frac{1}{2} \begin{bmatrix} 0 & \dot{\gamma}_{XY} \\ \dot{\gamma}_{XY} & 0 \end{bmatrix} = \frac{1}{2} \begin{bmatrix} 0 & \dot{\gamma} \\ \dot{\gamma} & 0 \end{bmatrix} \quad (7-49)$$

where

$$\dot{\gamma} = \dot{\gamma}_{XY} = 2 \frac{\dot{\epsilon}}{\sigma} N \sigma_{XY} = 2 \frac{\dot{\epsilon}}{\sigma} N \tau \quad (7-50)$$

Transform Eqs. 7-48 and 7-49 into principal direction to get:

$$\boldsymbol{\sigma}_{XOY} = \begin{bmatrix} \sigma_{XX} & \sigma_{XY} \\ \sigma_{YX} & \sigma_{XX} \end{bmatrix} = \begin{bmatrix} 0 & \tau \\ \tau & 0 \end{bmatrix} \rightarrow \boldsymbol{\sigma}'_{XOY} = \begin{bmatrix} \tau & 0 \\ 0 & -\tau \end{bmatrix} \rightarrow \begin{pmatrix} \sigma_1 = \tau \\ \sigma_2 = -\tau \end{pmatrix} \quad (7-51)$$

and:

$$\dot{\boldsymbol{\epsilon}}_{XOY} = \begin{bmatrix} \dot{\epsilon}_{XX} & \dot{\epsilon}_{XY} \\ \dot{\epsilon}_{YX} & \dot{\epsilon}_{XX} \end{bmatrix} = \frac{1}{2} \begin{bmatrix} 0 & \dot{\gamma} \\ \dot{\gamma} & 0 \end{bmatrix} \rightarrow \dot{\boldsymbol{\epsilon}}'_{XOY} = \frac{1}{2} \begin{bmatrix} \dot{\gamma} & 0 \\ 0 & -\dot{\gamma} \end{bmatrix} \rightarrow \begin{pmatrix} \dot{\epsilon}_1 = \frac{1}{2} \dot{\gamma} \\ \dot{\epsilon}_2 = -\frac{1}{2} \dot{\gamma} \end{pmatrix} \quad (7-52)$$

where $\boldsymbol{\sigma}'_{XOY}$ and $\dot{\boldsymbol{\epsilon}}'_{XOY}$ are the stress and strain rate “tensors” in the principal directions, respectively. Because in the $X - O - Y$ plane the material is transverse isotropic, the stress and strain rate tensor in the principal space should also meet the relation by Eq. 7-47, i.e.

$$\begin{bmatrix} \dot{\epsilon}_1 \\ \dot{\epsilon}_2 \end{bmatrix} = \frac{\dot{\epsilon}}{\sigma} \begin{bmatrix} F + H & -H \\ -H & F + H \end{bmatrix} \begin{bmatrix} \sigma_1 \\ \sigma_2 \end{bmatrix} \quad (7-53)$$

i.e.

$$\begin{cases} \dot{\varepsilon}_1 \frac{\bar{\sigma}}{\dot{\varepsilon}} = (F + H)\sigma_1 - H\sigma_2 & \dots (a) \\ \dot{\varepsilon}_2 \frac{\bar{\sigma}}{\dot{\varepsilon}} = -H\sigma_1 + (F + H)\sigma_2 & \dots (b) \end{cases} \quad (7-54)$$

$$(a) - (b) \rightarrow (\dot{\varepsilon}_1 - \dot{\varepsilon}_2) \frac{\bar{\sigma}}{\dot{\varepsilon}} = (F + 2H)(\sigma_1 - \sigma_2) \quad (7-55)$$

Injecting Eqs.7-50, 7-51 and 7-52 into Eq. 7-55, one can find:

$$F + 2H = N$$

End of proof.

A. 15 Scheil Summation to Predict Nucleation of γ' Phase

In Section 5.5.3 the γ' and γ'' are not considered in the exploration of source of anisotropy. One reason is that their lattices are in coherent with the matrix. Another reason is that during this testing duration, the γ' phase is not supposed to nucleate. The way to predict the nucleation is given below.

Firstly, according to the TTT diagram of IN718 published by Armida Oradei-Basile and J. F. Radavich [148], as shown in Fig. 7-32, one can have the following judgements:

- For tensile tests conducted at 800°C level, no new γ' or γ'' is supposed to appear during the short testing duration.
- For tests at 1000 or 1100°C, the minimum temperature value of the field in the selected ZOIs is higher than the solidus of γ' at about 886°C, thus

Only the tests at 900°C are critical regarding γ' nucleation. The summation of Scheil is used for this prediction.

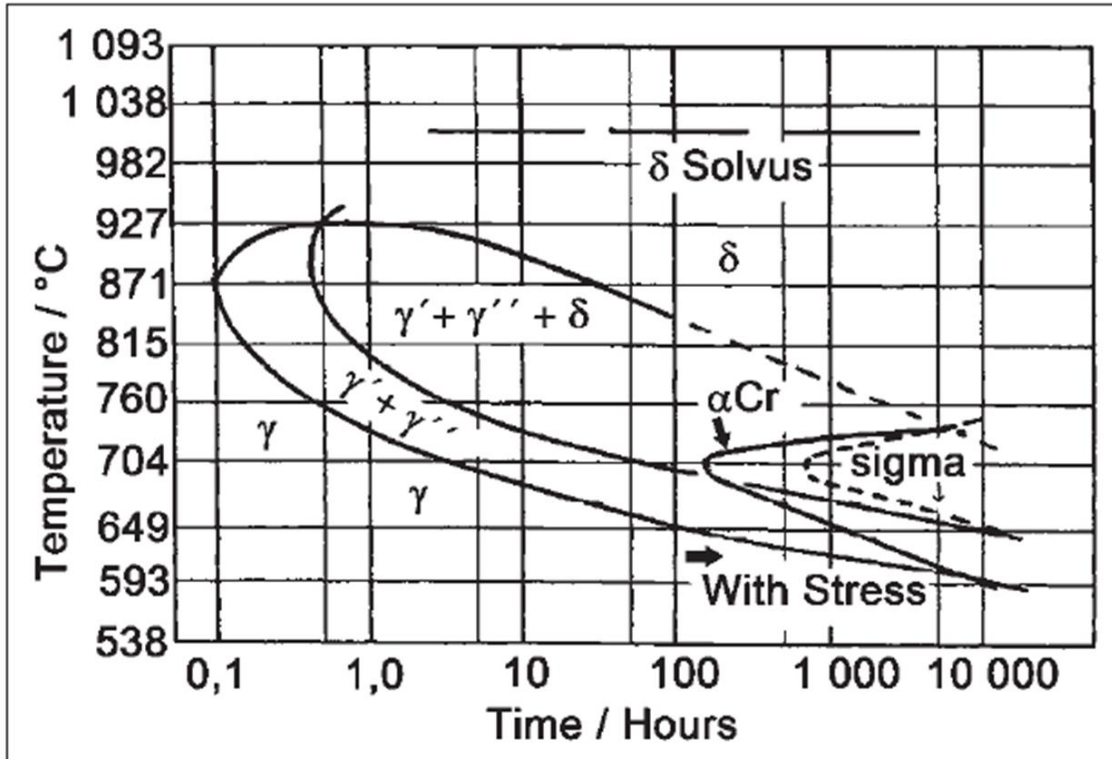


Fig. 7-32 TTT diagram of IN718 by Oradei-Basile, A. and Radavich, J.F. [148]

From Fig. 7-32 one can see that for any isothermal line there is a temporal threshold, which is marked as $\tau(T)$. This $\tau(T)$ means that at the isothermal condition T after a duration of τ , the γ' starts to nucleate.

Then, for a non-isothermal history, the thermal history can be divided into small fractions, and each of the fractions is deemed as isothermal condition, as shown in Fig. 7-33 (a). For each increment of time Δt_i , there is an assumed isothermal T_i , and under this temperature there is corresponding temporal threshold $\tau(T_i)$. Thus, the summation of Scheil [149] predicts that nucleation forms when:

$$\sum_i \frac{\Delta t_i}{\tau(T_i)} = 1 \quad (7-56)$$

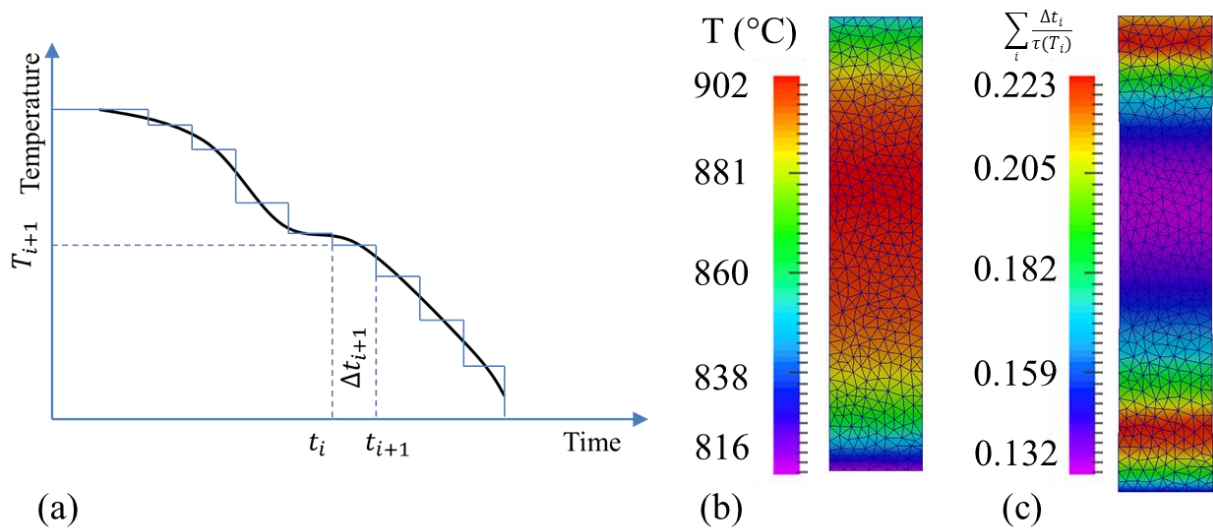


Fig. 7-33 (a): schematic decomposition of a non-isothermal history into fractions of isothermal steps, (b): initial temperature field of O1 at 900°C, and (c): final summation of Scheil at end of test

In Fig. 7-33 (b) is given the temperature field at the beginning of test of O1 at 900°C. The duration since the first velocity imposing to the end is 100s. Considering only those 100s, the final summation of Scheil is given in Fig. 7-33 (c). Taking the initial stabilization of temperature (of 180s) into account, the summation can be multiplied by 2.8 (because since the 180th second the temperature field on the sample evolves little, thus isothermal condition can be assumed). In both cases the maximum of summation is smaller than 1. Among all the tests at 900°C for all orientations, the maximum duration at the objective temperature is about 440s. It is easy to calculate that the summation could be around $4.4 \times 0.223 = 0.9812$, which is still smaller than 1.

So in any case, the nucleation of γ' and γ'' can be deemed not to happen.

A. 16 Error Analysis

In this section, the error or uncertainty of the experimental work is analyzed. It composes of 4 parts, which are caused by measurement of geometry, temperature, displacement field and force. All those four uncertainty are independent.

The error is defined as the “measured_value – real_value”. The following sections are grouped in two: the source of error, and the influence on the optimization.

A. 16.1 Source of Errors

A. 16.1.1 Error Introduced by Geometry Measurement

The samples prepared by the AM process have a certain surface roughness. The deposition layer thickness is about $50\mu\text{m}$, thus the roughness is expected smaller than half of this value. A typical roughness value by PBF processing is found between 12 and $16\mu\text{m}$ in some research [150,151]. In this work, sand blasting is used to modify the surface state of the sample, thus a compromised Ra value is assumed with $12.5\mu\text{m}$. Considering the narrowest thickness of $u = 2\text{mm}$ and the narrowest width of $w = 8\text{mm}$, we can calculate the sectional area error introduced by the roughness:

$$dS \approx \frac{\partial S}{\partial u} du + \frac{\partial S}{\partial w} dw = wdu + udw = 0.025 \cdot 2 + 0.025 \cdot 8 = 0.25\text{mm}^2 \quad (7-57)$$

$$err_S = \frac{dS}{S} = \frac{0.25}{16} \cdot 100\% = 1.5\% \quad (7-58)$$

This is a **positive uncertainty**, because the effective section area is always smaller than the measured value.

A. 16.1.2 Error Introduced by Temperature Measurement

In the final FEM calculation, the temperature measured by IR camera is used as the input. Thus, the uncertainty of temperature by IR camera (err_{TIR}) must be analyzed.

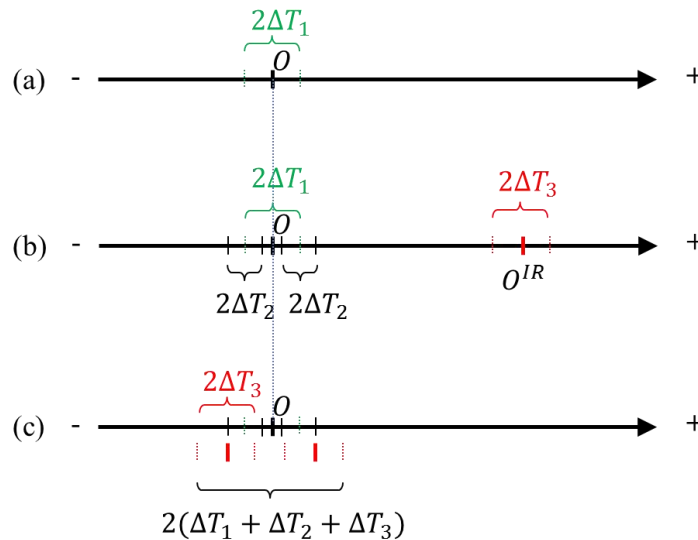


Fig. 7-34 schematic for explaining the uncertainty of T field by IR camera

Fig. 7-34 shows how the err_{TIR} works. In (a), the real temperature is supposed to be at position of O . The ΔT_1 is the uncertainty introduced during welding the thermocouple (indicated in green); refer to Chapter 7 for the reason.

For the thermocouple itself, there is measuring error brought in during the manufacturing, such as the chemical composition of the wires. This error is named as ΔT_2 , and it is an expansion based on the range of ΔT_1 , as shown in (b) in black.

Also in (b), the error the IR camera is shown in red. This error composes of two parts. The first part is the system error indicated by the distance between O^{IR} and O , and the second part is the uncertainty of the IR measurement indicated by ΔT_3 . The calibration was based on the hypothesis that the temperature measured by the thermocouple is the “right” one, thus the system position of IR camera is moved into the span of $\Delta T_1 + \Delta T_2$, as shown in (c). Thus, all together, the T field measured by the IR camera is expected to have a maximum error of $\Delta T_1 + \Delta T_2 + \Delta T_3$.

In experiments, it is found that the ΔT_1 can reach 15°C at objective temperature of 1000°C, i.e. 1.5% of objective temperature. The value of ΔT_2 is 0.75% of the objective temperature, and ΔT_3 is 2.2% of objective temperature. It is unfortunately to find that the sum of the three could go to about 45°C at extreme case.

This uncertainty can be **either positive or negative**.

A. 16.1.3 Error Introduced by Displacement Measurement

In section 3.6.1.1 a pure parallel condition is assumed, which is given by the transition matrix. However, in reality this is not exact. There is non-alliance error, which is shown in Fig. 7-35.

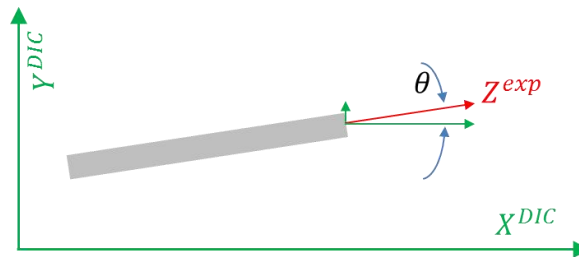


Fig. 7-35 Schematic for explanation of projection error during reference frame transformation

The green axis stand for the RF of DIC system and the red direction indicates the tensile direction of the sample. There is certain angle between the red Z^{exp} and green X^{DIC} , which is noted as θ . Suppose the velocity component along X^{DIC} is v_x^{DIC} , one can immediately find the v_z^{exp} meets:

$$v_x^{DIC} = v_z^{exp} \cdot \cos(\theta) \quad (7-59)$$

One can see that the imposed velocity is smaller than the real velocity, i.e. a **negative error**. In experimental work, this θ angle is smaller than 2° , thus, the difference of the velocity is smaller than $1 - \cos(2^\circ)$ times the v_z^{exp} , where $1 - \cos(2^\circ) \approx 0.0006 = 0.06\%$.

A. 16.1.4 Error Introduced by Force Measurement

With the verification conducted by CVM (centre de vérification de Metz), for load at 5kN, the relative error is smaller than 0.55%; for load under 7kN and above, the relative error is smaller than 0.4%. The maximum relative error during the verification should be smaller than 1%. Thus, for the load information, the error range of 1% is directly used as the error band. It can be **negative or positive**.

A. 16.2 Influence on Calculation Results

Taking Eq. 4-6 as the relation for analysis of error, which is again given below:

$$\bar{\sigma} = \left(\sigma_{Y,ref} + Q_{r,ref} (1 - \exp(-b\bar{\epsilon})) \right) \exp\left(\frac{Q_1}{R_g T} - \frac{Q_1}{R_g T_{ref}}\right) + k_0 \exp\left(\frac{Q_2}{R_g T} - \frac{Q_2}{R_g T_{ref}}\right) \dot{\bar{\epsilon}}^m \quad (7-60)$$

We use von Mises assumption for simplification of the analysis, in which case the σ_{zz} is equal to $\bar{\sigma}$ in the uni-axial tensile test along the z axis. The optimized parameters in Trial2 of Section 4.5.2 are used as input. One can see that three components in Eq. 7-60 are affected by experimental measurements, which are

- T directly by experimental measurements, and
- $\dot{\bar{\epsilon}}$ and $\bar{\epsilon}$ indirectly by experimental measurement.

For uni-axial tensile test, the relation $\dot{\bar{\epsilon}} = \dot{\epsilon}_{zz}$ is met, and further $\bar{\epsilon} = \epsilon_{zz}$. Thus, one can assume that the experimental error during the displacement measurement is transported into simulation.

For building the cost function, the force is used as the component. So we should consider:

$$F_{zz} = \sigma_{zz} \cdot S = \bar{\sigma} \cdot S \quad (7-61)$$

So the uncertainty of F_{zz} is:

$$dF_{zz} = \bar{\sigma} \cdot dS + S \cdot d\bar{\sigma} \quad (7-62)$$

Further we have:

$$d\bar{\sigma} = \frac{\partial \bar{\sigma}}{\partial \dot{\epsilon}} \cdot d\dot{\epsilon} + \frac{\partial \bar{\sigma}}{\partial \bar{\epsilon}} \cdot d\bar{\epsilon} + \frac{\partial \bar{\sigma}}{\partial T} \cdot dT \quad (7-63)$$

As previously mentioned in Section A. 16.1.1, A. 16.1.2 and A. 16.1.3,

$$\begin{cases} dS &= 0.015S \\ d\dot{\epsilon} &= -0.0006\dot{\epsilon} \\ d\bar{\epsilon} &= -0.0006d\bar{\epsilon} \\ |dT| &= 45^{\circ}\text{C} \end{cases}$$

Supposing $S = 16\text{mm}^2$, $\dot{\epsilon}$ varies from 0 to $3 \times 10^{-3}\text{s}^{-1}$, $\bar{\epsilon}$ varies from 0 to 0.06, T varies from 800 to 1100°C . It is found that the influence of $d\dot{\epsilon}$ and $d\bar{\epsilon}$ on final force is negligible after simple calculation. The dF value is linearly linked to dS , thus 1.5% positive uncertainty is contributed. The temperature is the biggest contribution to the force calculation.

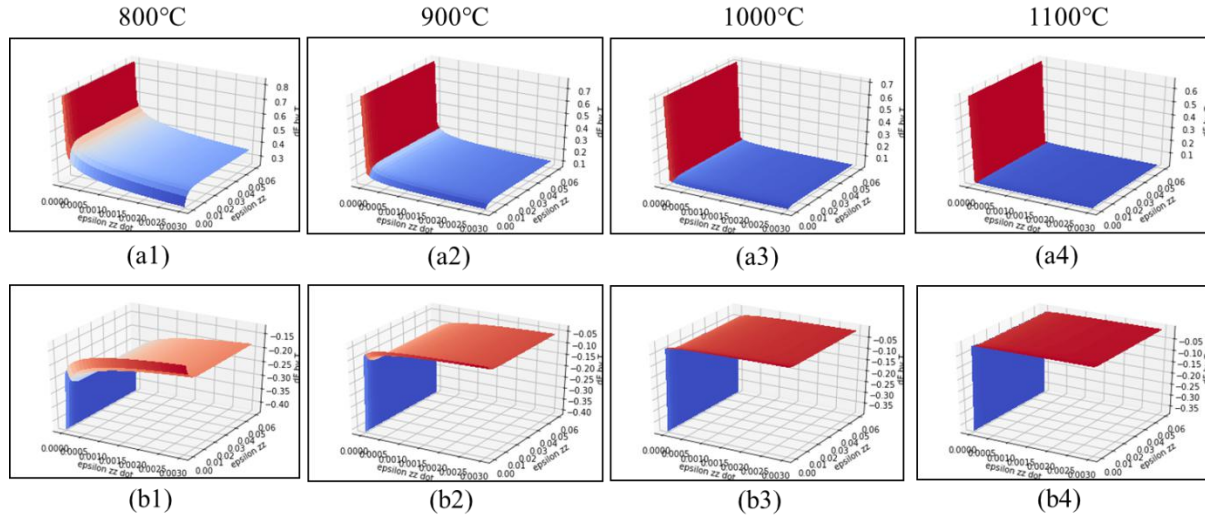


Fig. 7-36 Percentage of dF contributed by T uncertainty, where (a) series suffer a negative dT , and (b) series suffer positive dT

Fig. 7-36 shows the percentage of dF contributed by dT , with the aforementioned values of $\dot{\epsilon}$ and $\bar{\epsilon}$. For each of the 8 cases, the average of all points of $(\dot{\epsilon}, \bar{\epsilon})$ is calculated and shown in Table 18.

Table 18 maximum negative error (MNE) and maximum positive error (MPE) in the project

	800°C	900°C	1000°C	1100°C
MNE	-21.0%	-7.7%	-2.8%	-1.4%
MPE	40.3%	14.2%	5.1%	2.4%

One can see that the MNE and MPE values covers a big range at temperature level of 800°C , and from 900°C the MNE and MPE head for zero fast.

Based on the above analysis, one can see that the biggest uncertainty comes from the temperature measurement at moderate temperature (between 800 and 900°C), and at higher temperature levels, the measurement of geometry also plays an important part.

The force measurement is not considered in this uncertainty analysis, because the cost function is based on the measured experimental force.

As a summary, temperature measurement is the most important for this kind of thermomechanical processing.

Chapter Reference

137 Type K Thermocouple - Type K Thermocouples - K Type Thermocouples - K Type Thermocouple, <https://www.thermocoupleinfo.com/type-k-thermocouple.htm>

138 <https://en.wikipedia.org/wiki/Lens>

139 Cauchy's equation – Wikipedia, https://en.wikipedia.org/wiki/Cauchy%27s_equation, visited Feb. 18 ,2021

140 Li, J. and Wu, S.T., 2004. Extended Cauchy equations for the refractive indices of liquid crystals. *Journal of applied physics*, 95(3), pp.896-901.

141 Convection Heat Transfer Coefficient - an overview | ScienceDirect Topics, website: <https://www.sciencedirect.com/topics/engineering/convection-heat-transfer-coefficient>, visited Apr.26th, 2021

142 Greene, G.A., Finfrock, C.C. and Irvine Jr, T.F., 2000. Total hemispherical emissivity of oxidized Inconel 718 in the temperature range 300–1000 C. *Experimental Thermal and Fluid Science*, 22(3-4), pp.145-153.

143 Anwander, M., Zagar, B.G., Weiss, B. and Weiss, H., 2000. Noncontacting strain measurements at high temperatures by the digital laser speckle technique. *Experimental mechanics*, 40(1), pp.98-105.

144 Branson, Jim. Black Body Radiation. [Online] April 22, 2013. [Cited: June 26, 2018.] https://quantummechanics.ucsd.edu/ph130a/130_notes/node48.html.

145 Lienhard IV, John H. and Lienhard V, John H. *A heat transfer textbook. fourth*. Cambridge : Phlogiston Press, 2017. p. 533.

146 `scipy.interpolate.griddata` — SciPy v1.5.0 Reference Guide, <https://docs.scipy.org/doc/scipy/reference/generated/scipy.interpolate.griddata.html>, visited on Jun. 26th, 2020

147 Li, Z., Xiong, J., Xu, Q., Li, J. and Liu, B., 2015. Deformation and recrystallization of single crystal nickel-based superalloys during investment casting. *Journal of Materials Processing Technology*, 217, pp.1-12.

148 Oradei-Basile, A. and Radavich, J.F., 1991. A current TTT diagram for wrought alloy 718. *Superalloys*, 718(625), pp.325-335.

149 Scheil, E., 1935. Anlaufzeit der austenitumwandlung. *Archiv für das Eisenhüttenwesen*, 8(12), pp.565-567.

150 Whip, B., Sheridan, L. and Gockel, J., 2019. The effect of primary processing parameters on surface roughness in laser powder bed additive manufacturing. *The International Journal of Advanced Manufacturing Technology*, 103(9), pp.4411-4422.

151 Strano, G., Hao, L., Everson, R.M. and Evans, K.E., 2013. Surface roughness analysis, modelling and prediction in selective laser melting. *Journal of Materials Processing Technology*, 213(4), pp.589-597.

RÉSUMÉ

La fabrication additive d'alliages métalliques présente de nombreux avantages. Cependant, les gradients thermiques et les vitesses de refroidissement extrêmement élevés peuvent induire des défauts : distorsions, contraintes résiduelles, fissurations. La simulation numérique constitue une approche prédictive, ce qui nécessite pour chaque alliage un modèle du comportement mécanique en condition de fabrication. Dans ce projet, le comportement anisotrope du super-alliage à base de nickel In718, fabriqué par fusion laser de lit de poudre (L-PBF), est caractérisé entre 800 et 1100°C. Des éprouvettes, fabriquées par L-PBF avec différentes orientations laser, ont été soumises à des séquences combinant tractions uni-axiales à différentes vitesses et relaxations de différentes durées, sous chauffage résistif et sous vide, sur une machine développée spécifiquement (DEDIMET). La distribution de température non uniforme induite par le chauffage résistif a été capturée par caméra infrarouge bichromatique. L'évolution des forces a été mesurée, ainsi que les champs de déplacement par corrélation d'images numériques (DIC) avec une technique originale dite "auto-émettrice". La méthode des éléments finis (bibliothèque CimLib du laboratoire) a été utilisée pour simuler une partie limitée de chaque éprouvette, la zone d'intérêt, dans laquelle un modèle thermo-élasto-viscoplastique anisotrope, de type Hill48, a été adopté. Les conditions aux limites en vitesse appliquées à cette zone d'intérêt ont été fournies par DIC, la distribution de température imposée provenant de la caméra infrarouge. Les simulations ont permis de calculer la force axiale, les déplacements et les déformations. Par analyse inverse, la minimisation d'une fonction coût (écart expérience-calcul) a été réalisée sur la plateforme d'optimisation du laboratoire (MOOPI) pour identifier les paramètres du modèle sélectionné. Un très bon accord calcul/mesures a été obtenu. L'anisotropie résultant du procédé L-PBF, a également été étudiée, et identifiée par une technique d'optimisation alternée, bien adaptée au nombre important de paramètres à identifier. Ces paramètres d'anisotropie ont été trouvés thermo-dépendants. Différentes origines cette dépendance ont été brièvement investiguées et discutées. La loi de comportement complexe de l'alliage In718, ainsi caractérisée, peut être utilisée en simulation numérique des procédés de fabrication additive par L-PBF pour prédire les défauts potentiels, et optimiser les conditions de fabrication

MOTS CLÉS

Caractérisation haute température, In718, Loi de comportement, Elasto-viscoplasticité, Anisotropie, Corrélation d'images numériques, Optimisation, Simulation numérique, Fabrication additive

SUMMARY

Additive manufacturing of metallic alloys offers many advantages. However, extremely high thermal gradients and cooling rates may induce defects: distortions, residual stress, cracks. Numerical simulation is a predictive approach, but this requires a constitutive model for each considered alloy, under process conditions. In this project, the anisotropic mechanical behavior of the nickel-based superalloy In718, as processed from laser powder bed fusion (L-PBF), is characterized between 800 and 1100°C. Specimens built by L-PBF along different orientations were submitted to sequences combining uniaxial tensile load at different prescribed velocities and relaxation steps of different durations, operated under resistive heating and under vacuum, on a specifically developed testing machine (DEDIMET). The non-uniform temperature distribution on the sample induced by resistive heating was captured by a bichromatic infrared camera. The force evolution was measured, together with the displacement field via digital image correlation (DIC) with an original "self-emitting" method. The finite element method (lab library CimLib) was used to simulate a limited part of each sample, the zone of interest, in which a temperature dependent and anisotropic (Hill48) elastic-viscoplastic constitutive model was adopted. The kinematic boundary conditions applied to this zone of interest were provided by the DIC records, while an imposed temperature distribution was provided by the infrared camera. Numerical simulations gave access to the axial force, the displacement field, and the strain components. By inverse modelling, the minimization of a cost function (distance calculation-measurement) was achieved using the optimization platform of the lab (MOOPI), to evaluate the parameters of the selected model. A very good agreement calculation/measurement was obtained. The anisotropy resulting from L-PBF process, was also studied, and identified by an alternated optimization technique, well suited to the large number of parameters to identify. Anisotropy parameters were found to evolve with temperature. Different origins of this dependance were briefly investigated and discussed. The complex material constitutive law of In718, as identified, can be used in numerical simulation of L-PBF process, to predict potential defects and optimize manufacturing conditions

KEYWORDS

High temperature characterization, In718, Constitutive model, Elasto-viscoplasticity, Anisotropy, Digital Image Correlation, Optimization, Numerical simulation, Additive manufacturing